CRANFIELD UNIVERSITY

Cranfield Defence and Security

Department of Engineering and Applied Science
Aeromechanical Systems Group

PhD Thesis
2013

Varun Thangamani

The Effects of Scaling on High Subsonic Cavity Flow and Control

Supervisors:
Dr Alistair Saddington and Professor Kevin Knowles

October 2013

Abstract

The effects of scaling a cavity with respect to a fixed incoming boundary layer thickness on its flow dynamics and control was studied experimentally. Three cavity models with constant length-to-depth ratio of 5 and length-to-width ratio of 2 and with corresponding linear dimensions in the ratio $0.5 : 1 : 2$ were tested at freestream Mach number 0.71. Additionally, the 0.5 and 1 scale models were tested at freestream Mach number of 0.85. The experiments involved time-averaged pressure measurements, unsteady pressure measurements, and PIV measurements. Time-averaged pressure measurements made at the floor were used to study the 'flow-type' of the cavities. Unsteady pressure measurements were used to study the acoustic characteristics of the cavity. The cavity length-to-boundary layer thickness ratios tested were 10, 20 and 40.

The C_p distribution on the clean cavities indicated a change in the cavity flow-type with change in the cavity scale. Varying the L/δ from 10 to 40 changed the cavity flow-type from open to transitional. Analysis of the frequency spectra of the cavity revealed an increase in tonal amplitudes and OASPL with increasing L/δ. The PIV measurements indicated that this could be caused by an increase in energy exchange between the freestream and the cavity. The velocity magnitudes inside the cavities were found to increase with increase in L/δ.

A comparative study of different passive control methods on the largest cavity showed that leading-edge spoilers were superior in cavity tone suppression. Of these, the effectiveness of a sawtooth spoiler on the three cavities of different scales was tested. The results showed that while the spoiler was effective in eliminating tones and suppression of noise for the smaller cavities, it was unable to eliminate the tones completely for the largest cavity. To find the correct method for scaling the spoilers with the cavity dimensions, different spoiler heights were tested on the three cavities. The results showed that the cavity noise suppression for a given cavity attains saturation level at a particular spoiler height, called the critical spoiler height. An increase in spoiler height beyond the critical spoiler height was found to have no effect on the noise suppression. It is also found that this critical spoiler height can be scaled with the length of the cavity (for given L/D, M and spoiler profile) irrespective of the boundary layer thickness.

To
my parents & dew

Acknowledgements

I take this opportunity to thank my supervisors Dr.Alistair Saddington and Prof.Kevin Knowles for giving me the opportunity to work under their supervision. Their valuable help, support and guidance has provided a constant torque to drive this work towards the right direction and in the right speed.

I am thankful to Dr.Mark Finnis for helping me with the LIC plots and data acquisition programs for pressure measurements. His guidance at various stages of work has been of immense help. Special thanks to Mr. David Wasley for his help in setting up various experiments. His willingness to help and fix troubles (of course, accompanied with his classic British humour) in the experimental set-up & wind tunnel have saved me from numerous hours of delay. Thanks are also due to Dr.Simon Ritchie for his timely help & guidance and Dr.Nathan Philips for teaching me the lab's PIV system. I acknowledge the contribution of the workshop team for their valuable efforts to fabricate my designs. Special thanks to Mr.Brian of the workshop team for giving me valuable tips and help in the various design stages. Thanks to your efforts in fabricating all those 'tricky' spoilers. I also thank Dr. Derek Bray of the PhD committee for his suggestions to the work during the review meetings.

Life in the lab isn't complete without having fellow researchers to share your excitements and frustrations. My thanks to Joao Correia a.k.a JC (shame that I still can't pronounce your name correctly) for being an indispensable friend. The 'daily coffee-walks' and 'Friday English-breakfasts' will stay in my memory for a long time. My other fellow researchers and friends Tanmay, Nathan, Robin, Kan, Avanish, Abhisek, Rahim - thanks to you all for your friendship, help and support.

Last but not the least, my heartfelt thanks to my family for always being there for me. I am grateful to my parents, Thangamani & Rani and my parents-in-law, Srinivas & Sankari for their blessings and support. I am forever in debt to my dear wife, Vidya, for her priceless love, patience and understanding. Thanks for your constant support through the ups and downs of my life. Without you, this work wouldn't have been possible.

Contents

List of Tables

List of Figures

Nomenclature

All units are in SI unless otherwise stated

Alphanumeric

a	Speed of sound
C_p	Pressure coefficient
D	Depth of the cavity
d_i	CCD camera pixel diameter
D_p	Seeding particle diameter
e_{cr}	Correlation random error
e_{se}	Seeding error
f_{wave}	Frequency of longitudinal mode
H	Shape factor
h	Height of sawtooth spoiler
k	Vorticity convection ratio
L	Length of the cavity
L/D	Length to Depth ratio of the cavity
L/W	Length to Width ratio of the cavity
M	Magnification factor
m	Acoustic modal number
M_∞	Freestream Mach number
P'_{rms}	Root mean square pressure fluctuation
P_0	Stagnation pressure

P_∞	Freestream static pressure
$P_{0\infty}$	Freestream stagnation pressure
P_{atm}	Atmospheric pressure
P_{ref}	Reference pressure (20μPa)
q_∞	Freestream dynamic pressure
r	Temperature Recovery factor
Re	Reynolds number
Re^*	Reynolds number per unit length
Stn	Strouhal number
T_0	Stagnation temperature
T_∞	Freestream Static temperature
T_c	Recovery temperature
u or u_{mean}	Mean x-component of velocity
U_∞ or u_∞	Freestream velocity
u_{rms}	RMS of fluctuating $x-$component of velocity
V or V_{mean}	Mean total velocity
v or v_{mean}	Mean y-component of velocity
V_{rms}	RMS of fluctuating total velocity
v_{rms}	RMS of fluctuating $y-$component of velocity
W	Width of the cavity
x, y, z	Cartesian coordinates, x indicates streamwise direction

Greek Symbols

α	Phase lag in Rossiter's equation

Δt	laser pulse separation
δ^*	Displacement thickness
γ	Ratio of specific heats; $\gamma = c_p/c_v$
λ_a	Wavelength of acoustic wave
ω	Angular speed
ρ	Density of the fluid
ρ_∞	Freestream density
ρ_p	Fluid density of seeding particle
τ_a	Relaxation time
τ_t	Characteristic time of flow
θ	Momentum thickness

Abbreviations

AWS	Aft-wall Slant
CAP	Cavity Acoustic Prediction
CC	Clean Cavity
CP	Centreplane
DES	Detached Eddy Simulation
DNS	Direct Numerical Simulation
FTS	Flat-top Spoiler
FWS	Front-wall Slant
LDC	Leading-edge Deep Cavity
LES	Large Eddy Simulation
LR	Leading-edge Ramp

LS	Leading-edge Step
LW	Leading-edge Wedge
OASPL	Overall Sound Pressure Level
*OP*1	Off-centre Plane 1
*OP*2	Off-centre Plane 2
PAW	Porous Aft Wall
PFW	Porous Front Wall
PIV	Particle Image Velocimetry
PSD	Power Spectral Density
RANS	Reynolds-averaged Navier-Stokes
SPL	Sound Pressure Level
STS	Square-tooth Spoiler
SWS	Sawtooth Spoiler
TR	Trailing-edge Ramp
TS	Trailing-edge Step

Chapter 1

Introduction

Cavity flow is a type of fundamental flow phenomenon which can be defined as the grazing fluid flow over cut-outs in solid surfaces. The simplest and the most practical geometry is the rectangular cavity which has been investigated by numerous researchers since the 1950s. Flow over such a geometry can lead to self-sustained oscillations, in turn leading to intense pressure fluctuations inside and around the vicinity of the cavity. Apart from the interesting physics of the flow, grazing flow over rectangular cavities is applicable to a wide range of practical situations. It can lead to significant unsteady aerodynamic and acoustic loads on aircraft internal weapons bays, wheel wells, fuelling ports and many other situations. Aircraft bays, for example, can experience dynamic loads in excess of 160 dB when the bay doors are opened [Cattafesta et al. (2008)]. Such highly unsteady loads can lead to structural fatigue of the cavity and its contents. Flow over cavities can also lead to formation of adverse and steep pressure gradients inside the cavity which is undesirable for the safe release of stores. Stores under the effect of such adverse pressure gradients have been observed to pitch up dramatically into the weapons bay [Dix & Butler (1990)]. Suppression of oscillations is of practical importance and is particularly crucial in the case of a weapons bay.

Techniques to control cavity oscillations can be broadly classified into passive and active. Active control uses external energy input while passive control techniques are mostly geometrical modifications to the cavity and do not employ an external energy source. Active control is further divided into open- and closed-loop control. Passive methods are usually simpler and comparatively inexpensive. They are found to be effective but being a permanent feature, their performance is susceptible to degradation with changes in flow conditions. In contrast, the active methods have the potential to adapt themselves with the changing flow conditions and deliver a consistent performance in controlling the cavity oscillations. However, active control methods are generally found to be incapable of suppressing all the cavity tones effectively. In most cases, active control techniques only target suppression of a narrow range of frequencies while their effect on the amplitudes of other frequencies remain insignificant or are at

times amplified when compared with the baseline case.

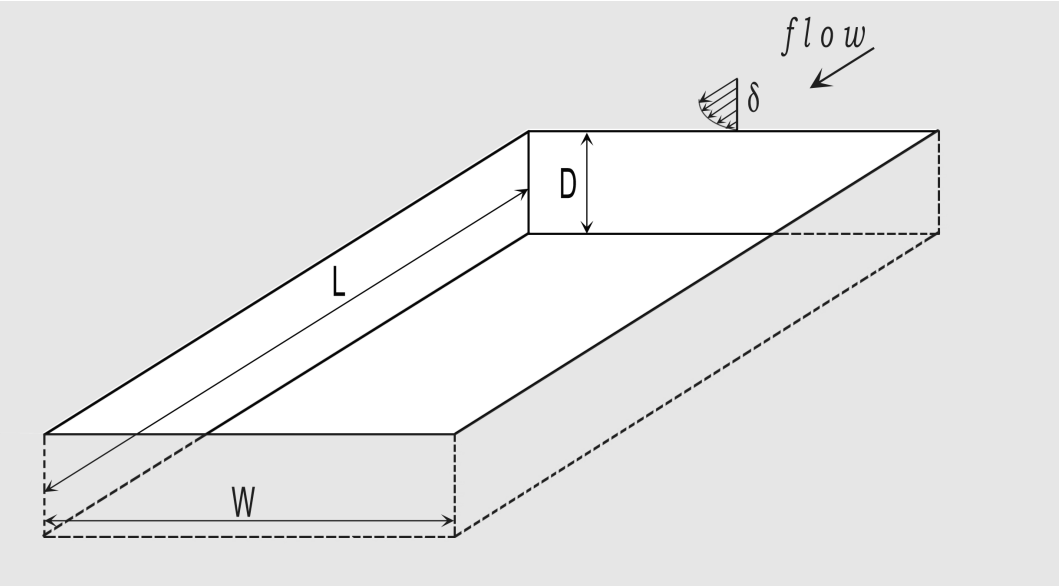

Figure 1.1: Flow over a generic cavity

Figure 1.1 shows the generic flow over a rectangular cavity with all the important parameters involved i.e the length (L), width (W), depth (D), freestream Mach number (M_∞) and incoming boundary layer thickness (δ). The important dimensionless parameters that are used for the testing of cavity flows are L/D, L/W and M_∞. Frequency spectra obtained from the unsteady surface pressures in a cavity with oscillations have tones present in them, known as cavity tones. Although there are methods to predict the frequency of these tones, there is no model that can predict their amplitudes with certainty. This makes the determination of a unique set of scaling parameters for accurate cavity flow-testing difficult. The same set back is suffered during the design of some passive control devices as well. Over the years, different passive control techniques have shown considerable promise in oscillation control in cavities. However, when the cavity model is up-sized, the effectiveness and the rules governing the scaling of the passive control devices are still not clear. This problem becomes critical to control techniques for which the size of the control device and thickness of the incoming boundary layer plays a very important role in suppression of oscillations (e.g. leading edge spoilers, bumps, steps etc.). A proper study to establish whether these passive control devices are to be scaled with respect to the size of the cavity

or with respect to the incoming boundary layer thickness is missing. However, devices like slant walls, ramps, aft wall wedges etc. do not necessarily address this question since the performance of these devices is influenced by shape rather than size and they do not need to be scaled independently from the cavity.

The factor L/δ could be an important scaling parameter in this regard whose influence has not been well understood in the design of control techniques. The ratio L/δ is important because it takes into account the scaling effect as well as the thickness of the incoming boundary layer with respect to the cavity size. Knowledge on the effects of this factor could ensure the successful implementation of a control technique from the wind-tunnel scale to the real scale. Also, it is a parameter that varies in flight depending on factors such as flight altitude, location of weapons bay, dimension of weapons bay etc. For example, increasing altitude for a typical combat aircraft from 1524 m (5000 ft) to 9144 m (30000 ft) can change the L/δ from approximately 30 to 60 for a weapons bay of length 3 m at a Mach number of 0.71 (assuming flat plate turbulent boundary layer growth over a length of 4.5 m from the aircraft nose tip to the cavity leading edge). It is not clearly understood if the different control techniques that have been studied by previous researchers are still successful when this parameter is varied. The variation of control effectiveness with changes in the cavity scale or relative incoming boundary layer thickness needs attention and requires an investigation.

Although there have been studies that demonstrate the significance of L/δ on clean cavities (cavities without control), an in-depth study of their physics is missing and would be essential to determine the impact of L/δ on a particular control technique. This work aims at filling these gaps in the knowledge of cavity flows and control. The first part of the work investigates the variation of a clean cavity flow field across three different values of L/δ. In the second part, the effectiveness of a passive control device is tested across these scales and finally the principles governing the application of the device to different cavity scales or using them across different values of L/δ is deduced. For this, a constant incoming boundary layer thickness has been used to study the flow over three cavities which have been scaled in size in the ratio 0.5 : 1 : 2. To change the ratio of L/δ, a constant δ has been chosen since artificially thickening the boundary layer alters its turbulent length scale characteristics and it is also easier to obtain

a wide and desirable range of L/δ by changing the cavity dimensions. The other ratios, including L/D and L/W, are kept constant in order to eliminate their effects and isolate the influence of L/δ. The work also aims to understand better the application of a leading-edge spoiler to different cavity scales or using it with different values of L/δ.

Chapter 2

Literature Review

In this section, a brief literature review of the basic cavity oscillation phenomenon, the major parameters affecting the flow and various control techniques previously investigated are presented.

2.1 Background

The crucial tasks of a fighter aircraft include the launch of bombs and missiles. These aircraft often operate in an intensely hostile environment which stimulates an increased demand for speed, performance and stealth. Their survivability and manoeuvrability is increased by reducing the radar cross section and drag. These necessities led to the evolution of weapons storage in a fighter aircraft from semi-submerged or tangential carriage to the internal weapons bay used in modern aircraft. However these methods have their own merits and demerits which need to be considered carefully during the design process.

The internal weapons carriage is a system wherein the stores are embedded inside the aircraft in cavities with doors that open when the weapons are to be deployed. It has superior drag reduction, enhances manoeuvrability and minimizes radar cross section. Some fighter aircraft which have internal weapons carriage include the F-22, F-117 and F-35. However, flow past an internal weapons bay can lead to unfavourable pressure conditions inside and around the vicinity of it. When the doors of an internal weapons bay are opened, the cavity which is exposed to the oncoming flow interacts with it. This interaction may lead to a highly unsteady pressure field and/or a steep pressure gradient on the cavity ceiling depending on the bay dimensions and flight Mach number. These problems are only intensified with increases in flight speeds. Flow over certain cavity geometries can lead to pressure oscillations high enough to cause fatigue and damage the aircraft components. Rapid structural failure can occur when the frequency of the oscillations match the natural frequency of a flight component. Also, the steep pressure gradients created inside the cavity can cause a pitch-up moment to the stores released and may cause them to regress back into the fuselage.

The above problems have necessitated the need to control the flow unsteadiness and prevent the build up of strong pressure gradients. Although the shape of the bays can differ depending upon the specific case, a reasonable and idealistic shape to assume would be a rectangular planform cavity. The majority of researchers have adopted this shape and the same is used in this work too. Control of cavity oscillations mainly involve suppressing the high amplitude tones that are generated and reducing the broadband noise. Apart from the case of internal weapons bays, cavity flow control has other potential applications in wheel wells, fuelling ports and a host of other situations also.

2.2 Classification of Cavity Flow Types

Flow over a rectangular cavity is an elementary one and is quite complicated. In a cavity flow, an incoming boundary layer of thickness, δ, separates from the leading edge of the cavity and forms a free shear layer over the cavity length. The development of this shear layer is dictated by the upstream conditions and conditions inside the cavity. The dimensionless parameters that are pertinent in a rectangular cavity flow are the length to depth ratio (L/D), length to width ratio (L/W), free stream Mach number M_∞, cavity length to boundary layer thickness L/δ and shape factor of the boundary layer H = δ^*/θ (where δ^* is the displacement thickness of the boundary layer and θ is the momentum thickness).

Cavity flows can be classified on the basis of different criteria. In terms of the freestream Mach number, it can be grouped as subsonic, transonic or supersonic cavity flow. In terms of the flow field behaviour, cavity flow is categorised as being open, transitional or closed. A cavity is considered as two dimensional if L/W < 1 and three dimensional if L/W > 1 [Tam & Block (1978)]. Three dimensional cavity flows are more influenced by the cavity corners, side walls and boundary layers on the side walls. Also, if L/D <1, it is considered as a deep cavity; otherwise it is termed a shallow cavity [Tracy & Plentovich (1993)].

Depending upon the flow field characteristics, cavity flows can be broadly classified into open, closed and transitional. The flow pattern described below in the following sections is based on the time-averaged mean flow on the centreline of two-dimensional cavities. In a three-dimensional flow, the flow behaviour can

get more complex near the walls. Depending on the flow type, a cavity can exhibit characteristic flow features. These flow features can be easily visualized in a supersonic flow. The explanation and figures given in the following sections are based on experiments carried out in supersonic cavity flows by using schlieren and shadowgraph techniques. The works of Stallings & Wilcox (1987) and Plentovich et al. (1993) demonstrated that there was a good relation between the flow features obtained in visualization and the shape of the cavity floor mean pressure distribution. Because of the problems concerning visualization of subsonic flows, the cavity floor mean pressure distribution obtained for supersonic speeds has been used as a basis to categorize the flow in subsonic speeds.

2.2.1 Open cavity flows

In an open cavity the shear layer separates from the leading edge of the cavity, bridges the length of the cavity and reattaches on or aft of the cavity trailing edge [Tracy & Plentovich (1993)]. Open cavities exhibit intense periodic pressure fluctuations caused by self-sustaining flow oscillations. These self-sustained oscillations are a consequence of the direct interaction of the shear layer with the aft wall. Generally, cavities with an L/D ratio < 10 are observed to exhibit this flow field. This range of L/D ratios are typical of military aircraft bomb bays.

Figure 2.1 shows the characteristic shape of the C_p curve for an open cavity at the centreline. The pressure is roughly uniform for up to almost 40 - 70% of the cavity length from the leading edge. Beyond this region, the pressure increases towards the aft wall and the distribution has a concave-up shape. Flow over open cavities can lead to generation of high-amplitude acoustic tones and the suppression of these tones has been the focus of numerous studies on cavity flows. The strong acoustic tones can induce vibrations in the environment of the internal weapons bay and can lead to structural fatigue. Sometimes the tones may be strong enough to damage the aircraft components.

In supersonic flows, open cavities are characterized by the formation of a shock near the leading edge of the cavity owing to the flow getting deflected away from the cavity. However this shock may be intermittent and the strength may vary in an oscillation cycle. The flow field, pressure distribution on the floor and acoustic signature of an open cavity are illustrated in Figure 2.1. It should

be noted that Figure 2.1 depicts a single large recirculation vortex which is more typical of cavities with L/D < 2. With higher L/D ratios, other flow structures are also possible.

2.2.2 Closed cavity flows

In a closed cavity, the shear layer separated from the leading edge dips into the cavity , reattaches at the cavity floor and separates again before reattaching near the trailing edge [Tracy & Plentovich (1993)]. Generally, cavities with an L/D ratio > 10-13 are observed to display this flow field. These are typical of missile bays on fighter aircraft. As the shear layer touches and separates from the cavity floor, two distinct recirculation regions are created in closed cavity flows. Closed cavity flow creates an adverse pressure gradient inside the cavity which can cause large nose-in pitching moments to the separating store. However, because the shear layer does not impinge on the aft wall directly, acoustic tones are absent in this case.

Figure 2.2 shows an idealized concept of closed cavity flow. It depicts two regions of recirculating flow, one located downstream of the front wall, and the other lying upstream of the rear wall. The centreline C_p distribution in the streamwise direction is significantly different from the open cavity flow. The C_p has negative values near the front wall of the cavity followed by an increase in pressure and a concave-down shape towards the aft wall of the cavity. There is a plateau formation in the curve where the C_p values remain constant. The plateau in the curve corresponds to the area where the shear layer reattaches at the cavity floor and this region elongates with increase in L/D.

2.2.3 Transitional cavity flows

Transitional cavity flow is an intermediate stage between open and closed cavity flows and can be sub-classified into transitional-open and transitional-closed. Generally, cavities with an L/D ratio in the range 7< L/D < 14 are observed to exhibit transitional cavity characteristics. In transitional-closed cavity flows, the impingement shock and the exit shock that normally occur for closed cavity

flow coincide and form a single shock (Figure 2.3). Large longitudinal pressure gradients occur here too as in closed cavity flows, leading to large nose-in pitching moments [Tracy & Plentovich (1993)]. Transitional-open cavity flows can be observed in transitional flows with lesser L/D ratios. In this type, the impingement- exit shock wave abruptly changes to a series of expansion and compression wavelets which indicates that the shear layer no longer touches the cavity floor. For this flow field, longitudinal pressure gradients in the cavity are not as large as those for transitional-closed cavity flow but are larger than pressure gradients formed in open cavities. In the C_p curves of the transitional-open flow, the pressure in the front portion remains similar to those of the open flow while the curve for the rearward portion of the cavity changes from concave-up to concave-down. The pressure coefficients become slightly more negative near the front wall of the cavity as the value of L/D is increased. A small inflection point occurs at approximately the midpoint of the cavity length when the flow becomes transitional-closed.

From the above discussion, it was seen that the type of cavity flow is determined chiefly by the L/D ratio. It has also been found that it is sensitive to the freestream Mach number. The characteristic shape of the C_p curve can be an important tool to identify the cavity flow type especially in a subsonic flow where accurate and informative flow visualization can be difficult. Figure 2.4 shows the change in shape of the C_p curve as the flow changes from open to closed. In this work it will be shown that apart from the factors mentioned above, cavity flow type is also influenced by the L/δ ratio.

2.3 Three-dimensional Cavity Flow Field

While the L/D ratio has a major impact on the nature of flow present in the cavity, the L/W ratio of the cavity can have significant effects on the three dimensionality of the cavity flow field. Three dimensional effects prevail in the locality of cavity walls and corners although three dimensional structures have been observed far from the cavity walls too. These effects become more pronounced for cavities with L/W < 1.

Keeping all other variables constant, Block (1976) studied the effect of L/W ratio by varying the width of the cavity. They used L/W values of 0.541, 1.0 and 1, 1.85 for cavities of L/D ratios 1 and 2 respectively. They observed an increase in the sound power levels and quality factors (ratio of the centre frequency to the frequency bandwidth of the peak) with a decrease in the cavity width but noted that were was no change in the resonant frequencies of the flow oscillations. However, no explanations were provided for the increase in sound power levels.

For a two dimensional cavity flow, the flow is uniform across its entire width resulting in a coherent shear layer. In contrast, for a three dimensional cavity flow, the shear layer is non-uniform across the cavity width and the end effects force the flow to spill over the sides of the cavity. This was observed in the tuft flow visualizations conducted by Ahuja & Mendoza (1995). Random movements of the tufts, especially near the side walls, were observed when the cavity depth was decreased. These end effects decrease the spanwise coherence of the excited instability waves present in the shear layer and alters the amplitude of the cavity tones.

In their experiments, Ahuja & Mendoza found a reduction in sound pressure levels with decrease in cavity width, which contradicts the findings of Block (1976). It was also found that the tonal amplitude reached an asymptote as L/W was reduced close to unity. They noticed that tonal frequencies were unaffected by change in L/W ratio. The results also showed that the parameter L/W, rather than W/D, was more appropriate in determining the three dimensionality of the flow.

2.4 Classification of Cavity Oscillations

The self-sustained oscillations present in cavity flows can also be broadly classified based on the mechanism involved in their generation. They are fluid dynamic, fluid resonant and fluid elastic oscillations, which are described in the following sections.

2.4.1 Fluid-dynamic oscillations

Fluid Dynamic oscillations arise from inherent instability of the flow. Purely fluid dynamic oscillations can occur if the ratio of the cavity length to the acoustic wave length (L/λ_a) is very small. The primary mechanism for excitation of the fluid dynamic oscillations is the amplification of shear layer disturbances and the oscillations are sustained by the presence of the trailing edge of the cavity [Rockwell & Naudascher (1978)]. Due to the presence of a trailing edge in the downstream, a feedback disturbance is propagated upstream through the cavity which amplifies the shear layer disturbances in selective frequencies. This selective amplification, is a necessary, but not sufficient condition for the generation of coherent oscillations. The interaction of the feedback disturbance with the shear layer leads to vorticity fluctuations in the shear layer and gets amplified in the downstream direction.

2.4.2 Fluid-resonant oscillations

This classification pertains to self sustaining cavity oscillations which are strongly coupled with the resonant wave effects in the cavity. For fluid-resonant oscillations, the frequency of oscillations are sufficiently high that the corresponding acoustic wavelength is of the same order of magnitude or smaller than the cavity characteristic length, L or W^2 [Rockwell & Naudascher (1979)]. Shallow cavities exhibit longitudinal modes of oscillations while deep cavities have transverse waves.

Tam & Block (1978) noticed cavity tones generated due to a normal mode resonance mechanism at very low Mach numbers (M<0.2). They have also indicated in their work that the transition between the feedback mechanism and normal

mode resonance was rather gradual which implied that a unified model of the phenomenon of flow-induced cavity tones is possible. The prediction of the exact value of L/λ_a at which standing waves will occur is difficult to deduce due to the presence of a cavity free shear layer, mass exchange near the trailing edge and other effects which alter the situation from the ideal rectangular resonator condition without any adjacent mass flow.

Rossiter's equation applies not only to fluid dynamic oscillations but also to fluid resonant oscillations if any possible effects of the resonating wave on the empirical constants α and k are considered. The empirical relation for Strouhal number for a resonant cavity, known as cavity resonance Strouhal number ($f_{wave}L/U_\infty$) was first analyzed by Bilanin & Covert (1978) and Tam & Block (1978) extended their analytical framework and included the wave reflection from the cavity floor. The resulting equation was of the same form as Rossiter's relation but included an additional term involving L/W.

Ahuja and Mendoza in their studies tried to compare the acoustic resonant tones and the feedback tones [Ahuja & Mendoza (1995)]. They used the following relation for estimating the resonant tones:

$$f_{wave} = \frac{a_c}{2}\sqrt{\left(\frac{n_x}{L}\right)^2 + \left(\frac{n_y}{2D}\right)^2 + \left(\frac{n_z}{W}\right)^2} \tag{2.1}$$

where n_x, n_y and n_z are the mode numbers for the length-wise ,depth-wise and width-wise duct resonance frequencies, respectively, and a_c is the sound speed in the cavity given by the expression

$$a_c = a_\infty \left[1 + r\,(\beta - 0.5)\,M^2\right]^{0.5} \tag{2.2}$$

where a_∞ is the freestream static sound speed, β is the adiabatic exponent. r is the recovery factor given by

$$r = \left(\frac{T_c - T_\infty}{T_0 - T_\infty}\right) \tag{2.3}$$

where T_c, T_∞ and T_0 are the recovery temperature, static and the stagnation temperature of the freestream flow respectively. The recovery temperature, T_c, is the adiabatic wall temperature acquired by a wall in a fluid flow if the condition of thermal insulation is observed on it.

The above equation for finding the normal mode frequencies are typically used for room acoustics and was modified for the open face of the cavity. From the results, they observed that high amplitude discrete tones were produced whenever the duct resonance tones match the feedback tones closely. They also suggested that there can be possible coupling between the feedback and resonant tones.

2.4.3 Fluid-elastic oscillations

Fluid elastic oscillations occur when one or more walls of a cavity are displaced to produce disturbances that are large enough to exert feedback control on the shear layer. In such type of oscillations, there is a complex interaction between the structure and the flow where the inertial, elastic and damping characteristics of the structure have a significant role on the flow.

2.5 Modes of Cavity Oscillations

Cavity flows can generate self-sustained oscillations which involve shear layer instability, flow-induced resonance and turbulence. However the basic mechanism of tone generation in cavity flows can differ based on certain aspects. Cavity oscillations can be due to the following modes :

a. Shear-layer mode

Shear-layer modes of cavity oscillations occur due to a feedback mechanism between the Kelvin-Helmholtz instabilities or vortical disturbances in the shear layer and disturbances created in the cavity due to the interaction between the shear layer and the aft wall of the cavity. It is the most applicable mode of oscillation in aircraft cavities. It is also called the Rossiter mode.

b. Wake mode

Wake modes of oscillations can be attributed to a mechanism quite different from the shear layer mode. It occurs due to an absolute instability of the shear layer and is characterised by a violent ejection of vortices from the cavity. Extremely large disturbance amplitudes are observed for the wake mode of oscillations. The shear-layer and wake modes are now described in more detail below.

2.5.1 Shear-layer mode

The shear-layer mode is the most common mode of cavity oscillation that has been observed and is of more practical importance since it is relevant to internal weapons bays.

A cavity with oscillations contains a shear layer that has a frequency spectrum with peaks. This is in contrast to an unforced free shear layer which has a broadband spectrum even with the presence of Kelvin-Helmholtz instabilities. The studies to determine the nature, mechanism and control of such flow-induced noise and oscillations have been the subject of various studies since the 1950s. Krishnamurty (1956), Plumblee et al. (1962), Rossiter (1964), Heller et al. (1971) and Bilanin & Covert (1978) were some of the early investigators in this field.

In his pioneering work, Krishnamurty (1956) observed that cavities exposed to a supersonic cross stream exhibited an oscillatory flow field and recognised the interaction between the shear layer and trailing edge of the cavity. Plumblee et al. (1962) suggested that the oscillations observed in the flow were a result of cavity resonance. According to their theory, the turbulent shear layer which spans the cavity length creates a broadband noise source near the trailing edge and the narrowband frequencies which have the maximum acoustic response from the cavities are selected for amplification. However, this theory cannot explain the cavity oscillations observed when the incoming boundary layer is laminar. Experimental results also contradict with the explanation of Plumblee. It has been observed that a laminar boundary layer produces stronger tones in a cavity than a turbulent boundary layer [Karamcheti et al. (1969), Heller et al. (1971)]. Following this, Rossiter (1964) is one of the earliest investigators who suggested a model for flow oscillations in a rectangular cavity based on an acoustic feedback. He observed that vortices were periodically shed near the leading edge which are then convected downstream in the shear layer until they reach the trailing edge and interact with it. However, schlieren visualizations by Krishnamurthy did not indicate any vortex shedding near the leading edge.

The Rossiter mode is one of the most widely studied cavity modes for both subsonic and supersonic flows. According to the explanation given by Rossiter, the tones were generated due to a feedback cycle. The shear layer that separates from the leading edge impinges on the trailing edge producing pressure distur-

bances that propagate upstream as acoustic waves. These acoustic waves reach the leading edge of the cavity and trigger vortical disturbances in the shear layer. In essence, the feedback cycle described by Rossiter basically consists of the following four elements :
1) creation of an oscillating pressure field through interaction of the shear layer with the aft wall of the cavity
2) feedback by upstream propagation of the acoustic waves inside the cavity
3) interaction of the acoustic wave with shear layer and triggering of vortical disturbances in the shear layer near the leading edge
4) growth and convection of vortical disturbances in the shear layer.

Figure 2.5 shows the various components of the Rossiter feedback described above. The frequency of these cavity tones is determined by the cavity geometry and flow conditions. Using the concept that the timing of the various elements of the feedback loop must be synchronized, Rossiter derived the following semi-empirical formula for the tone frequencies:

$$\frac{fL}{U_\infty} = \frac{m - \alpha}{M + \frac{1}{k}} \tag{2.4}$$

where f = frequency of tones, U_∞ = freestream velocity, m = an integer, M = Mach number, k = ratio of convection velocity of vortices to free stream velocity, α = a factor to account for the lag time between the passage of a vortex and the emission of a sound pulse at the downstream corner of the cavity. The model, however, does not provide the numerical values for k and α. They are treated as empirical constants to be determined by a best fit to measured data. Rossiter found that by taking α = 0.25 and 1/k = 1.75, the above equation agreed with his measured data very well. Figure 2.6 shows the values obtained by Rossiter in his experiments.

The Rossiter model, however, does not provide any further explanation about how the pressure disturbances are generated near the aft wall of the cavity or how the shear layer near the leading edge is excited by it. It also failed to explain the absence of vortex shedding in Krishnamurthy's schlieren visualizations. To account for these, Heller & Bliss (1975) gave an analytical treatment to the problem. They discarded the idea of vortex shedding near the leading edge and argued that

shear layer vortices are normally not observed at supersonic flows and suggested that vortex shedding behaviour was a manifestation of the oscillatory flow behaviour. They described the shear layer oscillations as a flapping motion which periodically adds and removes mass near the trailing edge. This periodic mass exchange between the cavity and the freestream created a 'pseudopiston' effect at the aft wall which creates pressure disturbances that travel upstream toward the leading edge. This process creates a wave structure that is responsible for the flapping motion of the shear layer.

Heller et al. (1971) used a correction factor in Rossiter's original equation to account for higher sound speeds in the cavity. The non-dimensional feedback frequency, Strouhal number, as expressed by them is

$$\frac{fL}{U_\infty} = \frac{m - \alpha}{M_\infty \left[1 + \left(\frac{\gamma-1}{2}\right) {M_\infty}^2\right]^{-0.5} + (1/k)} \tag{2.5}$$

where f is the frequency of the m^{th} mode, m= 1, 2 ....., α is a phase constant between the downstream propagating vortical disturbances and the upstream propagating acoustic waves, 1/k is a vorticity parameter. α and k are obtained empirically. The equation is referred to as the modified Rossiter equation. The empirical constant is the ratio of the average instability wave convection velocity to the free stream velocity and is a function of the freestream Mach number. The choice of k = 0.57 has proven to be in good agreement with experimental data for subsonic Mach numbers greater than M = 0.4. The constant, α, has been found to be a function of L/D. There has been good agreement, in general, between the measured frequencies of various researchers and the frequencies according to equation 2.5.

Bilanin & Covert (1978) proposed a model which described the shear layer disturbances as excitation of instability waves. They assumed that the shear layer was periodically agitated near the leading edge of the cavity which excites the instability waves in it that grow and convect downstream. The fluctuating motion of the shear layer near the aft wall induces a periodic influx of outflux of mass into and from the cavity respectively. This mass exchange acts as the source of acoustic disturbance. They modelled the shear layer as a thin vortex sheet and the noise source as a line source which pulsated periodically. However, they did

not explain the interaction between the flow instabilities and the acoustic waves as they used a line pressure force at the leading edge to simulate shear layer excitation by acoustic waves. The prediction of tones according to their model agreed reasonably well at high supersonic Mach numbers but didn't match the experimental results at low supersonic and high subsonic Mach numbers.

Tam & Block (1978) in their analytical model significantly improved the model proposed by Bilanin and Covert. They included the effects of finite shear layer thickness, L/D ratio and treated the excitation of shear layer instabilities by the acoustic waves more rigorously. Further, they also took the reflection of acoustic waves from the cavity floor into consideration. They compared their model with experiments performed at M<0.4 and found a good agreement of the tones with tones predicted from their model. They also observed that the oscillations switched to normal modes when M<0.2.

From the discussion above, it could be understood that the self-sustaining oscillations in a cavity can be strongly influenced by shear layer instability acting in conjunction with disturbance feedback and a resonant wave condition or a complex combination of these effects. However, there is no model which satisfactorily incorporates all the effects. Nevertheless, Rossiter's equation and its modified version are still being used to predict the cavity tone frequencies with fairly good accuracy. Ahuja & Mendoza (1995), in their extensive studies of cavities with different L/D ratios found that Rossiter's equation was a good indicator of cavity feedback tones and the values fell within 20% of the measurements on average.

2.5.2 Wake mode

The wake mode of oscillation is observed when the onset boundary layer is very thin and/or when the Mach number and Reynolds number are increased. The flow behaviour differs substantially to the shear-layer mode described in the previous section. A cavity oscillating under a wake mode exhibits large-scale vortex shedding from the leading edge. Gharib & Roshko (1987) were the first to describe the transition from shear-layer mode to wake mode in detail. They observed in their water-channel studies that the increase in the ratio of the cavity length to the momentum thickness of the incoming boundary layer (L/θ) beyond 120 was accompanied by a dramatic increase in drag of the cavity. They described

this as the onset of the wake mode. For values of L/θ in the range $80 < L/\theta < 120$, they noticed that the self-sustained oscillations occurred in the shear-layer mode.

Figure 2.7 details the flow features observed in a wake mode oscillation. A vortex forms at the leading edge after separation and grows to almost the size of the cavity. The formation of this vortex entraps irrotational freestream fluid into the cavity which impinges on the cavity walls. The growth in the size of this vortex leads to the formation of a secondary counter-vortex between it and the front wall. This secondary vortex becomes strong enough to eject the large vortex out of the cavity. The vortex becomes large enough and causes flow separation in the upstream boundary layer which convects the vortex formed due to separation. This separation vortex is again shed from the leading edge and the cycle continues. The wake mode has not been often observed in practice and is not as pertinent to aircraft situations as the shear-layer mode.

2.6 Effect of Boundary Layer on Cavity Oscillations

Studies on the effects of the incoming boundary layer on cavity oscillations have been very few. Earlier research in this area was focussed on classifying the effects of laminar and turbulent incoming boundary layers on cavity oscillations. Karamcheti et al. (1969) observed that laminar upstream boundary layers produced stronger tones than turbulent boundary layers. This was corroborated by Heller et al. (1971) who, in their study on the effect of a laminar and turbulent boundary layer on a Mach 3 cavity flow, noticed the absence of strong resonant peaks in the turbulent boundary layer case. Gloerfelt et al. (2003) in their numerical simulation of cavities with various boundary conditions using LES (large-eddy simulation) also observed similar results. They found that in a turbulent boundary layer, there was loss of coherence which can lead to a decrease in feedback strength and amplitude of tones. Sarohia & Massier (1977) studied the effects of a laminar boundary layer on the cavity shear layer and found that the growth rate of the shear layer was close to the entrainment rates of a turbulent mixing layer. They linked the high growth rate to the strong oscillations present in the cavity.

Koschatzky et al. (2011) investigated the acoustic emission characteristics of a cavity under the influence of incoming laminar and turbulent boundary layers. Experiments were performed with free-stream velocities of 10 m/s, 12 m/s and 15 m/s, producing a Reynolds number based on cavity length, L, in the range 20000 - 30000. While the power-spectrum results showed the presence of high amplitude tones in the laminar boundary layer case, they were found to be absent in the cavity with a turbulent incoming boundary layer. They also found from PIV studies that the size of the standing vortex inside the cavity had become smaller for the turbulent boundary layer. They attributed the absence of tones and reduction in the thicker turbulent boundary layer case to this reduction in size of the recirculation vortex inside the cavity and hence its inability to destabilize and generate vortical disturbances in the shear layer.

Vakili & Gauthier (1994) concluded that by injecting mass near the leading edge, the boundary layer was thickened which significantly altered the instability-wave growth characteristics of the shear layer. They studied different blowing ratios at M = 1.8 and reduction of tonal amplitudes of up to 27 dB was observed for a cavity with L/D = 2.54.

According to the model proposed by Tam & Block (1978), the excited instability waves in the cavity shear layer are an intrinsic component of the feedback loop which is responsible for generation of the tones. The growth rate of these instability waves can be a strong function of the shear layer thickness. Hence, they suggested that the thickness of the incoming boundary layer thickness could play a major role in the cavity oscillation mechanism. The most important work that is relevant to the present study is that of Ahuja & Mendoza (1995). In their studies, they thickened the upstream turbulent boundary layer using a backward-facing step to study the effect of boundary layer thickness on cavity noise. The experiments were done for a cavity with L/D = 3.75 and L/W = 0.468 at M = 0.4. The values of L/δ obtained after tripping the flow were 26.3, 22.2 and 15.1. It was found that an increase in boundary layer thickness from L/δ = 26.3 to L/δ = 22.2 eliminated the first and third modes, whereas it increased the amplitude of the second mode, which was the dominant mode. By increasing the boundary layer thickness to L/δ = 15.1, it was observed that the cavity tones were reduced to broadband level with a reduction of 23 dB in some cases. However, no explanation was given of the observations made. Also, there was no mention of the

effect on the pressure gradients on the cavity floor and besides the narrow range of L/δ values, experiments were not extended to higher Mach numbers.

Dix & Bauer (1991) developed the Cavity Acoustic Prediction (CAP) code based on fluid dynamic relations in conjunction with Chapman-Korst mixing analysis [Chapman & Korst (1954)] to develop an analytical method for predicting amplitudes. The influence of boundary layer thickness was also taken into account. Though the CAP code was not accurate in predicting the amplitude, it demonstrated the influence of incoming boundary layer on cavity tones. The constants in Rossiter's equation was found to vary with boundary layer thickness. The importance of the parameter L/δ in determining the overall acoustic levels in the cavity was demonstrated. They compared the prediction with results obtained by the scaling studies of Shaw (1989).

Ross (2001) studied scaling effect of cavities by using three cavities scaled in the ratio 1 : 0.5 : 0.25, with L/D = 5 and W/D = 1 at Mach numbers ranging from 2.5 to 4.5. He noted that the effect of cavity scale on pressure oscillations is quite complex. For the rear 5% of the cavity length, he observed a decrease in the tone amplitude for the two smaller cavities. He noted that this result was in accord with the work of Shaw (1989), who suggested that a reduction in cavity tone amplitudes can occur when L/δ > 33. However, these studies which are very relevant to the current work, could not provide a deep insight into the fluid mechanics relevant to the change in scale. Ross also failed to mention the values of L/δ that were used in his work. A complete study of the flow field with visualization can help to explain the results obtained by these researchers, which is one of the objectives of the current work.

The turbulence levels and thickness of the boundary layer could also have considerable effects on the pressure gradients along the cavity floor. Charwat et al. (1961) found that, in general, an increase in δ/D smoothed out the pressure gradients on the cavity floor. This was presumed to be due to the decreased momentum transfer to the cavity. Stallings & Wilcox (1987) did extensive studies on mean pressure distribution on cavity floor. They found that by keeping the ratios L/D and L/W constant and by varying the dimensions of the cavity, the pressure levels at the rear portion of the floor and aft wall decreased with increase in the ratio δ/D. This result was consistent with the observation of Charwat. However, the studies were limited to purely closed and purely open cavity flows.

There were no studies in the transitional regime and the researchers have failed to notice any change in the flow type with variation in δ/D.

Yang et al. (2010) studied the effects of boundary layer thickness on a flow of Mach number 1.5 by studying two models of L/D and L/W ratios 8, 1.45 and 8, 2.567 respectively. They used cavities of different sizes and boundary layer thickness. The δ/D measured was 2.4 for the first and 0.16 for the second model respectively. It was found that a decrease in δ/D caused an increase in SPL, oscillation amplification and peak frequency splitting. This is another study which corroborates the importance of using the ratio of boundary layer thickness to a cavity dimension as a factor for investigating scaling effects and the influence of δ.

Computational studies to investigate the effect of boundary layer thickness on cavity flows have been very few. In this regard, Togiti et al. (2009) studied three different boundary layer profiles - a laminar, turbulent and a thick turbulent boundary layer on a cavity with L/D = 5.2 at M = 2. The thicknesses of the three different boundary layers were 2.6 mm, 1.5 mm and 7.5 mm respectively. In the case of the laminar boundary layer, an earlier flow separation compared to the turbulent cases was observed and the inability of the oncoming boundary layer to sustain the adverse pressure gradient was cited as the reason for this. This led to strong vortical disturbances in the free shear layer causing strong entrainment of fluid into the cavity. For the cavity flows with the turbulent boundary layers, it was found that the reverse velocities inside the cavity, overall sound pressure level (OASPL) and size of vortical structures in the shear layer decreased with increase in the thickness of the boundary layer.

2.7 Control of Cavity Oscillations

Control of oscillations has gained significant attention recently due to the use of internal weapons bays in modern aircraft. Over the years, researchers have studied various control techniques for cavity oscillations and a few of the more important works will be discussed in this section.

Techniques to suppress cavity oscillations can be broadly classified into passive and active. Active control uses external energy (e.g. mechanical or electrical) for the control while passive control techniques do not [Cattafesta et al. (2008)]. Active control techniques are expensive and more difficult to design and implement, while passive control techniques are relatively cheap and simpler. However, most passive control devices do not work with the same efficiency at a wide range of flow conditions and cannot be adapted to the changing conditions while active control holds the promise of that. However, active control methods mostly target specific frequencies and adaptive-control techniques have not been successful yet at higher flow speeds. At a given Mach number, passive control methods have definite advantages as it is easier to implement and achieves satisfactory suppression of all the cavity tones.

2.7.1 Passive control

Passive control of cavity oscillations has been researched since the 1960s and some of the successful implementation of passive control methods has been via rigid fixed fences, spoilers, ramps and slant walls. Though passive control devices do not require external energy, certain devices like un-powered or passive resonance tubes extract energy from the flow and have been called active in some works. However, these devices do not possess the same control effectiveness at all flow conditions. Among the many passive control techniques explored, leading-edge spoilers, aft-wall slants and trailing-edge ramps have been shown to be very effective and in some cases achieve complete attenuation of cavity tones. There are numerous works published on passive control of cavity oscillations and a few of them are discussed below.

Perng & Dolling (2001) studied the effects of different passive control techniques in high speed flows. They studied different downstream modifications

like slotted, vented and beak aft walls and also leading edge spoilers and vortex generators (see Figure 2.8. With the use of mean wall pressure distribution and power spectra, they found that slant and beak aft walls are effective methods to reduce cavity unsteadiness both in a clean cavity case as well as in the presence of vortex generators at the leading edge.

The effectiveness of slant aft walls (Figure 2.9) as control devices was demonstrated by Ben-Yakar & Hanson (2001). They proposed that the shear layer reattachment at the trailing edge was responsible for the cavity tones and by modifying the aft wall, the generation of acoustic disturbances can be suppressed. They corroborated the concept by using instantaneous schlieren photographs. Later, Vikramaditya & Kurian (2009) also studied the effect of aft wall modifications and ramp angle modifications (Figure 2.10) in oscillation control in supersonic flows. It was found that cavities with smaller slant angles of the aft wall achieved a large suppression and it was proved that the acoustic feedback was absent in such cases. The absence of acoustic feedback infers the disruption of the feedback loop that causes tone generation.

Zhang et al. (1998) studied the effects of a slant wall (Figure 2.9) and a curved ramp (Figure 2.11) on cavity oscillations by computational methods. The studies were carried out at a Mach number of 1.5 and it was observed that both the methods were effective in suppressing the cavity oscillations by modifying the interaction between the shear layer and the trailing edge. It was found that a 45^0 slant wall and curved ramp with height 0.6D were most effective in decreasing the cavity unsteadiness. They also noticed a considerable reduction in the drag coefficient with the use of these trailing edge devices. This was attributed to the decrease in the high pressure area near the aft wall of the cavity.

Kok et al. (2008) used various computational schemes to study the supersonic flow over a clean cavity and a cavity with a 45^0 ramp. They used L/D and L/W ratios of 4.5 and conducted the studies in a free-stream Mach number of 1.2. They noticed a reduction in the amplitude of pressure oscillations with the use of a ramp. The use of ramps also decreased the OASPL along the cavity floor centreline barring a small region near the beginning of the ramp.

Lee et al. (2008) investigated the effectiveness of triangular bumps (Figure 2.12) and sub-cavities (Figure 2.13) near the leading edge of cavity at Mach number 1.8 by using time-dependent, mass-averaged Navier- Stokes computation based on

large eddy simulation . The results obtained from their simulation showed a reduction in the pressure oscillation energy near the trailing edge with the use of the passive control devices. They found the use of sub-cavities below the leading edge to be a more effective control method than the triangular bump. However they noted that parameters like the depth of the sub-cavity and its position with respect to the leading edge need to be carefully considered when implementing this method.

MacManus & Doran (2008) studied the effectiveness of a number of leading-edge step arrangements (Figure 2.14) in a cavity with L/D = 5 in the transonic Mach number range 0.7 - 0.9. The leading-edge step that had a step height to step length ratio of 0.4 was found to achieve the maximum attenuation. This configuration achieved a tonal suppression of up to 18.6 dB and an OASPL reduction of approximately 7.5 dB. From oil flow visualisations, they hypothesized that the step face may have a large recirculation bubble which deflects the separated shear layer away from the cavity. Introduction of the step arrangement was also found to decrease the frequency of the tones by approximately 19%. Although the leading-edge step had a very notable impact on the unsteady flow characteristics at Mach 0.9, the results also showed that the effectiveness was poor at lower Mach numbers.

Lada & Kontis (2011) studied the effects of placing wedges (Figure 2.15) on a transonic cavity flow of M = 0.8 over cavities with L/D = 2 and 6. They investigated the acoustic signature of the cavity when a 15^0 and 30^0 wedge was placed respectively near the front wall and aft wall of the cavity. They obtained maximum suppression for the L/D = 2 cavity with the 30^0 wedge placed on the trailing edge. They attributed the suppression to the disturbance of the shear layer by the wedge. For the L/D = 6 cavity, they noticed that the cavity flow type changed from open to transitional. They observed that introducing a wedge on the cavity could have an impact on the amplitude as well as frequency of the tones since it effectively changes the L/D ratio of the cavity across the span. Control of cavity oscillations by using wedges were studied in closed cavities too and it was found that placing the wedges at the leading edge of a cavity with L/D ratio 18 decreased the adverse pressure gradient on the floor [Lada & Kontis (2010)]. This result has a desirable effect on reducing the pitching moment of missiles stored in the weapons bay. For a transitional cavity with L/D =11, the change in

the pressure gradients with the use of wedges was much less than for the closed cavity.

The use of spoilers as a means of suppressing cavity tones and noise was first tested by Rossiter. Rossiter (1964) in his experiments found tone attenuation with increase in boundary layer thickness. Using this concept of thickening the boundary layer to suppress the oscillations, he used spoilers with rectangular elements of various dimensions at the leading edge of a cavity of L/D = 1. The flow Mach numbers tested were M = 0.7, 0.9 and 1.2 and two different spoiler heights (0.77δ or 0.063D and 0.38δ or 0.031D) were employed. It was observed that the cavity tone amplitudes reduced with the use of spoilers and the suppression increased with spoiler height and the maximum suppression was observed for the spoiler with height equal to the boundary layer thickness. Later, Shaw et al. (1988) studied the effects of a sawtooth spoiler and found that at M = 0.9, the spoiler reduced the broadband noise but was not effective in suppressing the tones. The two studies mentioned above highlight the spoiler height and Mach number dependence of spoiler effectiveness.

Arunajatesan et al. (2002) conducted a hybrid RANS-LES simulation of a 3D cavity of L/D = 5 at M = 0.6 for a clean cavity and a cavity with a cylindrical wire submerged in the upstream boundary layer which was used as a control spoiler. Results showed that in the presence of the control spoiler the shear layer deflects away from the cavity, is spread out over a greater extent, and is less intense. The magnitude of peak intensity and gradients of the turbulent shear stress were lowered while the integrated turbulent kinetic energy of the shear layer was increased with control. Ukeiley et al. (2004) found that the reduction inside the cavity was less than on the aft wall and noted that the effect of a solid fence was to minimize the interaction of the shear layer with the aft cavity wall. Geraldes (2005) in his experiments at M = 0.85 on a cavity with L/D = 4 observed that the tones attenuated with the use of spoilers .

The effectiveness and the mechanism of control of cavity oscillations by employing spoilers have been studied by Ashworth (2008) through DES computations and experiments. Pressure measurements were made at Mach number 0.85 in a clean cavity of D : W : L = 1 : 1 : 5 and compared to cavities with spoilers. The spoilers used had 10 triangular elements with height equal to the incoming boundary layer thickness. A reduction in 7-15 dB in the tonal amplitudes was

observed with the use of spoilers. The numerical simulations matched with the experiments and from the vorticity contours, a rise in the level of the shear layer up to $1/5^{th}$ of the cavity length was observed. It was reasoned that the deflection of the flow was caused by the obstruction created by the spoiler and was responsible for the reduction in cavity tone amplitudes. Ashworth noted that the deflection caused the point of interaction of the shear layer with the rear wall to be shifted downstream. For the clean cavity, the mean line of the shear layer was found to remain at the level of the open face of the cavity. The spoiler was also found to thicken the shear layer. It was reasoned that the tone attenuation observed with the spoilers is simply an effect of the vertically-displaced shear layer having a weaker interaction with the aft wall of the cavity. It was also noted that the number of teeth on the sawtooth spoiler has no significant influence on the shear layer development.

Lawson & Barakos (2009) studied the effectiveness of a sawtooth and flattop spoiler, sloping wall and transverse rod on a cavity with L/D = 5 and M = 0.85 using DES and compared their simulation results with experimental values . This work gave an insight into various mechanisms responsible for the attenuation of noise in leading edge (flattop spoiler and transverse rod) and trailing edge (slant wall) passive control . Results showed that by using the transverse rod and the spoilers, the shear layer was lifted and thus reduced its interaction with the aft wall. However, the tones were not completely absent and an increase in their frequency was also noted. It was noted that the reduction of interaction between the shear layer and aft wall as well as reduction of oscillations of the shear layer - both were keys to achieve a reduction in OASPL and not just a single factor alone. The trailing-edge devices were found to be more effective and they were observed to achieve reduction by deflecting the acoustic waves away from the aft wall of the cavity. This deflection resulted in a more stable shear layer along the entire length of the cavity.

2.7.2 Active control

Many passive control methods described in the previous section are usually successful only within a narrow range of flow conditions. Certain passive control devices also induce significant drag to the body. The ability to adapt to changing

flow conditions has recently highlighted the potential of active control systems. There are many principles upon which active control techniques work but a majority of them either replicate the effects of a passive control device or force the shear layer at a frequency different than the cavity resonant frequency. Shear layer forcing at a frequency different to the acoustic feedback frequency prevents the amplification of the disturbances downstream and enables suppression of the cavity tones. Active control is further divided into open and closed loop control. A closed-loop control has a feedback loop in which the control signal is modified based on a feedback signal from the flow. An open-loop control has no feedback although the input signal can be varied. Further classifications of closed-loop cavity control are those of quasi-static and dynamic feedback control. Most of the experiments related to the control of cavity oscillations are open-loop based. Some of the active control actuators that have been studied are oscillating flaps, steady and unsteady air injection systems and microjets.

Air injection has been successfully demonstrated as a promising active control technique. A commonly used parameter to describe the forcing amplitude of air injection, defined by Vakili & Gauthier (1994), is the blowing coefficient given by

$$B_c = \frac{\dot{m}}{\rho_\infty U_\infty A_{cavity}} \tag{2.6}$$

where $\dot{m}$ is the injection mass flow rate and A_{cavity} is the cavity plan area (L x W) and A_{inj} is the cross-sectional area of the injector. Sarohia & Massier (1977) studied the effect of steady mass injection at the floor of two axisymmetric cavity models in a subsonic flow. They found that large mass flow rates were required (B_c = 5 - 15%) to suppress the tones through base flow injections. Mendoza & Ahuja (1996) studied the effect of steady wall injection via a coanda surface. By comparing the boundary layer profiles of the baseline and injection cases, they concluded that boundary layer thickening was responsible for tonal attenuation. Further studies related to cavity control using steady and pulsed injection were conducted by Vakili & Gauthier (1994), Sarno & Franke (1994), Lamp & Chokani (1997), Shaw & Northcraft (1999), Lin & Rockwell (2001) and Stanek et al. (2003).

Cavity oscillation control studies were done using microjets also. Microjets are small, robust actuators which cause minimal total pressure losses but create

a high momentum flux with a relatively small mass flux. Bueno et al. (2002), Zhuang et al. (2006) and Thangamani & Kurian (2013) were some researchers who studied the effectiveness of microjets as control devices. In general, all these works suggest that cavity unsteadiness is decreased by a combination of effects involving thickening of the boundary layer, introduction of streamwise vortices and increase in three dimensionality of the shear layer that decreases coherence and deflection of the shear layer which reduces interaction between the shear layer and the cavity trailing edge. These are elements of a feedback loop and the weakening of any of these constituents weakens the feedback loop leading to a reduction in cavity unsteadiness. The position of the microjet injection was also found to affect the suppression of oscillations achieved [Thangamani & Kurian (2010)].

Successful studies on closed-loop and quasi-static closed-loop control have been very few. Cattafesta et al. (2008) worked on a dynamic closed-loop control using a real time adaptive feedback on a cavity of L/D = 5 and Mach number range 0.4 - 1.35. The method was based on wave cancellation which can have significant drag benefits and energy efficiency. However, the experiment was not entirely successful due to the degradation of the bi-morph crystal used in the actuators. Shaw & Northcraft (1999) developed a quasi-static closed-loop control device at a Mach number range 0.6 - 1.05 on cavities with L/D = 6.46 and 3.67. They used oscillating fluidic injections in which the mass flux and frequency of injection were adjusted based on a feedback signal. Although the device was successful at suppressing the cavity tones, it unfortunately also excited tones at other frequencies. This is a general drawback seen in control devices with a closed-loop control approach.

Yuan et al. (2009) studied two active-control techniques for a cavity with L/D = 4 in the Mach number range 0.25 - 0.5. The first method was an open-loop approach which generated oscillations at an optimum frequency with zero net mass forcing. Introduction of such an artificial resonant frequency introduces mode switching between the resonant and forcing modes. Such a switching process is not instantaneous and dissipates energy into the flow between the switching which leads to a less efficient cavity resonance. The second method termed a Parallel-Proportional (PP) controller was a linear control method which suppressed the cavity tones by spreading the tonal energy across the acoustic

spectrum. This method was based on real-time feedback. Although both the methods were reported to give satisfactory performance, the second method was able to control in a wider range of flow conditions.

Yuan et al (2004) also used a feedback control approach in a cavity of L/D = 1 at 31 m/s freestream velocity. They used a vibrating surface placed at the trailing edge to control the volume velocity generated by the interaction of vortices with the trailing edge. Feedback was provided from pressure fluctuations in the cavity floor to which the vibrating surface was synchronised. The method was quite successful and tonal attenuation of up to 20 dB was observed.

2.8 Motivation for the Current Work

From the review of past experimental studies, it could be noted that there exist some successful techniques, both passive and active, to control cavity oscillations. Some of them, however, are not equally effective at all conditions. It was seen that one variable that can significantly offset the performance of control devices is the Mach number. Control devices should be designed such that they perform satisfactorily over a wide range of Mach numbers since it is a crucial flight variable. Another significant factor that can offset the performance of these devices is the scale of the model, whose influence is of practical importance. Alternatively, the influence of the scale of the model can also be seen as the change in the thickness of the incoming boundary layer with respect to the model. This is a very important parameter without which a control technique cannot be successfully implemented on an actual aircraft weapons bay.

The relevance of the scale of a model can be seen in two different aspects. First, at a given Mach number, cavities can be exposed to different thicknesses of the incoming boundary layer depending on factors like the position of the weapons bay on the aircraft and the altitude at which the aircraft is flying. Secondly, it determines the factors to be considered when a control technique that has been tested in the wind tunnel only at sub-scale, is implemented at full scale. A literature survey conducted on passive control, however, revealed that this aspect has been ignored in almost all the cases and a study on their effect on control methods is virtually non-existent. Also rules for scaling a passive control method

with change in model scale is missing.

The ratio L/δ is a relevant parameter here that can be used to describe both the effects of scaling as well as boundary layer thickness. Shaw (1989) and Ross (2001) in their experiments with different cavity scales and a fixed boundary layer thickness attributed the cause of their observations to the variation in boundary layer thickness with respect to the cavity length and used it as a parameter. The same ratio was used by Ahuja & Mendoza (1995) to study the effects of boundary layer thickness on a fixed cavity. Hence the ratio L/δ has been concurrently used to study both the scaling effects as well as boundary layer thickness effects and the same will be used in the current work.

2.9 Aims and Objectives

The aims of this research programme are to :
1) study the effect of scaling on clean cavities;
2) study the effectiveness of a passive control method across different scales;
3) determine the scaling principles for the passive control device.

For this, the entire study is categorized into two phases. The first phase investigates the effect of scaling (or the factor L/δ) on clean cavities. For this, three different cavities whose corresponding linear dimensions are in the ratio 0.5 : 1 : 2 are selected while the incoming boundary layer thickness is kept fixed. The L/D and L/W ratios of the cavities have been chosen as 5 and 2 respectively as these values have been generally well studied. The Mach number of the flow is chosen as 0.71, a high subsonic value which is relevant to the speed at which operations of internal weapons bays are carried out. The two smaller cavities are tested additionally at Mach number 0.85 to look at the effects of Mach number variation.

In the second phase, the effectiveness and variation in performance of a control technique with respect to the change in L/δ is investigated by testing them on the three cavities with different scales. Since it is not possible to study the effect of scaling on all the passive control methods due to time constraints, a suitable technique was selected from a set of pilot experiments. A spectrum of different passive control devices was tested on the largest cavity (which is closest to full

scale); the results of which indicated that leading-edge devices were most effective in the suppression of cavity oscillations. Among the leading-edge devices, a sawtooth spoiler was selected to be tested across different scales since it showed good suppression results and has also been previously investigated by many researchers [Shaw et al. (1988), Geraldes (2005), Ashworth (2008), Lawson & Barakos (2009)]. The performance of the sawtooth spoilers is dependent on the height of the spoilers, the incoming boundary layer thickness and the size of the cavity which makes them an ideal candidate for this study. Sawtooth spoilers also have minimum radar cross section when compared to the other leading-edge devices. The effectiveness of the sawtooth spoilers is tested on three models having the same geometric ratios but different scales. This throws light on the effect of the factor L/δ on the control effectiveness. Different spoiler heights are tested at different values of L/δ to determine the correct spoiler height that needs to be chosen for a particular scale or a particular value of L/δ.

The experimental programme consists of mean pressure measurements, unsteady pressure measurements and flow-field velocity measurements using particle image velocimetry (PIV). The pressure measurements were made using pressure tappings on the cavity floor and can shed light on the cavity flow type and aeroacoustics. PIV studies were conducted in selected cases to ascertain the fluid mechanics that are involved while changing the factor L/δ.

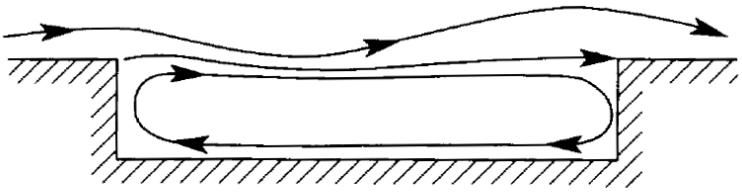

(a) Flowfield model

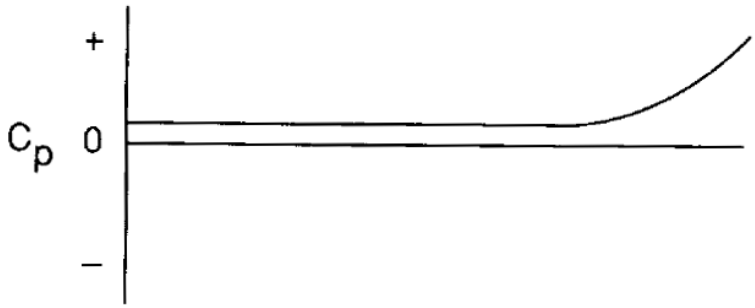

(b) Typical static pressure distribution

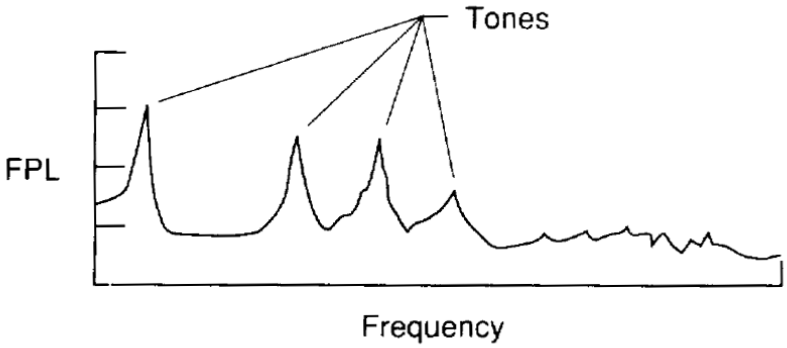

(c) Typical fluctuating pressure distribution

Figure 2.1: Open cavity flowfield description [Tracy & Plentovich (1993)]

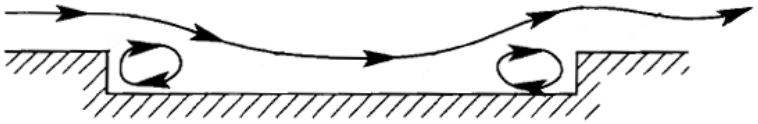

(a) Flowfield model

(b) Typical static pressure distribution

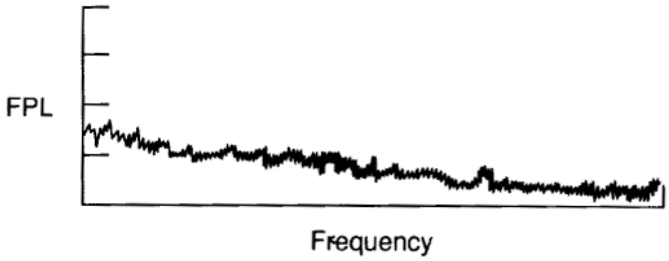

(c) Typical fluctuating pressure distribution

Figure 2.2: Closed cavity flowfield description [Tracy & Plentovich (1993)]

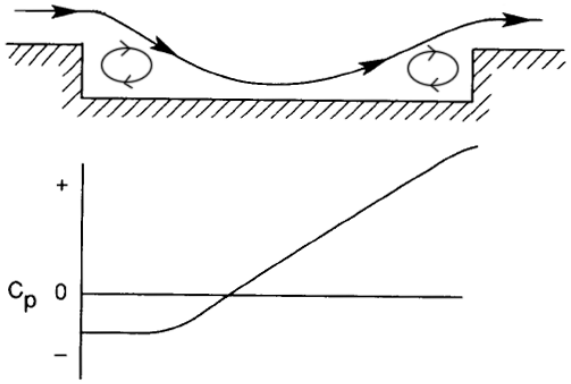

(a) Transitional closed flowfield

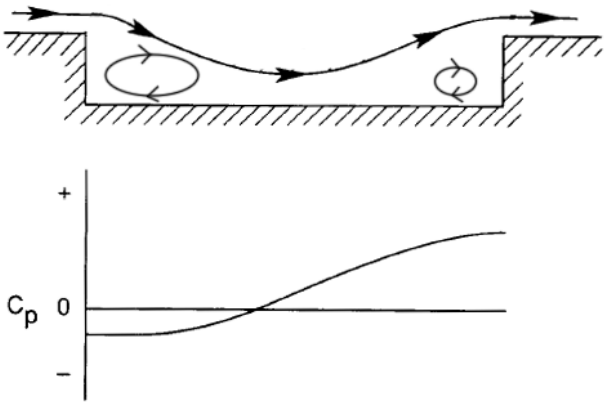

(b) Transitional open flowfield

Figure 2.3: Transitional cavity flowfield description [Tracy & Plentovich (1993)]

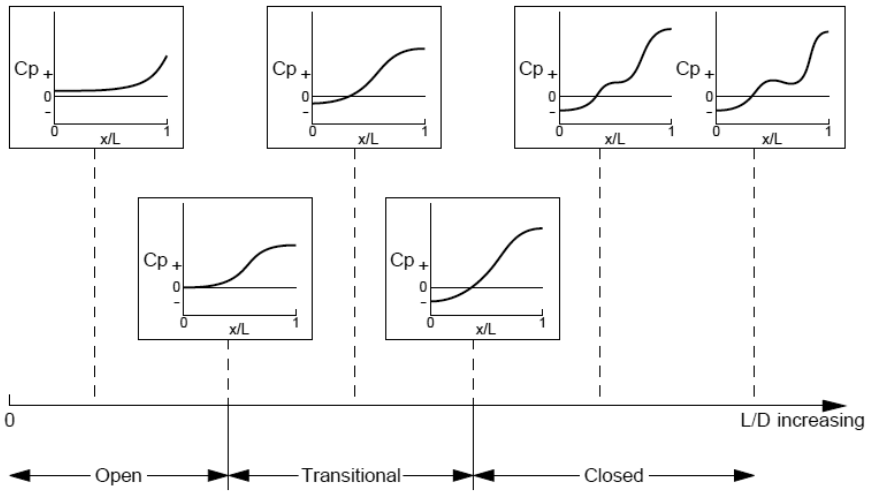

Figure 2.4: Transition of the flowfield from open to closed configuration [Plentovich et al. (1993)]

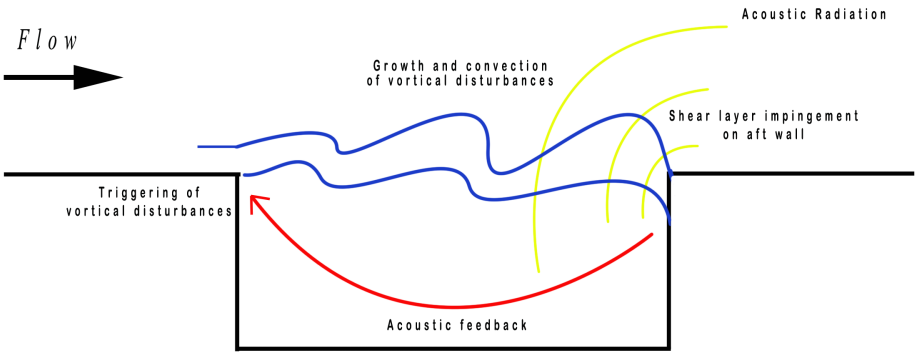

Figure 2.5: Feedback loop described by Rossiter

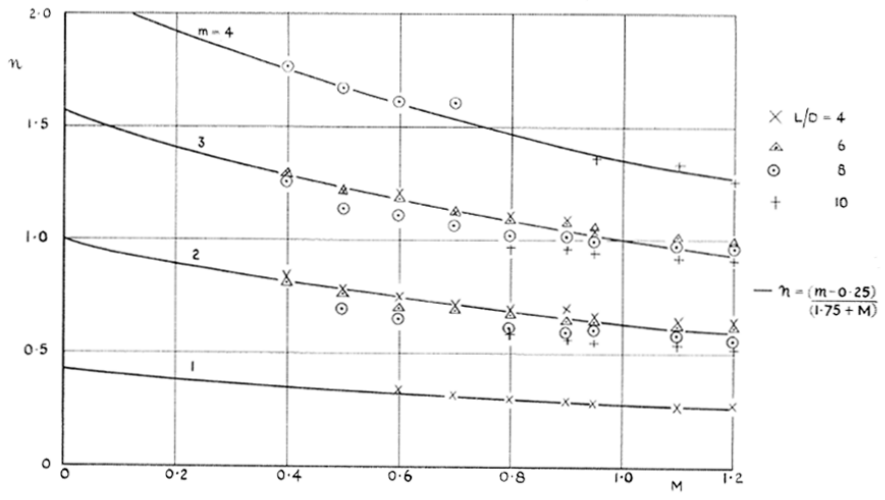

Figure 2.6: Experimental mode frequencies obtained by Rossiter (1964)

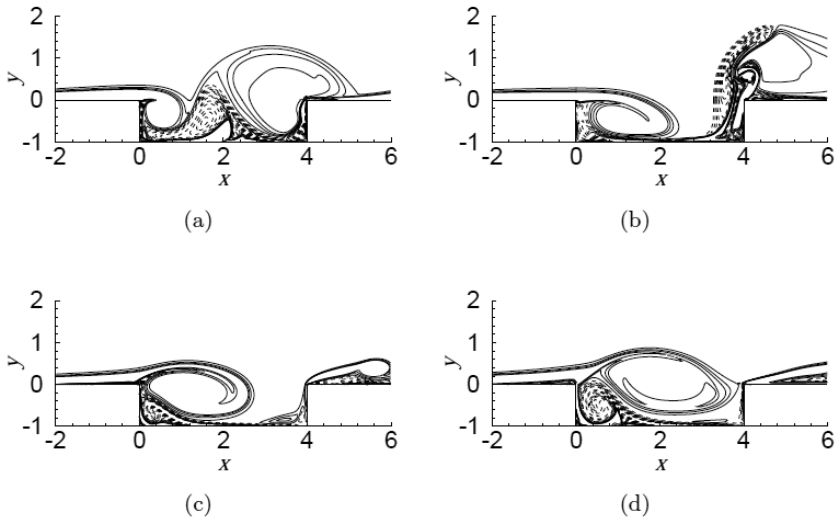

Figure 2.7: Vorticity contours for wake mode at four different instants (a-d) [Rowley (2002)]

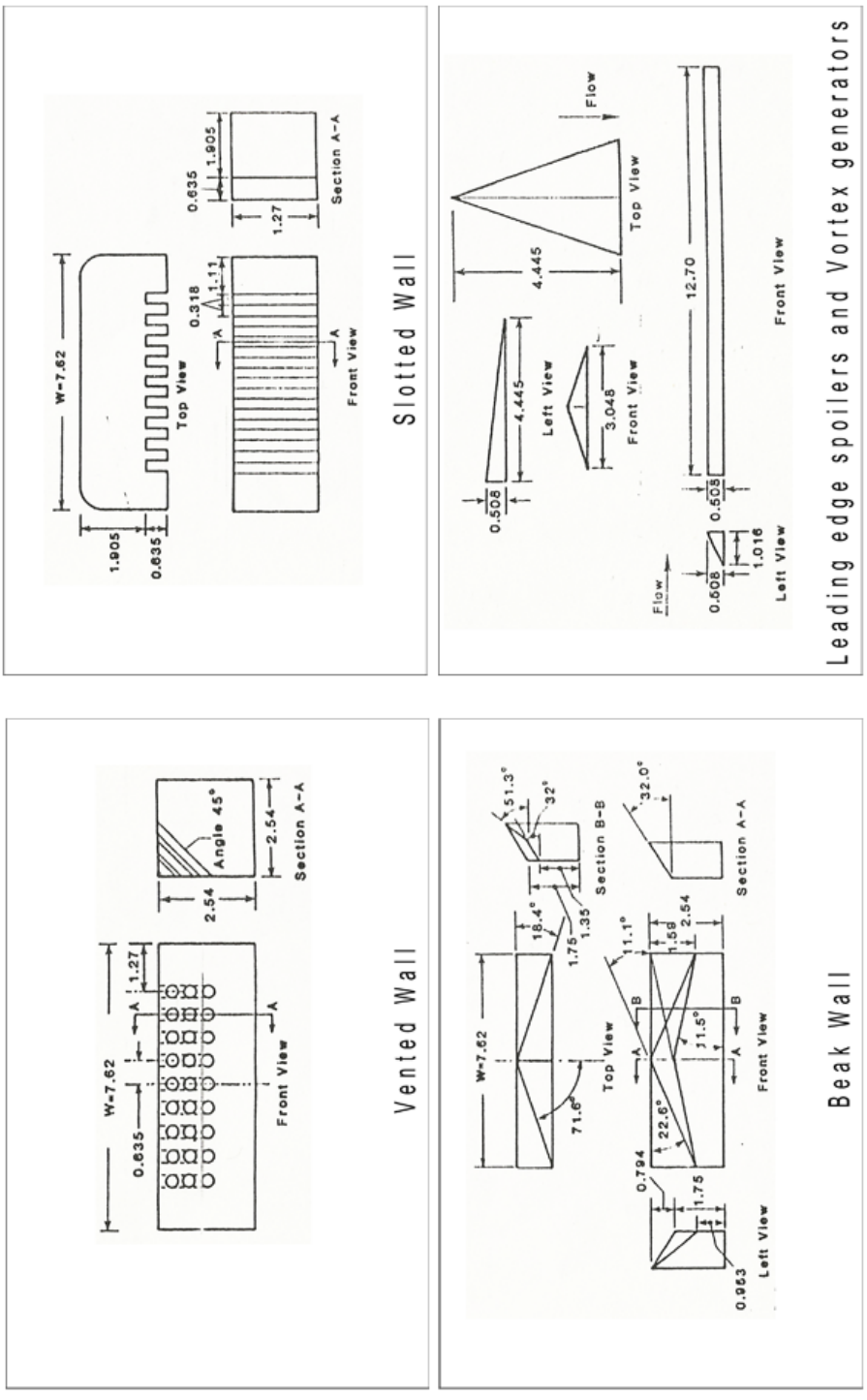

Figure 2.8: Passive control methods used by Perng & Dolling (2001)

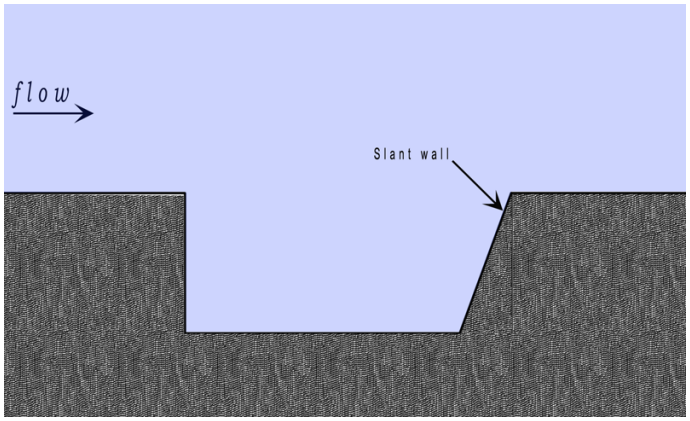

Figure 2.9: Illustration of passive control method using slant-wall

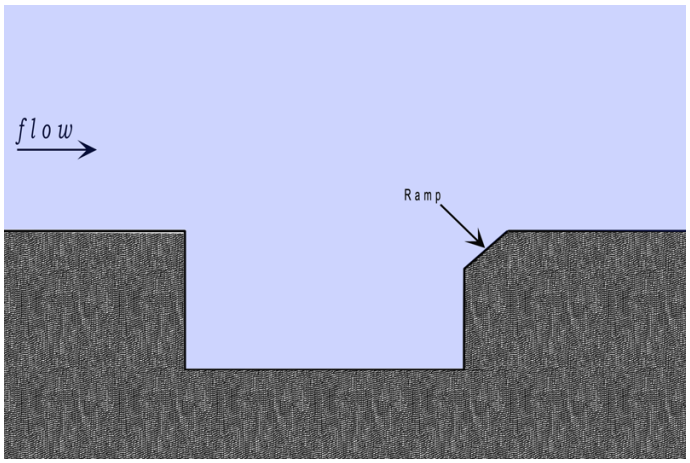

Figure 2.10: Illustration of passive control method using aft-wall ramp

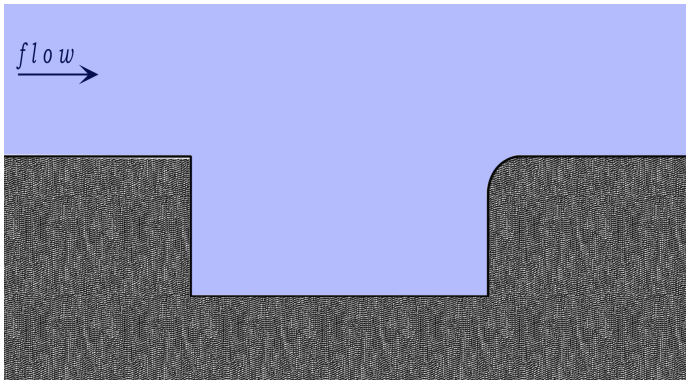

Figure 2.11: Illustration of passive control method using aft-wall curved-ramp

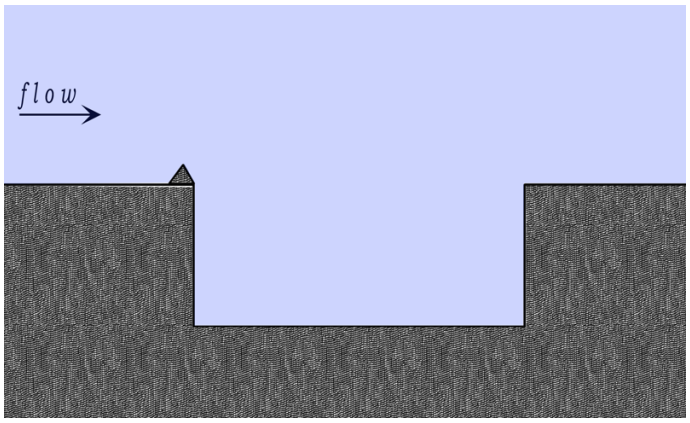

Figure 2.12: Illustration of passive control method using triangular bump

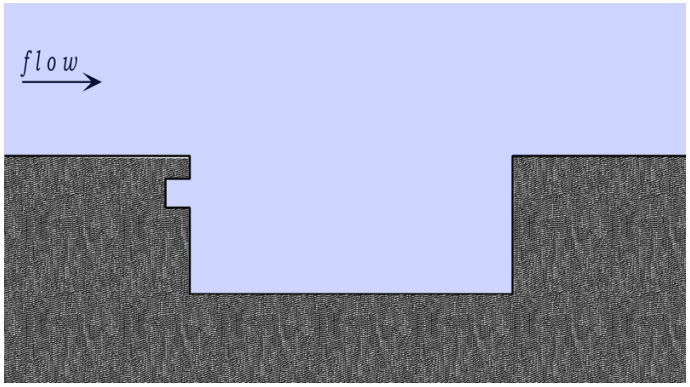

Figure 2.13: Illustration of passive control method using leading-edge subcavity

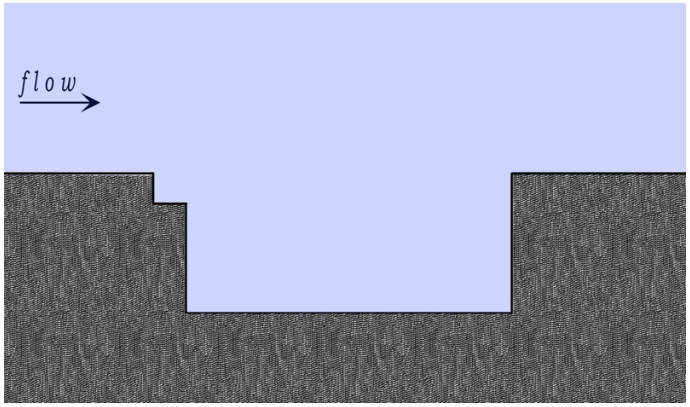

Figure 2.14: Illustration of passive control method using leading-edge step

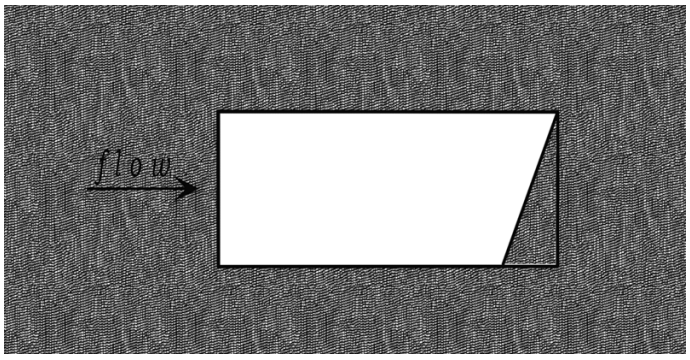

Figure 2.15: Illustration of passive control method using wedges (top view)

Chapter 3

Experimental Details

This chapter describes the experimental facilities and various model configurations used in this study. Three major measurement techniques have been used in this work - mean pressure measurement, unsteady pressure measurement and PIV flow field measurement. The details of the experimental procedures adopted for these measurements are also presented in this chapter.

3.1 Experimental Set Up

This section details the wind tunnel facility and test rig, including the description of the models and the different passive control techniques that have been used in the experiments. The experiments were conducted in a transonic wind tunnel with the cavity models attached to the side wall of the test section allowing the measurements listed above. For this, one of the side doors of the test section is converted to a test rig where the different cavity models can be fitted.

3.1.1 Transonic wind tunnel

All the experimental studies were carried out in the closed-circuit, ejector-driven transonic wind tunnel facility at the Defence Academy, Shrivenham. A general layout of the wind tunnel is shown in Figure 3.1. The wind tunnel has a working section which is 500 mm long, 206 mm high and 228 mm wide. Using a Compair L110-10, air is compressed, dried and stored at 724 kPa(g) in a 34 m^3 reservoir that supplies the air to the wind tunnel. The amount of air stored in the tank provides the tunnel with a limited run time, which is approximately 8 seconds at a flow Mach number of 0.85 for a blowing pressure of 500 kPa(g) at a tunnel stagnation pressure of approximately 101 kPa (1 atm). The wind tunnel is designed for free-stream Mach numbers ranging from 0.5 to 1.4. The free-stream Mach number of the flow passing through the test section can be regulated by using either a Boeing-flap mechanism located downstream of the test section or by changing

the area ratio of the convergent-divergent nozzle upstream of the test section. At a specific setting of the Boeing flap and the nozzle throat, the free stream Mach number in the wind tunnel can also be controlled by regulating the ejector blowing pressure.

For the calibration of the wind tunnel, static and total pressures were measured on the centre-line of the exit plane of the tunnel nozzle. A pitot-static tube was used to measure both these quantities simultaneously. A Kulite PT 213 - 225 (0 - 1 bar) and a Druck PDCR 810 (3.5 bar) pressure transducers were used for static and stagnation pressures respectively measured using the pitot-static tube. The pressure values obtained were then used to compute the Mach number using the isentropic flow relation :

$$\frac{P}{P_0} = \left(1 + \frac{\gamma - 1}{2} M^2\right)^{\frac{\gamma}{1-\gamma}} \tag{3.1}$$

The Mach number of the test section was calibrated to a value of 0.85 at a blowing pressure of 500 kPa(g) by adjusting the Boeing flaps while the nozzle area-ratio was kept fixed. This flow calibration was done in a clean tunnel first without any cavities being fixed to the test section and then verified with the cavities fitted to the side wall. Although it was initially planned to test all the three cavity scales at M = 0.85, it was found later that the blowing pressure was insufficient to drive the tunnel at this Mach number with the largest cavity in the test section. The maximum Mach number attainable with reasonable tunnel run-time with the cavity with the largest dimensions (L x W x D = 320 mm x 160 mm x 64 mm) was M = 0.71. Hence this Mach number was fixed as the test Mach number for the studies in this work. However, the two smaller cavities were tested additionally at M = 0.85 in order to look at the effects of Mach number variation. Therefore at M = 0.71, the data are available for comparison between the three model scales, while at M = 0.85 the measurements had to be restricted to the two smaller models.

Table 3.1: Static & stagnation pressures in clean wind tunnel

P_∞ (in Pa)	$P_{0\infty}$ (in Pa)	M_∞
63507	101919	0.85
73069	102220	0.71

The uncertainties in the centre-line Mach number arise from random error due to fluctuations in the flow conditions (Type A error) and measurement error (Type B error) due to transducers used in the experiments. The random error, ϵ_{ran}, is obtained from 5 tunnel runs of 65536 samples each, calculated at 95% confidence level as

$$\epsilon_{ran} = \pm 1.96 \frac{\sigma_m}{\sqrt{N}} \tag{3.2}$$

where σ_m is the standard deviation of the mean and N is the number of samples. The values of ϵ_{ran} thus obtained for M = 0.71 and M = 0.85 is given in Table 3.2. The accuracy of the transducers, ϵ_t, is quoted as ± 0.1% including non-linearity, hysteresis and repeatability. In general, the uncertainty in a function w = f(x,y,z...) is given by

$$(\Delta w)^2 = \left(\frac{\partial f}{\partial x}\right)^2 \Delta x^2 + \left(\frac{\partial f}{\partial y}\right)^2 \Delta y^2 + \left(\frac{\partial f}{\partial z}\right)^2 \Delta z^2 + ... \tag{3.3}$$

where Δw, Δx, Δy and Δz is the uncertainty in w, x, y and z respectively. The relation between M, P and P_0 can be rearranged from Equation 3.1 for $\gamma = 1.4$ as

$$M = 2.23 \sqrt{\left(\frac{P}{P_0}\right)^{-0.286} - 1} \tag{3.4}$$

Using Equation 3.4 and Equation 3.3, the error in M can be evaluated as

$$(\Delta M)^2 = \left(\frac{\partial M}{\partial P}\right)^2 (\Delta P)^2 + \left(\frac{\partial M}{\partial P_0}\right)^2 (\Delta P_0)^2 \tag{3.5}$$

where

$$\left(\frac{\partial M}{\partial P}\right) = \frac{-0.319\,(P)^{-1.286}}{P_0^{-0.286} \sqrt{\left(\frac{P}{P_0}\right)^{-0.286} - 1}} \tag{3.6}$$

and

$$\left(\frac{\partial M}{\partial P_0}\right) = \frac{0.319\,(P)^{-0.286}\,(P_0)^{-0.714}}{\sqrt{\left(\frac{P}{P_0}\right)^{-0.286} - 1}} \tag{3.7}$$

The transducer error, ϵ_t, can thus be evaluated by using Equation 3.5. The influence of the transducer error on Mach number was found to be relatively small and was found to have negligible variation across the different runs. The error in the Mach number due to transducer accuracy was therefore evaluated for the mean values of P_∞ and $P_{0\infty}$ for the respective Mach numbers. The various values thus obtained are given in Table 3.2.

Table 3.2: Uncertainties in centre-line Mach number

M	ϵ_{ran}	ϵ_t
0.71	±0.01	±0.001
0.85	±0.02	±0.001

Since these two sources of error are independent, the total error in the quantity can be evaluated as the root sum square of the individual errors. Hence the total error in the centre line mean Mach number is given as

$$\Delta M = \sqrt{(\epsilon_{ran})^2 + (\epsilon_t)^2} \tag{3.8}$$

Using Equation 3.8, the total uncertainty in the Mach number was found to be ± 0.02 and ± 0.01 for Mach numbers 0.85 and 0.71 respectively. This corresponds to 2.3% and 1.4% errors in the Mach numbers 0.85 and 0.71 respectively.

3.1.2 Test rig and models

In the transonic wind tunnel, the test rig is attached to the side wall of the test section (see Figure 3.1). It was decided to use the natural boundary layer developed inside the tunnel for the studies. For this, the test rig necessitated a design in which the three different models could be placed in such a way that the leading edge of the models is coincident, so as to maintain a uniform boundary layer

thickness for all the experiments. The test rig design layout is given in Figures 3.2 and 3.3. The material selected for fabrication was aluminium owing to its light weight and non-corrosive properties. The design includes a basic rig with a rectangular hole (Figure 3.2) in which a cavity model constituted of blocks can be fastened (Figure 3.3). The different blocks are fastened securely using bolts and the edges were sealed with silicone gasket to make them leak-proof.

The PIV studies necessitate a transparent cavity floor as well as a transparent wall for firing the light sheet and photographing it from a perpendicular angle. The floor and wall were made transparent by using polished acrylic as the material, which enables the light sheet to pass through. However, the design of the tunnel does not allow optical access from a perpendicular angle through the transparent wall and hence the light sheet had to be photographed from the same direction as the light source. To enable this, a front-coated mirror, aligned at 45^0 to the transparent cavity wall was used. The light sheet was photographed using the reflection from the mirror. This method was used by Ritchie (2005) in his works with cavity flows in the same facility and has proved to be successful.

The scaling studies have been done using three model cavities whose corresponding linear dimensions are in the ratio 0.5 : 1 : 2. These cavities are referred to as cavity A, cavity B and cavity C respectively for convenience. The same nomenclature will be followed in the rest of the work while referring to the respective cavity models. The cavity dimensions chosen are L x W x D = 80 mm x 40 mm x 16 mm (cavity A), 160 mm x 80 mm x 32 mm (cavity B) and 320 mm x 160 mm x 64 mm (cavity C), giving the L/D and L/W ratios as 5 and 2 respectively. Keeping the incoming flow conditions constant, the dimensions of the cavity are changed by fastening different inserts to the test rig (see Figure 3.3). The reference axes used throughout are shown in Figure 3.4; the origin for each cavity is chosen at the centre of the leading edge of the cavity, which is a common point for all the three cavities. The x-axis is parallel to the flow direction, while the y-axis is normal to the tunnel wall. For static pressure measurements, holes of 0.8 mm radius were drilled on the floor of the cavities and flush-mounted with stainless steel tubes. For a given cavity, nine pressure tappings were spaced linearly in the streamwise direction at a uniform distance of x/L = 0.1 from each other. Three such rows are placed at planes z/W = 0, 0.1625 and 0.325 which are referred to as Centreplane (CP), Offsetplane1 (OP1) and Offsetplane2 (OP2) respectively. In total, there are

27 static pressure tappings for each cavity model, forming a measurement grid on the floor as shown in Figure 3.5. Cavity flow pressure distributions are usually described with reference to the non-dimensional length, x/L, and hence the difference in physical spacings of the pressure tappings in the different cavities were not deemed important in the context of location. Flow visualization of a cavity with the same L/D and L/W ratios by Ritchie (2005) indicates that the cavity flowfield is symmetric about the centreline. Hence symmetry is assumed and the grid points have been made only for a half of the floor plane. Pressure measurement across the grid points can give sufficient insight to the streamwise and spanwise flow dynamics.

3.1.3 Passive control devices

A comparative study of different passive control techniques would prove useful to evaluate the relative performance of a control device and can also help to select the most desirable technique for the scaling tests. Thirteen different passive control techniques were tested in cavity C and the following section gives details of the different control methods. Only those passive control methods were selected for this study which did not alter the cavity floor area. This will enable a consistent comparison of the pressure data obtained from the measurement grid on the cavity floor. Some of the methods experimented are novel and are tested for the first time.

Leading-edge spoilers with three different profiles were tested - flat top, saw tooth and square tooth (Figures 3.6 - 3.8). The sawtooth spoilers are composed of triangular elements. The blockage ratio of all the sawtooth and square-tooth spoilers is maintained equal for consistency. Rossiter (1964) in his pioneering study with spoilers reported maximum suppression when the spoiler height the boundary layer thickness. Hence the height of all the spoilers was chosen to be 8 mm, which is equal to the incoming boundary layer thickness in the current study. The chosen set of spoilers can give information to determine if the spoiler profile has an effect on the cavity oscillations. In addition to the spoilers, a leading-edge wedge (Figure 3.9) of the same height was also tested. The spoilers were securely bolted to the front wall of the cavity to prevent vibrations and loosening of the spoilers during the tests. All the spoilers were made of 2 mm-thick aluminium

sheet and a pocket of 2 mm was given in the block which constituted the front wall of the cavities, in order to maintain the same L/D ratio for the cavity.

Porosity of the cavity walls could have an effect on the cavity oscillations. Since there was no detailed reference literature available on the effect of porosity of walls on cavity oscillations, a large value of porosity (50%) was used on the aft and front walls (Figures 3.10 and 3.11). The hypothesis behind the effect of porous walls is that porous walls can diffuse and dissipate the pressure waves generated, which leads to weakening of the acoustic resonant feedback.

Ramps have been found to be effective in suppression of cavity oscillations in the studies of Kok et al. (2008) and Vikramaditya & Kurian (2009). Although only trailing-edge ramps were used in these previous works, in the present study the ramp was tested both at the leading and trailing edges (Figures 3.12 and 3.13). Vikramaditya & Kurian (2009) in their study on the effects of ramp angles and slant aft-wall angles found best suppression results at an angle of 45^0. Kok et al. (2008) also noticed a considerable reduction in oscillation amplitude at 45^0 ramp angle. Since 45^0 was not available because of a design constraint for the set up, the closest possible angle was chosen for the ramps (LR and TR) and slant walls (AFW and FWS). Vikramaditya & Kurian (2009) also noted that the suppression due to ramps and positively-angled slant walls occurs due to the deflection of the disturbance created by the shear layer impingement away from the cavity due to the surface inclination. This infers that the height of the ramp (h_{LR}) should approximately be up to the depth where shear layer influence inside the cavity is maximum. On the basis of PIV data of clean cavity C, this height of the ramp was chosen as 35.5% of the cavity depth. Vikramaditya & Kurian (2009) in their work noticed similar levels of suppression for positively-angled slant walls and cavities with ramps since, in principle, the ramps and slant walls have the same mechanism of cavity oscillation suppression. Hence only positively-angled ramps were tested in this study whereas positively-angled slant walls were not. Due to the constraint posed by the size of the test rig, positively-angled slant walls could not be tested without changing the cavity floor area which was mentioned as a criterion for selection of passive control devices above. However, negatively angles slant walls have not been tested so far and it would be of interest here to determine their effect on cavity unsteadiness. Negatively-angled slant walls were tested both in the front and the aft walls.

Thickening the boundary layer has been found to reduce the amplitude of cavity oscillations [Ahuja & Mendoza (1995), Zhuang et al. (2006)]. Based on this concept, a leading-edge step (Figure 3.16), which is postulated to thicken the boundary layer and thus reduce the cavity unsteadiness, was tested. The leading-edge step acts like a backward-facing step and thus thickens the boundary layer due to separation. The height of the step is chosen as 10 mm which is close to the boundary layer thickness used in this study. The reattachment of the shear layer for a backward facing step takes places at a downstream distance of approximately 60 - 90% of the step height [Plentovich et al. (1993)]. Sufficient length has been given in the leading-edge step used in this study (100% of step height) to ensure reattachment on the step floor. The step was also placed at the trailing edge (Figure 3.17) to test if it has an effect in cavity unsteadiness by influencing the interaction between the shear layer and the trailing edge. To thicken the boundary layer, a deep cavity placed near the leading-edge was also tested (Figure 3.18). Associated literature reports show that deep cavities with L/D < 1 have transverse modes of oscillations [Tracy & Plentovich (1993)]. Such a deep cavity placed near the leading edge is postulated to thicken the boundary layer by perturbing it in the wall-normal direction and contribute to cavity oscillation control. The L/D of the leading-edge deep cavity used in this study is 0.4. The specifications of the different passive control devices are given in Table 3.3.

Based on the results of the comparative study of the different passive control methods, sawtooth spoilers were selected for the scaling tests. To determine the correct spoiler height for a particular scale requires different spoiler heights to be tested. Table 3.4 shows the different sawtooth spoiler heights and the different cavities on which they have been tested.

3.2 Instrumentation

This section presents a description of the instrumentation used for measurements in the experiments.

Table 3.3: Passive control methods for initial tests on cavity C

Passive control method	Abbreviation	Parameters (see Figures 3.6 - 3.18)
Flattop spoiler	FTS	$h_{FTS}/\delta = 1$
Sawtooth tooth spoiler	SWS	$h_{FTS}/\delta = 1$
Square-tooth spoiler	STS	$h_{FTS}/\delta = 1$
Leading-edge wedge	LW	$h_{LW}/\delta = 1$, $\alpha_{LW} = 38.65^0$
Porous front wall	PFW	l_{PFW}/L = .0625, Porosity = 50%
Porous aft wall	PAW	l_{PAW}/L = .0625, Porosity = 50%
Leading-edge ramp	LR	h_{LR}/H = 0.35, $\alpha_{LR} = 46^0$
Trailing-edge ramp	TR	h_{TR}/H = 0.35, $\alpha_{TR} = 46^0$
Aft-wall slant	AWS	l_{AWS}/L = 0.19, $\alpha_{AWS} = 44^0$
Front-wall slant	FWS	l_{FWS}/L = 0.19, $\alpha_{FWS} = 44^0$
Leading-edge step	LS	$h_{LS}/\delta = 1.25$, $l_{LS}/\delta = 1.25$
Trailing-edge step	TS	$h_{TS}/\delta = 1.25$, $l_{TS}/\delta = 1.25$
Leading-edge deep cavity	LDC	$h_{LDC}/\delta = 2.125$, $l_{LDC}/\delta = 0.875$

Table 3.4: Different sawtooth spoiler heights tested

Sawtooth spoiler height, h_{SWS} (in mm)	h_{SWS}/δ	Cavity A	Cavity B	Cavity C
2	0.25	✓	x	x
4	0.50	x	✓	x
8	1	✓	✓	✓
16	2	✓	✓	✓
24	3	x	x	✓
32	4	x	x	✓

3.2.1 Cavity floor pressure measurements

Both the mean and unsteady pressure measurements were made using an integrated pressure measurement device, the Scanivalve ZOC22B (ZOC). The Scanivalve ZOC22B, or the ZOC block, is an electronically-scanned pressure transducer containing a calibration and reference pressure input manifold together with 32 input manifolds (Px). Each of the 32 inputs connect to individual silicon pressure sensors (numbered from 0 to 31) and there are two pneumatic control inputs labelled CAL CTL and Px CTL.

The ZOC22B can be operated in four different modes :

1. operate mode;
2. calibrate mode;
3. purge mode;
4. isolate mode.

The different modes are selected by applying control pressures in a predetermined logical order. They can be activated by applying a control pressure of 65 psi to the appropriate control inputs. This control pressure is obtained using a TPI hand pressure and vacuum pump through a pressure manifold block with two ball valves connected to each of the control inputs. When the ZOC block is in 'operate' mode, each of the 32 Px inputs is connected to its corresponding pressure sensor. This mode is used for acquiring the pressure readings. 'Calibrate' mode is used for calibration purposes. In this mode, all the sensors are connected to a common calibration manifold thus maintaining the same pressure to all of the transducers. The 'purge' mode connects all the transducers with the common calibration manifold and the Px inputs. A safe purge pressure applied through a Px input can clear the manifolds of impurities. The 'isolate' mode isolates the transducers from the corresponding Px inputs and the common calibration manifold. The ZOC22B also features a high speed multiplexer (20 kHz) and an instrumentation amplifier, capable of reading a full-scale pressure range of ±25 psi with a full-scale output of ± 2.5 V.

The layout of the data acquisition system using the ZOC block is given in Figure 3.19. A 15 V DC power supply is given to the ZOC block. The analog signal from the ZOC22B is fed through a 15-pin connector to a DEWE-RACK, which is a modular amplifier system with an A/D converter. The signal is amplified, conditioned and digitized here before being sent to a PC. A National Instruments DAQ card 6036E is used as the interface between the PC and DEWE-RACK. The data acquisition in the PC is managed with an in-house control program called ES1aw .The various settings of data acquisition like the sampling rate, sampling time, gain, sampling channel etc. can be set using ES1aw. Also, the ES1aw can be used to control and scan the different transducers in the ZOC block. Another program called Scope1W is used to capture the unsteady data from the ZOC block. Though this program cannot be used to scan the ZOC block, it can be set

to acquire the unsteady data from a single channel. The final output is stored in the PC as volts which are later converted to pressure units using post-processing. The calibration of the ZOC block is described in Appendix A.

3.2.2 PIV measurements

Particle image velocimetry, or PIV, is a technique which measures the global instantaneous velocity vector field in a section of a flow. The technique is non-intrusive and can be used to measure velocities ranging from zero to supersonic. In PIV, the flow is seeded with micron-sized particles and the velocity vectors are derived by measuring the movement of the particles between two light pulses. Generally, the plane of measurement is illuminated in definite intervals of time with a pulsed light sheet and the target area is captured onto the sensor array of a digital camera. The digital camera captures the two light pulses in separate images. Once a pair of images is captured, each image is then subdivided into small sections known as interrogation areas (IA). The corresponding interrogation areas from each image are then cross-correlated, pixel by pixel, with each other [Keane & Adrian (1992)]. The cross-correlation results in the production of a signal peak, which denotes the common particle displacement, ΔD. Knowing ΔD, the velocity at the point can be calculated as

$$V = \frac{\Delta D}{\Delta t} \tag{3.9}$$

where Δt is the pulse separation. With the use of sub-pixel interpolation, more accurate measurement of particle displacement, and thus velocities, is possible. A velocity vector map of the whole measurement plane is obtained by repeating the cross correlation procedure for each interrogation area over the whole image. The interrogation area should be small enough such that flow velocity variation across its area is negligible [Keane & Adrian (1990)] but large enough to contain enough particles for a good correlation. Figure 3.20 illustrates the concept of PIV measurement.

Two-dimensional, time-averaged velocity field measurements were made in this study using PIV. A New Wave Gemini 120-15 pulsed Nd:YAG laser was used

as the light source for illuminating the measurement plane. The New Wave Gemini has a maximum power output of 120 mJ per pulse with pulse separations down to 1 μs. The laser has a maximum double-pulse rate of 15 Hz and pulse duration of 3-5 ns. A Kodak ES 1.0 CCD camera, which has a resolution of 1008(horizontal) x 1018(vertical) pixels was used in combination with Nikon micro-Nikkor AF lenses for recording the light sheet. A Dantec Flow Map 500 acquisition controller was used as the hardware box, which works in conjunction with Flow Manager (v3.21) software. Both the camera and laser are connected to the hardware box and the timing and acquisition functions of both can be controlled using the Flow Manager software.

Measurements were made at the centre plane of the cavities and the laser position was fixed in a traverse at the respective heights. The Gemini laser can be operated both in internal mode using control panels or in external mode through the Flow Manager software. The control panels are used while setting up the laser and aligning the light sheet. The light sheet was obtained by using a pair of spherical lenses described by Raffel et al. (2007). The illuminated measurement plane was recorded using the image on a front-coated mirror using an arrangement described in Section 3.1.2. The set up and arrangement of the PIV system is shown in Figures 3.21 and 3.22. With the exception of the transparent floor and wall, all the sides of the cavity models and the test rig were painted black for the PIV experiments to prevent stray reflections of the laser. Water was used for seeding the flow. Filtered clean water was pressurised using a three-stage pump and sprayed through a rake of *Bete*® atomizing nozzles positioned across the span of the settling chamber of the wind tunnel. The rake consisted of three atomizers located at equal intervals at the mid-height position of the test section. The nominal seeding particle diameter based on a feeding pressure of 2000 psi is quoted by Ritchie (2005) as 10 μm.

3.3 Experimental Procedure

The procedure and protocols followed in the various experiments are explained in the following sections.

3.3.1 Boundary layer measurements

The onset flow boundary layer thickness was estimated by measuring the velocity profile at a distance of 45 mm from the leading edge of the cavity models. The measurements were made at M = 0.71 with cavity attached to the test rig. The boundary layer profile was constructed using static and stagnation pressures from points at regular intervals, Δy, normal to the tunnel wall. To measure the stagnation pressure, a small pitot probe made of stainless steel tubing that was carefully bent into an L-shape, was used. The opening of the probe which faces the flow is flattened to an elliptical cross-section so as to minimize positional errors due to gradients in the wall-normal direction. The internal minor-axis length of this elliptical cross-section measured as 0.2 mm. This measurement probe was fixed in such a way that it could be traversed only in the y-axis, by the use of a single-axis micro-traverse.

Temperature measurements were made using a k-type thermocouple. Freestream stagnation temperature was measured as 298 K. A layout of the experimental set-up is shown in Figure 3.23. The measurements started at y = 1.15 mm from the wall, with increments of Δy = 0.3175 mm. The closest distance measurable near the wall was limited by the stem design and bend-radius of the probe. However,this arrangement was sufficient to calculate the value of δ for the current experiments. The static pressure was measured using a pressure tapping at the point corresponding to the location of the profile and was found to be 73 kPa(abs). The static pressure gradient in the y direction was assumed to be zero and hence this value was used for the calculation of Mach number throughout the boundary layer. The pressure measurements were made using the ZOC block and were calculated from the average of 32768 samples that were acquired at a rate of 10 kHz. Using the values of stagnation pressure and static pressure, the Mach number can be calculated from the relation

$$\frac{P}{P_0} = \left(1 + \frac{\gamma - 1}{2} M^2\right)^{\frac{\gamma}{1-\gamma}} \tag{3.10}$$

The value of freestream velocity, U_∞, was calculated as 233.4 m/s using the relation

$$M_\infty = \frac{U_\infty}{\sqrt{\gamma R T}} \tag{3.11}$$

Assuming that the stagnation temperature across the boundary layer is constant, the value of U/U_∞ was calculated from the isentropic relations

$$\frac{U}{U_\infty} = \frac{M}{M_\infty}\sqrt{\frac{T}{T_\infty}} \tag{3.12}$$

$$\frac{T}{T_0} = \left(1 + \frac{\gamma - 1}{2}M^2\right)^{-1} \tag{3.13}$$

$$\frac{T_\infty}{T_0} = \left(1 + \frac{\gamma - 1}{2}M_\infty^2\right)^{-1} \tag{3.14}$$

Giving :

$$\frac{U}{U_\infty} = \frac{M}{M_\infty}\sqrt{\frac{1 + \frac{\gamma-1}{2}M_\infty^2}{1 + \frac{\gamma-1}{2}M^2}} \tag{3.15}$$

The boundary layer thickness, δ, was defined as the height from the wall to where U/U_∞ = 0.99. This value was deduced as approximately 8 mm from the measured velocity profile (see Figure 3.24).

The boundary layer profile at the same location was measured previously by Richardson et al. (2011) in a clean wind tunnel without the presence of a cavity downstream. The boundary layer profile thus obtained in a clean wind tunnel is shown in Figure 3.25. The boundary layer thickness in the presence of a cavity is found to be thicker than in a clean wind tunnel. The displacement thickness (δ^*), momentum thickness (θ^*) and shape factor (H) of this boundary layer calculated using numerical integration are 0.74 mm, 0.5 mm and 1.46 respectively. The shape factor of the boundary layer indicates the turbulent nature of the boundary layer (typically 1.3 - 1.4).

The boundary layer thickness measured with the presence of a cavity downstream is representative of the true onset conditions. Empirically, turbulent boundary layers on flat plates have a velocity profile which approximately follows

a $1/7^{th}$ power law [Schlichting & Gersten (2000)]. This is a reasonable approximation to boundary layer profiles up to Reynolds number (based on x) = 2x10^7. Based on the $1/7^{th}$ power law, the thickness of the boundary layer can be expressed as

$$\delta = \frac{0.37x}{Re_x^{0.2}} \tag{3.16}$$

Using the value of δ obtained from experiments, i.e 8 mm, in Equation 3.16, we obtain the value of Re_x and x as 6.45x10^6 and 497.5 mm respectively for M = 0.71. This is the equivalent Reynolds number of a flat plate flow for M = 0.71 at a distance, x = 497.5 mm, from its leading edge. Using this value of x and U_∞ = 275 m/s, the value of δ for M = 0.85 can be estimated as 7.9 mm. This value is very close (1.25% difference) to the boundary layer thickness at M = 0.71. This is because the growth of a boundary layer in a high speed compressible flow is very small [Schlichting & Gersten (2000)]. Hence, this small change in δ between M = 0.71 and M = 0.85 is neglected in the value of L/δ for the different cavities. The value of δ is, therefore, fixed as 8 mm in all cases and the values of L/δ for cavities A, B and C are 10, 20 and 40 respectively.

3.3.2 Cavity floor mean pressure measurements

Mean static pressure measurements were made from the surface of the cavity floor using the ZOC block. Series of pressure tappings were made on the cavity floor to form a 3 x 9 measurement grid as described in Section 3.1.2. Stainless steel tubes of 1.59 mm OD and 0.79 mm ID were flush-mounted into the holes drilled and connected to the transducers of the ZOC block through vinyl tubing of 120 mm length. Before any data were acquired, air was allowed to flow in the tunnel for 2 seconds to prevent transient effects from affecting the readings. The mean pressure was calculated by averaging the values obtained from at least 3 tunnel runs. 32768 samples were acquired at a sampling rate of 12.5 kHz for each run. Transducer no.31 in the ZOC block was used in all the pressure measurements. The mean pressure was non-dimensionalized and plotted in terms of the pressure coefficient, C_p which is expressed as

$$C_p = \frac{2}{\gamma M_\infty^2}\left(\frac{P}{P_\infty} - 1\right) \tag{3.17}$$

The accuracy of the ZOC block is quoted as ±0.1% F.S. and the error in the measurement of atmospheric pressure is ± 0.1%. The specified DAQ resolution error for NI 6036E, which was used for the current experiments, was found to be negligible (0.035%). A calibration curve gradient error of approximately 0.1% was measured during the calibration process. The pressure measured using the ZOC block is given by the relation

$$P_{absolute} = Av + P_{atm} + c \tag{3.18}$$

where A is the slope obtained from the calibration curve, v is the voltage measured, P_{atm} is the atmospheric pressure and c is a constant. The zero error of the ZOC block is accommodated before each measurement. Applying Equation 3.3 to Equation 3.18, we get

$$(\Delta P_{absolute})^2 = v^2(\Delta A)^2 + A^2(\Delta v)^2 + \Delta P_{atm}^2 \tag{3.19}$$

This shows that the error associated with a particular value of pressure measurement using the ZOC block is dependant on the magnitude of the pressure. Considering the worst-case scenario, the maximum error occurs for the highest value of v, which corresponds to the lowest pressure measured. The lowest pressure measured in the whole programme is 42 kPa. The value of v corresponding to $P_{absolute}$ = 42 kPa is measured as -0.74197 volts and the value of A is obtained as 79517.6 for transducer no. 31 from the ZOC block calibration studies (see Appendix A). For this value of pressure, the error caused due to transducer accuracy (±0.1% F.S.), calibration curve error (0.1%) and error in atmospheric pressure measurement (± 0.1%) can be evaluated as Δv = 0.0025 volts, ΔA = 79.5 Pa and ΔP_{atm} = 101 Pa respectively. Using these values for $P_{absolute}$ = 42 kPa in Equation 3.19, we obtain the maximum uncertainty in $P_{absolute}$ for transducer no. 31 as ±231 Pa or 0.55%. Typical values of statistical error in the mean value of pressure from 3 tunnel runs of 32768 samples each were found to be 0.3%. The systematic and

random error of the pressure measurements are combined to obtain the total error by taking their root square sum as

$$\frac{\Delta P_{tot}}{P} = \sqrt{\left(\frac{\Delta P_{sys}}{P}\right)^2 + \left(\frac{\Delta P_{ran}}{P}\right)^2} \tag{3.20}$$

where ΔP_{tot}, ΔP_{sys} and ΔP_{ran} are the total,systematic and random errors respectively. Hence the maximum total combined uncertainty for pressure measurements is obtained as 0.62%.

The pressure inside the cavity is expressed in terms of the pressure coefficient, C_p. To calculate the uncertainties in C_p, Equation 3.3 is applied to Equation 3.17 to obtain

$$(\Delta C_p)^2 = \left(\frac{4}{\gamma M^2} - \frac{4P}{\gamma M^3 P_\infty}\right)^2 \Delta M^2 + \left(\frac{2}{\gamma M^2 P_\infty}\right)^2 \Delta P^2 + \left(\frac{2P}{\gamma M^2 P_\infty^2}\right)^2 \Delta P_\infty^2 \tag{3.21}$$

The maximum error for measurements on the cavity floor occurs for P_{abs} = 62830 Pa and P_{abs} = 52103 Pa for M = 0.71 and M = 0.85 respectively which are the least pressure values measured for the respective Mach numbers. For M = 0.71, the values of P, P_∞, Δ M, ΔP, Δ P_∞ can be obtained as 62830 Pa, 73069 Pa, 0.01, 226 Pa and 225 Pa respectively. This gives the value of maximum uncertainty in C_p value, ΔC_p, from Equation 3.21 as ±0.016 for M = 0.71. Similarly for M = 0.85, the values of P, P_∞, Δ M, ΔP, Δ P_∞ can be obtained as 52103 Pa, 63507 Pa, 73069 Pa, 0.02, 228 Pa and 226 Pa respectively. From this, the maximum uncertainty in C_p, ΔC_p, can be obtained as ±0.019 for M = 0.85. Typical values of statistical error in the mean value of C_p from 3 tunnel runs of 32768 samples each were found to be of the order of ±.001. This deviation in the mean value is a random error in C_p as opposed to the systematic error calculated before. Since they are independent sources, the maximum combined uncertainty for the C_p values can be found from the root square sum of the systematic and random errors as

$$\Delta C_{p-tot} = \sqrt{(\Delta C_{p-sys})^2 + (\Delta C_{p-ran})^2} \tag{3.22}$$

where ΔC_{p-tot}, ΔC_{p-sys} and ΔC_{p-ran} are the total, systematic and random errors respectively. Using the values of ΔC_{p-sys} and ΔC_{p-ran} for M = 0.71 and M =

0.85 respectively in Equation 3.22, we get the values for their total combined uncertainty for C_p as ±0.016 and ±0.019.

3.3.3 Cavity floor unsteady pressure measurements

The same set of pressure tappings was used to sample the unsteady pressure on the cavity floor. Over the years, researchers have found that the dominant mode of oscillation in a cavity mostly remains within the first three Rossiter frequencies [Rossiter (1964), Tracy & Plentovich (1993), Ahuja & Mendoza (1995)]. Hence, attention is given only up to mode 3 and the higher modes are neglected in this study. In this regard, the highest frequency that was estimated using the modified Rossiter formula was for mode 3 of cavity A, which was 3641 Hz. Therefore, the sampling rate should be at least twice this frequency according to the Nyquist criterion. For the spectral analysis of the unsteady pressure samples, a total of 65536 samples averaged over four tunnel runs were recorded at a sampling rate of 12.5 kHz. The power spectra were plotted using an FFT algorithm to determine the amplitude of the different frequency components. The frequency resolution of the power spectra used in this work is 0.76 Hz. The experiments were found to be repeatable and the typical error over four different runs was found to be ±0.208 dB in tone amplitude and ±1.93 Hz in tone frequencies. The frequency response error due to the use of pneumatic tubing was found to be negligible by comparing the frequency response of the ZOC block transducer along with tubing with an Entran transducer connected directly to a pressure tapping.

The same time series has been used in constructing the spectrograms. For the spectrograms, the total number of samples have been divided into windows of 512 points each. A Hanning function has been used for windowing and the overlap between the windows is 50%. The temporal and frequency resolution are 20.5 ms and 6.1 Hz respectively.

Another noise parameter obtained from the signals was the Overall Sound Pressure Level (OASPL), which describes the contribution of all measured frequencies. OASPL, in dB, is defined as:

$$OASPL = 20log_{10}\left(\frac{P'_{rms}}{P_{ref}}\right) \tag{3.23}$$

where P'_{rms} is the root mean square pressure fluctuation and P_{ref}= 20μPa is the commonly-used reference pressure.

3.3.4 PIV flow-field measurements

All the PIV measurements given in this work were obtained from the mid plane of the cavity (z/W = 0). The images were acquired using a Kodak ES 1 Megaplus camera fitted with a Nikkor 60 mm f2.8 lens. A total of 700 image pairs acquired over 10 tunnel runs were used to create a single mean velocity plot. The double-pulse frequency of the laser was set at 15 Hz. The size of the interrogation area should be selected such that a particle moves across 25% of the interrogation area between the pulses. Hence the interrogation area was set at 32x32 pixels based on an 8 pixel movement. The pulse separation, Δt, is given by

$$\Delta t = \frac{\Delta n_\tau d_i}{M U_{max}} \tag{3.24}$$

where Δn_τ is the number of pixels the particles are displaced on the image plane between the pulses (ideally 5-8 pixels), d_i is the pixel diameter (9 μm for the current case), M is the magnification (0.114, 0.057 and 0.028 for cavities A, B and C respectively) and U_{max} is the maximum expected velocity. Ritchie (2005) assumed the value of U_{max} as 150 m/s based on CFD results but subsequent PIV experiments showed a value of 135 m/s. For a particle displacement of 8 pixels on the image plane, we obtain the values of pulse separation as 4.6 μs, 9.3 μs and 18.6 μs for cavities A, B and C respectively. However, in flow fields like cavity flows where huge strain gradients, velocity variation and flow unsteadiness exist, the best pulse separation should be tested iteratively through trial and error. A pulse separation of 6 μs gave the best results for the current experiments. Due to the large size of the cavity model and limited resolution of the camera, the PIV data for cavity C were created from two separate sets of acquisitions. 700 image pairs each for cavity segments x/L = 0 to x/L = 0.5 and x/L = 0.5 to x/L = 1 were acquired separately and combined together to get the final data for the whole length of the mid-plane.

Post processing was done using DaVis software from LaVision. The DaVis software has been demonstrated to extract vectors effectively from complex ro-

tating flows with high velocity gradients [Ritchie (2005)]. A three-pass window deformation algorithm, with initial and final interrogation sizes of 32x32 pixels and 12x12 pixels and a 50% overlap between subsequent interrogation areas was used to create the vectors. The window deformation algorithm deforms the subsequent interrogation areas based on the velocity gradients present.

The uncertainties in PIV measurements stem from a number of factors which includes error occurring due to the particle flow dynamics, bias errors, random errors and statistical error in the mean and RMS velocities which are strongly related to the sample size N. Each of the sources of error will be discussed below and the contribution to the error in velocity will be estimated. Firstly, the seeding particles introduced to the flow should faithfully track the flow. Smaller particles follow the flow more accurately. However, the particle size should also be large enough to be captured by the camera. In flows where high fluid velocities and accelerations exist, the equations of the particle motion become very difficult to be solved. Nevertheless, the relaxation time or aerodynamic time constant, τ_a, given by $\tau_a = \rho_p D_p^2/18\mu$ is a convenient measure for the tendency of the seeding particles to attain velocity equilibrium with the fluid [Raffel et al. (2007)]. Samimy & Lele (1991) demonstrated that particles in a compressible shear layer will follow the flow within 2% accuracy if $\tau_a/\tau_t < 0.20$. In the expression of τ_a, ρ_p is the density of fluid particle (1000 kg/m^3), D_p is the diameter of the particle (10 μm) and μ is the freestream fluid viscosity. This gives the value of τ_a as 3.268 x 10^{-4} seconds for the current experiments. The term τ_t is the characteristic time of the flow. One way of describing τ_t for cavity flows could be based on the dominant frequency of oscillation. Zhuang et al. (2006) in his PIV studies with supersonic cavity flows has taken the value of τ_t as 1/f where f is the frequency of the dominant tone observed in the power spectra. The dominant frequencies for cavities A, B and C are 836 Hz, 1072 Hz and 553 Hz respectively and hence their corresponding values of τ_a/τ_t are 0.27, 0.35 and 0.18. This corresponds to 2.7%, 3.5% and 1.8% velocity lags for the respective cases.

Errors in the flow field obtained with PIV can also occur at the processing stage mainly by means of outliers, bias errors and random errors. To remove outliers, the median filter proposed by Westerweel (1994) was used to locate spurious vectors and replace them by interpolation. On average, over 95% of the vectors in a given field were found to be valid prior to replacement and interpolation. The

accuracy with which the position of the correlation peak is determined can be affected by bias errors. A source of bias error in PIV measurements is the velocity gradients present inside the interrogation area. This is because particles with higher velocities tend to leave the interrogation area between the pulses, biasing the result towards lower velocities. This has been minimized by selecting displacement limits between the pulses and by using window deformation algorithms as described before to increase the number of matched particles. Progressively decreasing the interrogation window size reduces the loss of particles from the interrogation area leading to improved accuracy and better signal-to-noise ratios [Keane & Adrian (1992)]. Bias error can also occur due to the phenomenon of peak-locking. Peak-locking occurs because of the bias of the estimation of the position of the correlation peak towards an integer number of pixels. Peak-locking is attributable mainly to the choice of the sub-pixel estimator used to locate the correlation peak. In the current experiments, a Gaussian sub-pixel estimator was used which was shown by Westerweel (1997) to be superior in terms of mitigating peak-locking effects. Random errors in PIV can arise from background noise, shot noise (which can vary from pixel to pixel) and random errors associated with properly identifying the sub-pixel displacement. Although these errors can play an important role in the determination of instantaneous PIV results, their effect on ensemble averages of large number of samples (as is the current case) can be considered negligible owing to the random nature of their occurrence. Therefore, random errors do not degrade the accuracy of statistics derived from larger PIV ensembles [Christensen (2004)].

The mean and fluctuating velocity-field plots used in this work has been derived from 700 individual samples of flow-field plots. There is always error associated with the determination of statistical quantities such as mean and RMS velocities from the samples. The number of samples, N, is significant to the contribution of this error as these errors can be minimised by taking a very large number of samples. However, it is impractical to use an exceedingly large value of N owing to the constraints imposed by the corresponding increase in computer storage space and processing time. Hence a careful balance has to be made while choosing N based on the available resources. The relative error in the mean velocity value due to sample size N can be given as

$$\epsilon_{Nm} = \frac{\sigma}{\mu\sqrt{N}} \tag{3.25}$$

where σ and μ are the standard deviation and mean of the samples. Similarly for the statistical uncertainty in the values of V_{rms}, the standard error in the estimation of its value can be evaluated using a method given by Evans et al. (1993) for large samples (N > 10), as

$$\epsilon_{Ns} = \frac{1}{\sqrt{2(N-1)}} \tag{3.26}$$

The values of ϵ_{Nm} and ϵ_{Ns} thus obtained due to various number of samples from a point in the shear layer of cavity C is plotted in Figure 3.26. It can be seen that the values of both the error quantities, ϵ_{Nm} and ϵ_{Ns}, drop steeply from N = 1 to N = 300 and gradually after that. For N = 700, which is the value used in the current experiments the errors in the mean and RMS velocities can thus be deduced as 2.8% and 2.6% respectively.

The vector fields obtained from the PIV measurements have been used to plot line integral convolution (LIC) images. LIC is a flow-visualization method which when applied to fluid-dynamic vector fields yields images resembling long-exposure surface-trace photographs of water flows. Application of LIC to a vector field gives a high-density streamline plot which shows the features of the input vector field plane. Figure 3.27 illustrates the input and output of the LIC technique as applied to a solid-body-rotation vector field. The basic process is initiated by combining a given vector-field, defined on a rectangular grid with an input image at the same resolution as the grid. Each pixel therefore corresponds to one grid of the vector field. The corresponding pixel in the output image is then assigned the mean intensity of the pixels lying under that streamline and the process is repeated at the next pixel/cell. As the process is progressed, pixels on the same streamlines are assigned similar intensity values, resulting in the filtering, or smearing of the input image along the streamlines. An in-house LIC software which was developed using the method given by Cabral & Leedom (1993) which is described here was used. For the LIC technique, the local behaviour of the vector field is approximated by evaluating a local stream line that starts at the

centre of pixel (x,y) and moves out in both the positive and negative directions. The forward coordinate advection is given by Equation 3.28.

$$L_0 = (x + 0.5, y + 0.5) \tag{3.27}$$

$$L_i = L_{i-1} + \frac{V(\lfloor L_{i-1} \rfloor)}{\|V(\lfloor L_{i-1} \rfloor)\|} \Delta s_{i-1} \tag{3.28}$$

where $V(\lfloor L \rfloor)$ is the vector from the input vector field at lattice point ($\lfloor L_x \rfloor$,$\lfloor L_y \rfloor$).

$$s_e = \begin{cases} \infty \; if \; V \| e \\ 0 \; if \; \frac{\lfloor L_c \rfloor - L_c}{V_c} < 0 \\ \frac{\lfloor L_c \rfloor - L_c}{V_c} \; otherwise \end{cases} \tag{3.29}$$

for

$$(e, c) \in \left\{ \begin{array}{l} (top, y) \\ (bottom, y) \\ (left, x) \\ (right, x) \end{array} \right\} \tag{3.30}$$

$$\Delta s_i = min(s_{top}, s_{bottom}, s_{left}, s_{right}) \tag{3.31}$$

Only the directional component of the vector is used in this advection. Δs_i is the positive parametric distance along a line parallel to the vector field from L_i to the nearest cell edge. To maintain the symmetry, the local streamline is alo advected backwards by the negative of the vector field as shown in Equation 3.33

$$L'_0 = L_0 \tag{3.32}$$

$$L'_i = L'_{i-1} + \frac{V(\lfloor L'_{i-1} \rfloor)}{\|V(\lfloor L'_{i-1} \rfloor)\|} \Delta s'_{i-1} \tag{3.33}$$

Primed variables represent the negative direction counterparts to the positive direction variables. In the algorithm implementation, a small round off term is added to each Δs_i to ensure its entry into the adjacent cell. The local streamline calculation is illustrated in Figure 3.28. The straight line segments in Figure 3.28 is treated as parameterized space curves in s and the input texture pixel mapped to a cell as a continuous scalar function of x and y^2. For each segment, i, an exact integral of a convolution kernel k(w) is computed and used as a weight in the LIC as shown in Equation 3.34.

$$h_i = \int_{s_i}^{s_i+\Delta s_i} k(w)\, dw \tag{3.34}$$

where

$s_0 = 0$ and $s_i = s_{i-1} + \Delta s_{i-1}$ The entire LIC for output pixel F'(x,y) is given by Equation 3.35.

$$F'(x,y) = \frac{\sum_{i=0}^{l} F(\lfloor L_i \rfloor) h_i + \sum_{i=0}^{l} F(\lfloor L'_i \rfloor) h'_i}{\sum_{i=0}^{l} h_i + \sum_{i=0}^{l} h'_i} \tag{3.35}$$

where F($\lfloor L \rfloor$) is the input pixel corresponding to the vector at position ($\lfloor L_x \rfloor$,$\lfloor L_y \rfloor$) and l = i such that $s_i < l < s_{i+1}$

The technique can be used to deform any input image along any vector field. A more detailed analysis of the LIC technique can be found in the work of Knowles et al. (2006) and Cabral & Leedom (1993). The technique is very useful in the identification of vortical structures in mean flow which will be utilised in this study.

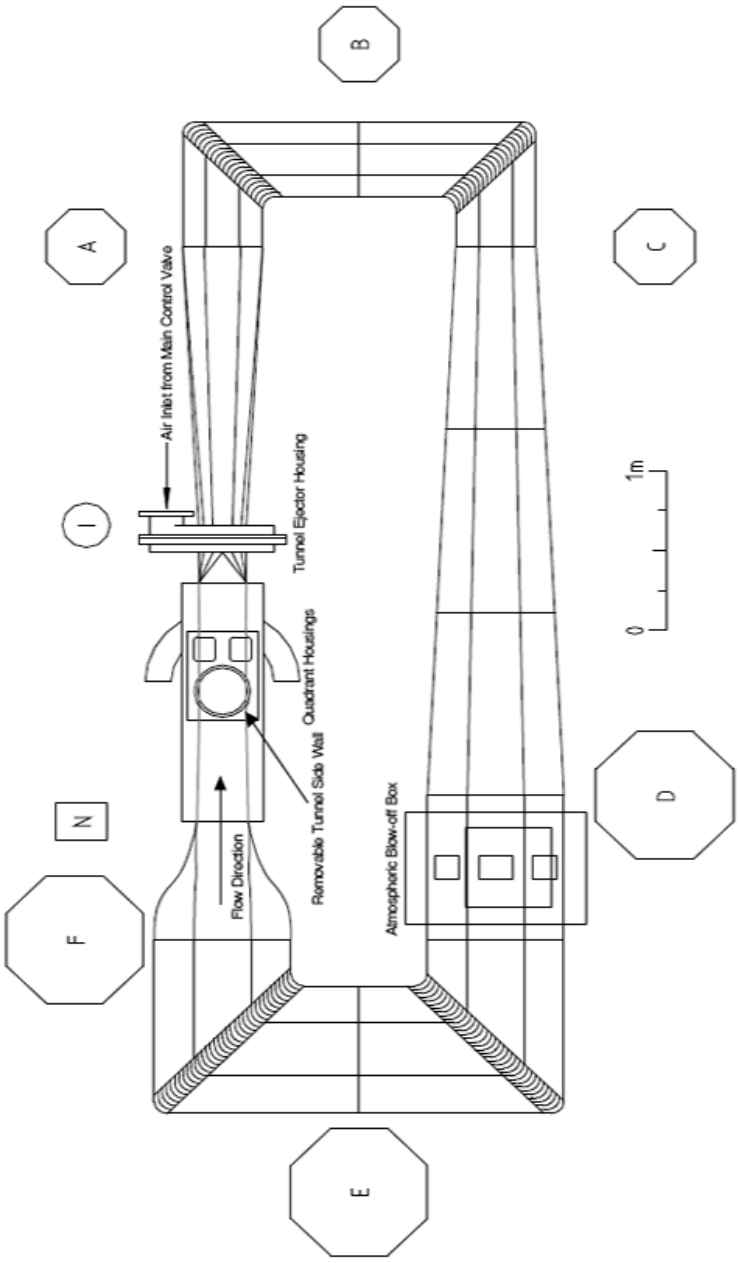

Figure 3.1: Transonic wind tunnel layout - Sections A-F show wind tunnel cross sections at various points ; N and I are the nozzle and ejector planes respectively

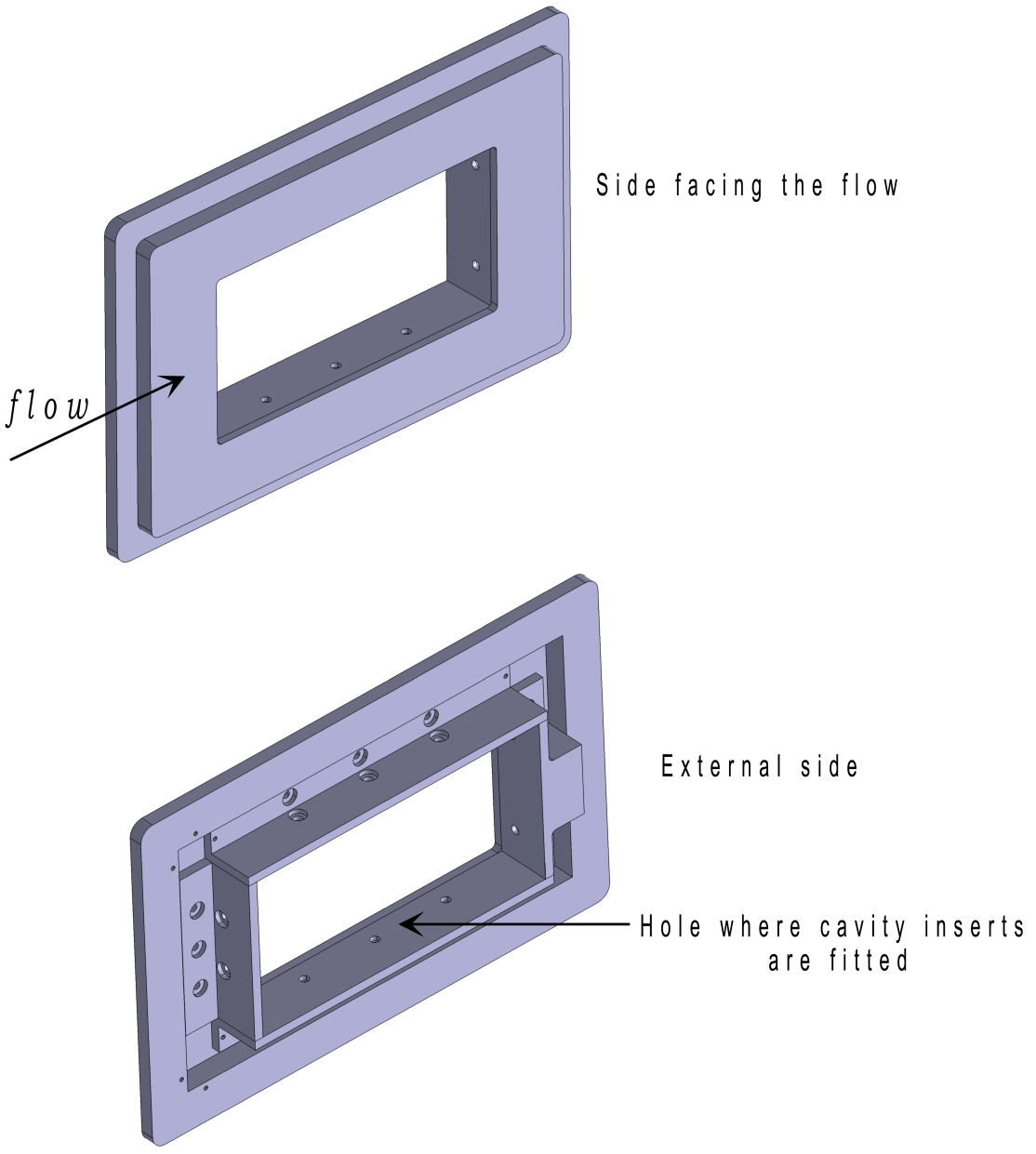

Figure 3.2: Test rig

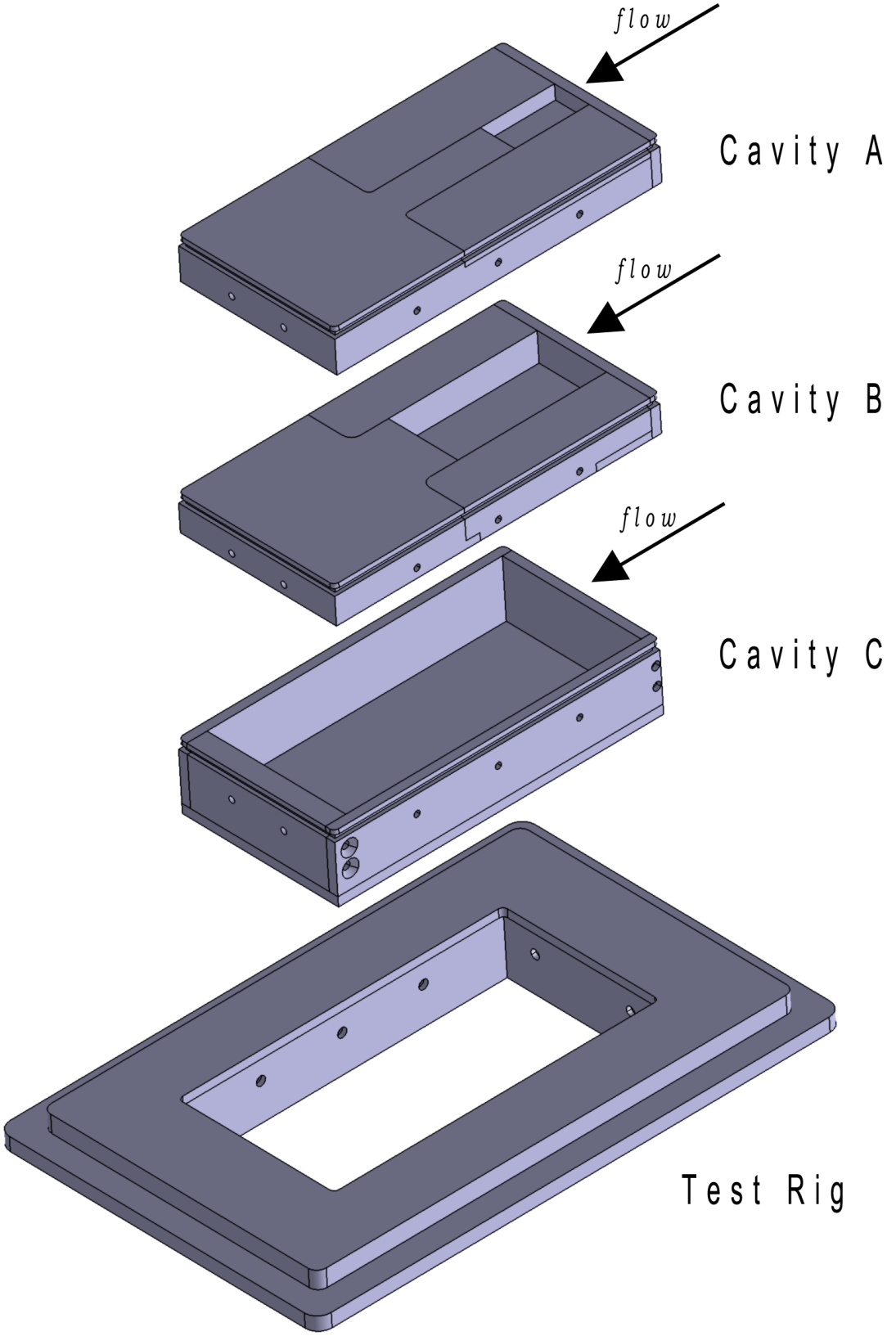

Figure 3.3: Exploded view of test rig with different cavity models

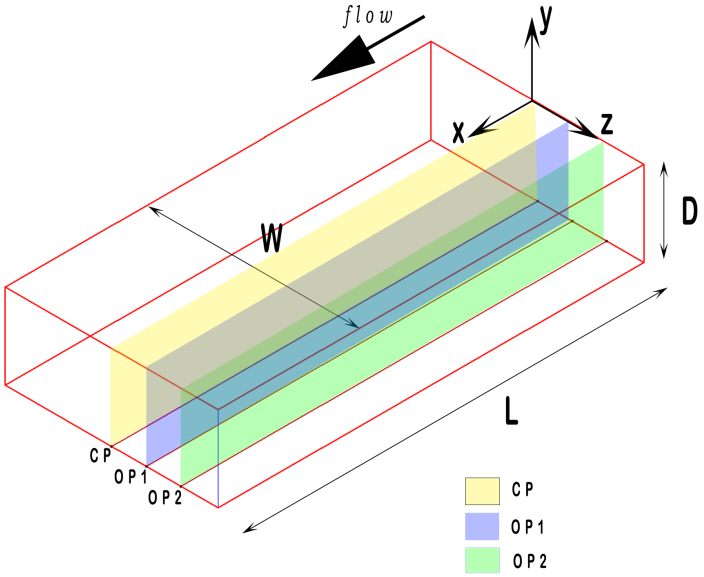

Figure 3.4: Cavity coordinate system

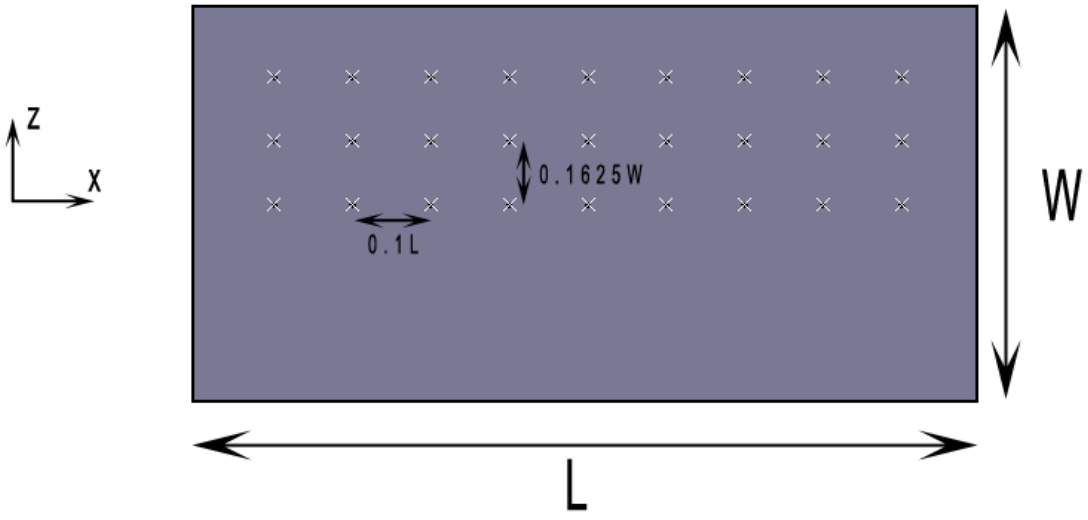

Figure 3.5: Pressure measurement grid on cavity floor

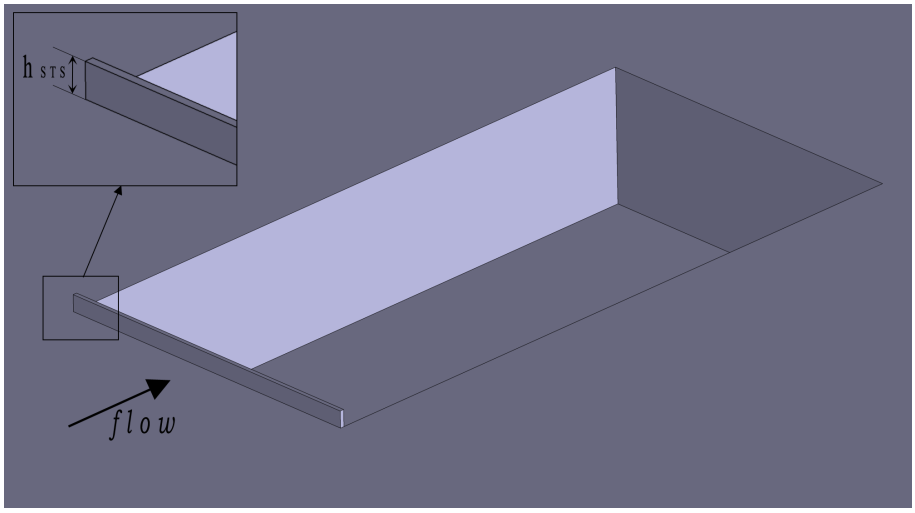

Figure 3.6: Flat-top spoiler (FTS)

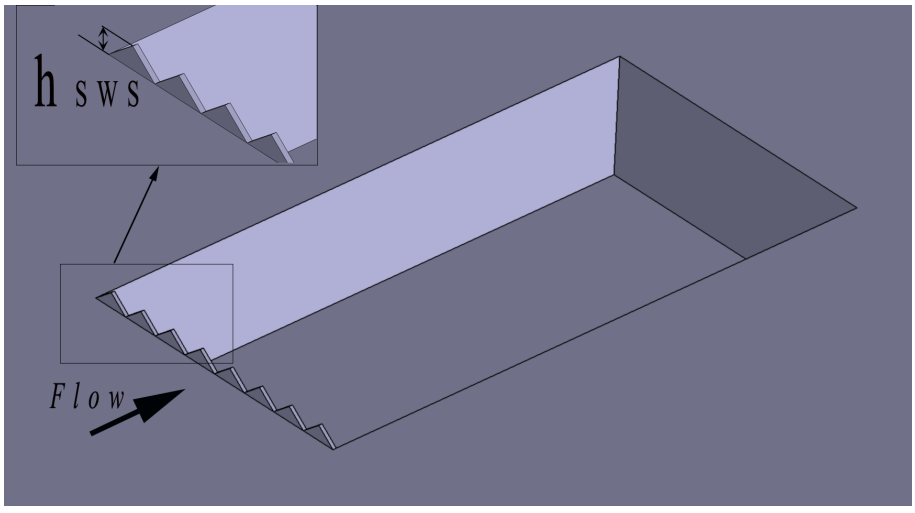

Figure 3.7: Sawtooth spoiler (SWS)

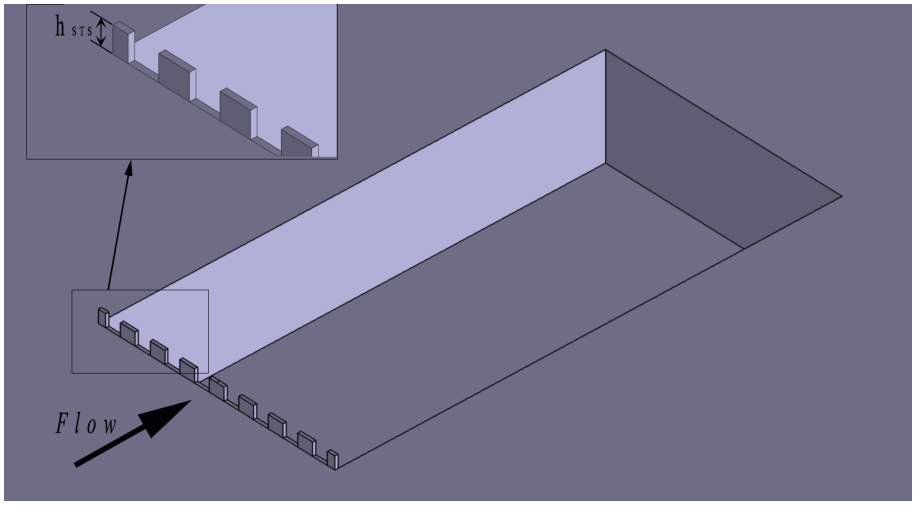

Figure 3.8: Square-tooth spoiler (STS)

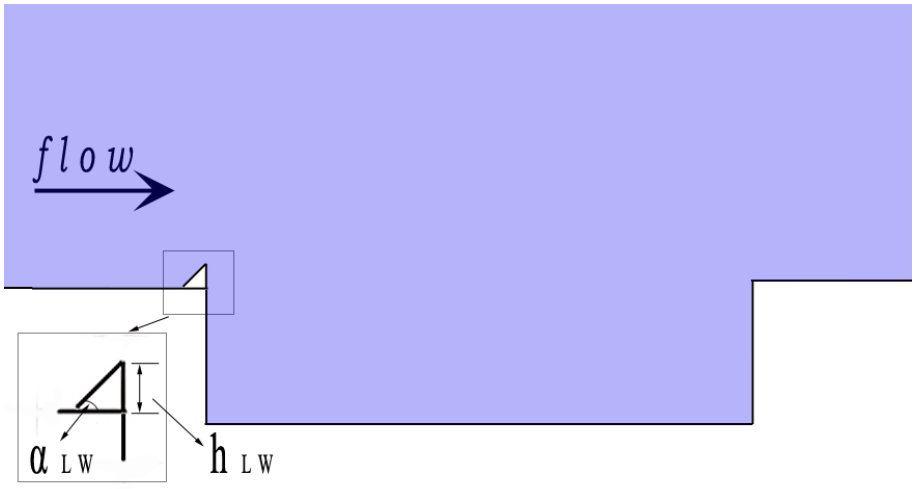

Figure 3.9: Leading edge-wedge (LW)

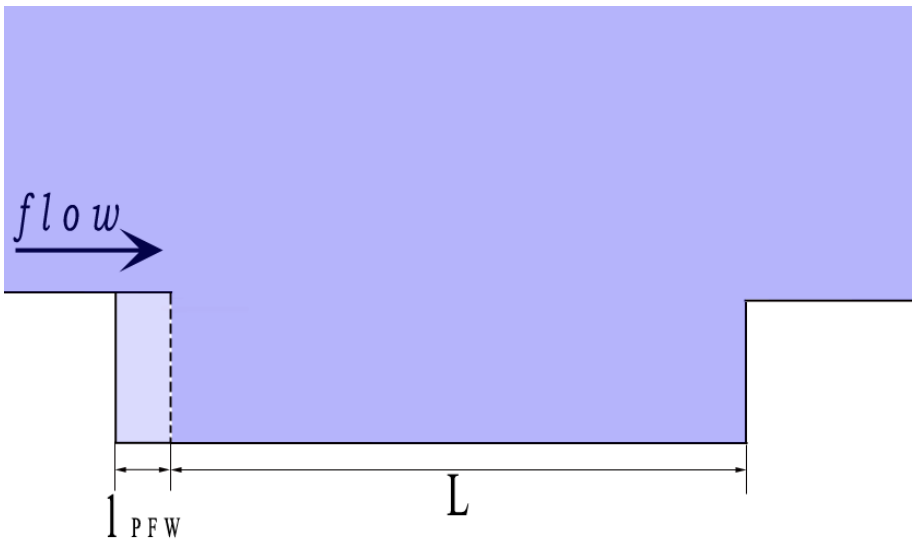

Figure 3.10: Porous front wall (PFW)

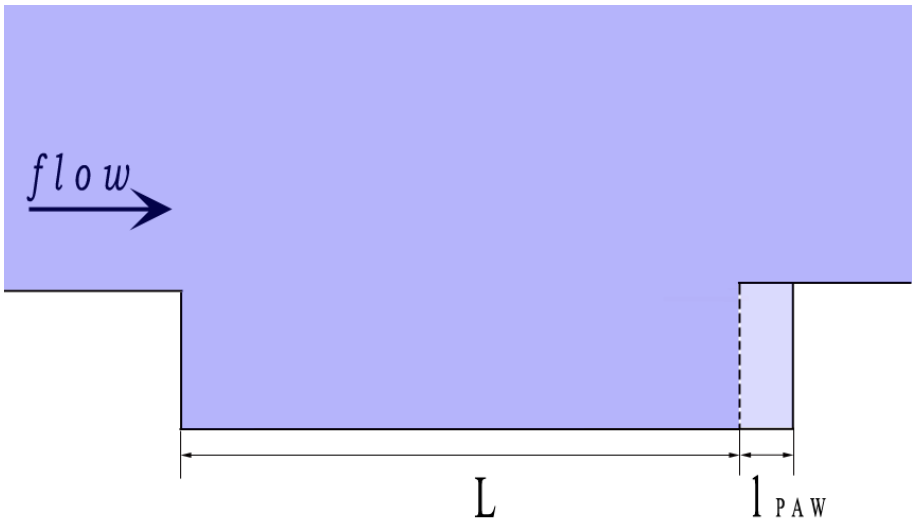

Figure 3.11: Porous aft-wall (PAW)

Figure 3.12: Leading-edge ramp (LR)

Figure 3.13: Trailing-edge ramp (TR)

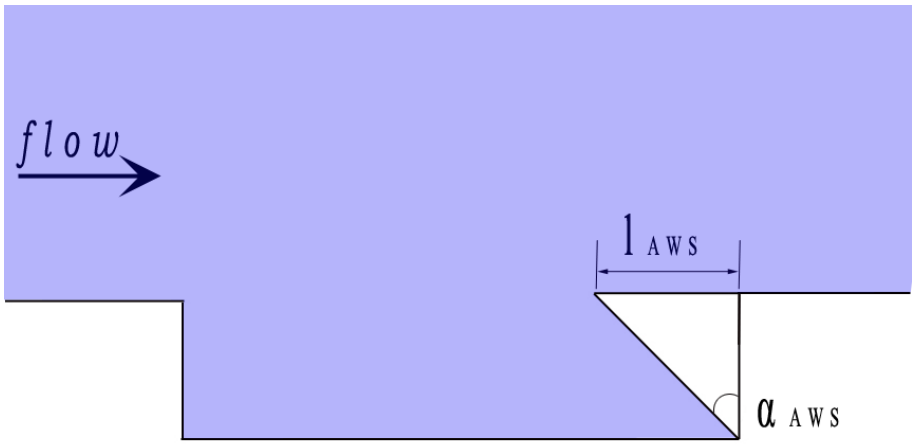

Figure 3.14: Aft-wall slant (AWS)

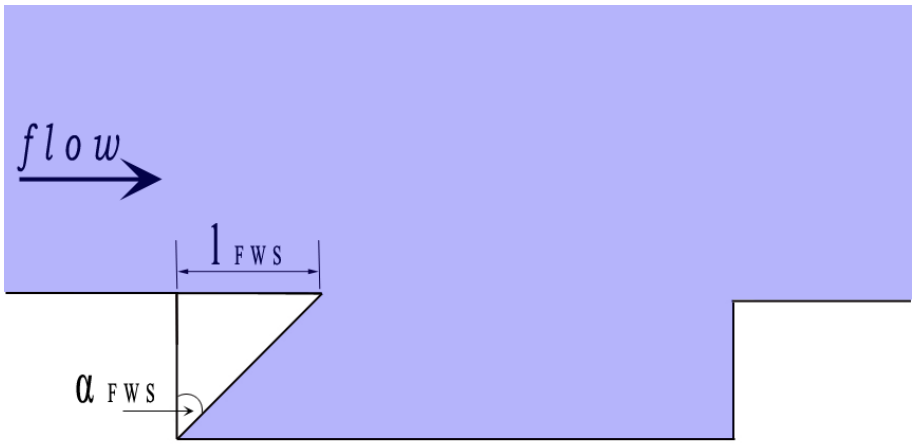

Figure 3.15: Front-wall slant (FWS)

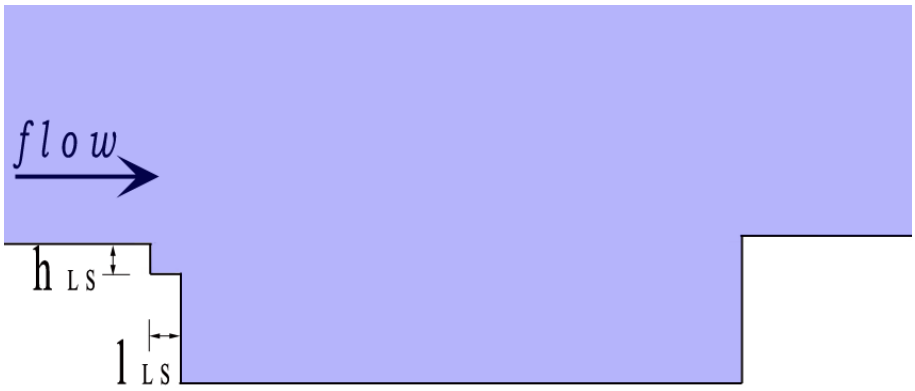

Figure 3.16: Leading-edge step (LS)

Figure 3.17: Trailing-edge step (TS)

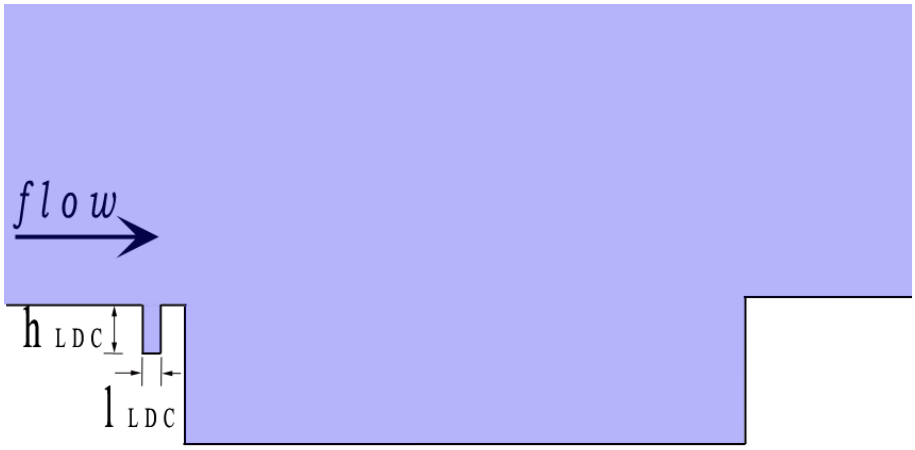

Figure 3.18: Leading-edge deep cavity (LDC)

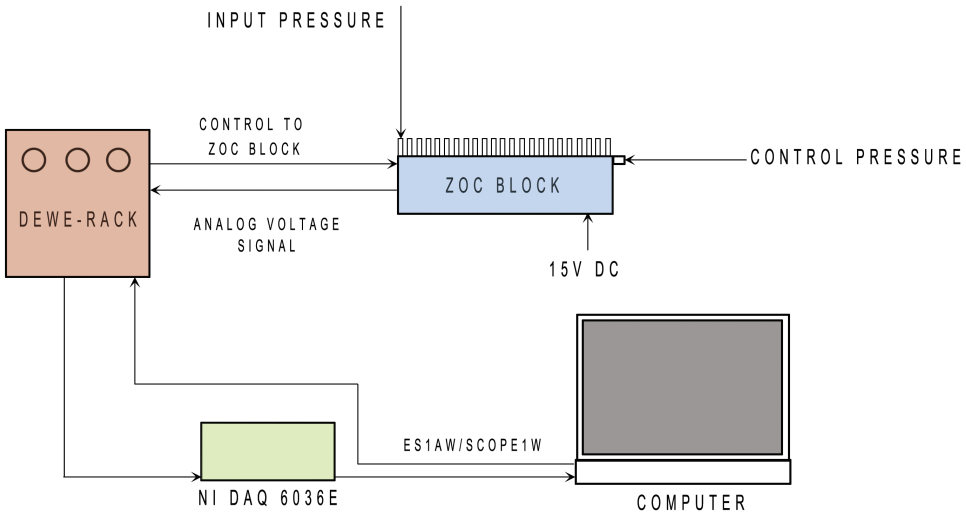

Figure 3.19: Layout of data acquisition system using ZOC block

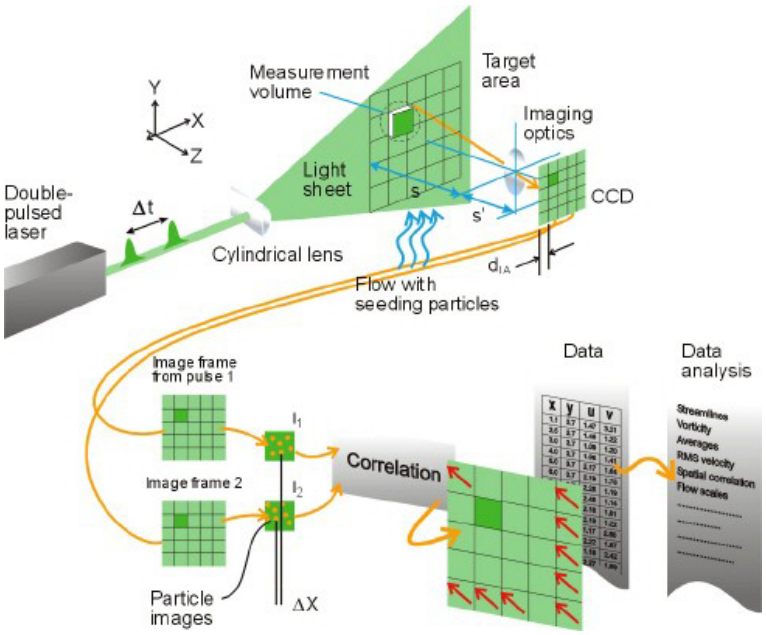

Figure 3.20: Principle of PIV measurement - courtesy of Dantec

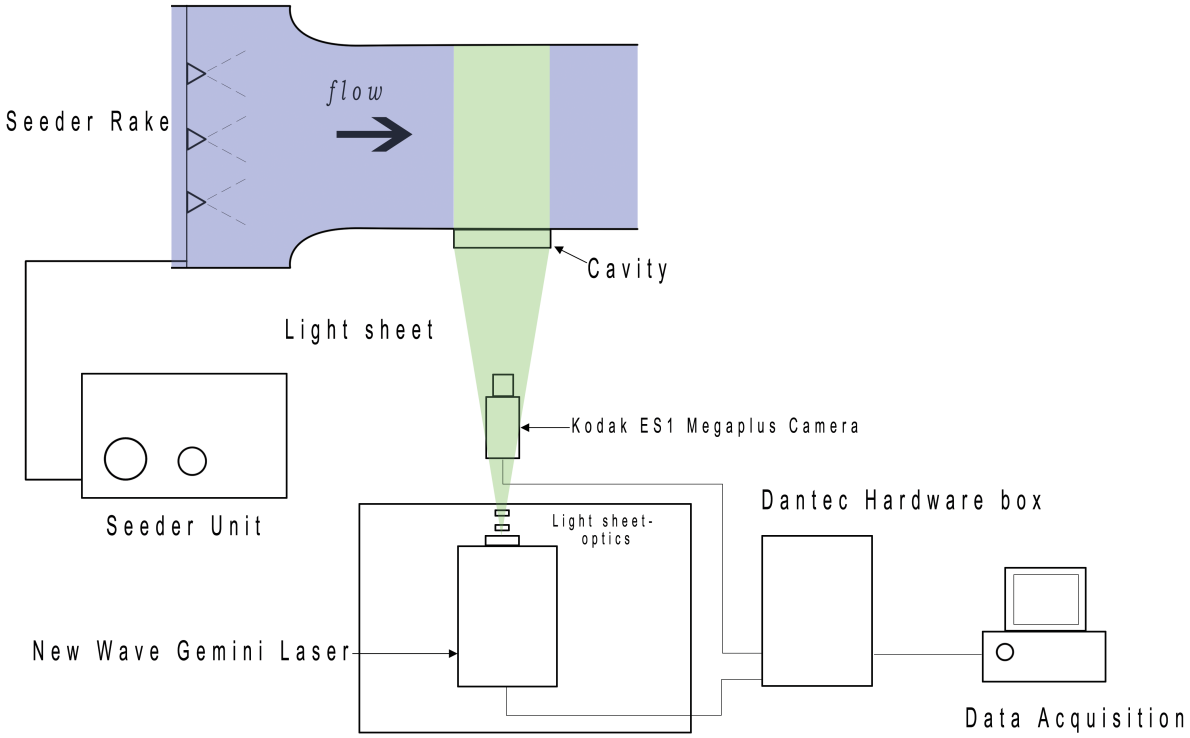

Figure 3.21: PIV experiment lay out - top view

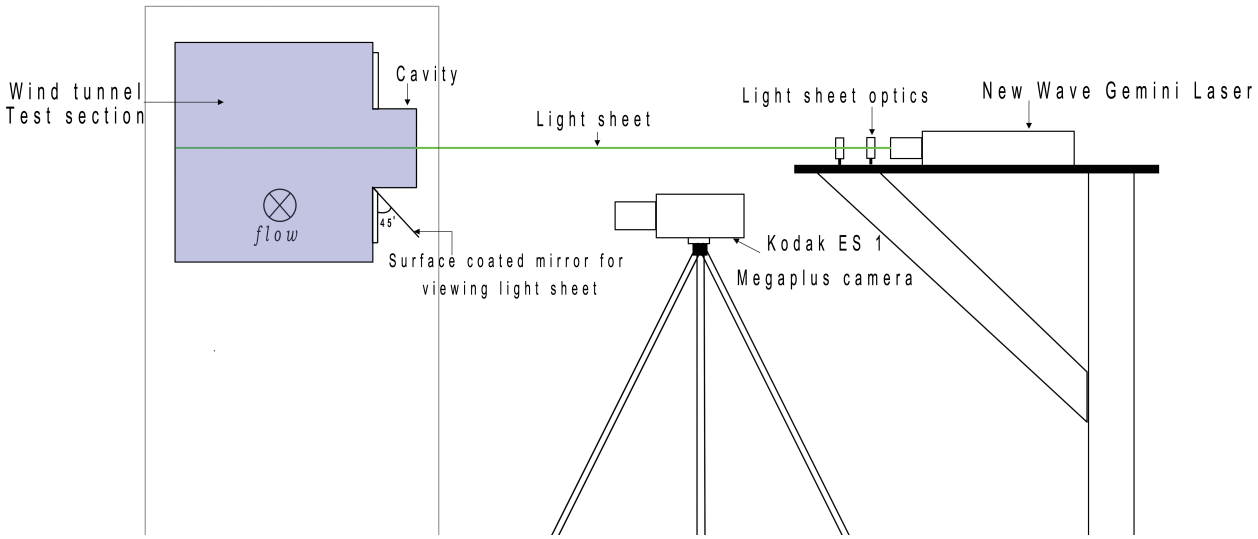

Figure 3.22: PIV experiment lay out - side view

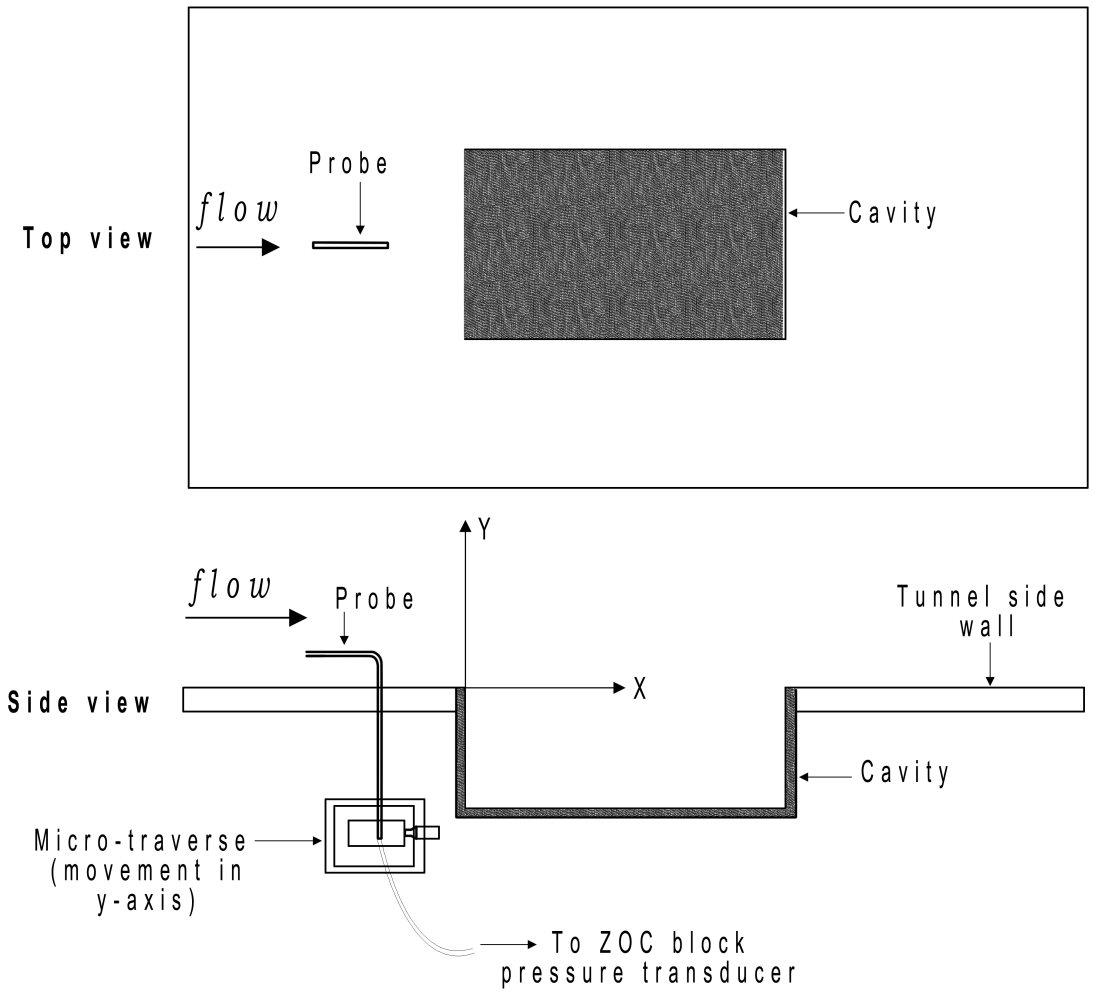

Figure 3.23: Boundary layer measurement set-up

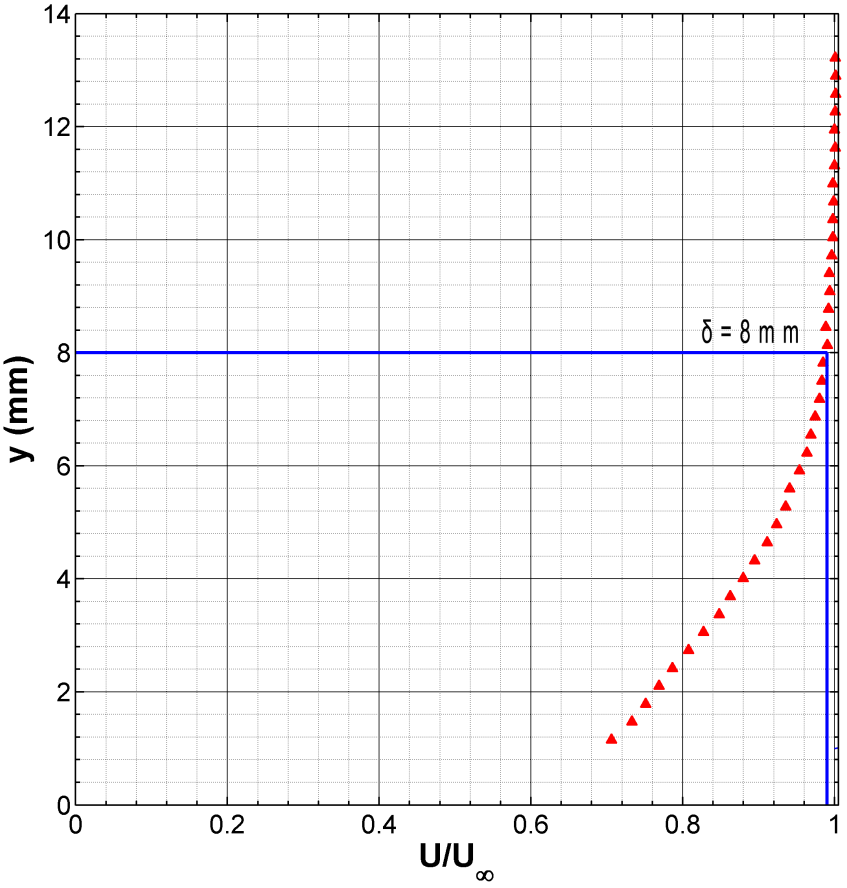

Figure 3.24: Experimental boundary layer profile with cavity at M = 0.71

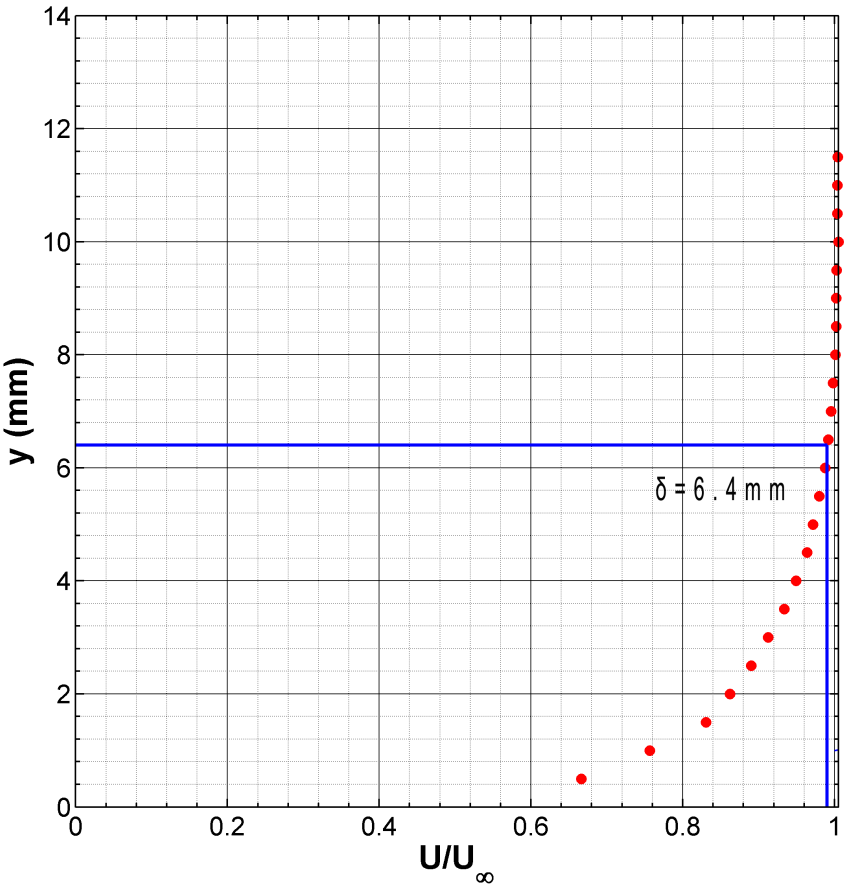

Figure 3.25: Experimental boundary layer profile in clean wind tunnel at M = 0.71 [Richardson et al. (2011)]

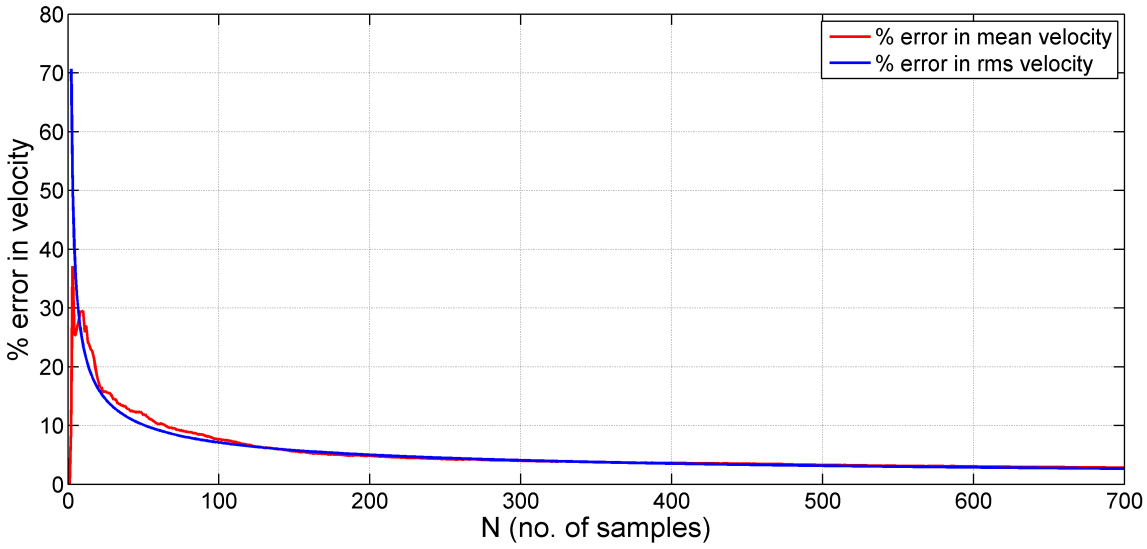

Figure 3.26: Variation of error in velocity with number of samples

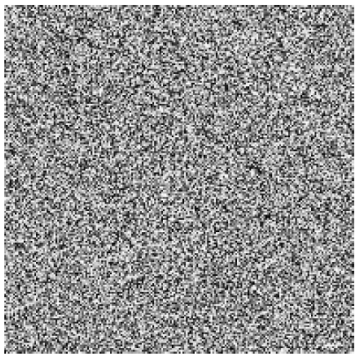

(a) Input - white noise

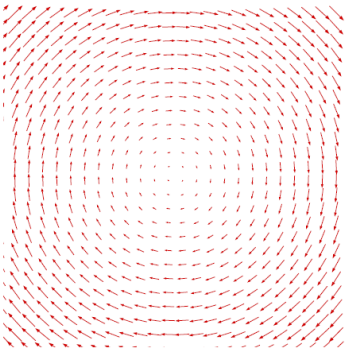

(b) Input - vector field B

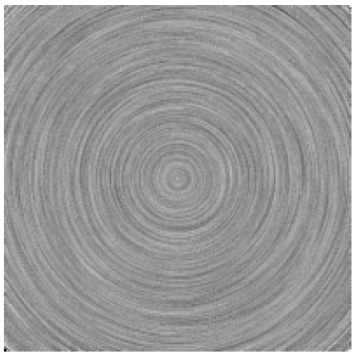

(c) Output - LIC image C

Figure 3.27: Example of line integral convolution (LIC) technique applied to a vector field [Knowles et al. (2006)]

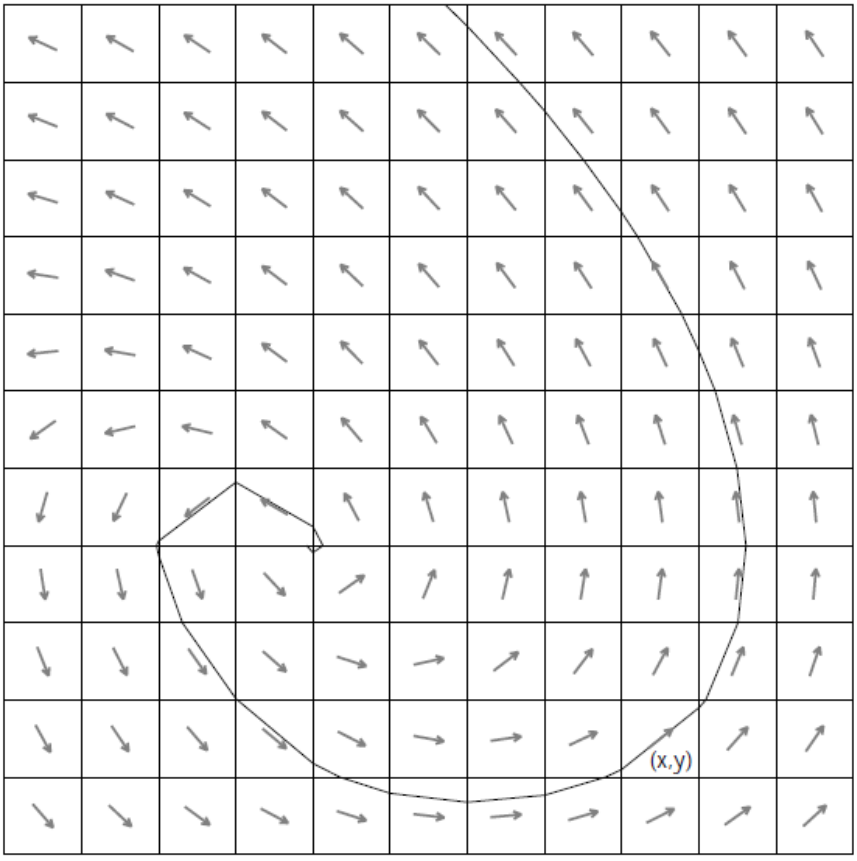

Figure 3.28: 2-D vector field showing the local starting in cell (x,y) [Cabral & Leedom (1993)]

Chapter 4

Results and Discussions

The salient results obtained from the experiments are presented in this chapter along with discussions. The chapter has been divided into three sections. The first section describes the effects of scaling on clean cavities. The effect of scaling on three of the most important aspects - the cavity flow type, cavity unsteadiness and cavity flow field have been addressed separately. In the second section, a comparative study of all the different passive control methods tested on the largest scale available is presented. Based on the results of this study, a suitable passive control method has been identified and the effects of scaling on its control effectiveness have been discussed in the third section. The empirical rules governing the scaling of this passive control device have also been deduced and presented in this section.

4.1 Effect of Scaling on Clean Cavities

It was seen in the literature review that barring the works of Shaw et al. (1988) and Ross (2001), there have been no major studies on the effects of scaling on cavity flows. These two studies, however, could not present a comprehensive report on the scaling effect on the cavity flow field and aeroacoustics. For example, Ross investigated the effect of scaling on power spectra and OASPL but did not look at the effects on other aspects, like cavity flow type, which is also very important in describing a cavity flow. In this section, the effects of scaling on all the major aspects of cavity flows including cavity flow-type and unsteadiness along with data on the cavity flow field are presented. The experiments were conducted on a cavity with L/D = 5, L/W = 2 and at Mach numbers 0.71 (for cavities A, B and C) and 0.85 (for cavities A and B).

4.1.1 Cavity flow-type

The time-averaged pressure distributions across the cavity floor can shed light on the three dimensionality and flow type of a cavity. Assuming symmetry across CP

and that there are no discontinuities in the pressure field on the cavity floor, the mean pressure measurements made along the CP, OP1 and OP2 planes were used to sketch contour plots of time-averaged pressure (Figures 4.1 to 4.5). Although, the spatial resolution of the pressure tappings are insufficient to capture accurately all the mean flow structures on the cavity floor, nevertheless the purpose of this discussion is to study the spanwise and streamwise variation of the pressure field. The contour plots reveal significant mean pressure variation in the streamwise direction especially towards the aft wall. There is a moderate effect in the spanwise direction due to the three-dimensional effects of the flow although the trend of the pressure variation is the same across each of the planes. From Figures 4.1 to 4.3, it can be seen that the magnitude of the pressure near the downstream wall increases in the order cavity C > cavity B > cavity A. It can be noticed from Figure 4.1 that for cavity A, the first 55 - 62% of the length of the cavity has relatively very low pressure values and gradients. The length of this low pressure-gradient region decreases with increase in scale and can be deduced as approximately 52% (centreline-based) for cavity B and 46% for cavity C (see Figures 4.2 and 4.3). The pressure levels are relatively uniform (less than 0.9% variation) in the spanwise direction in the range $0.1 < x/L < 0.45$ for all the cavities. This observation is due to the fact that the shear layer influence in that region is presumably minimal. The pressure gradient observed on a cavity floor is primarily due to the influence of the shear layer formed across its length. The streamwise and spanwise pressure gradients in this region are negligible and slight variations are induced due to local three-dimensional effects especially near the walls. In addition to the local three-dimensional effects near the front wall, the pressure in the region $0.1 < x/L < 0.5$ of the cavity is also influenced by the presence of tornado vortices present in the front half of the cavity. Their existence was demonstrated using three-dimensional computational simulations by Khanal (2010) for the same L/D and L/W ratios used in this study (see Figure 4.6). Near the aft wall where the shear layer influence is a maximum, local three-dimensional and corner effects become inconspicuous and are overwhelmed by the shear layer effects. The interaction between the cavity and the shear layer is a maximum near the aft wall.

Three-dimensional effects start from approximately mid-length of the cavity and extend towards the aft wall. The pressure rises rapidly and there is a steep gradient established. This pressure rise becomes higher with increase in scale. For

the downstream 40% of the cavity length, the pressure levels reduce in the order CP > OP1 > OP2. The effect of the pressure rise in the streamwise direction is more pronounced for cavities B and C and steep pressure gradients are established. This increase in pressure is due to the shear layer impingement on the aft wall of the cavity. When the shear layer deflects down into the cavity, as described by the model of Tam & Block (1978), it brings along a portion of freestream flow inside the cavity which stagnates momentarily due to the presence of the aft wall. The stagnation of the flow in front of the cavity aft wall leads to the pressure rise before it. This pressure increase near the aft wall acts as a source of acoustic disturbance inside the cavity, which is a constituent of the feedback process responsible for the Rossiter tones. The lower pressure gradients for cavity A could hint that the shear layer penetration into the cavity is less, leading to a reduction in the strength of the acoustic feedback. This observation will be substantiated by the unsteady pressure measurement results in Section 4.1.2.

The spanwise variation at the rear 40% of the cavity is due to the three dimensionality of the shear layer, induced by the walls and corners of the cavity and revealed by the CFD-derived flow visualization of Khanal et al. (2011). It can be seen that the pressure level on the plane CP, is slightly higher than on planes OP1 and OP2. This effect is conspicuous as a triangular high-pressure region near x/L = 0.9 at the mid-plane. This suggests that the shear layer which is impinging on the aft wall has a three-dimensional structure. As explained before, the high pressure observed is due to stagnation of freestream flow entering the cavity upstream of the aft wall. Hence the pressure level measured at a particular point near the trailing edge is indicative of the penetration of the shear layer into the cavity. The results show that the penetration of the shear layer is not uniform across the span. In fact it is highest on plane CP and reduces towards the side walls. The reduction in penetration at OP2 is presumably due to the effect of corners which try to deflect the shear layer out of the cavity. This behaviour of the shear layer was also noted by Ritchie (2005) who observed a decrease in shear layer interaction with the aft wall near the corners in his PIV data of different planes across the span. The pressure contours obtained for cavities A and B at M = 0.85 are shown in Figures 4.4 and 4.5. It can be seen that the change in Mach number has no significant effect on the trend of pressure variation in the downstream half of the cavity length although there are some variations near the leading edge.

From the available literature, it could be stated that the nature of a cavity flow can be determined by studying the C_p distribution along the cavity floor and it has been known to be influenced by the parameters L/D, L/W and M [Stallings & Wilcox (1987), Plentovich (1990), Tracy & Plentovich (1993)]. Researchers so far have not observed a change in the nature of the flow with the scale of a model. The C_p distribution on the cavity floor along the planes CP, OP1 and OP2 for cavities A, B and C are shown in Figures 4.7 - 4.9. The plots show that there is a considerable variation in the nature of the flow with change in scale (or L/δ). At the centre plane, the C_p is almost constant up to x/L = 0.5 for cavity A and rises steadily after that. The values are slightly negative until x/L $\simeq$ 0.7 and attain positive values after that. For cavity B, the value of C_p decreases gradually until x/L $\simeq$ 0.4 and increases after that. For cavity C, the C_p curve has a negative slope until x/L = 0.3 and rises steeply after x/L = 0.4 towards the aft wall. When the incoming boundary layer is very thin, under certain Mach number ranges, there is a change in the mode of cavity oscillations. Under such conditions, the cavity flow is characterized by a large-scale shedding of vortices and is known as the wake mode (Section 2.5.2). Despite a relatively thin boundary layer, the C_p curve shows that cavity C is in shear-layer mode of oscillation and has not transitioned to wake mode of oscillation. The C_p curve obtained for a cavity in wake mode is very different from a cavity oscillating in shear-layer mode as can be seen from the studies of Gharib & Roshko (1987).

The data obtained on CP, OP1 and OP2 show similar trends for the three cavities. With increasing L/δ, the C_p values become slightly more negative for the front portion of the cavity and more positive for the aft portion of the cavity. This observation is in agreement with the studies of previous researchers like Charwat et al. (1961), Stallings & Wilcox (1987) and Plentovich (1990). Nevertheless, in addition to this observation made by them, there is an additional important conclusion in this specific case there is a shift in the type of the flow. To deduce this, some data from previous researchers on the nature of the flow over a cavity has been referenced. Figure 4.10 shows the data obtained by Stallings & Wilcox (1987) for the transition of the flow type from open to transitional-open for W/D = 5 in a supersonic flow. According to Plentovich et al. (1993), an open flow is one in which the C_p is uniform and approximately close to zero from the leading edge to x/L $\simeq$ 0.6 and has a concave-up shape thereafter. A transitional flow is defined

as a flow for which mean-pressure distribution for the rear portion of the cavity changes from the concave-up shape of the open flow to concave-down shape and the C_p values in the forward region assume negative values. A closed flow can be easily identified by the presence of a point of inflexion which extends into a plateau upon further increase of L/D. The comparison between the current data and data obtained by Tracy & Plentovich and Stallings & Wilcox for the different regimes is shown in Figures 4.11 and 4.12.

Following the above definitions, it can be inferred from Figure 4.7 that the flow-type shifts from open to transitional flow as we move from cavity A to C. It can be seen that the C_p curve for cavity A is a concave-up shape as defined for an open cavity by Plentovich et al. (1993). The small negative values at the front portion of the cavity indicate that cavity A has just transitioned from a 'purely open' flow. Hence it can be said that cavity A is on the boundary of an open cavity flow regime. But for cavities B and C, the C_p values increase significantly at the rear portion of the cavity and the curve changes to a concave-down curve. Additionally, the C_p values for cavity C are no longer uniform for the front portion of the cavity and show large deviations from zero. Hence it can be deduced that cavity C has a transitional-open flow. Cavity B is in an intermediate stage where the C_p at the front begins to differ from zero and the rear portion of the cavity starts assuming a concave-down shape. This shows that increasing the scale of the cavity has an effect on the cavity flow-type which is tantamount to increasing L/D of the cavity. The change of the curvature from concave-up to concave-down can be shown by fitting a straight-line between the endpoints of the curve. For a concave-up curve, all the points on the curve lie below a line connecting the end points. In contrast, for a concave-down curve, a line connecting the endpoints of the curve lies completely below it without intersecting it at any other point. Figure 4.13 shows the C_p curves over the downstream half of the cavity with the line connecting the endpoints. It can be seen that for cavity A, the C_p curve lies completely below the straight line while for cavity C the curve lies above the straight line. For cavity B, the straight line intersects the curve in between and the points of the curve lie both above and below the line. Hence the C_p distribution curvature changes from concave-up to concave-down from cavity A to C.

Transitional cavity flow occurs when the shear layer dips into the cavity and is again deflected away from the cavity to impinge on the aft wall. For lower L/δ

values, the shear layer is postulated to bridge straight across the cavity length due to the shorter length and insufficient stagnation pressure region in front of the aft wall to deflect it away from the cavity. For cavity C, the shear layer dips into the cavity and rises up again before the aft wall. Such a behaviour of the shear layer results in a secondary recirculation region before reattaching with the aft wall. This shall be confirmed with data from PIV in Section 4.1.3. Nevertheless, it can be seen that the scaling parameter L/δ plays an important role in defining the flow type of a cavity. This variation in flow type could be more critical especially for cavities with L/D ratios which are on the border of open flow regimes. The reason why Plentovich (1990) could not have noticed such a change in flow type could be due to the fact that the impact of L/δ was tested on a cavity with L/D = 11.7 which already falls well within a transitional zone. The range of L/δ tested was also narrow in their studies (71.4 - 83.3). A change in flow type from open to transitional like the one demonstrated here can cause additional complications for store separation from an internal weapons bay. The increased pressure gradient causes higher nose-up pitching moments leading to difficulties in safe release and control of stores. The effect on the C_p distribution of varying the Mach number from 0.71 to 0.85 was not found to be large as can be seen from Figures 4.14 and 4.15. An extensive study of various cavity configurations by Plentovich (1990) showed that there was no consistent trend of C_p variation with Mach number for all the cavity geometries.

4.1.2 Cavity unsteadiness

A. FREQUENCY SPECTRUM

The flow oscillations in a cavity can be explained by studying the frequency spectrum of the unsteady pressure signal obtained from within the cavity. The unsteady pressure amplitude is a maximum near the aft wall of the CP and the values corresponding to x/L = 0.9, which is closest to the aft wall, will be focussed more in this work for comparative studies. Figures 4.16 and 4.17 show the narrowband spectra for the different clean cavities at x/L = 0.9 (on CP) for M = 0.71 and M = 0.85 plotted in terms of Strouhal numbers. It can be noticed that the spectra consist of broadband and multiple distinct 'peaks' ; these peaks constitute the cavity tones. These peaks have very high amplitudes compared to the other

frequencies. The feedback oscillation mechanism proposed by Rossiter (1964) is suitable for explaining the physics of cavity flow dynamics in many situations. Cavity oscillation studies by various researchers have found good agreement between the peaks determined by their data and the modified Rossiter formula by Heller & Bliss (1975), which is used as a technique to identify the Rossiter peaks. To find whether the oscillations here are caused by the mechanism explained by Rossiter, we evaluate the theoretical Rossiter frequencies using the semi-empirical equation

$$\frac{fL}{U_\infty} = \frac{m - \alpha}{M_\infty \left[1 + \left(\frac{\gamma-1}{2}\right) {M_\infty}^2\right]^{-0.5} + (1/k)} \tag{4.1}$$

where f is the frequency of the m^{th} mode, m = 1,2,3.., α is a phase constant between the downstream propagating vortical disturbances and the upstream pressure waves and 1/k is a vorticity parameter. Based on a review of past literature, α and k have been taken as 0.31 and 0.57 respectively. The difference between experimental and theoretical values are within the bounds reported by Ahuja & Mendoza (1995) in their extensive benchmark study of numerous cavity dimensions. They noticed that experimental values lie within an average of ±20% of the theoretical values and also observed a larger deviation in cavity tones from Rossiter's prediction at lower Mach numbers. Therefore the peaks in Figures 4.16 and 4.17 can be called the Rossiter tones and hereafter, they will be denoted as R1, R2 and R3. From the frequency spectrum, it can be observed that there are other peaks besides the ones described by Rossiter's equation. These peaks can arise due to the interaction between different Rossiter modes and their harmonics and sub-harmonics. The different frequencies interact non-linearly with each other and the resultant frequency is the sum/difference/multiple or a combination of the constituent frequencies [Kegerise et al. (2004)].

The spectra measured at different points on the cavity floor had peaks at the same frequencies which show that the cavity oscillations are global in nature (see Figure 4.18). For the spectra for cavity B at M = 0.71 (see Figure 4.19), the peak frequencies measured are 498 Hz (R1), 1072 Hz (R2) and 1646 Hz (R3) and the corresponding values according to the modified Rossiter formula are 413 Hz, 1012 Hz and 1611 Hz respectively. It can be seen that while the second and third

modes are well predicted by Equation 4.1, the first mode is under-predicted in this particular case. It can also be observed that the dominant tone here is R2 (1072 Hz) and has a very high amplitude compared to the other tones (SPL = 161.3 dB). For cavity B, at M = 0.85, the peaks are formed at frequencies corresponding to 460 Hz, 1229 Hz and 1952 Hz (Figure 4.20). The estimated values of Rossiter frequencies for M = 0.85 are 464 Hz, 1138 Hz and 1812 Hz for m = 1, 2 and 3. By comparing the calculated values with the peaks obtained in the frequency spectrum, it can be seen that there is a good agreement between experimental and estimated values for all the modes at M = 0.85. The Strouhal numbers of R1 and R2 can be observed to decrease slightly with increase in Mach number in Figure 4.21 which is consistent with Equation 4.1.

For cavity C at x/L = 0.9 for M = 0.71 (Figure 4.22), all the salient features explained for cavity B can be observed here as well. The Rossiter tones R1, R2 and R3 occur at 206 Hz, 553 Hz and 946 Hz respectively. In this case also, the dominant mode is R2 (553 Hz). Near R1, there are a range of frequencies with high amplitude. The deviation for R1 of cavity B and R3 of cavity C from the modified Rossiter's formula is 20.4% and 17.4% respectively - just at the limit of Ahuja and Mendoza's observed accuracy for the Rossiter model. Peaks observed in a cavity power spectrum can be due to Rossiter's mechanism, longitudinal oscillations ("duct oscillations") or through a non-linear interaction of the different modes and their harmonics or sub-harmonics. The estimated duct oscillation frequencies (based on Equation 2.1) are 1062 Hz for cavity B and 531 Hz for cavity C which are very close to the second Rossiter mode of the respective cavities. Similar to the observation of Ahuja & Mendoza (1995), high amplitude oscillations are noted here also when the longitudinal and Rossiter modes are close enough. Such high amplitudes could be a consequence of the cavities' enhanced response to these particular 'natural' frequencies.

Unlike cavity B and cavity C, the peaks obtained by plotting the spectrum of cavity A are not prominent for M = 0.71 (Figure 4.23). R1, R2 and R3 occur at 836.9 Hz, 2061 Hz and 3454 Hz for M = 0.71 and 972.7 Hz, 2373 Hz and 3885 Hz for M = 0.85 (Figure 4.24). The Strouhal numbers for M = 0.71 are 0.28, 0.69 and 1.13 as against the theoretical values of 0.28, 0.69 and 1.10 corresponding to m = 1, 2 and 3. However, the Rossiter tones become more prominent for cavity A when the Mach number is increased to 0.85, as seen in Figure 4.24. R1 is the dominant

tone for Cavity A at both the Mach numbers. With increases in Mach number, it can be seen from Figure 4.25, that the Strouhal numbers are slightly shifted to lower values.

Figure 4.26 shows the measured tone Strouhal numbers of the current experiments compared against the theoretical predictions by Rossiter (Equation 2.4) and Heller & Bliss (Equation 4.1). Except R1 for cavity B (at M = 0.71) and R3 for cavity C (at M = 0.71), all other values agree well and fall within ±10% of the theoretical predictions. Figure 4.27 shows that there is generally a scatter in the data obtained by different researchers from the theoretical values and the deviation becomes relatively large at lower Mach numbers. One reason for the deviation from theoretical values is the choice of the constants α and k in Rossiter's equation. Although researchers use empirical values based on data-fit, the true values depend on various conditions including the incoming boundary layer characteristics.

All the measured Strouhal numbers of the corresponding modes of the different cavities, except the two above-mentioned cases, lie within an absolute deviation of ±10% from the theoretical values. This shows the validity of Rossiter's feedback mechanism and the corresponding empirical formula across different scales. However, the accuracy of the prediction is not always the same as was seen above. One significant feature that can also be noticed from Figures 4.16 and 4.17 is that the amplitude of oscillation modes along with the broadband levels increase with increases in L/δ. A possible explanation for this behaviour can be given using the cavity oscillation model proposed by Heller et al. (1971). According to their model, the unsteady motion of the shear layer causes a periodic mass addition and removal process at the cavity trailing edge. This process produces a piston-like effect at the rear bulkhead, which sets up an internal wave structure that forces the shear layer. This shear layer motion is responsible for the trailing-edge mass addition and removal. When a shear layer is disturbed by an acoustic wave, the disturbance amplifies in the direction of the flow during convection and the shear layer displacement becomes a maximum at the trailing edge. With an increase in length from cavity A to C, this amplification of the shear layer increases and so does the displacement of the shear layer from the mean position at the trailing edge. This leads to an increase in the amplitude of pressure pulses produced by the 'pseudopiston' and is responsible for the high sound pressure levels observed

in cavity C. However, the exact mechanism can only be ascertained with the help of flow field data which will be discussed in Section 4.1.3. The broadband noise in a cavity is caused mainly due to the turbulent fluctuations in the shear layer. The amplitude of the fluctuations tend to increase with scale leading to a larger broadband level observed in the power spectra. It is speculated that this is due to the growth and convection of large scale structures or eddies present in the turbulent shear layer along the downstream direction. Nevertheless, the dominant frequencies of all the cavities agree well with Rossiter's formula and it can be said that they are generated due to the feedback mechanism proposed in his work. Hence the aim of any control techniques should be directed towards disrupting the feedback mechanism to achieve suppression of tones.

B. TIME-FREQUENCY ANALYSIS

It was seen from the results of the frequency spectra above that multiple modes of oscillation exist in all the cavities with a very visible dominant mode of oscillation noted for cavities B and C at M = 0.71. Oscillation of the shear layer in multiple modes leads to another critical question - whether these modes coexist all the time or if there is a 'mode switching' occurring between them. Kegerise et al. (2004) suggested that the Rossiter-mode peaks in an unsteady pressure spectrum may not coexist independently of each other but might be a result of mode switching. Experimental studies by Kegerise at M = 0.6 for a cavity of L/D = 4 showed the existence of mode switching and the dominant mode was seen to switch between primary Rossiter modes. The mode-switching phenomenon has also been numerically investigated by Gloerfelt et al. (2003). They noted that the dominant mode at a particular instant corresponds to the number of vortices in the shear layer bridging across the cavity.

Since the frequency spectrum does not give information about the temporal behaviour of the different modes, time-frequency analysis was employed to study the same. Figure 4.28 shows the spectrogram of cavity C. It can be seen that the second mode, R2, is the only mode that is present for the major part of the measurement time. Its strength is almost the same, barring mild fluctuations, for most of the time except for the two intervals : 0.3277 - 0.3482 s and 0.7782 - 0.8192 s. In these two intervals the second mode is almost non-existent. In contrast, the third mode, R3, can be observed to be energetic only during these two periods. This is significant and clear evidence of mode switching between R2 and R3.

During these periods, the energy of the flow is extracted by the cavity oscillation in the third mode and accounts for the high amplitude observed for R3 in the power spectrum of cavity C. For instance, at t = 0.7578 s, the strength of R2 and R3 is 171.7 dB and 152.9 dB respectively. After the occurrence of mode switching, at t = 0.7987 s, the strength of R2 is reduced to 154.7 dB while the strength of R3 has increased to 171 dB. Similar to the observation of previous researchers, here also the mode switching seems to occur randomly and not periodically throughout the sampling. However, longer time samples are required to verify this. The presence of R1 is not consistent with time and occurs randomly and mostly coexists with R2. From the above observations, it follows that any control experiment for cavity C should be designed to suppress R2 since it is the most dominant tone in terms of amplitude as well as prevalence in the time domain. This aspect becomes very pertinent in active control systems which are designed to force the shear layer at a particular frequency.

The evidence of mode switching was observed for cavity B as well at M = 0.71. In this case, there is a mode switching occurring between R2 and R1. It can be seen that R2 has its presence felt over most of the time period except intervals like 0.3277 - 0.3891 s and 0.6758 - 0.7782 s where it is dormant (Figure 4.29). At this interval R1 can be seen to dominate the spectrum. The occurrence of R1 during the other intervals is not prominent due to the presence of R2. The presence of R3 is intermittent and weak during most of the time intervals. For M = 0.85, there was no conspicuous presence of mode switching and R1 coexisted for a major part of the measurement time (from 0 - 0.8806 s) with R2. From the literature, mode switching has not been reported in all cases and the reason behind the occurrence of mode switching or coexistence of modes is still not clear.

For cavity A, because the peaks are less distinct than for cavities B and C, it is difficult to identify the time trace of R1 amidst the heavy envelope of broadband frequencies. Nevertheless, R2 and R3 are distinct and show some levels of intermittency. The occurrence of R2 seems to be periodic with very strong presence during the intervals 0.4096 - 0.4710 s, 0.6144-0.6554 s, 0.7782 - 0.8602 s and 0.9626 - 1.065 s.

Time-frequency analysis of all the cases shows that the different cavity modes do not coexist for all time and clear evidence of mode switching was observed for cavities B and C for M = 0.71. When mode switching occurred, the dominant

frequency switched from one mode to another. Also a larger deviation from Rossiter's formula was observed in the frequency of the new mode. It was noted earlier that R1 of cavity B and R3 of cavity C showed the greatest deviation from Rossiter's formula. The reason behind this deviation might not be the phenomenon of mode switching but due to a change in the flow conditions between the switches. Such changes are not represented by Rossiter's semi-empirical formula. This is the first report to note such deviations in the frequency values from Rossiter's equation when mode switching occurs. No such deviation was observed in other cases when mode switching was absent. During the mode switching, the energy was almost completely redirected from one mode to another. Gloerfelt et al. (2003) note that mode switching is more likely to be observed in fully turbulent shear layers i.e. at high Reynolds numbers. According to them, the vortices are then clusters of small scales rather than a single roll. It was also observed that the dominant frequency's presence was felt for more than 90% of the measurement time. The main aim of any control experiments would be to suppress the broadband as well as these dominant tones which follow Rossiter's mechanism. This is done by disrupting the feedback mechanism at one or more critical points.

C. MODE SHAPES

From the spectrogram studies it was shown that all the primary modes did not always coexist and there was mode-switching occurring between them. While certain modes were relatively 'steady' with time and existed for longer periods of the measurement, the occurrence of certain other modes was random. For example, R3 of cavity C (at M = 0.71) was found to be dominant only for two short intervals i.e. 0.3277 - 0.3482 s and 0.7782 - 0.8192 s which is approximately 19 cycles and 38 cycles respectively. However R2 occurred for more than 95% of the measurement time and it would be useful to look at the mode shape of such dominant tones for the different cavities. Figures 4.31 and 4.32 show the variation of the SPL values of the dominant tones of different cavities and their corresponding theoretical mode shapes that have been developed by Smith & Shaw (1975). The equation as a function of modal number (m), cavity L/D and streamwise position x/L can be written as

$$(SPL_m)_{x/L} = (SPL_m)_{x/L=1} - 10\left[1 - |cos\left(\Pi m(x/L)\right)| + (.33(L/D) - .6)\left(1 - x/L\right)\right] \quad (4.2)$$

The value at x/L =1 was calculated based on the value obtained at x/L =0.9. It can be seen from Figures 4.31 and 4.32 that the measured mode shapes are in general agreement with the theoretical mode shapes. The mode shape of the dominant frequency of the different cavities have standing-wave patterns. Mode shapes corresponding to different mode numbers, undergo different phase changes within the cavity. The mode R1 undergoes a phase change of π across the cavity length. It can be observed that there is a small lag of the measured shapes from the theoretical mode shapes. This slight variation is due to the assumption made for the equation that the pressure anti-node occurs at the rear wall while in reality it occurs slightly upstream of the rear wall. This is a manifestation of the periodic mass addition and removal at the trailing edge. Further, the accuracy of the mode shapes is also limited by the spatial resolution of the measurements made. Furthermore, Equation 4.2 is semi-empirical and was formulated based on data obtained predominantly from open cavities.

D. OASPL DISTRIBUTION

The Overall Sound Pressure Level (OASPL) gives the total energy under the frequency spectrum and describes the contribution of all the frequencies. Figure 4.33 shows the OASPL distribution for the three cavities at M = 0.71. It can be seen that the OASPL generally has higher values near the trailing edge. This increase is due to the amplification of the shear layer disturbances in the downstream direction. For cavity A, the OASPL rises monotonically downstream of 50% of the cavity length. In the case of cavities B and C, the region of monotonically-increasing OASPL in the rear of the cavity becomes progressively shorter. The shapes of the OASPL curves have a variation similar to the mode shapes of the dominant tones of the respective cavities (see Figures 4.31 and 4.32). This shows that the major contribution to the OASPL levels of the cavities is from the Rossiter tones. For cavities B and C, R2 is the dominant tone and the OASPL curve follows a variation similar to that of the amplitude of R2 along the streamwise direction. The steady increase in OASPL for cavity A from x/L = 0.5 to x/L = 0.9 is due to R1 being the dominant tone which has a steady rise in that range. For cavity A, the similarity of the OASPL curve to the mode shape of R1 is more evident in Figure 4.34 for M = 0.85, where the Rossiter tones were more prominent. The OASPL values increase as the cavity size is increased, with a fixed boundary layer thickness.

4.1.3 Cavity flow-field

With the increase in scale of the cavity, the mean pressure measurement results showed that the cavity flow type changes from open to transitional. It was seen from the unsteady pressure measurement results that the acoustic signature of the cavity, characterised by the modal number of the dominant mode and the mode switching, differed at different scales. The tones were amplified and the total energy of all the frequencies increased with scale. The mean velocity flow field measurements can shed light on the various mechanisms leading to these observations. The PIV measurements were made for all the clean cavities at the centre plane. The vector field of cavities A and B are constructed with 2100 vectors while cavity C is composed of 2204 vectors. Laser reflections from the floor and walls led to poor signal-to-noise ratios and, due to this, data within 1 mm of the floor and side walls have been omitted from the results. Due to the use of mirrors for imaging, the top 2 mm of the cavity flow close to the freestream was also not available from the results of cavities A and B. In the case of cavity C, an additional 8 mm has been omitted owing to the thickness of the opaque test rig into which the model was directly fitted.

Figures 4.35 - 4.39 show the mean velocity vector field obtained for the different cavities at M = 0.71 and M = 0.85. It can be seen that there is significant variation in the flow field of the different cavities. The velocity magnitudes and flow structures inside the cavity change with scale. In general, it can be seen that the velocity magnitudes in the shear layer inside the cavity increase with increasing scale. The velocity fields also show flow recirculation occurring inside the cavities. The recirculation vortex is formed due to the shearing action of the free shear layer and the resistance of the cavity walls on the fluid present inside the cavity. It can also be seen that the velocity magnitude is very low near the front wall. Cavity flow-visualization studies have shown that a small local vortex exists between the front wall and the primary recirculation region [Ritchie (2005), Khanal (2010)]. The velocities inside this enclosed vortex are very low as there is poor exchange of energy between the freestream and this vortex. The vortex is caused mainly due to the action of the primary recirculation vortex on the fluid between it and the walls. It can be seen that the vortex has not been well captured by the PIV velocity fields. This is because the flow seeding in this region is relatively low due to a lack of mass exchange between the vortex and the freestream. The flow field

here is also disturbed by the local three-dimensional effects which were observed in the pressure contours of the different cavities (Section 4.1.1).

In addition to the C_p profile on the cavity floor, the vortex configuration inside a cavity mean flow field can also be used as an aid to identify the cavity flow type. Line integral convolution (LIC) is a vector field visualization technique which has been found to be a suitable method for clearly identifying vortical structures in a flow [Knowles et al. (2006)]. Figures 4.40 and 4.41 show LIC images of the different cavities for M = 0.71 and M = 0.85 respectively. At M = 0.71 for cavity A, there is a single large recirculation region occupying the rear 75% of the cavity length. This vortex can be seen to be very weak. This could be due to the weak shear force caused by the shear layer. The tangential force exerted by the shear layer in this case is weak and the strength of the vortex is dissipated by the resistance of the cavity walls. The core of the vortex is formed at $0.25 < x/L < 0.35$. The region near the front wall for cavity A at M = 0.71 was seen from the OASPL and power spectral studies to be laden with noise. For M = 0.85, the recirculation vortex is stronger and more fully developed as can be seen in Figure 4.41. The presence of noise for cavity A for M = 0.85 was found to be significantly reduced. However the centre of the recirculation vortex has been pushed further downstream to $0.35 < x/L < 0.45$ with the increase in Mach number. As the scale is increased, the shear-layer velocities inside the cavity increase and so does the strength of the vortex. This causes a strong and fully-developed recirculation vortex for cavity B which can be seen in Figure 4.40 for M = 0.71. The core of this recirculation vortex lies in the region $0.3 < x/L < 0.4$ and is pushed downstream to $0.42 < x/L < 0.55$ with an increase in Mach number to 0.85 (Figure 4.41). Cavities A and B have a single recirculation vortex. Such a vortex configuration is generally found in open cavity flows. However, for cavity C, two distinct recirculation vortices can be observed from Figure 4.40. The centre of the primary and secondary recirculation regions occur at $0.25 < x/L < 0.4$ and $0.8 < x/L < 0.9$ respectively. This shows that the recirculation-vortex configuration system inside the cavity has changed and corresponds to transitional cavity flow. This is further evidence of the change in flow type of the cavity from open to transitional that has been observed in the mean pressure measurements on the cavity floor. Based on C_p measurements, cavity B was classified as transitional, however no secondary vortex was identified in the PIV measurements. Since cavity B is near the threshold of an open cavity

regime, the strength of the secondary vortex is weaker. Also the small area between the interface of the primary and secondary vortices is a region of high strain gradient which makes it difficult to be captured by the PIV, leading to the absence of the vortical structure in the LIC images. However the secondary vortex has been well captured in the case of cavity C. The formation of such a secondary recirculation region near the aft wall is due to the shear layer dipping into the cavity. For transitional cavities, the shear layer enters into the cavity but due to the stagnation effect in front of the aft wall is deflected away from the cavity before reattachment at the trailing edge. The deflection of the shear layer away from the cavity near the aft wall causes the secondary recirculation in front of the aft wall. Whereas for an open cavity, the shear layer bridges the length between the cavity leading edge and the trailing edge and the mean shear layer-streamline is approximately a straight line. Graphical interpretations of the flow-field configurations are given in Figure 4.42.

After separating from the leading edge, the shear layer thickens in the streamwise direction due to the velocity gradient existing between the freestream and cavity as illustrated in Figure 4.43. This separated shear layer transfers momentum from the freestream into the cavity. As the length of the cavity is increased, the momentum transferred, and thus the mean energy transferred into the cavity is also higher. This can be seen by the maximum u-velocities recorded in the mean flow for each cavity case. Figures 4.44 - 4.46 show the x-component of the velocities for the different cavities at M = 0.71, with Figures 4.47 - 4.48 showing the data for M = 0.85. While the peak velocities reach up to a 43.3 m/s for cavity A, it is 84.4 m/s for cavity B and is 95.8 m/s for cavity C. This increase in the magnitude of the u-velocities indicates an increase in the average momentum transfer into the cavity from the freestream over the different cycles. This increased momentum transfer leads to an increased momentum flux into the cavity in the streamwise direction near the aft wall region. The cavity tones are a result of feedback caused by the acoustic disturbances and the region near the aft wall acts as the source of the acoustic feedback which has been described in certain analytical works as a dipole source due to the periodic addition and removal of mass in that region [Tam & Block (1978)]. Within a single cycle, the pressure (and density in a compressible flow) of this region fluctuates from a minimum to a maximum value corresponding to the flapping motion of the shear layer. The momentum flux in

the positive x direction is primarily responsible for the stagnation and a pressure variation which acts as an acoustic source. The increased momentum transfer in the positive x direction in a large-scale cavity leads to the creation of a potentially stronger acoustic dipole, or source, near the aft wall, which could lead to higher pressure and density changes. The increase in the acoustic source strength can cause a strong feedback to exist inside the cavity leading to larger amplitudes of cavity tones. Although evidence of strong fluctuating pressure field was seen in Section 4.1.2, the consequence of such fluctuations in the velocity field can be confirmed with the study of fluctuating velocity fields which will be discussed further next.

While the mean velocity field can be used to explain the flow features occurring inside the cavity and mean energy transfer into the cavity, the fluctuating velocity field can be used to study the unsteady flow field. It was seen from the study of unsteady pressure measurements that increase in cavity scale was accompanied with a remarkable increase in the magnitudes of pressure fluctuations. With the increase in cavity scale, an increase in the amplitude of cavity tones as well as the broadband frequencies was noticed before. The shear layer fluctuates up and down during cavity oscillations due to the feedback cycle. Such an unsteady flapping motion of the shear layer is accompanied by energy and mass exchange between the freestream and the cavity flow. An increase in the mean energy transferred to the cavity with increase in scale was seen before in Figures 4.49 and 4.50. Whether this increase in energy contributes to the increase in flow oscillation energy and exchange between the freestream and the cavity per cycle can be seen from the contours of the rms of total velocity, V_{rms} inside the cavity. Figures 4.51 and 4.52 shows the contours of V_{rms} at the centre plane for the three different cavity scales at M = 0.71 and M = 0.85 respectively. It can be seen that as the cavity scale increases, the magnitudes of V_{rms} also increases. While the peak value of V_{rms} occurring for cavity A is 8.4% of the freestream velocity, it increases to 16% for cavity B and 17.5% for cavity C at M = 0.71. The corresponding values for cavity A and cavity B at M = 0.85 are 10.2% and 14.6% respectively. The increase in V_{rms} magnitudes indicates an increase in the quantity of energy exchange between the freestream and the cavity per cycle. It shows the fluctuation of the velocity field inside the cavity which is seen here to increase with scale. This fluctuation of the velocity field is caused due to the freestream entering and leaving the cavity

over a cycle as the shear layer flaps up and down. This increase in the magnitude of the fluctuating field with increase in scale is evidential and corroborates the increase in cavity pressure oscillations seen in Section 4.1.2. Such an increase in oscillation-energy is caused due to an increase in energy exchange per cycle leading to increased acoustic source strength and feedback. It also indicates a higher mass exchange taking place near the trailing edge of the cavity.

Since the shear layer impinges the aft wall and momentarily stagnates in front of it, the fluctuations in the x-component of the velocity is more significant. The contours of the x-component of the rms velocity, u_{rms} can be seen from Figures 4.53 and 4.54. It can be seen that u_{rms} increases substantially with increase in scale. This fluctuation in the u-velocity field is caused due to an increase in the strength of the oscillations. While the increase in u_{mean} indicates an increase in mean energy transfer to the cavity, the increase in u_{rms} indicates the increase in the strength of the flow oscillations. The maximum values occur near the top of the cavity due to the occurrence of large scale structures that convect across the cavity length in the shear layer. The quantity V_{rms}/V_{mean} at a given point can give the intensity of fluctuations there. However in cases such as cavity flows, the value of local mean velocity varies widely over the measurement region. The local mean velocity is nearly zero at regions near the front wall and near the centre of recirculation and therefore giving rise to large values of $1/V_{mean}$ and $1/u_{mean}$ there as can be seen from the case of cavity B from Figures 4.55 and 4.56. Due to the domination of this variation in the local mean flow, contour plots describing the quantities V_{rms}/V_{mean} and u_{rms}/u_{mean} yield little information.

A hypothesis regarding the possible mechanism for increase in the amplitude of cavity oscillation with scale is described here. It is known from the discussion in Section 2.5 that the source of the oscillations is pressure variation near the cavity aft wall. Heller & Bliss (1975) in their works described the aft wall as analogous to a pseudo-piston that periodically creates disturbances that travel upstream of the cavity. The pseudo-piston effect is essentially created due to an increase and decrease in pressure at the aft wall during an oscillation cycle. It was seen in Section 4.1.2 that the amplitude of this pressure variation increases with scale. It is proposed here that this increase in the pressure variation on the aft wall is majorly contributed by an increase in net momentum flux density into the cavity aft wall region. This is because the cause of pressure variation near the aft wall

region is the net momentum influx and outflux from there as the shear layer flaps in and out of the cavity. For this, consider a control surface adjoining the aft wall of a cavity as shown in Figure 4.57. Ignoring three-dimensional effects, the net momentum flux (H) into the control surface ABCD at a given time, t, can be expressed as

$$H(t) = \oint_{ABCD} \rho_t[(\overrightarrow{V}_{mean} + \overrightarrow{V'}_t).\hat{n}ds](\overrightarrow{V}_{mean} + \overrightarrow{V'}_t) \tag{4.3}$$

where ds is an infinitesimally small element of ABCD, $\overrightarrow{V}_{mean}$ is the mean total velocity at the element and ρ_t and $\overrightarrow{V'}_t$ are instantaneous values of density and fluctuating component of total velocity at the given location respectively. However, to evaluate the function H(t), the instantaneous values of velocity and density over a cycle are required. The momentum flux density, D(t), over the control surface is defined as

$$D(t) = H(t)/S_{ABCD} \tag{4.4}$$

where S_{ABCD} is the perimeter of the control surface ABCD. As mentioned before, the variation in D(t) is proposed to cause the pressure variation at the aft wall which creates the disturbance and acts as a pseudo-piston. The mean increase in net momentum flux density into the control surface during a half-cycle can be evaluated as

$$\overline{D}_{T/2} = \frac{2}{T}\int_0^{T/2} D(t)\,dt \tag{4.5}$$

where T is the time-period of oscillations. This increase in D(t) during a half-cycle occurs due to the shear layer dipping into the cavity. From the evidence of a general increase in V_{mean} and V_{rms} values seen with increase in scale from the PIV studies, it is postulated that the function $\overline{D}_{T/2}$ could also increase with scale. Although S_{ABCD} for cavity C is four times that of cavity A, the significantly higher values of velocities could lead to a higher value of D(t). For section DA of the control surface, D(t) is proportional to square of the local x-component

velocity. This implies an increased amplitude of D(t) for the control surface with scale and thus an increase in amplitude of pressure change near the aft wall as a consequence. Hence it follows that $\overline{D}_{T/2-cavityC} > \overline{D}_{T/2-cavityB} > \overline{D}_{T/2-cavityA}$. This could be the reason for the increase in the amplitude of oscillations seen with the increase in scale.

4.1.4 Summary and remarks

The effect of changing the scale of a clean cavity was studied in detail. The results showed that changing the scale of a cavity can profoundly affect the flow characteristics inside the cavity and its aeroacoustic signature. Mean pressure measurements show that the cavity flow type changes with the scale of the cavity, which has never been reported before. The results stress the need to include the factor L/δ as well as M and L/D to accurately define the flow type. Using the unsteady pressure measurements, it was seen that cavity tones along with broadband levels are amplified with the increase in scale. Certain aeroacoustic characteristics, such as mode switching and the dominant mode, also differed with a change in scale. This entails additional control challenges and draws attention to the needs of tailoring a control device to the variable L/δ. An increase in the amplitude of the cavity tones with scale necessitates a change in input parameters for passive control methods and input energy for active control methods. The mode switching and variation in the dominant mode is, however, more relevant and crucial to active control where selective tonal frequencies are targeted. The effect on a passive control technique of the change in unsteadiness characteristics of a cavity with scaling will be discussed in Section 4.3 and suggestions for adapting the passive control technique to this variable will also be given.

The study of the cavity flow field confirmed the change in flow type inside the cavity. The vortex configuration inside the cavity changed with scale. A steady increase in the magnitude of u_{mean} and u_{rms} with scale showed an increase in momentum transfer into the cavity aft wall region and increase in velocity field fluctuations associated with it. Such an increase in momentum transfer is primarily attributed to the length of the cavity with respect to the boundary layer thickness. The increased momentum transfer into the cavity aft wall region increases the strength of the acoustic source and feedback. This strong feedback

results in a larger displacement of the shear layer from the mean position leading to stronger vortical disturbances in the shear layer. These vortical disturbances grow in size as they convect along the downstream direction and further amplification takes place with length. This process continues in a positive feedback cycle and is responsible for the louder tones observed for the large-scale cavity. The mechanism explained for the cavity tone amplification shows the inherent behaviour of the shear layer that is sensitive to cavity scale. It is essentially responsible for the transfer and exchange of the energy between the freestream and the cavity, which is decisive of the aeroacoustic and flow-field behaviour of the cavity. The total net energy transferred to a cavity in a cycle manifests as flow oscillatory energy and entropy loss.

4.2 Passive Control of Cavity Flows

Before studying the effect of scaling on passive control, it would be useful to have insight into the comparative performance of different palliative devices. It would be preferable to choose a passive control technique that is superior and has features suitable to application in an aircraft weapons bay. The most appropriate method for the scaling study shall be chosen based on the results of this study. Thirteen different passive control techniques listed in Section 3.1.3 have been tested for this purpose. Figures 4.58 - 4.63 show the effect of the different passive control devices on the power spectrum as compared against that of the clean cavity (CC). It can be seen that there is a significant variation in the suppression of the tones by the different methods. Leading-edge spoilers show the maximum attenuation of cavity tones and noise near the trailing edge (Figure 4.58). Of these spoilers, the square-tooth spoiler (STS) shows maximum suppression of the tones with R2 being reduced to 153.4 dB, which is a reduction of 8.8 dB. This is very high considering the scale of the cavity and is followed by the flat top spoiler, FTS (8.5 dB), the leading-edge wedge, LW (7.5 dB) and the sawtooth spoiler, SWS (7.4 dB) respectively. Another observation that can be noted from Figure 4.58 is the increase in the tonal frequencies when the leading-edge spoilers are used. This increase in frequency may be caused by an increase in convective velocities of vortices in the deflected shear layer and/or an increase in the reverse velocities inside the cavity with the use of spoilers. The increase in reverse velocities in

a cavity with spoilers will be discussed later in Section 4.3. Similar increases in frequency with use of leading-edge spoilers was also noted by Lawson & Barakos (2009). It should be noted that even with the presence of control devices, the tones are not completely attenuated.

Certain passive controls methods involved modifications to the walls of the cavity and these methods were tested on both the front and aft walls. Such testing revealed interesting variations in the suppression results. While the front-wall slant (FWS) reduced R2 by only 1.2 dB and increased R1 by 0.8 dB, it completely attenuated R3 to a broadband noise level (Figure 4.59). The aft-wall slant (AWS) had no effect on tonal suppression and, in fact, increased the amplitude of the tones. However, a decrease in broadband noise was observed. While the trailing-edge ramp (TR) decreased the tone intensity slightly, the leading-edge ramp (LR) increased the same (Figure 4.60). The other methods tested were not found to be very effective in tone suppression as can be seen from Figures 4.61 to 4.63.

The overall sound pressure level (OASPL) was calculated across the cavity length and showed variations at different measurement points. The leading-edge spoilers FTS, SWS, LW and STS showed a significant reduction in OASPL as can be seen in Figure 4.64. The maximum reduction is 11.05 dB for STS at x/L = 0.4. The square-tooth spoiler (STS) also shows the maximum average reduction in OASPL across different locations (8.13 dB). This is followed by the sawtooth spoiler with an average reduction of 7.9 dB and then by the flat-top spoiler (FTS) and leading-edge wedge (LW) which have the same average reduction values (7.65 dB). From previous studies, it is known that the height of the spoilers plays a crucial role in noise suppression [Rossiter (1964), Shaw et al. (1988)]. However, the results here show that the profile of the leading-edge spoiler also plays a significant role in noise suppression. The variation of the OASPL reduction across the length of the cavity for FTS, SWS, LW and STS is similar to the mode shape of the dominant tone R2 of the clean cavity (refer to Figure 4.31). This shows that the reduction in noise has resulted significantly from the reduction of the amplitude of the dominant tone. Thus, these methods have a direct impact in disrupting the Rossiter mechanism of cavity oscillation and thus reducing the tonal amplitudes. The shape of the OASPL curves for the aft-wall slant (AWS) and the front-wall slant (FWS) differs from these curves because these methods do not have a significant effect on R2, as was seen in their unsteady power spectra

(Figure 4.59). The OASPL reductions for FWS result from the suppression of R3 and R2 as well as a decrease in the broadband noise. The other passive control methods do not show a significant noise reduction and at some points certain methods like the leading-edge step (LS) and leading-edge ramp (LR) increase the noise.

As mentioned previously in Section 4.1.1, the steep pressure gradient established on the cavity floor can be unfavourable for store release and it is therefore pertinent to reduce the gradients established along with the suppression of flow unsteadiness. Figure 4.65 shows the time-averaged pressure on the floor across the cavity length. It can be seen that there is a steep pressure gradient for the clean cavity (CC) and the curve is typical of a transitional cavity flow, as discussed in Section 4.1.1. Most of the passive control devices reduce the pressure inside the cavity. The leading-edge spoilers, which were shown to have very good suppression results, can be seen to reduce the cavity floor pressures significantly. In addition to the reduction, the pressure is also approximately uniform for up to 80% of the cavity length. The pressure magnitudes increases slightly towards the trailing edge indicating a very weak interaction there between the cavity and flow. For the leading-edge wedge (LW) and the flat top spoiler (FTS), the absolute pressure is reduced by an average of 23% up to x/L = 0.7, while for the square-tooth and sawtooth spoilers (STS and SWS) the value is 19%. This suggests that the pressure reduction inside the cavity is a result of the flow being deflected away from the cavity. For the leading-edge wedge and rectangular fence (LW and RF), the blockage to the flow is high and results in more deflection of the flow away from the cavity and lower pressure inside the cavity. The front-wall slant (FWS) also shows a 7% reduction in absolute pressure. However, the gradient established in this case is smoother than with the spoilers and is slightly more favourable for the release of stores. This can have practical implications since the front-wall slant (FWS) produces less drag compared to the leading-edge spoilers and the angle (α_{FWS}) can be optimised to disrupt the pressure gradients inside and ensure the safe release of stores. The other passive control methods show only a slight flattening of the pressure gradients and are not as significant.

4.2.1 Summary and remarks

A comparative study of 13 different passive control techniques on a large scale (L/δ = 40) cavity was conducted. None of the passive control methods were able to suppress the cavity tones completely at this value of L/δ. However, the results showed that leading-edge spoiler designs, such as the square-tooth spoiler, sawtooth spoiler, flattop spoiler and leading-edge wedge have superior tone suppression capabilities when compared to the other methods. The suppression of the dominant tone near the aft wall was highest for STS (8.8 dB) followed by FTS (8.5 dB), LW (7.5 dB) and SWS (7.4 dB). The performance of the leading-edge spoilers were better in terms of OASPL reduction and reducing the mean pressure gradient on the floor. STS and SWS showed highest average reduction of OASPL along the centreline of 8.13 dB and 7.9 dB respectively.

Certain considerations must be weighed up when choosing a passive control device for an aircraft weapons bay. Among the leading-edge spoilers FTS, STS and SWS are more desirable as they are simple, occupy minimal space and can be deployed with ease during a weapons bay operation. A leading-edge spoiler, being exposed to the high velocity freestream flow can cause significant drag. In this regard, the FTS is expected to produce relatively more drag than STS and SWS. Unlike the other passive control methods tested, leading-edge spoilers are also prone to increase the radar signature since they protrude out of the aircraft. One of the primary aims of using an internal weapons bay is to reduce the radar signature and of the two remaining spoilers, SWS and STS, SWS is expected to have a smaller radar cross section due to the lack of 90^0 corners. Also STS are expected to cause more aerodynamic self-noise due to the larger perimeter of blunt edges and more vertices [Brookes et al. (1989)]. Overall, SWS appears to be a desirable candidate for passive control in a weapons bay and it was the profile used by Shaw et al. (1988) in testing on a $1/17^{th}$ scale of an F-111 weapons bay. For these reasons, SWS is chosen as the technique to be tested for the scaling studies. The effects of scaling on the control effectiveness of SWS will be studied by testing it across the three different cavities - A, B and C. Nevertheless, the implications of the effects of scaling on the sawtooth spoiler can be extrapolated to other leading-edge spoilers as well.

4.3 Effect of Scaling on Passive Control

This section explains the effects of scaling the cavity on the control effectiveness of a sawtooth spoiler. The effectiveness of SWS across different scales was tested by using spoilers of the same profile and height, $h_{SWS}/\delta = 1$ on cavities A, B and C. Spoilers with height approximately equal to the boundary layer thickness were previously tested by many researchers including Rossiter (1964), Shaw et al. (1988), Ashworth (2008), Lawson & Barakos (2009). Figures 4.66 - 4.70 show the power spectra of cavities A, B and C with the use of SWS. It can be clearly observed that the effectiveness of the spoilers is not the same for all three cavities. While strong tones still exist for cavity C with the use of SWS, there are no high amplitude peaks visible for cavities A and B. For cavity A, the tones are almost completely attenuated to a broadband level.

It can be seen that, with the use of spoilers, there is a decrease in both the broadband as well as tonal amplitudes for cavities A and B for both Mach numbers. For M = 0.71, cavity A has a maximum reduction of 5 dB in the dominant tone (R1), while for cavity B there is a maximum reduction of 12.7 dB for the dominant tone (R2), which is very high. For M = 0.85, there is a reduction of 5.7 dB for cavity A in the dominant tone, whereas there is a maximum reduction of 11.4 dB for cavity B in the dominant tone at the same Mach number. For cavity A, it can be observed that the frequency spectra are almost reduced to a broadband level with the use of SWS of height equal to the boundary layer thickness. For cavity B, most of the cavity tones have disappeared and the only peak observable is R1.

Figure 4.71 shows the comparison of the power spectra of cavities A, B and C with the use of SWS. While all three cavity modes are existent for cavity C, only R1 is visible for cavity B and no cavity tones are present for cavity A. This shows a significant disruption of the feedback mechanism by the spoilers leading to an almost complete attenuation of cavity tones for cavity A. For cavity C there is significantly less reduction in the cavity unsteadiness. Although there is a reduction of 7.4 dB in the dominant tone, the power spectrum is not reduced to broadband. There are high amplitude peaks present even after the use of spoilers, although with reduced magnitude when compared to the clean cavity. This shows that the same spoiler is unable to cope with the increase in flow unsteadiness caused by the increase in scale. It proves the loss in the effectiveness

of the spoiler as a tone suppression method for large values of L/δ. It can also be noted from Figure 4.71 that the dominant tone for cavities B and C shifts from the second mode to the first mode. Similar observations can be made for M = 0.85.

Figure 4.72 shows the centreline mean pressure distribution on the cavity floor with the use of various spoilers. It can be seen that with the use of spoilers, there is significant reduction of pressure on the cavity floor. The pressure reduction indicates a possible lifting of the shear layer by the spoiler. Experimental and numerical studies with fences and cylindrical rods placed on the cavity leading edge show a similar observation [Lawson & Barakos (2009), Ukeiley et al. (2004)]. The presence of the spoiler in front of the cavity causes the flow in front of it to decelerate and create a region of high pressure. This causes the shear layer to deflect towards the freestream instead of going into the cavity. This 'lifting' of the shear layer can potentially affect the interaction of the shear layer with the aft wall and reduce the feedback strength, which leads to a decrease in the oscillation amplitude. Also, there is a pressure rise in all the cases near the trailing edge, indicating a weak interaction between the shear layer and aft wall. The extent of the mean pressure reduction, however, does not correlate directly with the unsteadiness in the cavity. The mean pressure distribution change however indicates a change in the mean flow structures inside the cavity.

To assess an overall reduction in the total energy of all the frequencies, overall sound pressure levels (OASPL) have been plotted. Figure 4.73 shows the OASPL variation along the streamwise direction for the three cavities with the use of spoilers. It can be seen that cavity C has generally higher OASPL values compared to cavities A and B especially in the rear 40% of the cavity length. For the front 30% of the cavity length, the OASPL values of cavities A and B are closer to the values of cavity C. This is due to the increase in broadband noise associated with increase in shear layer turbulence for cavities A and B. Although the spoiler effectively reduces the feedback strength of the Rossiter mechanism, it also increases the turbulence of the shear layer. The influence of this increase in shear layer turbulence becomes significant with decreasing L/δ. The use of a spoiler at the leading edge increases the turbulence in the shear layer and thickens it. When the shear layer is close to the floor, the turbulence in the shear layer is felt by the cavity floor. This can be appreciated by looking at the reduction of OASPL from clean cavity cases at different locations (Figure 4.74). It can be seen that for the

front 60%, the reduction in OASPL for cavities A and B are less than cavity C. This is due to the increase in turbulent noise created by the presence of spoilers. The effect is predominant in the front half of the cavity. Similar observations have been made by Ukeiley et al. (2004), in their work with a solid fence. According to them, sources in the shear layer contribute to the surface pressure sensed in the front part of the cavity so that not all of the surface pressure fluctuations are entirely due to the interaction between the shear layer and the aft wall. However, for the rear 20% of the length, cavity B shows the greatest reduction. Cavity C shows a reduction level similar to the OASPL variation of the clean cavity across the cavity length because of the negligible effect of shear layer turbulence on the cavity floor. Here the reduction in OASPL is proportional to the reduction in the feedback strength and is not influenced by broadband turbulence and hence follows the shape of the OASPL variation of the clean cavity. The variation of OASPL reduction in the streamwise direction is related to the variation of the amplitude of the dominant tone for the large scale. With lower values of L/δ, this trend gets disturbed by the turbulence in the shear layer. Figure 4.75 shows the variation of OASPL and maximum dominant tone with the use of SWS for the three different cavities at x/L = 0.9. Both the OASPL and the dominant tone amplitude increase significantly with increase in L/δ, as can be seen from the figure.

Figure 4.76 shows the reduction in OASPL for cavities A and B for M = 0.85. It can be seen that the trend is similar to the measurements made at M = 0.71 for cavity B, though the suppression levels are higher. This observation shows that the disruption of the feedback loop increases at M = 0.85 for cavity B, compared with M = 0.71. This is speculated to be due to increased lifting of the shear layer at M = 0.85 as the C_p values on the cavity floor were found to be lower in this case indicating an increased lifting. The reduction in OASPL is less for cavity A for the front 60% of the cavity length. However, the streamwise variation of OASPL reductions for cavity A shows a clearer trend at M = 0.85 and is less influenced by the shear layer turbulence. The shape of the reduction curve is similar to the mode shape of the dominant tone R1 of cavity A (refer to Figure 4.32). This again corroborates the earlier statement that the reduction at a particular point is related to the amplitude of the dominant tone at that point.

The suppression levels show significant spanwise variation too. The variation of OASPL reductions at the three streamwise planes CP, OP1 and OP2 can be seen

in Figures 4.77 - 4.79. For both cavity A and cavity B, the reduction at CP and OP2 is slightly out of phase with the reduction at OP1. This could be due to the three-dimensionality induced by the spoilers for cavities A and B. This fluctuating OASPL across different planes shows that the use of a sawtooth spoiler disturbs the coherence of the shear layer. The phase differences seen in the reductions correspond to the peaks and valleys in the sawtooth spoiler and show that the interaction of the shear layer and the trailing edge is not uniform across the span. It can also be seen that, while cavities A and B have significant three dimensionality, the variation of OASPL reduction across different planes for cavity C is almost the same and shows less spanwise variation. This shows that the shear layer is coherent and thus becomes relatively more effective in causing acoustic feedback for cavity C. For cavities A and B, the OASPL reduction is also influenced by the effect of the shear layer turbulence on the cavity floor as explained before. The spoilers induce significant spanwise three-dimensional effects in the shear layer. For cavity C, a more coherent and less disturbed shear layer is partly responsible for the high-amplitude tones observed in the spectrum. The results of the streamwise variation analysis shows that apart from the lifting of shear layer, disturbance of the spatial coherence is also responsible for the attenuation of cavity tones. A shear layer with severe three-dimensional variation produces a weaker acoustic source at the aft wall. This is due to a reduction of the momentum flux in the streamwise direction which was explained in Section 4.1.3. At higher scales, the spatial disruption is less and the shear layer is more coherent, leading to higher amplitude tones.

Figures 4.80 - 4.94 show the velocity fields of cavities A, B and C with the sawtooth spoiler attached. There is a significant change in the flow field inside the cavity due to the presence of the spoilers. The velocity magnitude, in particular the velocity in the streamwise direction, has been reduced significantly when compared to the clean cavity cases (Figures 4.82, 4.85 and 4.88). This reduction in the u-velocity and reduction in mean pressure already observed corroborates that the use of spoilers deflects the shear layer away from the cavity. Due to the presence of the spoiler, the shear layer is vertically displaced or 'lifted' which decreases its interaction with the aft wall. This leads to a decreased momentum transfer to the acoustic source region which was seen attributed in Section 4.1.3 as the driving reason for tone amplification. However, it is to be noted that lifting

of the shear layer alone would not be responsible for the decrease in momentum transfer. Spoilers introduce severe three dimensionality to the shear layer and decrease their spatial coherence. It also thickens the shear layer due to vorticity induced in the streamwise direction. These reasons also contribute to reduced momentum transfer from the freestream to the vicinity of aft wall. The decreased momentum transfer and strength of the acoustic feedback results in tone attenuation that has been observed in the frequency spectra. While the maximum values of u_{mean} for cavities A, B and C were observed to be 18.1%, 36.1% and 41% of the freestream velocity for the respective clean cavities, the values have reduced to 4.9%, 15.2% and 28% for cavities with spoilers. This indicates a 73.2%, 57.7% and 31.3% reduction in the values of peak u-velocity for cavities A, B and C respectively. It can be noted that cavity A has the maximum reduction in u while cavity C has the minimum reduction. The fluctuating velocities, V_{rms} was also seen to be reduced to 6.8%, 9.1% and 11.2% of the freestream velocities for cavities A, B and C respectively. This indicates the reduction in the strength of flow oscillations in the cavities with the use of spoilers (see Figures 4.95 and 4.96). The largest reduction in V_{rms} occurred for cavity B where a 42.8/ % reduction in peak values from the baseline case were observed.Ashworth (2008), in his computational studies of a cavity at M = 0.85 with L/D = 5 and fitted with spoilers, noticed that the shear layer rose for up to $1/5^{th}$ of the cavity length. Due to the use of the spoilers with the same h_{SWS}/δ, the length up to which the shear layer is vertically displaced should be equal. After a particular length, the effect of the shear layer lifting could diminish as the shear layer spreads downstream. This could be the reason for stronger interaction between the shear layer and the trailing edge and accompanying unsteadiness with increases in L/δ.

Another significant change that occurs due to the spoilers is the increase in the mean values of negative streamwise velocity (-u). The increase in negative velocities is due to the lifting of the shear layer and a decrease in pressure inside the cavity. The decrease in the streamwise velocity and increase in the negative velocity across the different cavities can be clearly seen in Figure 4.97, which shows the percentage change in the values of maximum +u and -u with the use of spoilers. Cavity A is most affected by the use of spoilers and the effects of the spoiler is least on cavity C. The spoiler deflects the shear layer away and creates relatively low pressures inside the cavity. As the scale of the cavity decreases, the

shear layer becomes close to this low pressure trough leading to an increase in negative velocities observed in Figure 4.97 for cavity A. The increase in negative velocities with the use of spoilers is responsible for the increase in frequency of the tones observed in the power spectra. The velocity of the feedback acoustic wave increases with increase in local velocity. As the negative velocity is increased, the acoustic wave travels faster in the upstream direction inside the cavity leading to a lower time period of oscillation and higher frequencies.

The effect of using spoilers in the flow structures inside the cavity can be studied using LIC. Figures 4.98 - 4.102 show the effect of using spoilers on the recirculation vortices of the different cavities. With the use of a spoiler, all the cavities have a single large recirculation vortex. The two recirculation regions observed in the clean cavity are replaced by a single recirculation vortex in cavity C with the use of a spoiler. For cavity A at M = 0.71, the recirculation vortex was found to be weak for the clean cavity case. However, with the use of spoiler Figure 4.97 shows that the peak negative velocities increase by 303.8%. This large increase in negative velocity causes a stronger recirculation vortex inside the cavity as can be seen in Figure 4.98. It can also be noticed that the central vortex of the different cavities changes in shape and becomes more aligned with the cavity floor with the use of a spoiler. This is another effect of the reduction in u-velocities. To better understand this mechanism, a superposition of an isolated potential vortex flow with a uniform flow in the x-direction is illustrated in Figure 4.103. It can be seen that the addition of velocity in the +x direction causes the vortex to change shape. This analogy can be applied to the current situation where the recirculation vortex of the cavity with a spoiler gets distorted due to the addition of flow in the +x direction in the clean cavity case. This effect is more pronounced for cavities A and B where the reduction in u-velocity is relatively higher.

While spoilers of the same h_{SWS}/δ ratio were able to totally attenuate the cavity tones and reduce the frequency spectrum to broadband level for smaller scales, it was also found that the spoilers were incapable of removing cavity tones and unsteadiness for a large scale cavity. This shows that leading-edge spoilers cannot be scaled to the boundary layer thickness alone to achieve suppression. When a variation in such L/δ incapacitates a spoiler, the only practical approach to solve it is to increase the height of the spoiler. To deduce the correct spoiler height required for a particular value of L/δ requires the testing of different spoiler heights

at different values of L/δ. Sawtooth spoilers of different heights were tested in the three cavities (details given in Table 3.4). Figures 4.104 - 4.108 show the power spectra of the different cavities with various spoiler heights. It can clearly be seen that, in general, increasing the spoiler height, h_{SWS}, decreases the amplitude of the cavity tones and the broadband noise. It can be seen from Figure 4.104 that increasing the spoiler height from h_{SWS}/δ = 0.25 to 1 for cavity A decreases the tonal amplitudes and broadband noise significantly. However, increasing the spoiler height from h_{SWS}/δ = 1 to h_{SWS}/δ = 2 does not have much effect. This shows that the reduction in cavity noise reaches a saturation level at a particular height of spoiler. This happens when all the cavity tones get reduced to a minimum broadband level achievable. The same behaviour can also be noticed for cavity C when h_{SWS}/δ is increased from 3 to 4. Cavity A at M = 0.85 also follows this trait which can be seen in Figure 4.107. Once the tones are attenuated to a broadband level by increasing the spoiler height, further increase in spoiler height has no effect on noise reduction. The value of spoiler height at which this saturation is attained will be called the critical spoiler height, h_{cr}. However the value of OASPL reached after attaining the h_{cr} is not the same for the different scales. This is because the OASPL obtained after attenuation of all tones is due to broadband noise. This broadband noise is created mainly due to turbulent fluctuations in the shear layer. With changes in scale or L/δ, the turbulent fluctuations could change as mentioned before. At larger scales, the broadband noise is higher due to the growth and convection of the turbulent fluctuations in the streamwise direction.

The values of OASPL obtained near the aft wall for different values of h_{SWS}/δ are shown in Figure 4.109. It can be seen that the OASPL curves are dependent on the L/δ value of the cavity. It was seen before that a spoiler with height equal to the boundary layer thickness was insufficient to attenuate the tones for cavity C. However when the spoiler height was raised to three times the height of the boundary layer thickness, the tones were completely attenuated to the broadband level (see Figure 4.106). This shows that the spoiler heights have to be adjusted with a change in L/δ. In the literature, the size required for a leading-edge control (h_{cr} here) has been known to depend only on factors like Mach number, L/D and L/W. But here, the results prove that the critical spoiler height, h_{cr}, required for a particular cavity is dependent on the factor L/δ. Hence for a given cavity, h_{cr} = f(M, L/D, L/δ). A comparison of curves for cavities A and B for M = 0.71 and M

= 0.85 plotted in Figure 4.109 show that it may be more sensitive to L/δ than M. The value of h_{cr} is defined in this work as the least value of h_{SWS} where all the tones are completely eliminated and the OASPL is a minimum or within ±0.25 dB of the minimum value. The value of h_{cr}/δ for cavities A, B and C obtained from the current experiments can be observed as 1, 2 and 3 respectively from Figure 4.109. This value remains the same for cavities A and B for M = 0.85 also, which shows that the ratio h_{cr}/δ might not be very sensitive to M. It can also be seen from Figure 4.109 that increasing the value of h_{SWS}/δ beyond h_{cr}/δ slightly increases the OASPL. This is because when the value of h_{SWS}/δ is increased beyond h_{cr}/δ, further increase stops being beneficial and increases the OASPL due to the increase in turbulent broadband noise generated by the spoiler. This can be clearly seen in the h_{SWS}/δ - OASPL curves in Figure 4.109 for cavity C at M = 0.71 and cavity A at M = 0.85.

The values of h_{cr}/δ obtained are plotted against the corresponding values of L/δ including the point (0,0) in Figure 4.110. Uncertainty bars (based on 50% of Δh_{SWS}) are given for the different values of h_{cr}/δ since all the values of h_{SWS}/δ have not been tested. Since h_{cr}/δ is chosen as the least value of h_{SWS}/δ when all tones are eliminated, only a lower limit is taken. Figure 4.110 shows the data points obtained with their uncertainties. Using the points available, a linear approximation has been made. A linear regression curve, weighted according to the error at each point is constructed. Due to the uncertainties, a confidence band (at 95% confidence level) is also shown. It can be seen from Figure 4.110 that the confidence band is bound within the regression lines y = 0.082x and y = 0.065x. From this linear approximation, it is clear that the value of h_{cr} is dependant only on the cavity length L such that

$$h_{cr} = SL \tag{4.6}$$

where S is defined as the spoiler scaling factor. This implies that oscillations in a cavity can be suppressed as long as the ratio $h_{SWS}/L \geq h_{cr}/L$, called the critical ratio. It must be noted that although the critical ratio, h_{cr}/L, is independent of the boundary layer thickness, suppression is not achieved for a cavity until this ratio is achieved. Up to the critical ratio, cavity oscillations are vulnerable to the changes in the ratio L/δ. Once h_{SWS}/L equals the critical ratio, oscillations are

suppressed and the ratio L/δ no longer plays a role in cavity unsteadiness as can be seen in Figure 4.111. It was mentioned in Section 2.7.1 that Shaw et al. (1988), Geraldes (2005) and Lawson & Barakos (2009) were some of the researchers who have tested sawtooth spoilers similar to the one used in this work. However, it must be noted that although they observed cavity tone attenuations, Shaw et al and Lawson & Barakos were unable to suppress successfully all the tones to broadband level as can be seen in Figures 4.112 and 4.113. The value of h_{SWS}/δ used in their work is also shown in Figure 4.110. It can be clearly seen that the values used by them fall well under the value of h_{cr}/δ recommended by the linear model. However the value of h_{SWS}/δ used by Geraldes (2005) is close to the linear approximation. Geraldes (2005)) was able to achieve a good level of suppression in his studies with cavity L/D = 4 and M = 0.85 (see Figure 4.114). Shaw conducted the test with spoilers at M = 0.9 with a cavity of L/D ratio 6.7. Lawson & Barakos reported tests on a cavity with L/D = 5 at M = 0.85. This data again confirms that h_{cr} is less sensitive to M but could be more sensitive to L/D. According to the linear approximation model explained here, a cavity with L/D = 5 achieves suppression when the height of the sawtooth spoiler used is 6.5% - 8.2% of the cavity length. This is irrespective of the L/δ value faced by the cavity. This shows that sawtooth spoilers with critical height have to be scaled according to the cavity dimensions and not according to the incoming boundary layer thickness as previously thought. Once the critical spoiler height, h_{cr}, of a particular cavity is determined, then the spoiler can be scaled according to the cavity dimensions. It is presumed that the critical spoiler height is mainly dependent on factors like spoiler profile and L/D ratio of the cavity. For the current case, a spoiler with height equalling 6.5% - 8.2% of the cavity length achieves critical height. A more accurate estimate of h_{cr}/L can be estimated by testing a large number of the intermediate values in the h_{SWS}/δ - OASPL curves. Shaw et al. and Lawson & Barakos quote spoiler heights equalling 4.7% and 3.76% of the respective cavity length which is short of the critical spoiler height required.

4.3.1 Summary and remarks

The mechanism and effect of scaling on the effectiveness of a passive control method was studied. The mechanism of oscillation control by spoilers was found to be both from lifting the shear layer and by reducing the spatial coherence of

the shear layer. By using spoilers of the same h_{SWS}/δ ratio on cavities of different scales, it was found that there was significant variation in the control effectiveness. Spoilers with $h_{SWS}/\delta = 1$ were able to suppress the cavity tones effectively at smaller scales while they failed at larger scales. These results show that scaling the spoiler with respect to the boundary layer thickness is not the correct method. It also shows that the factor L/δ has significant impact on the effectiveness of the passive control.

Different spoiler heights were tested for a given cavity or L/δ and it was found that spoilers were completely effective in eliminating the cavity tones when the ratio h_{SWS}/δ reached a particular value. After this value, any further increase in spoiler height was found to have insignificant effect. The spoiler height at which this phenomenon was achieved was termed the critical spoiler height, h_{cr}. By correlating the ratios, h_{cr}/δ and the factor L/δ it was found that they are approximately linearly related to each other. The linear model implied that the ratio h_{cr}/L is constant for a cavity of given L/D and is immune to the effects of L/δ. This means that as long as the critical ratio of a spoiler is maintained the cavity is expected to have no tones and exhibits the least OASPL possible for that particular L/δ. Thus h_{cr} can be scaled with respect to the cavity dimensions. Once h_{cr}/L for a particular cavity specification (L/D, L/W, M and spoiler profile) is known, then the passive control method can be scaled according to the cavity dimensions. If the spoiler height is under the value of h_{cr}/L, then the cavity is not immune to the changes in L/δ. Also, the critical ratio is a more suitable criterion for scaling a passive control because it depends only on the magnitude of known variables and not the flow conditions.

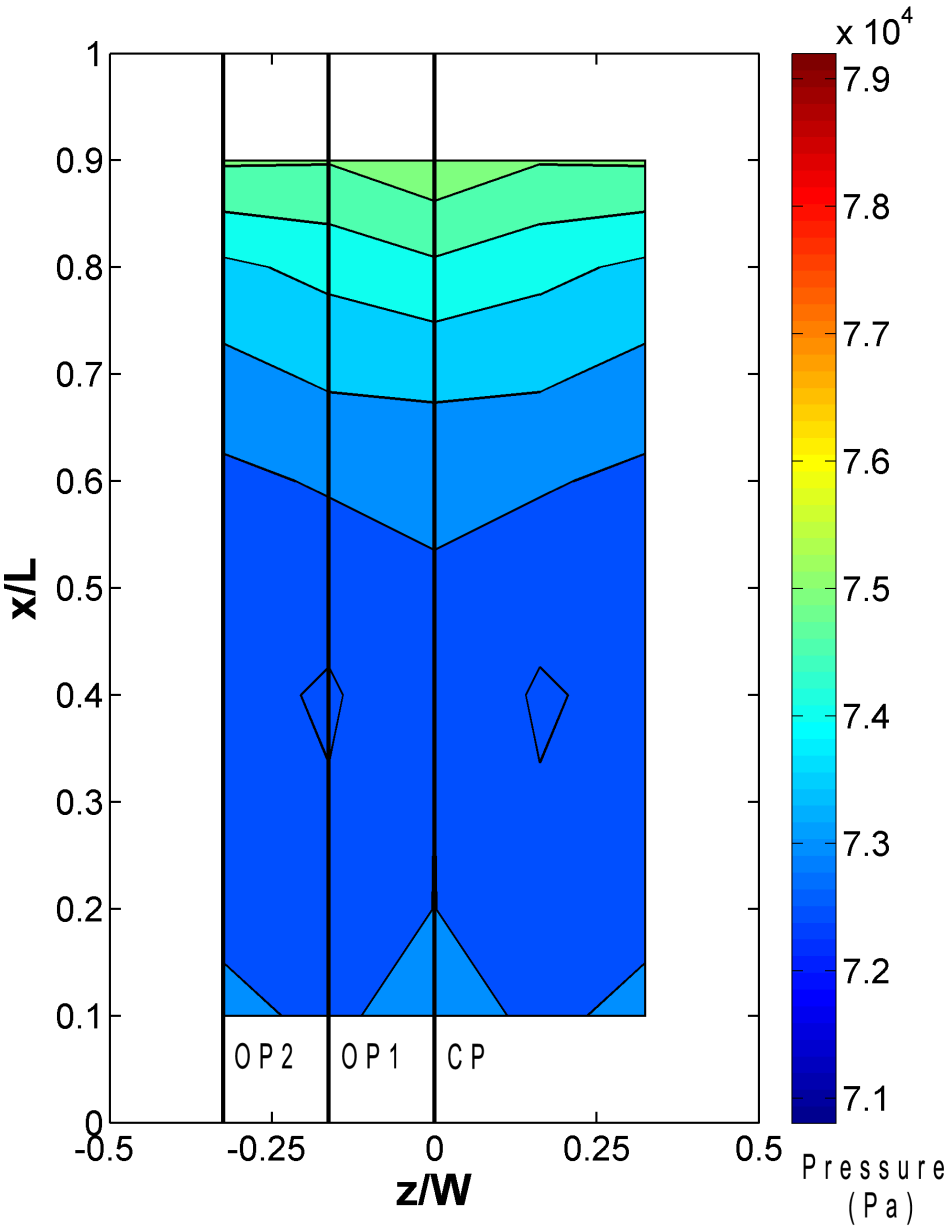

Figure 4.1: Pressure contour on floor of cavity A (M = 0.71)

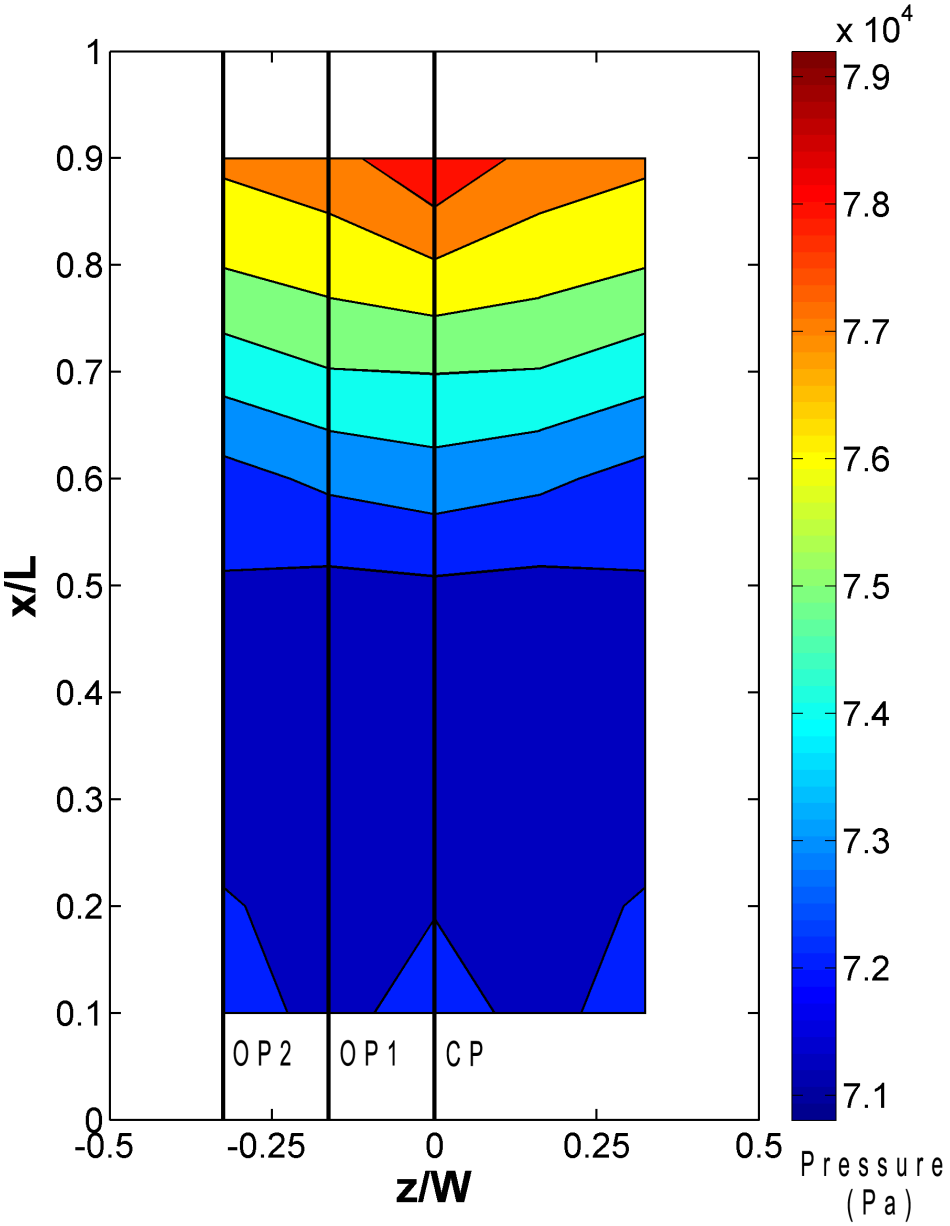

Figure 4.2: Pressure contour on floor of cavity B (M = 0.71)

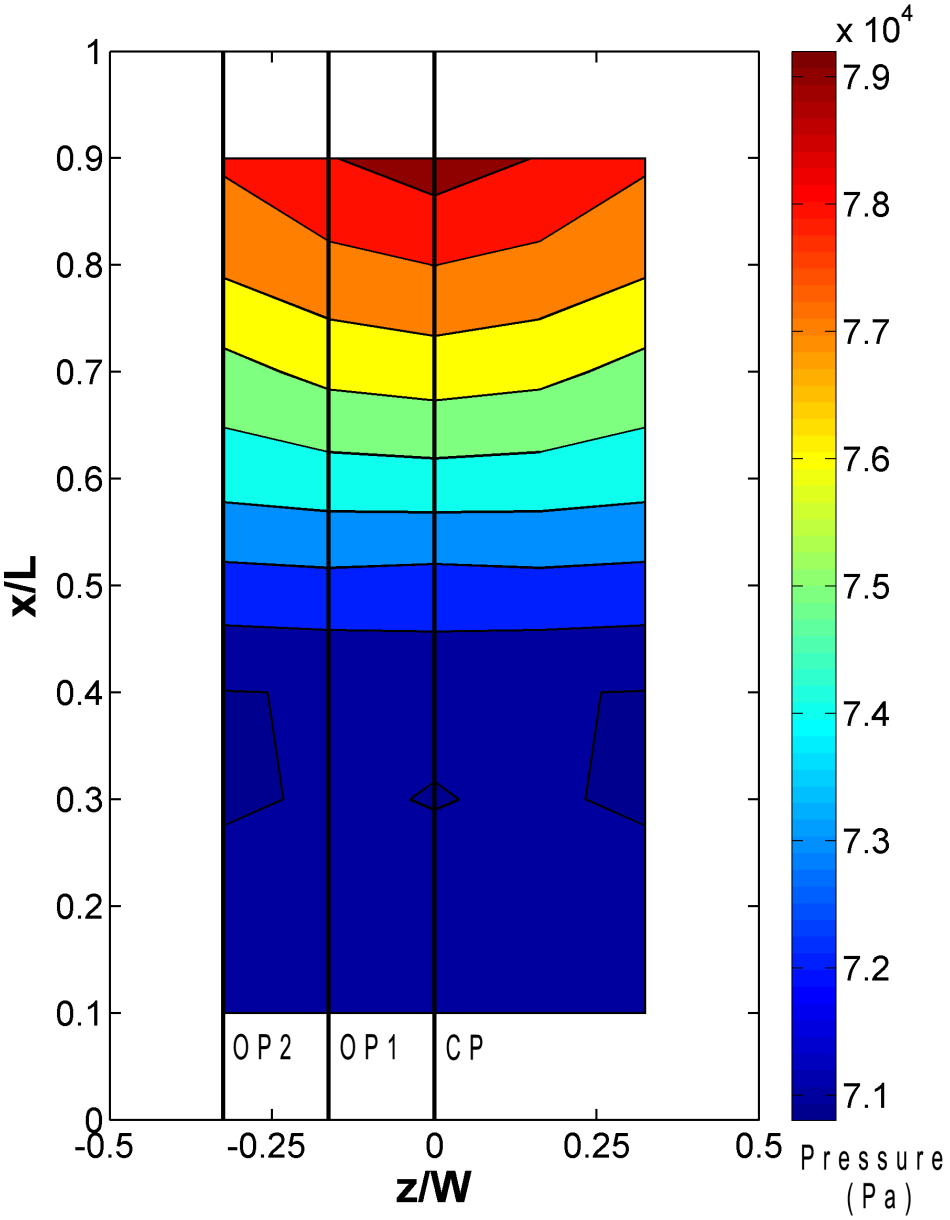

Figure 4.3: Pressure contour on floor of cavity C (M = 0.71)

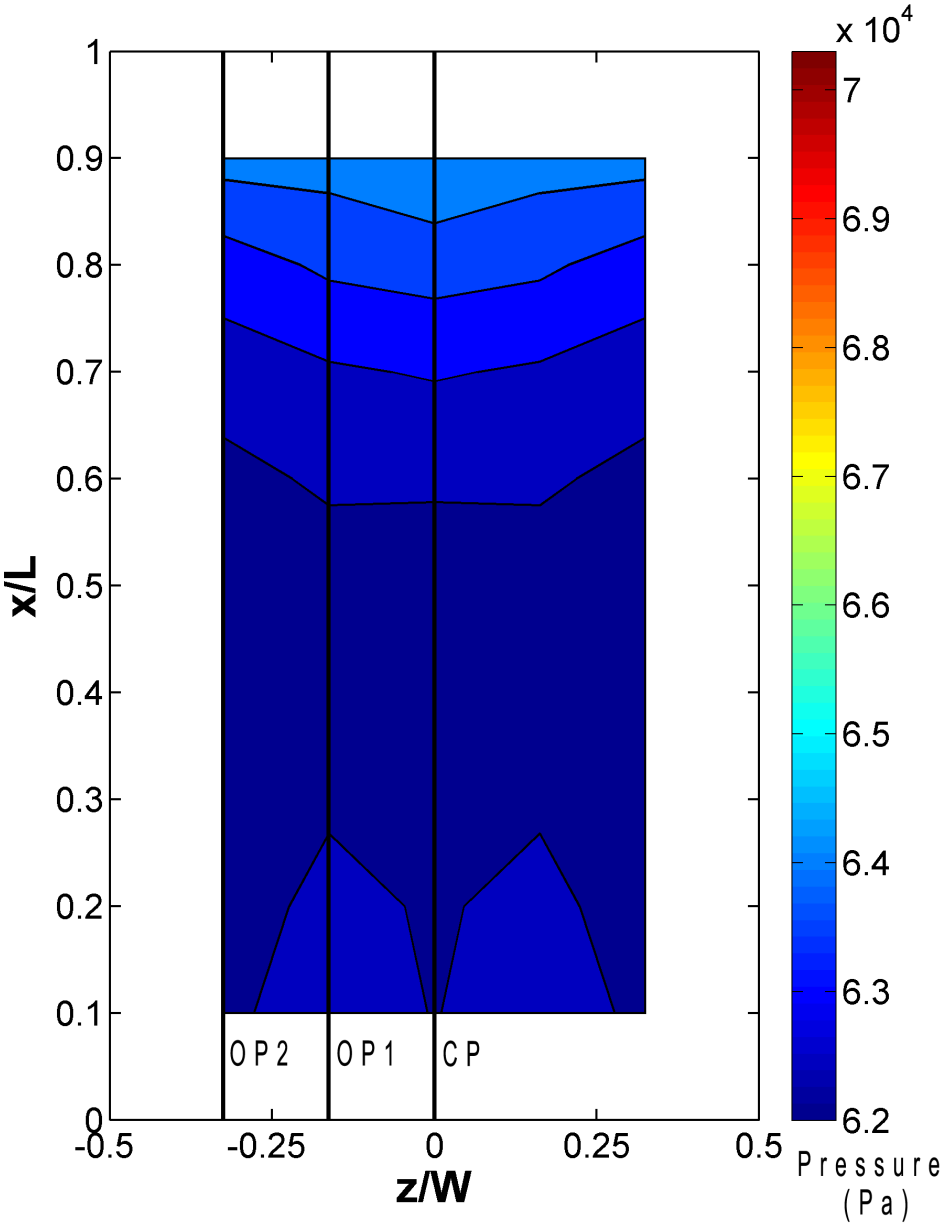

Figure 4.4: Pressure contour on floor of cavity A (M = 0.85)

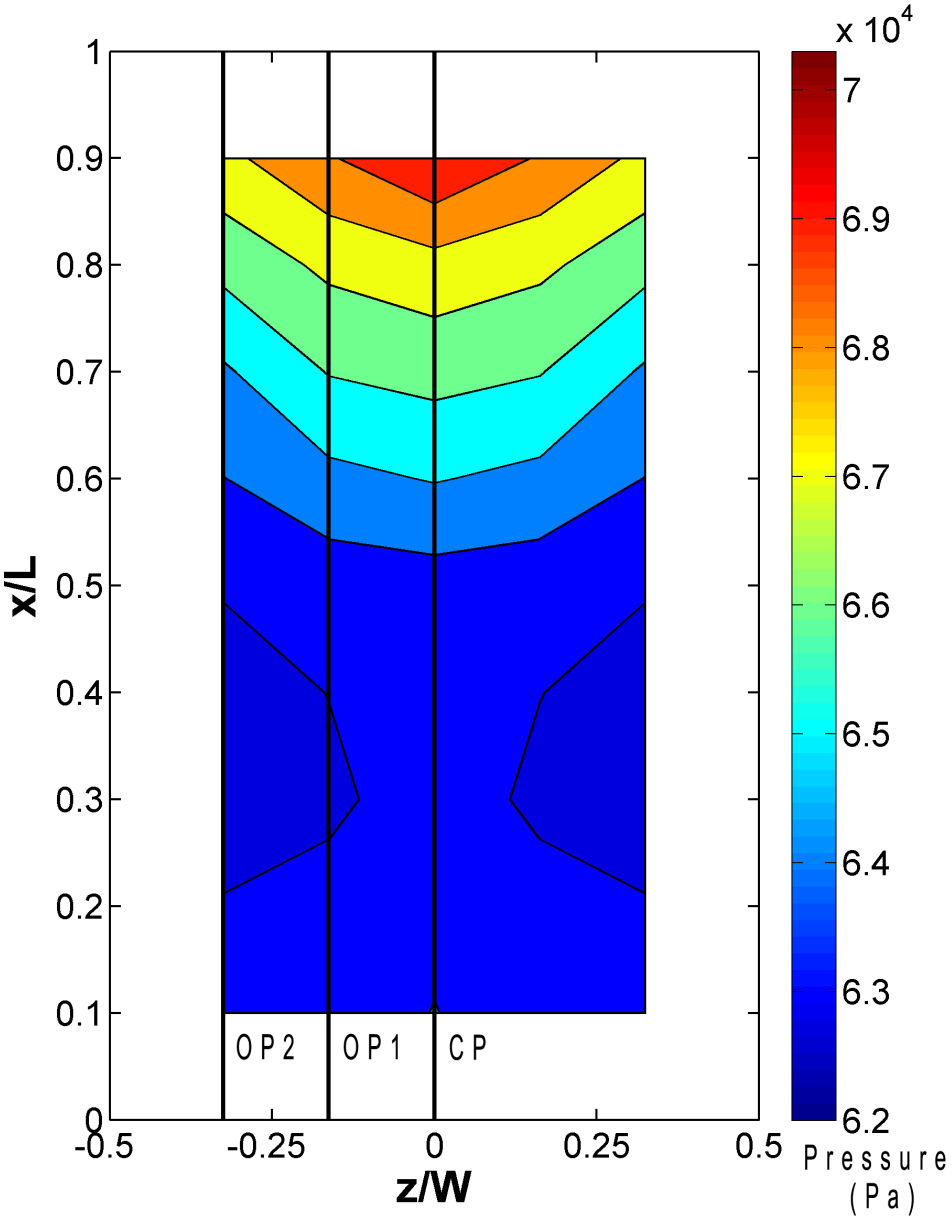

Figure 4.5: Pressure contour on floor of cavity B (M = 0.85)

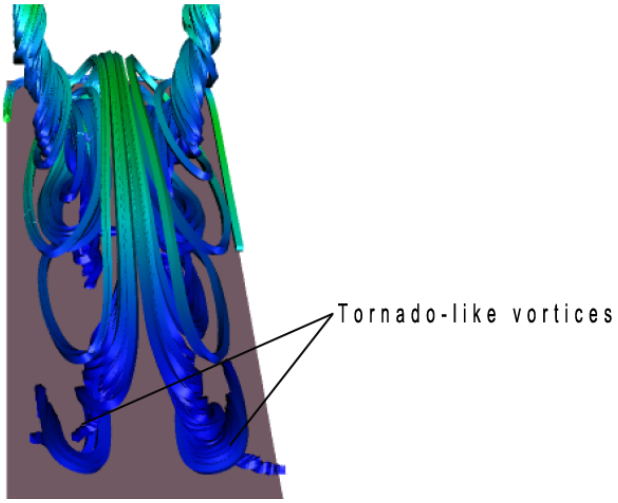

Figure 4.6: Tornado vortices in cavity with L/D = 5 obtained using CFD by Khanal (2010)

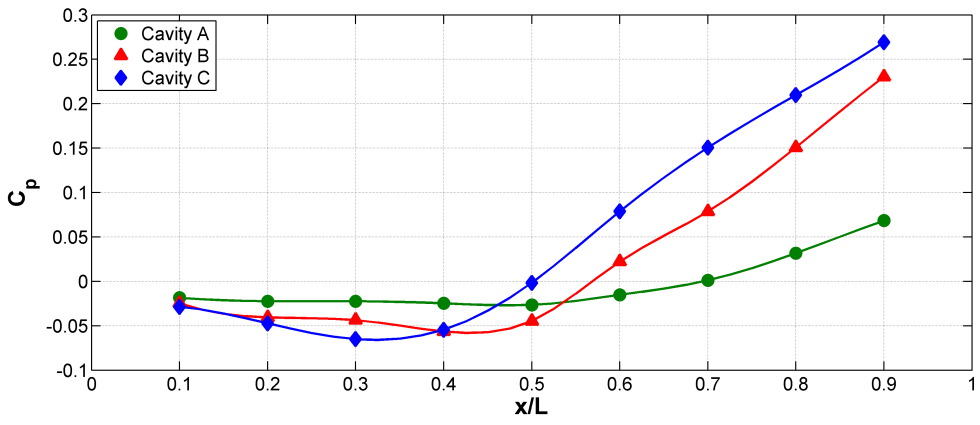

Figure 4.7: C_p distribution on cavity floor along plane CP (M = 0.71)

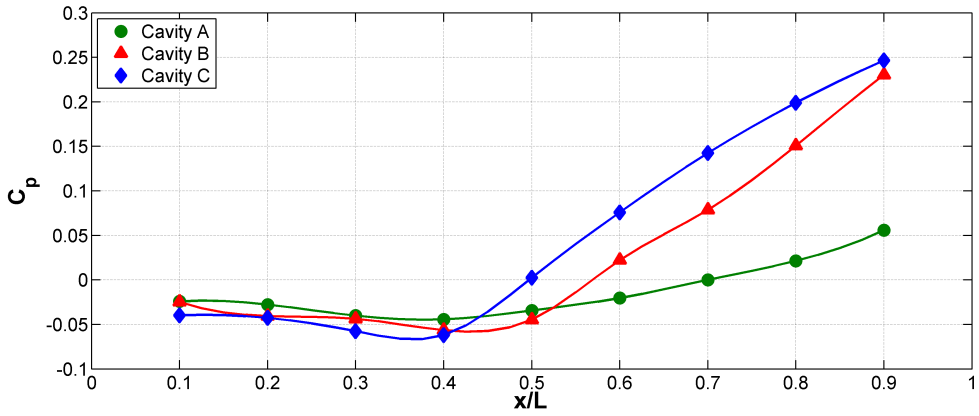

Figure 4.8: C_p distribution on cavity floor along plane OP1 (M = 0.71)

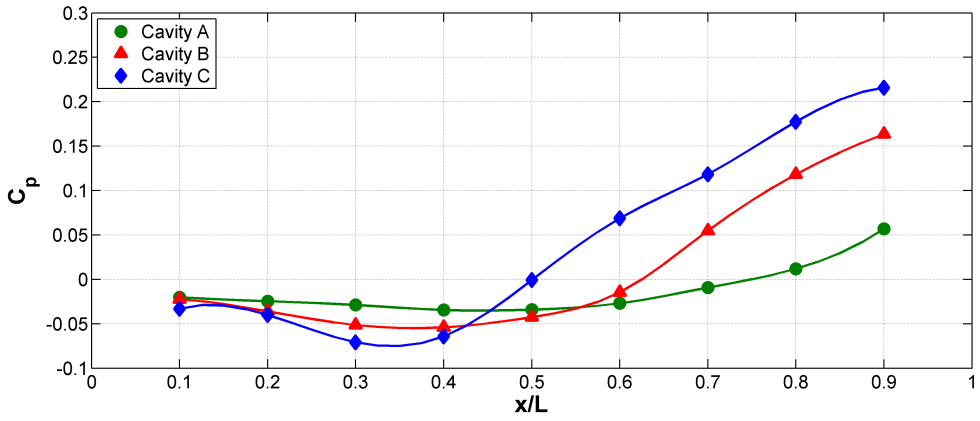

Figure 4.9: C_p distribution on cavity floor along plane OP2 (M = 0.71)

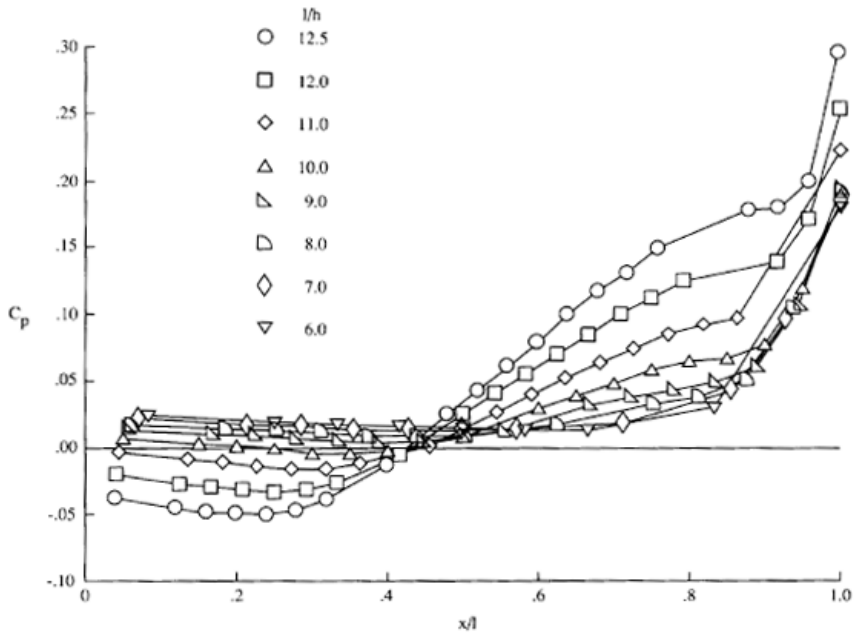

Figure 4.10: Change in C_p curve from open to transitional regimes obtained by Stallings & Wilcox (1987)

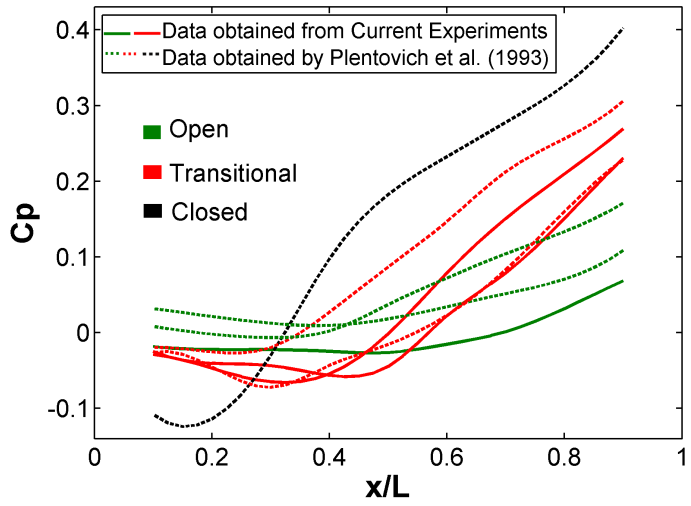

Figure 4.11: Comparison of current data (M = 0.71) with data obtained by Plentovich et al (1993) for transonic flow (M = 0.80)

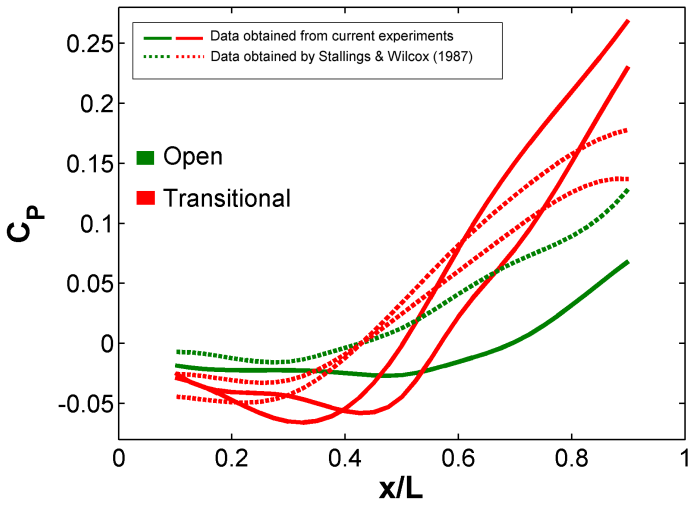

Figure 4.12: Comparison of current data with data (M = 0.71) obtained by Stallings & Wilcox (1987) for supersonic flow (M = 1.5)

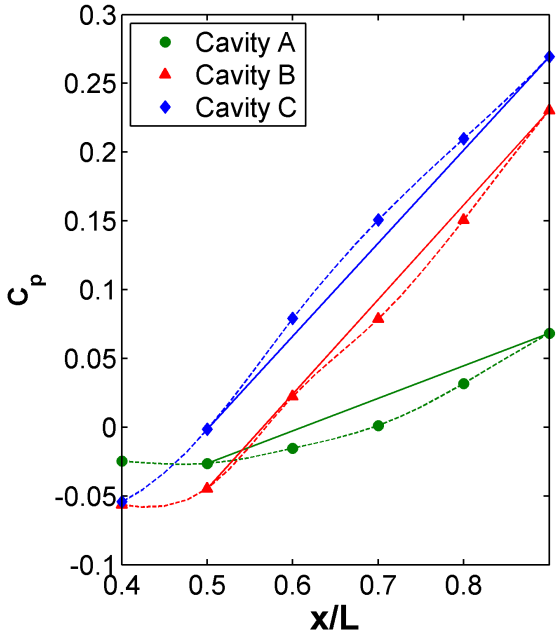

Figure 4.13: Shapes of C_p curves for different cavities (M = 0.71)

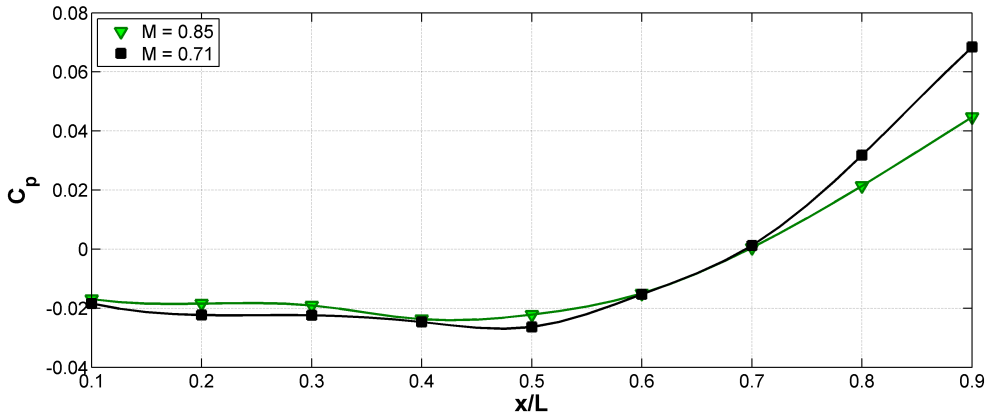

Figure 4.14: Variation of C_p curve with Mach number for cavity A

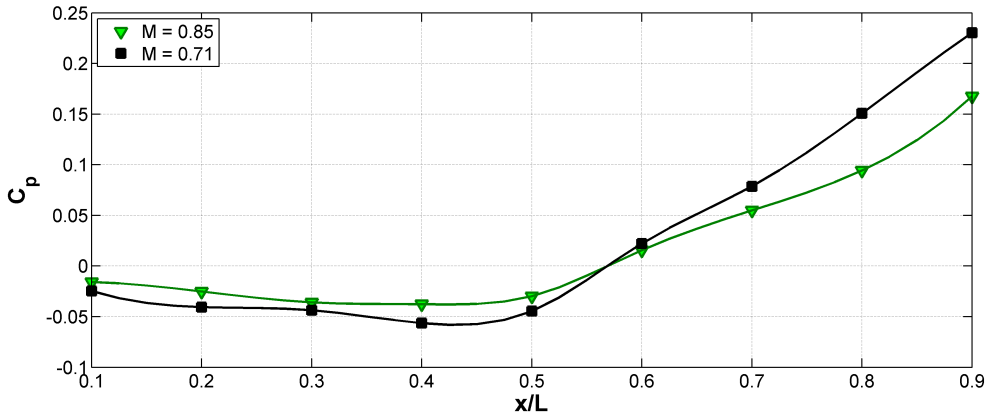

Figure 4.15: Variation of C_p curve with Mach number for cavity B

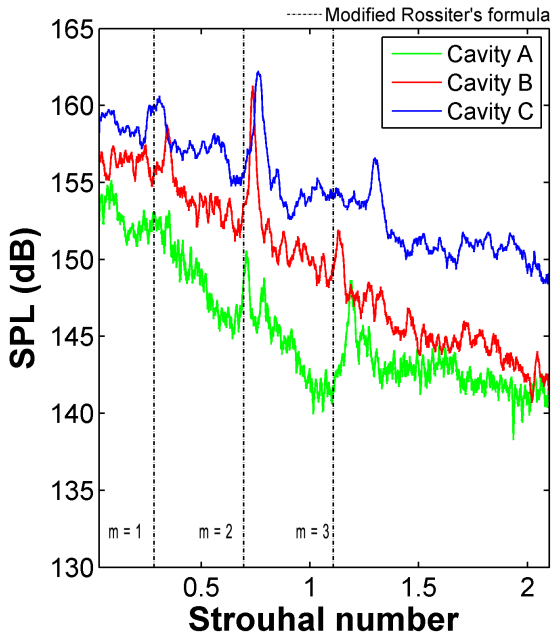

Figure 4.16: Power spectra at x/L = 0.9 for M = 0.71

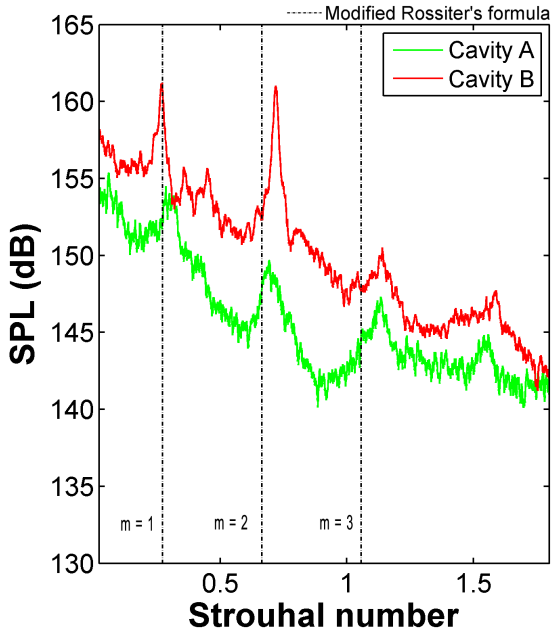

Figure 4.17: Power spectra at x/L = 0.9 for M = 0.85

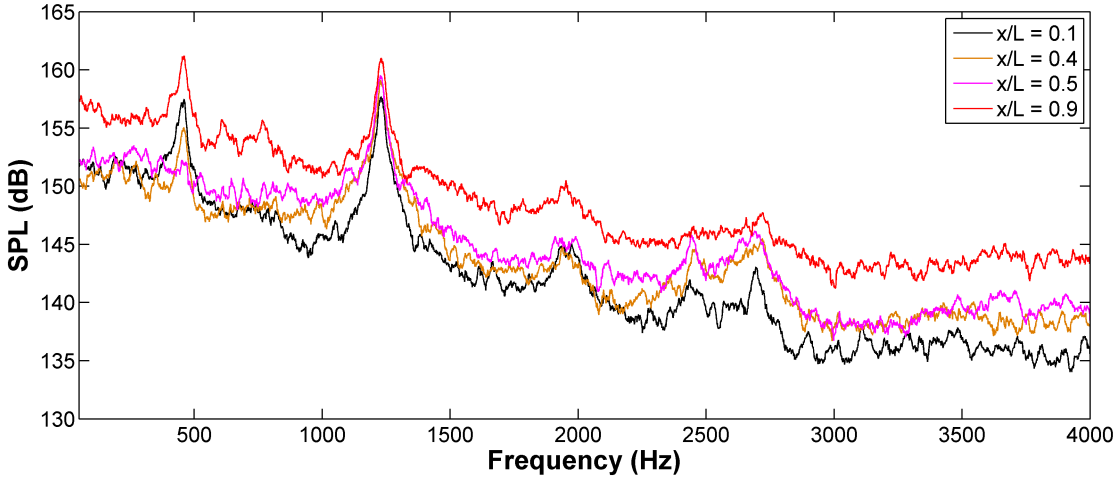

Figure 4.18: Power spectra for cavity B at various locations (M = 0.85)

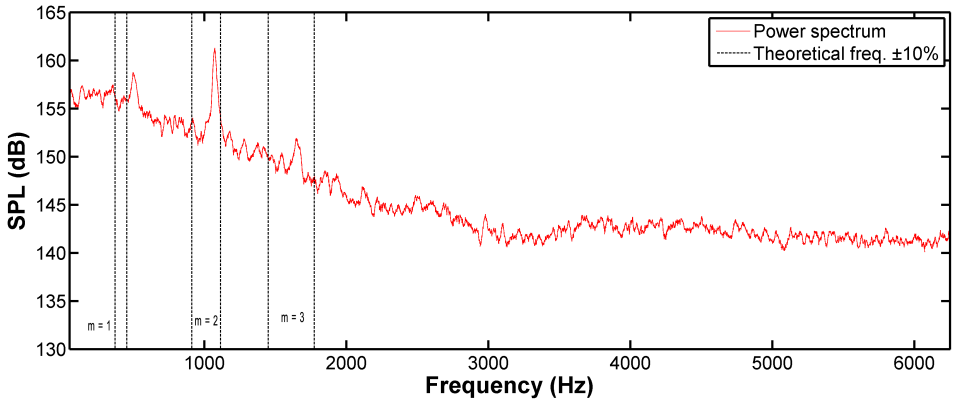

Figure 4.19: Power spectra for cavity B at x/L = 0.9 (M = 0.71)

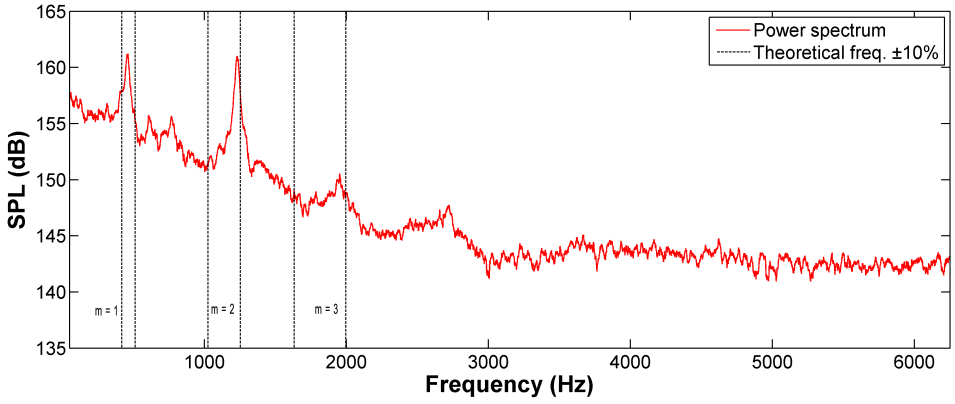

Figure 4.20: Power spectra for cavity B at x/L = 0.9 (M = 0.85)

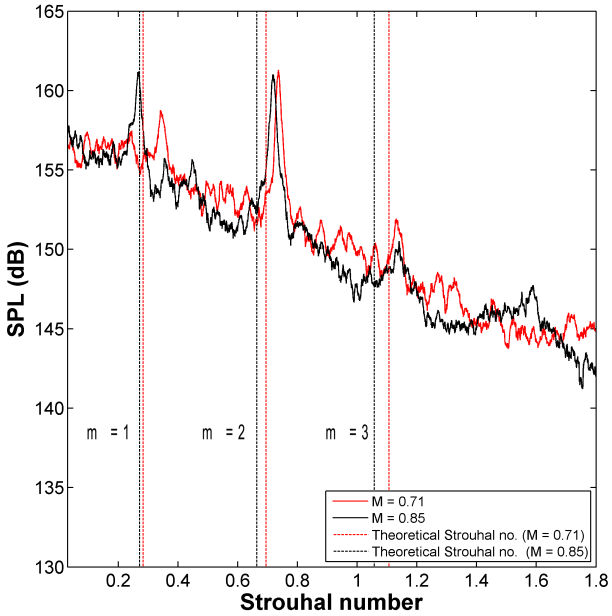

Figure 4.21: Power spectra of cavity B at x/L = 0.9 for M = 0.71 and M = 0.85

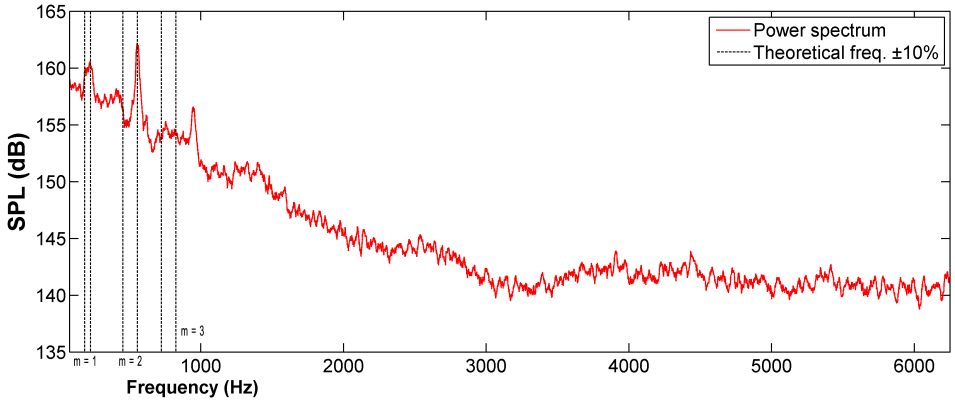

Figure 4.22: Power spectra for cavity C at x/L = 0.9 (M = 0.71)

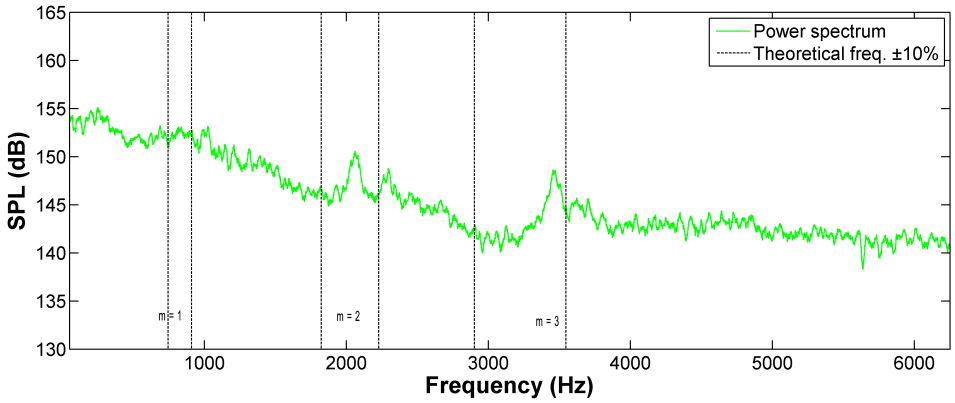

Figure 4.23: Power spectra for cavity A at x/L = 0.9 (M = 0.71)

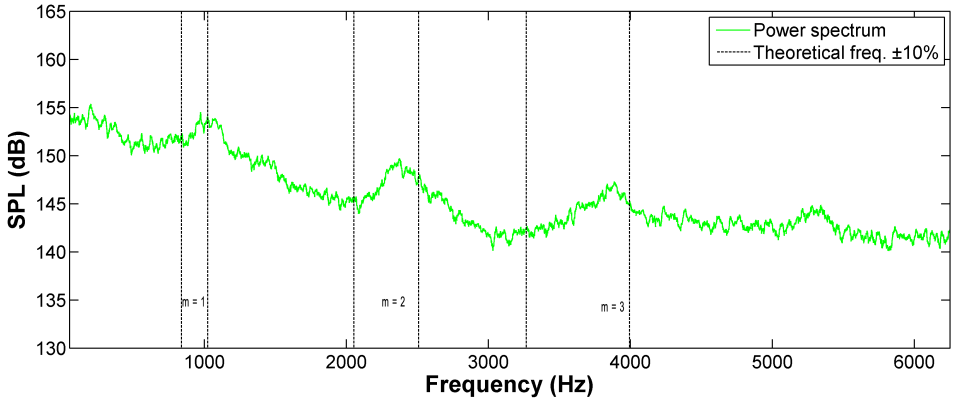

Figure 4.24: Power spectra for cavity A at x/L = 0.9 (M = 0.85)

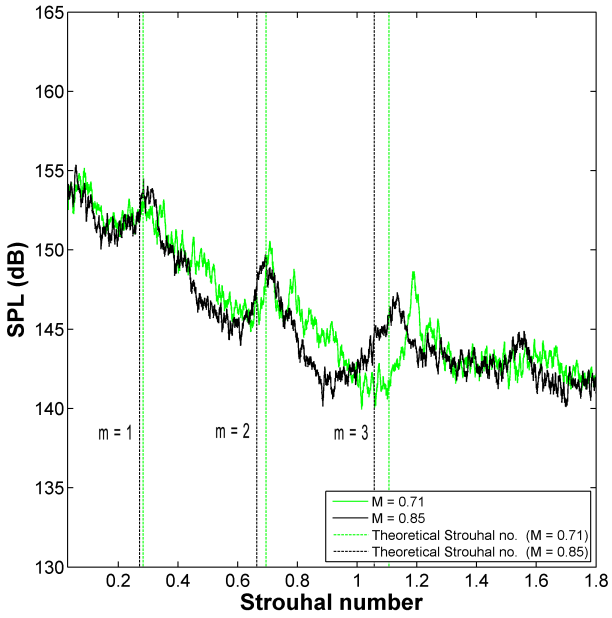

Figure 4.25: Power spectra of cavity A at x/L = 0.9 for M = 0.71 and M = 0.85

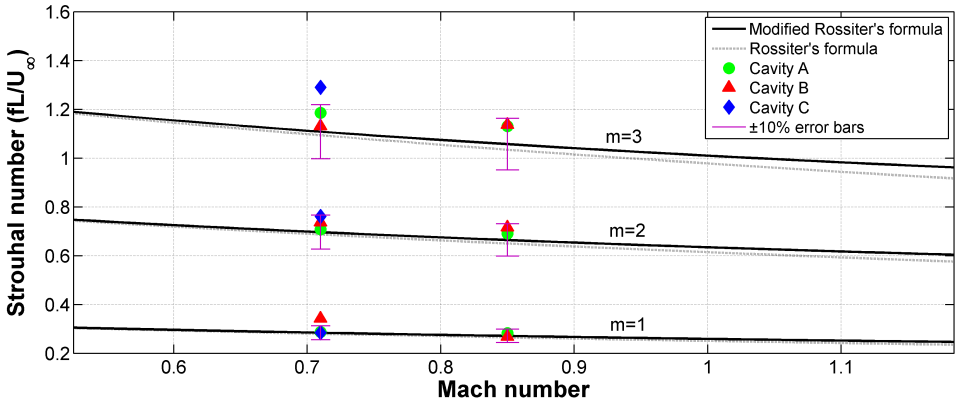

Figure 4.26: Strouhal numbers obtained for clean cavities

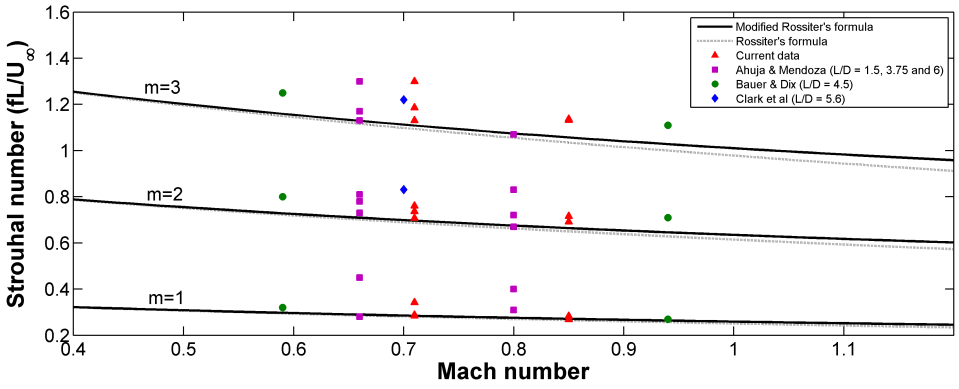

Figure 4.27: Strouhal numbers obtained by various researchers

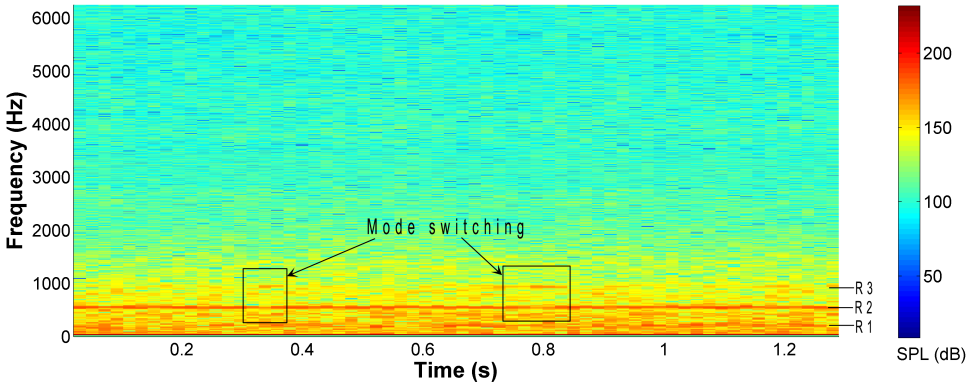

Figure 4.28: Spectrogram of cavity C at x/L = 0.9 (M = 0.71)

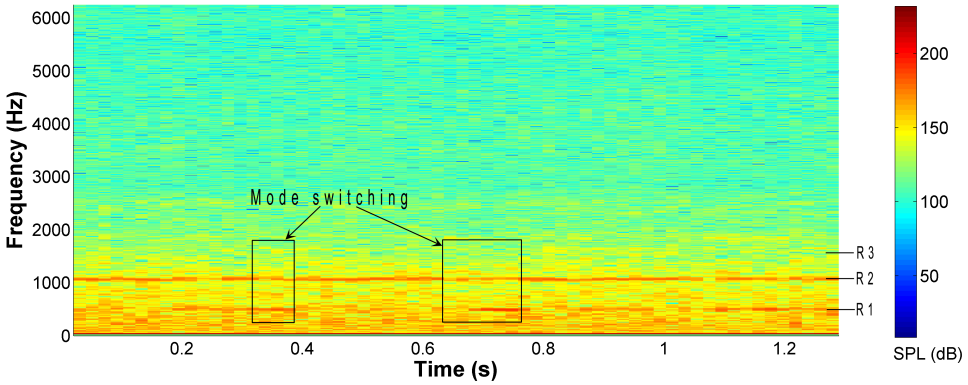

Figure 4.29: Spectrogram of cavity B at x/L = 0.9 (M = 0.71)

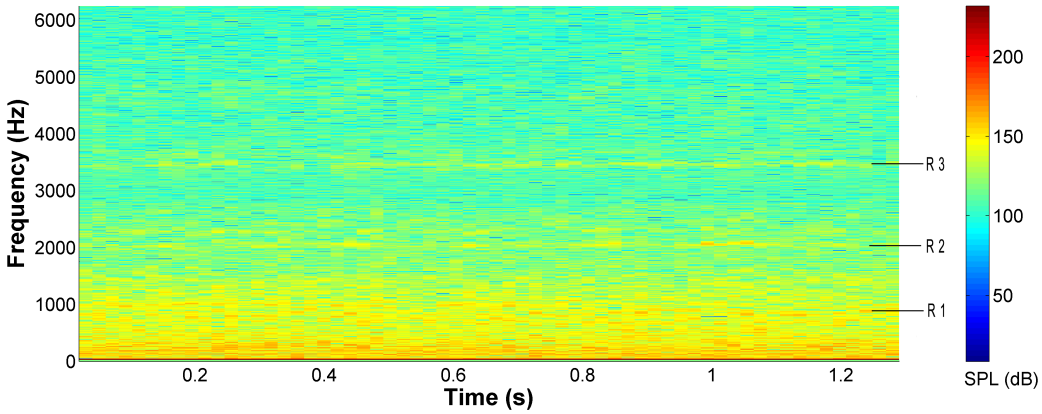

Figure 4.30: Spectrogram of cavity A at x/L = 0.9 (M = 0.71)

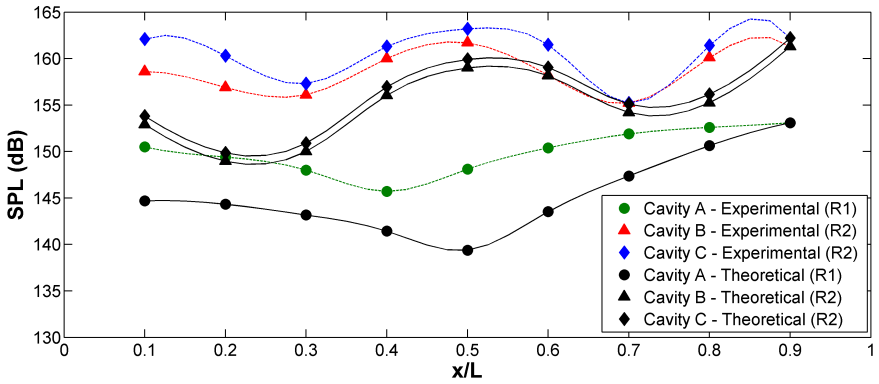

Figure 4.31: Mode shapes of dominant modes at M = 0.71

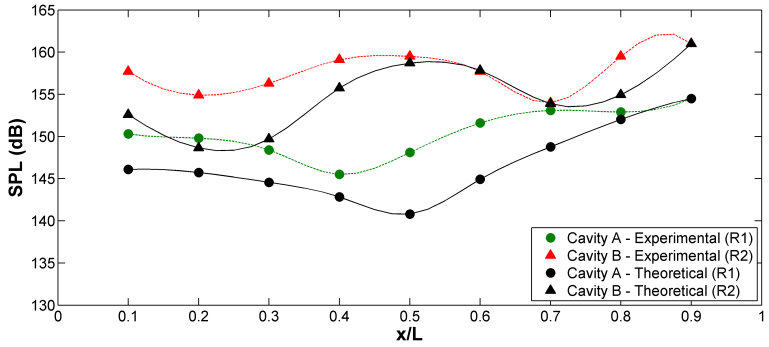

Figure 4.32: Mode shapes of dominant modes at M = 0.85

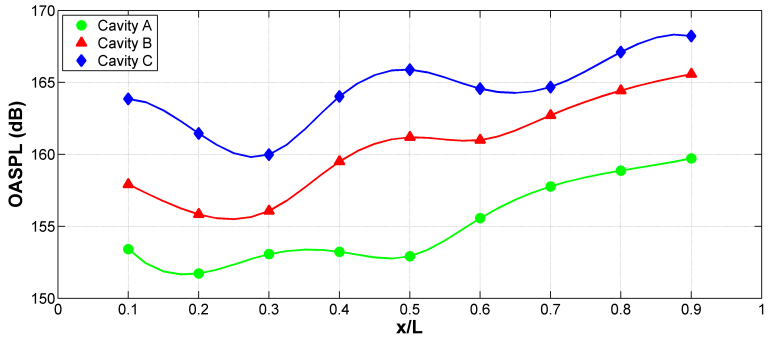

Figure 4.33: OASPL distribution across cavity length M = 0.71

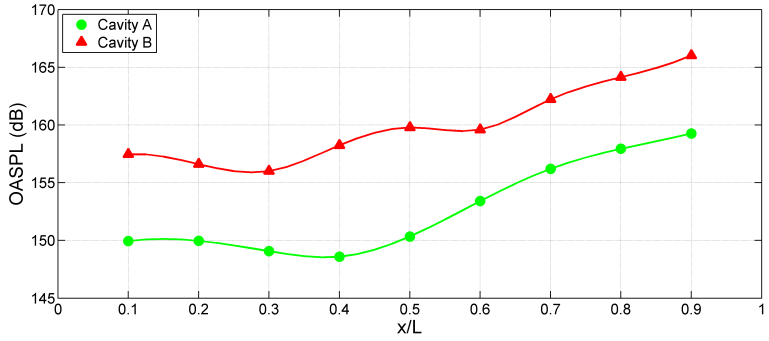

Figure 4.34: OASPL distribution across cavity length at M = 0.85

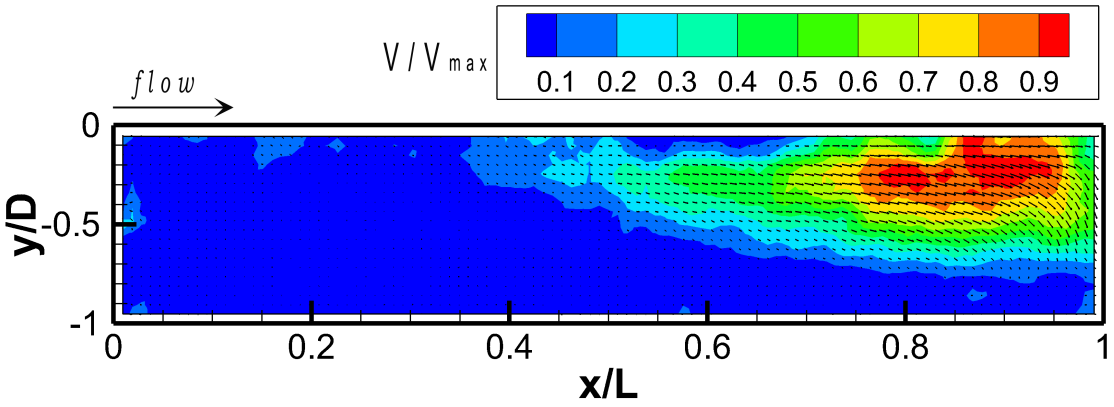

Figure 4.35: Centreplane velocity field of cavity A at M = 0.71 (V_{max} = 43.3 m/s)

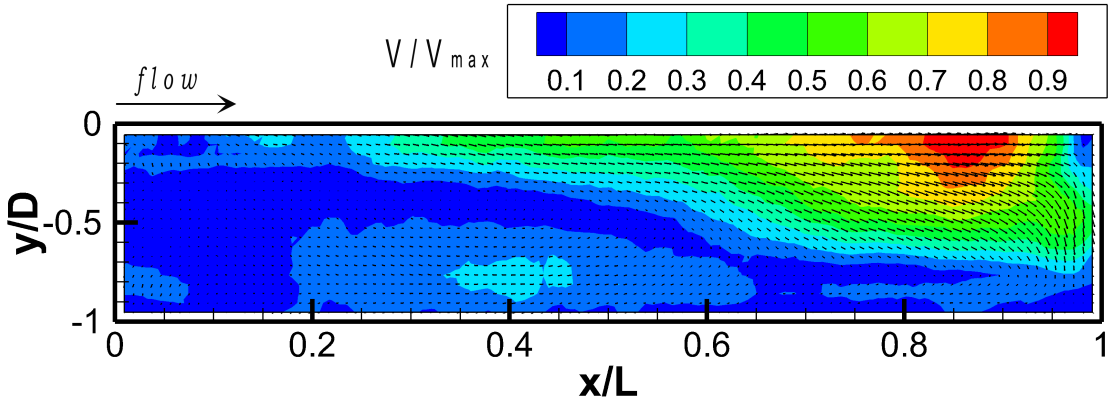

Figure 4.36: Centreplane velocity field of cavity B at M = 0.71 (V_{max} = 84.4 m/s)

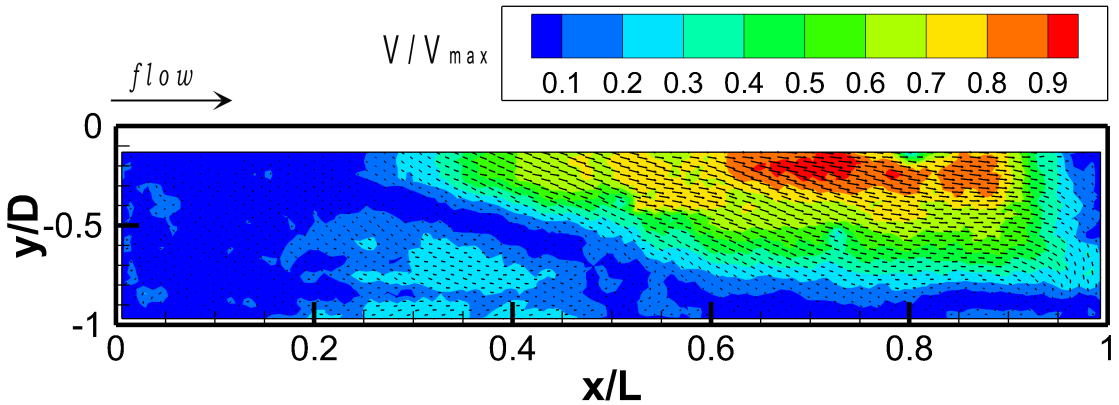

Figure 4.37: Centreplane velocity field of cavity C at M = 0.71 (V_{max} = 95.8 m/s)

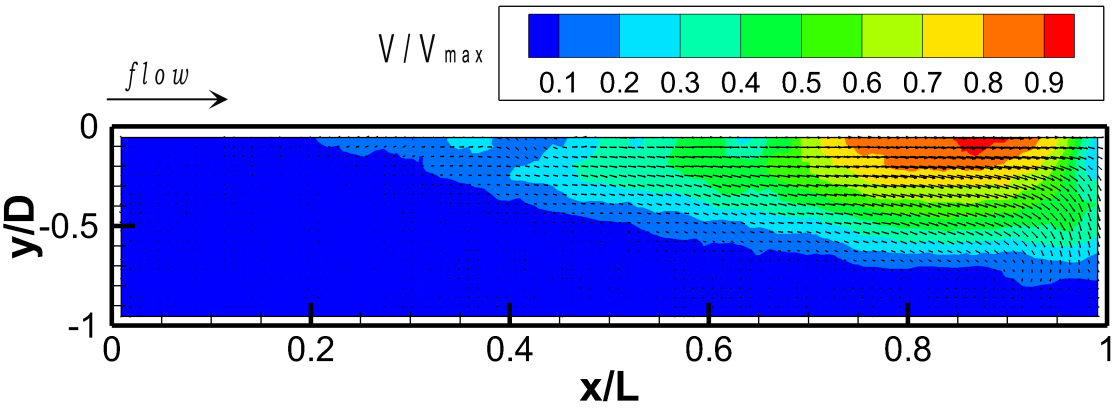

Figure 4.38: Centreplane velocity field of cavity A at M = 0.85 (V_{max} = 78.2 m/s)

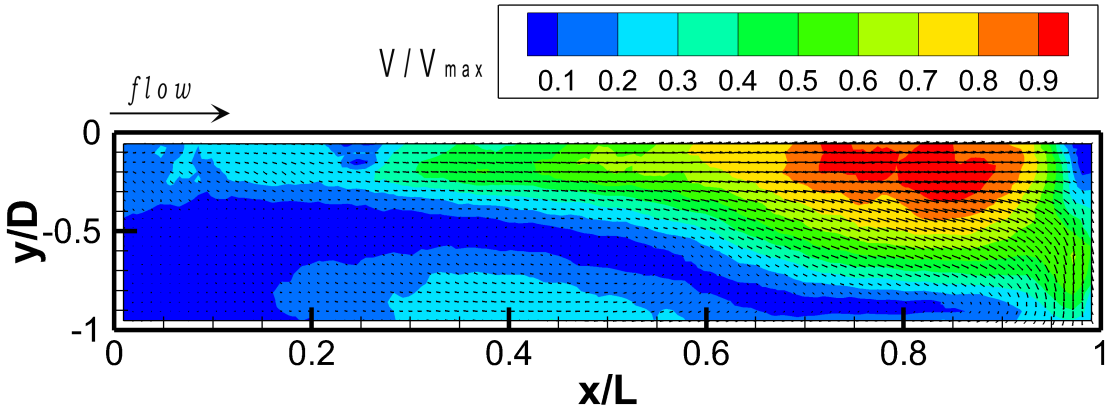

Figure 4.39: Centreplane velocity field of cavity B at M = 0.85 (V_{max} = 108.1 m/s)

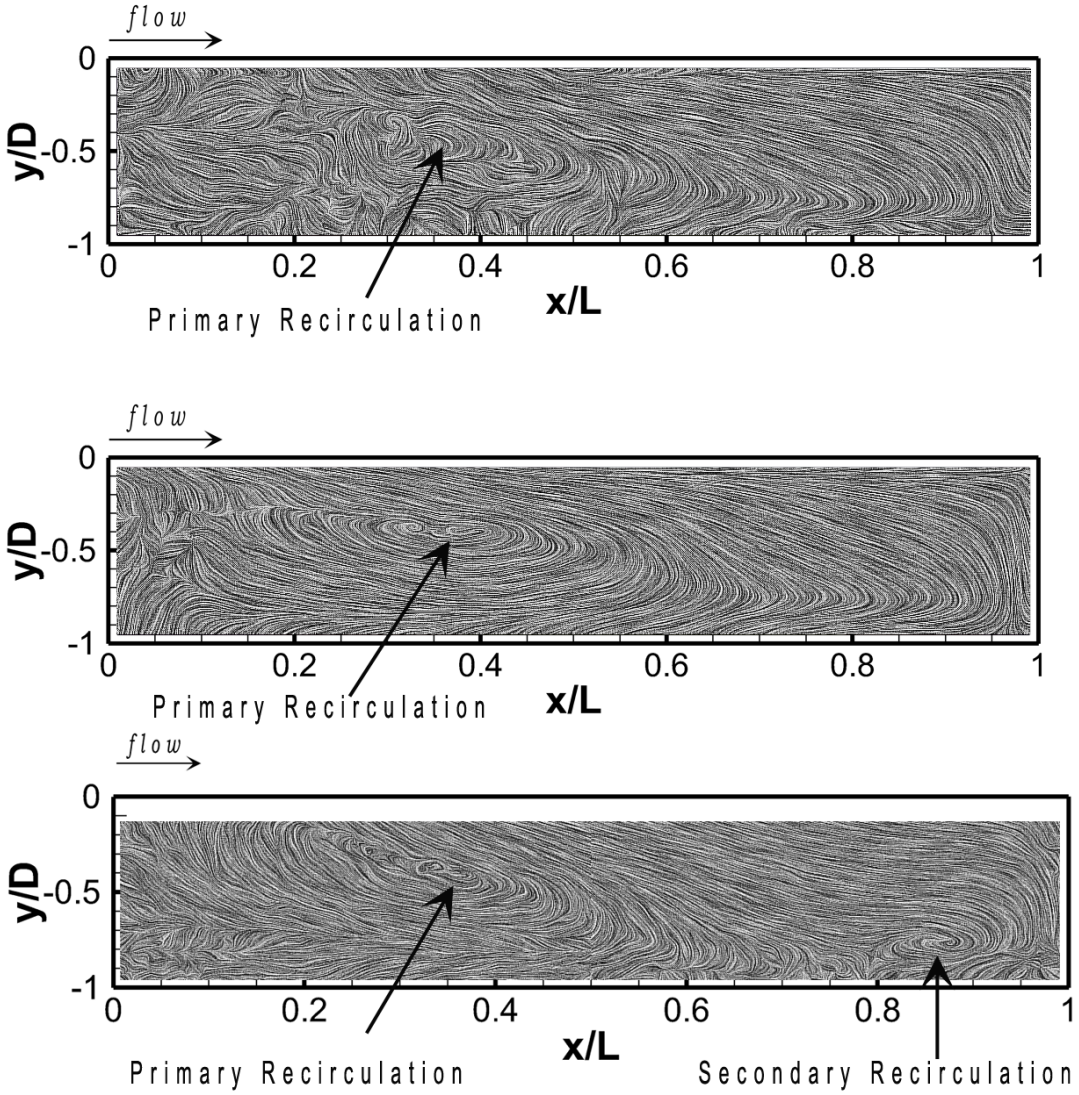

Figure 4.40: Centreplane LIC images of cavities A, B and C (order from top to bottom) at M = 0.71

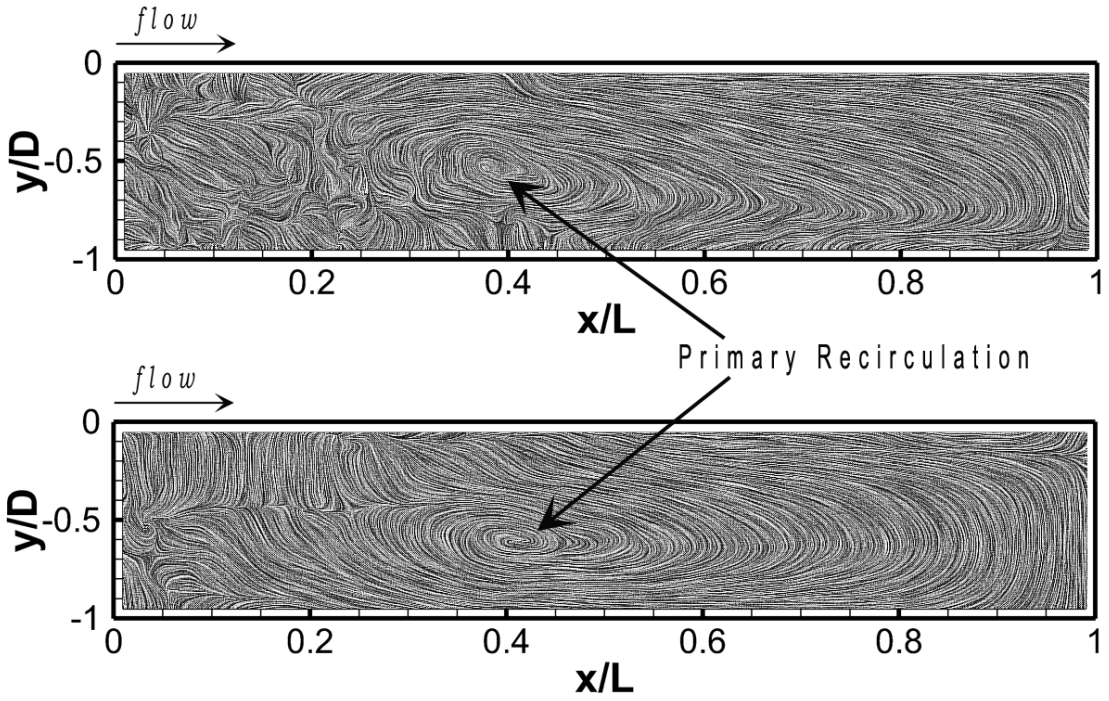

Figure 4.41: Centreplane LIC images of cavities A and B (order from top to bottom) at M = 0.85

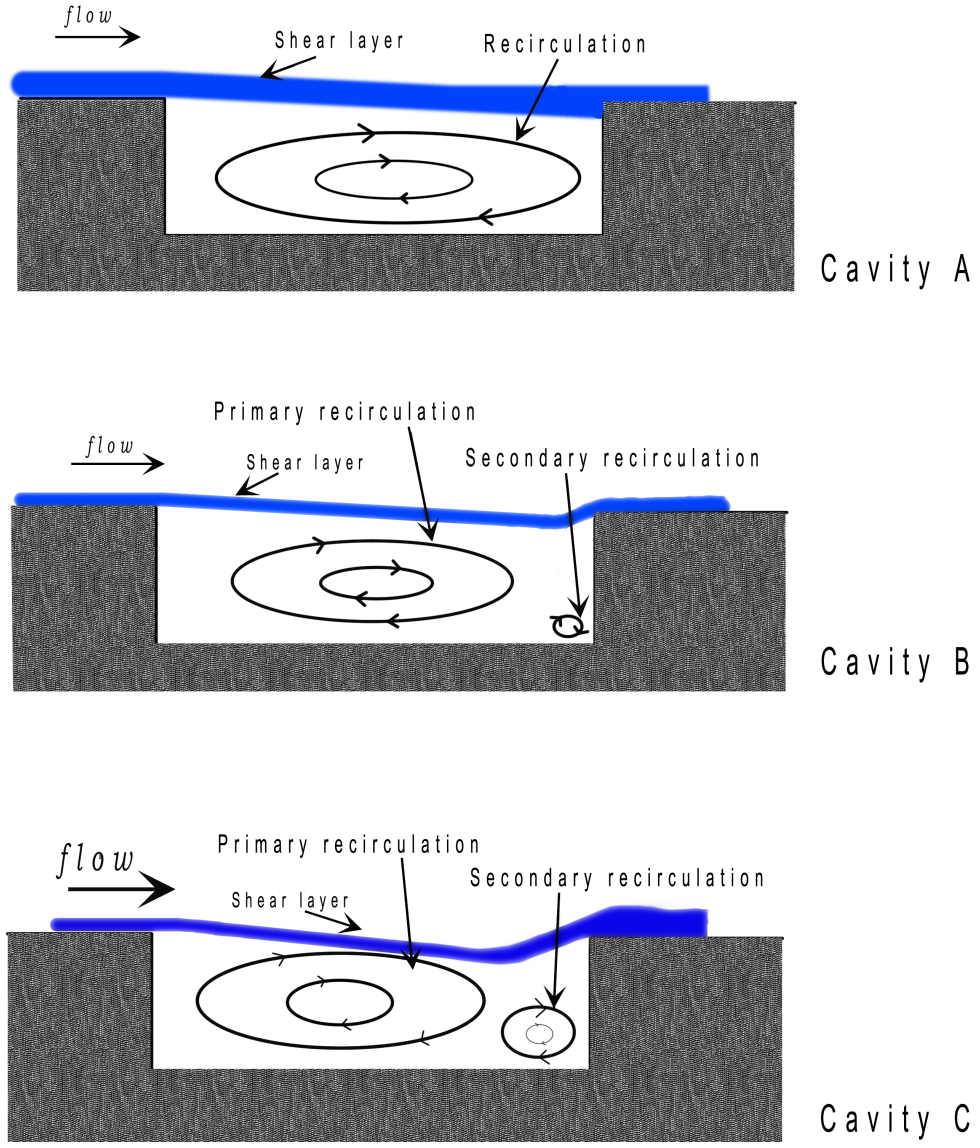

Figure 4.42: Illustration of flow field inside different cavities

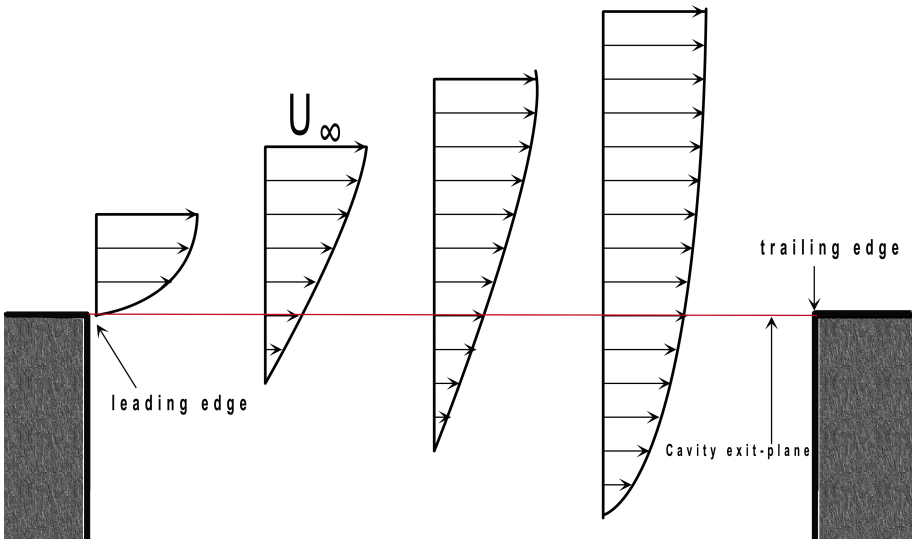

Figure 4.43: Illustration of shear layer development across the cavity length

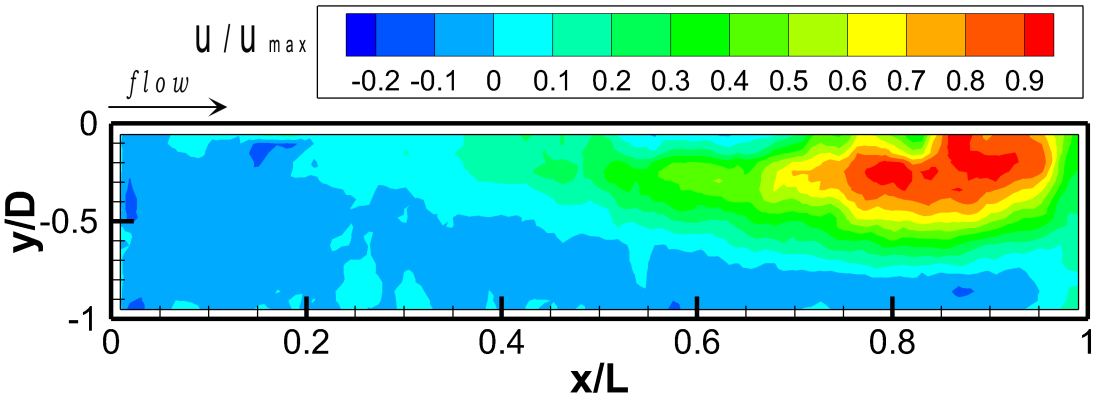

Figure 4.44: Centreplane u-velocity contour of cavity A at M = 0.71 (u_{max} = 42.3 m/s)

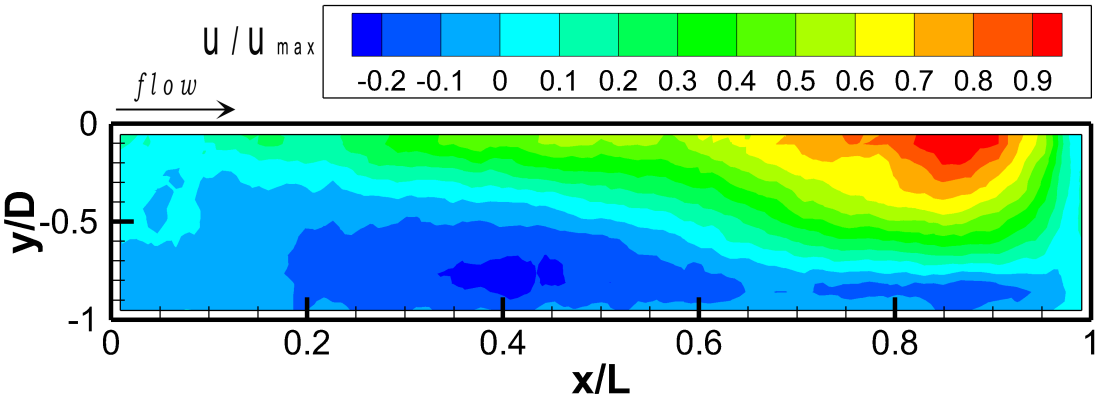

Figure 4.45: Centreplane u-velocity contour of cavity B at M = 0.71 (u_{max} = 84.3 m/s)

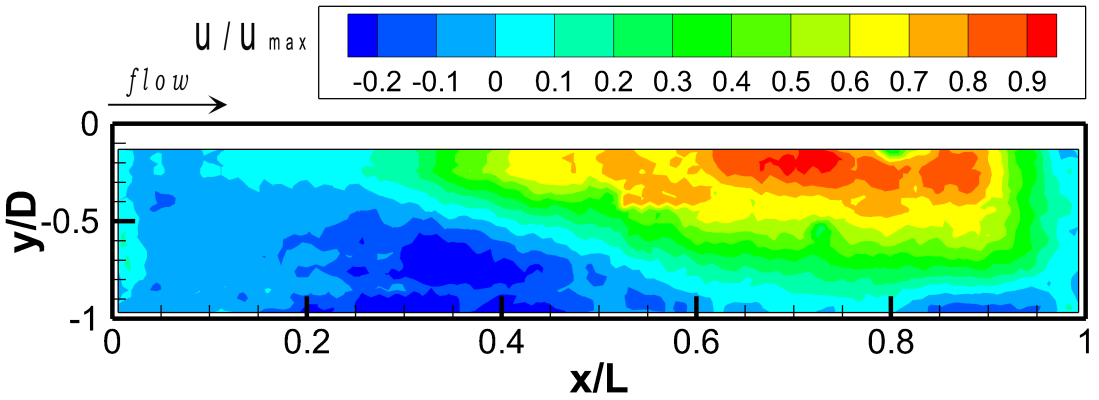

Figure 4.46: Centreplane u-velocity contour of cavity C at M = 0.71 (u_{max} = 95.4 m/s)

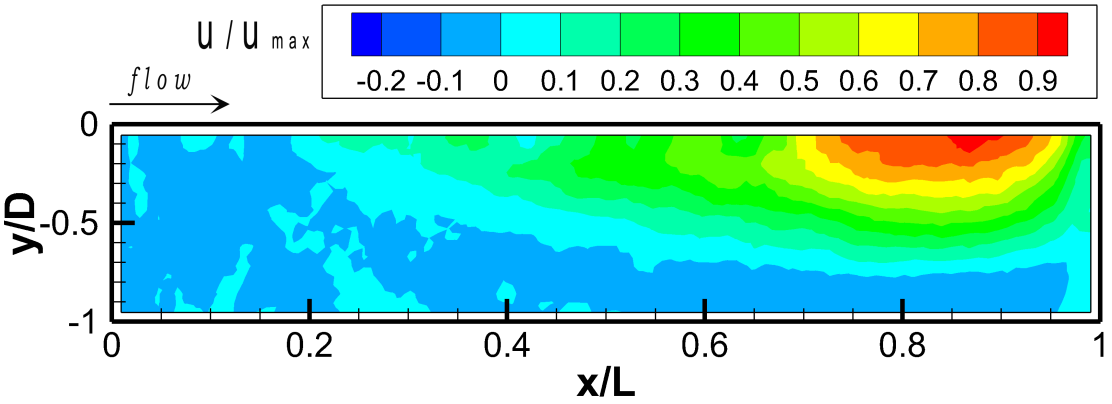

Figure 4.47: Centreplane u-velocity contour of cavity A at M = 0.85 (u_{max} = 78.1 m/s)

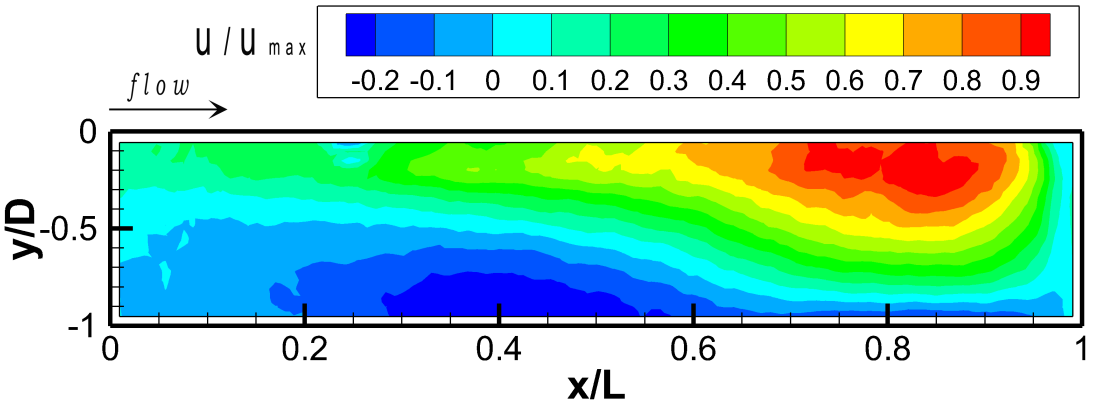

Figure 4.48: Centreplane u-velocity contour of cavity B at M = 0.85 (u_{max} = 107.3 m/s)

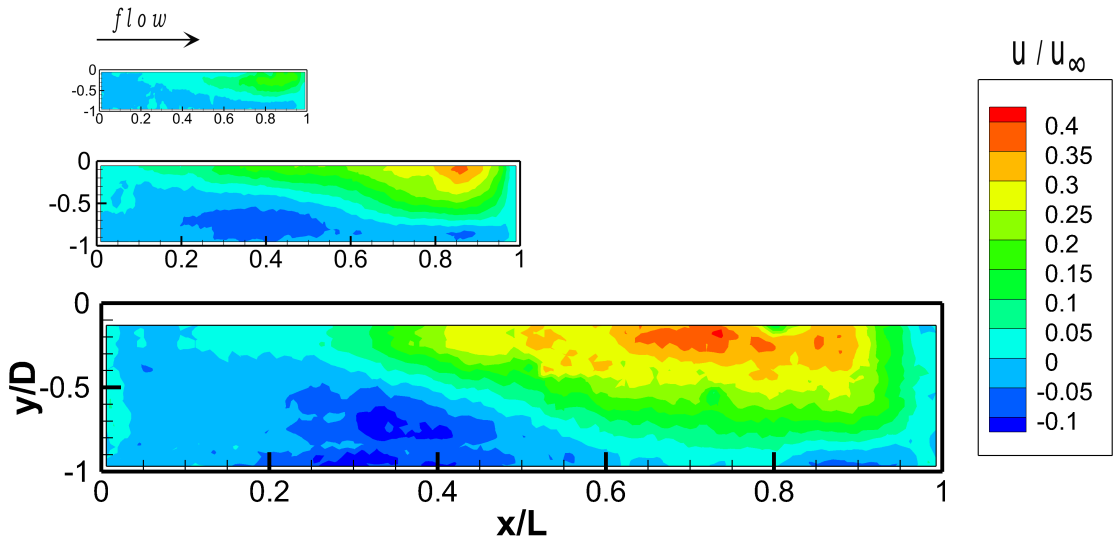

Figure 4.49: Effect of scaling on centreplane u-velocity contour of cavities at M = 0.71 (U_∞ = 233.4 m/s)

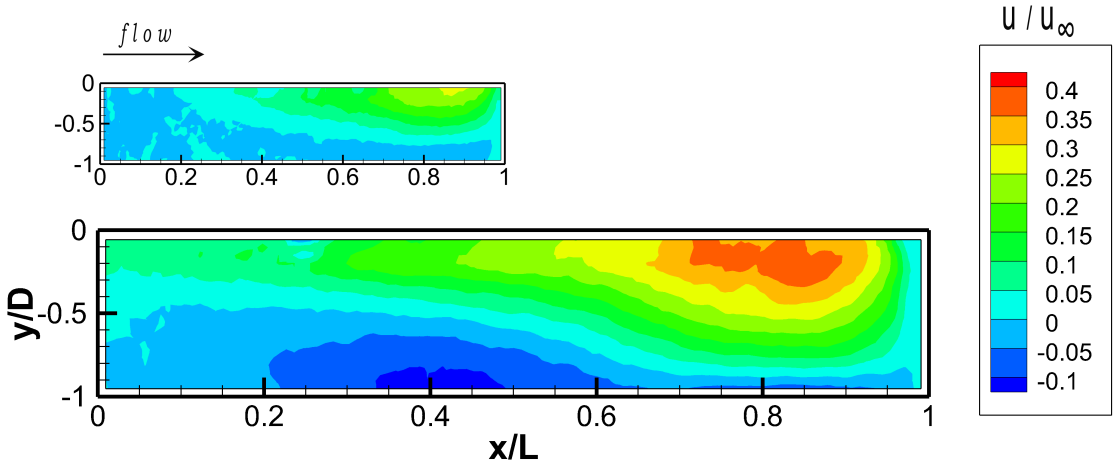

Figure 4.50: Effect of scaling on centreplane u-velocity contour of cavities at M = 0.85 (U_∞ = 275 m/s)

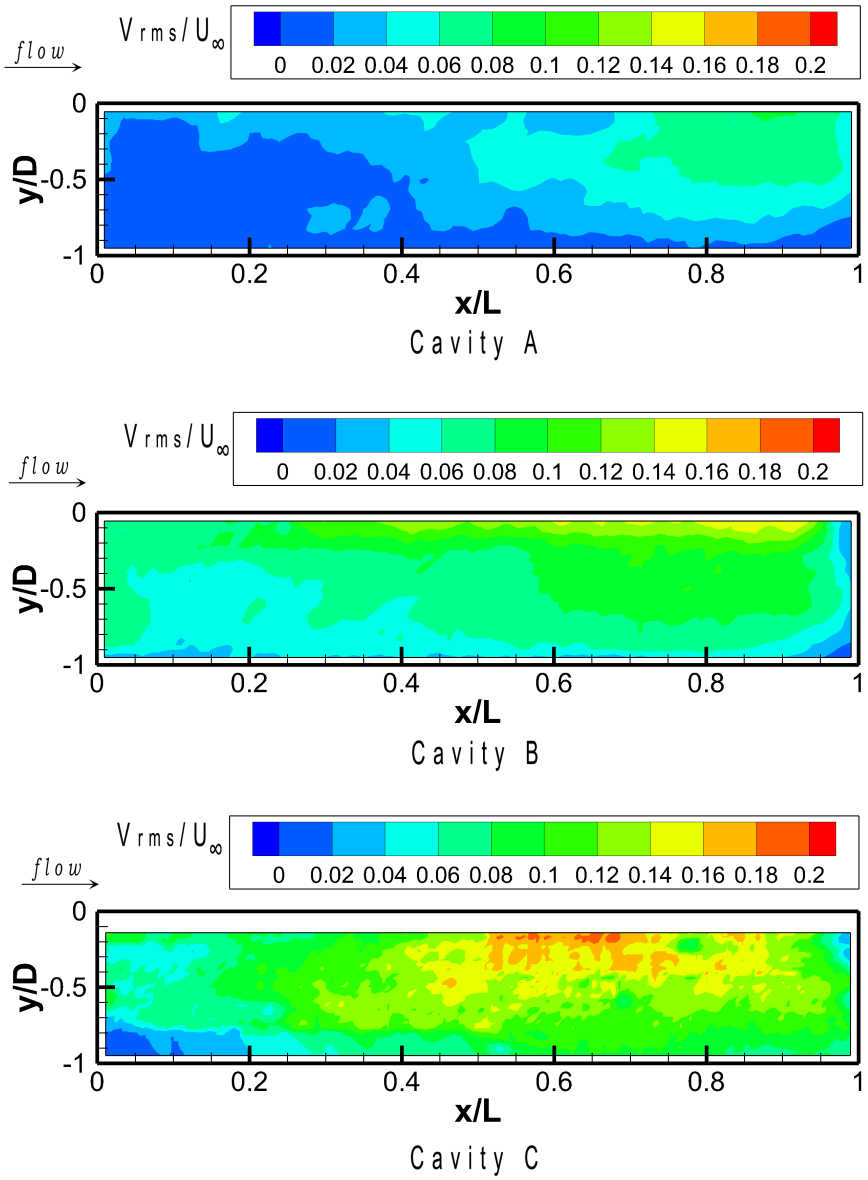

Figure 4.51: Effect of scaling on fluctuating total velocity, V_{rms}, at M = 0.71 (U_∞ = 233.4 m/s)

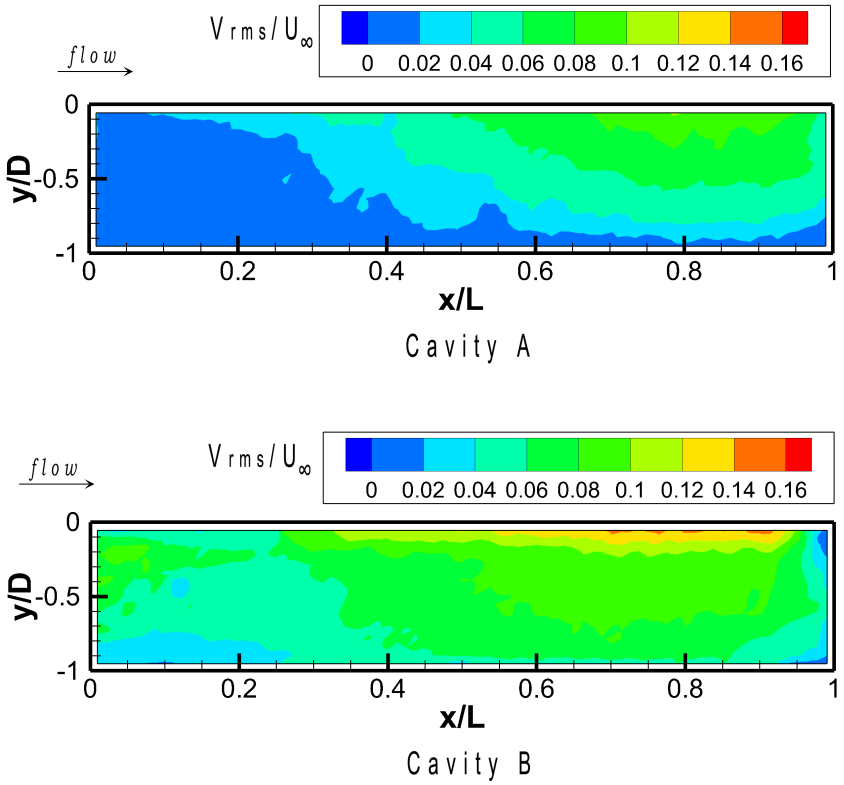

Figure 4.52: Effect of scaling on fluctuating total velocity, V_{rms}, at $M = 0.85$ ($U_\infty = 275$ m/s)

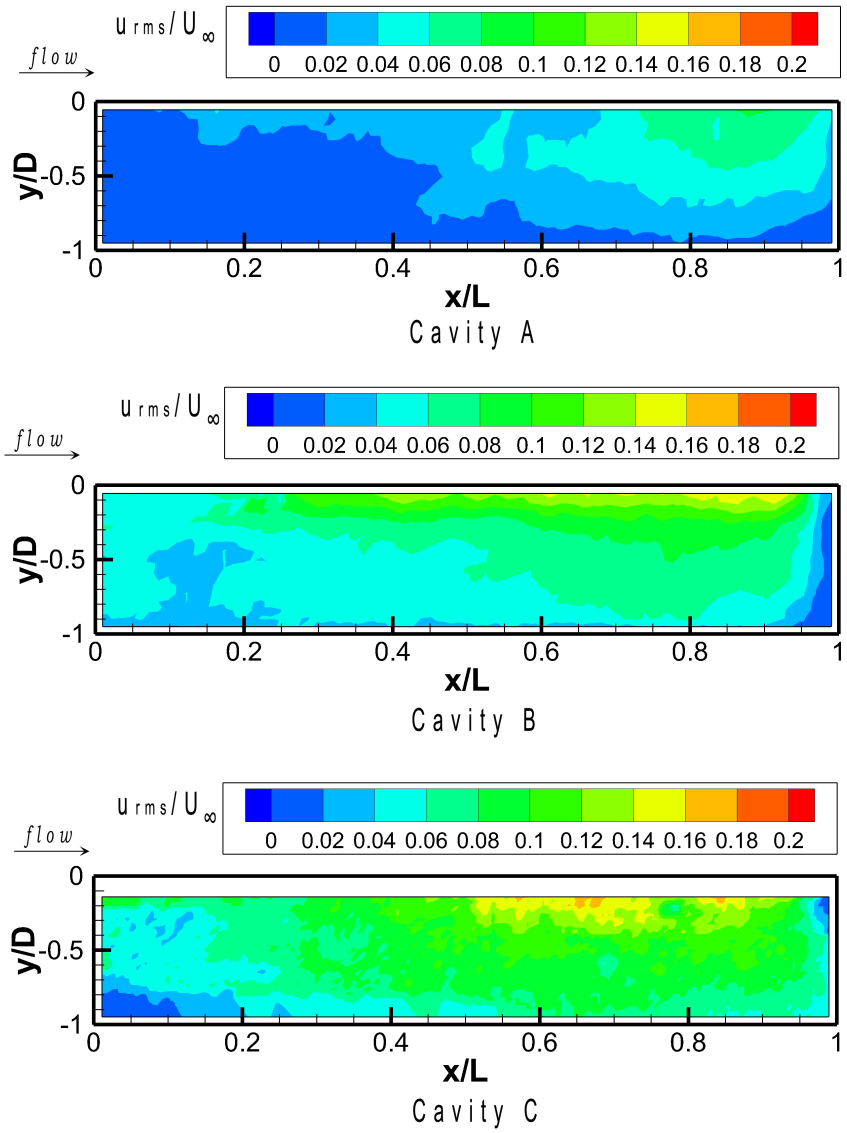

Figure 4.53: Effect of scaling on fluctuating u-velocity, u_{rms}, at M = 0.71 (U_∞ = 233.4 m/s)

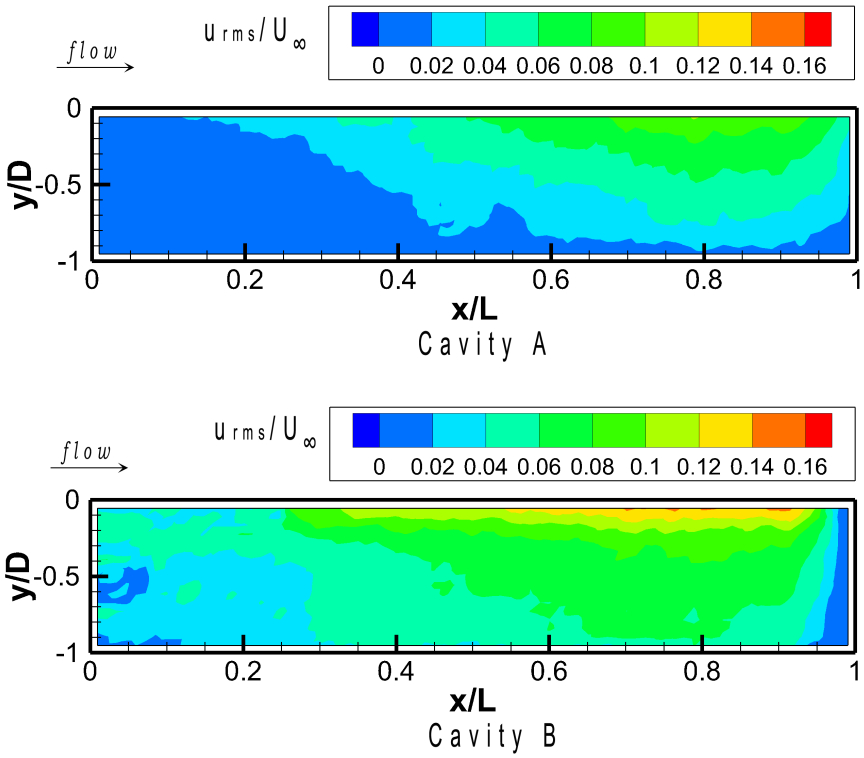

Figure 4.54: Effect of scaling on fluctuating u-velocity, u_{rms}, at M = 0.85 (U_∞ = 275 m/s)

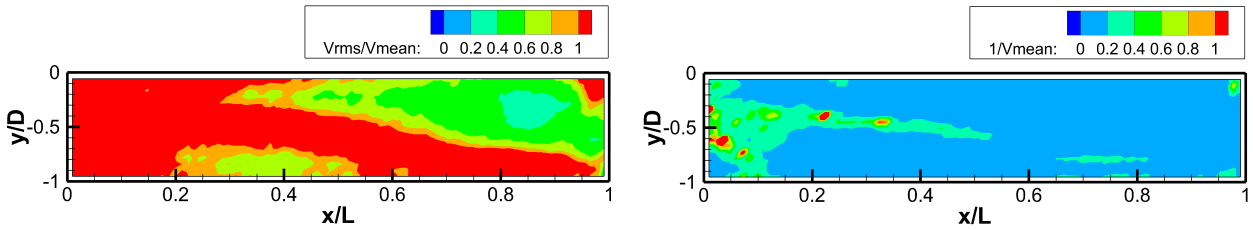

Figure 4.55: Contour plots of V_{rms}/V_{mean} and $1/V_{mean}$ for cavity B at M = 0.71

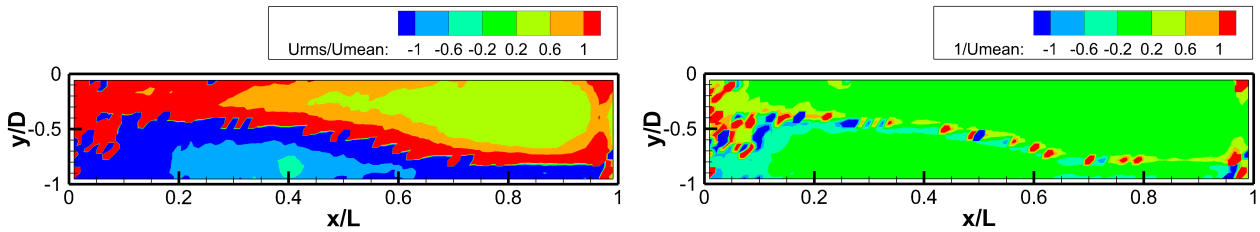

Figure 4.56: Contour plots of u_{rms}/u_{mean} and $1/u_{mean}$ for cavity B at M = 0.71

Figure 4.57: Control surface, ABCD, for aft wall region (AB < 0.2x/L)

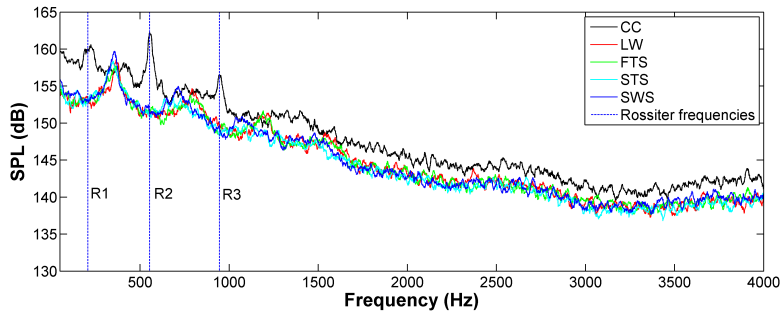

Figure 4.58: Effect of leading edge spoilers on the power spectrum of cavity C at M = 0.71 (x/L = 0.9)

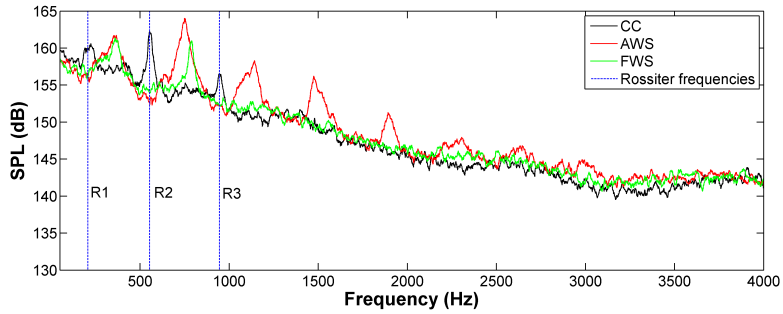

Figure 4.59: Effect of slant walls on power spectrum of cavity C at M = 0.71 (x/L = 0.9)

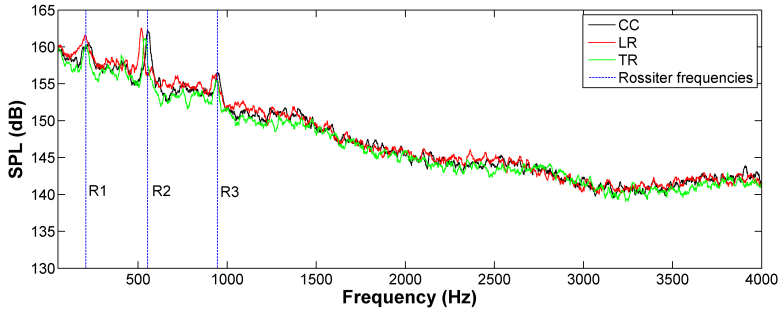

Figure 4.60: Effect of ramps on the power spectrum of cavity C at M = 0.71 (x/L = 0.9)

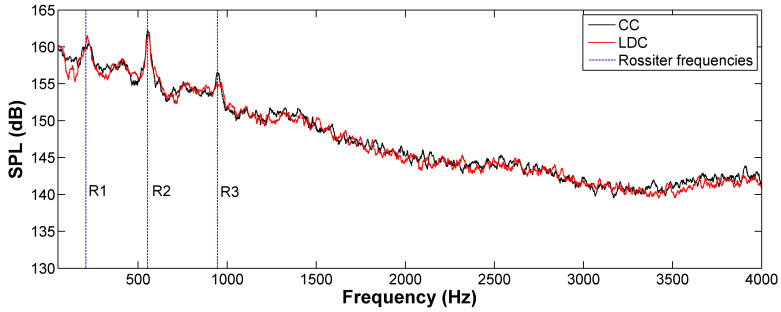

Figure 4.61: Effect of LDC on the power spectrum of cavity C at M = 0.71 (x/L = 0.9)

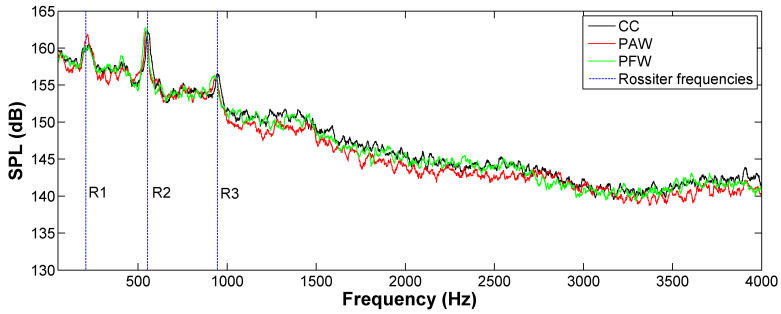

Figure 4.62: Effect of porous walls on the power spectrum of cavity C at M = 0.71 (x/L = 0.9)

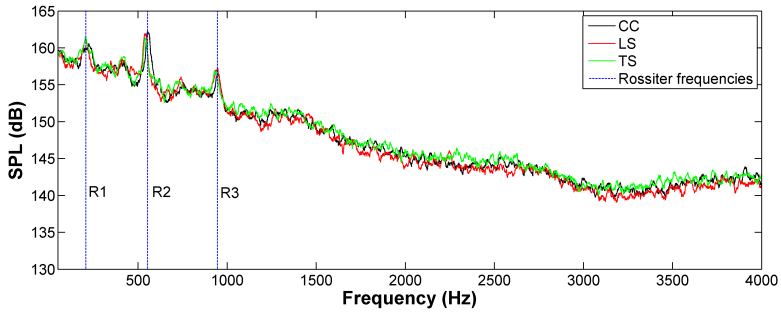

Figure 4.63: Effect of steps on the power spectrum of cavity C at M = 0.71 (x/L = 0.9)

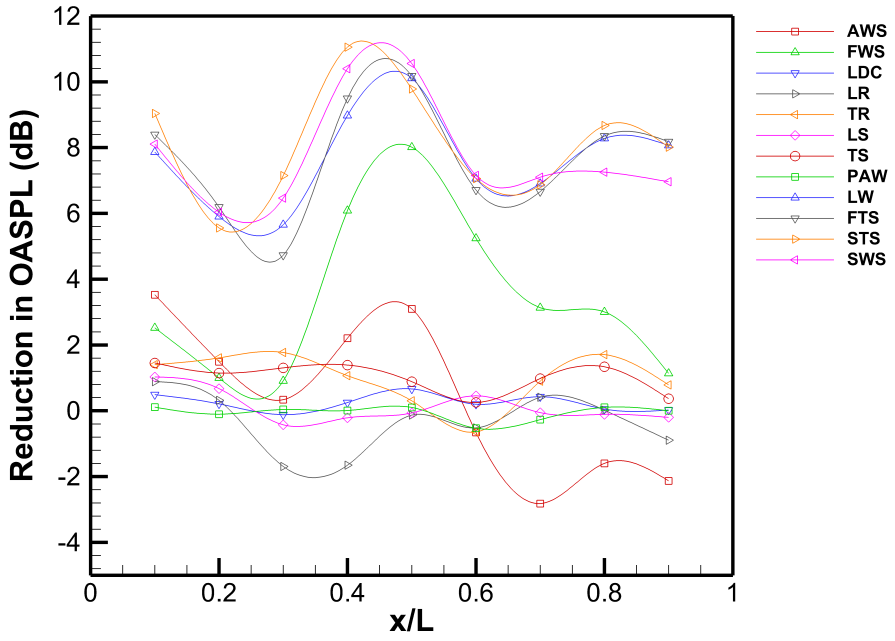

Figure 4.64: Effect of the different passive control devices on centreline OASPL of cavity C at M = 0.71

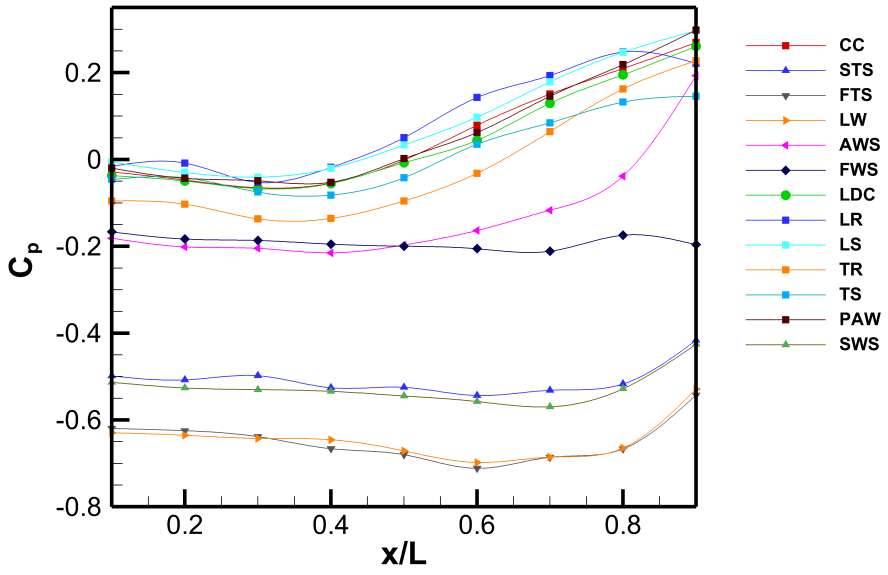

Figure 4.65: Effect of the different passive control devices on centreline mean pressure distribution of cavity C at M = 0.71

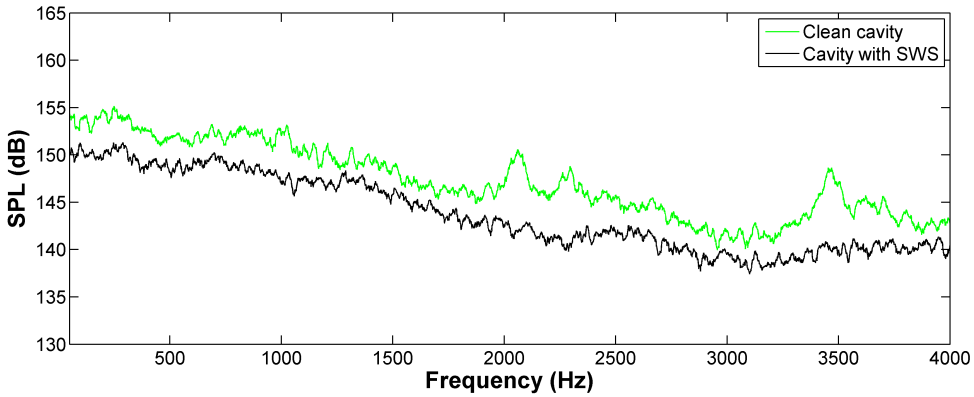

Figure 4.66: Effect of SWS with $h_{SWS} = \delta$ on power spectrum of cavity A at M = 0.71 (x/L = 0.9)

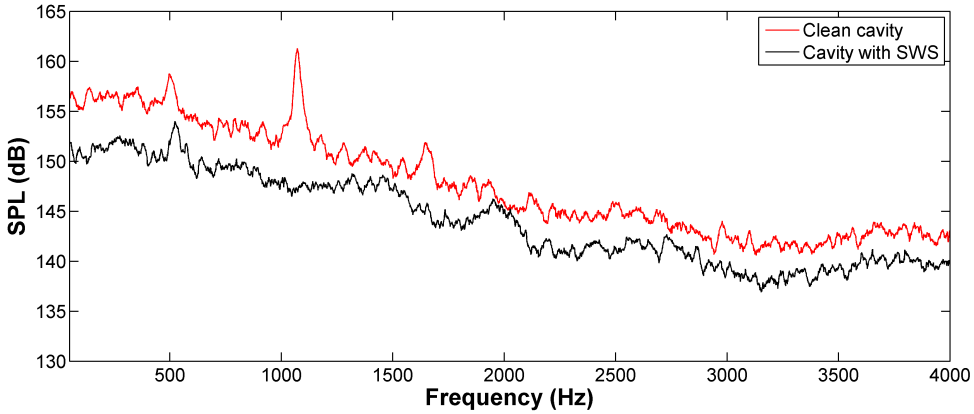

Figure 4.67: Effect of SWS with $h_{SWS} = \delta$ on power spectrum of cavity B at M = 0.71 (x/L = 0.9)

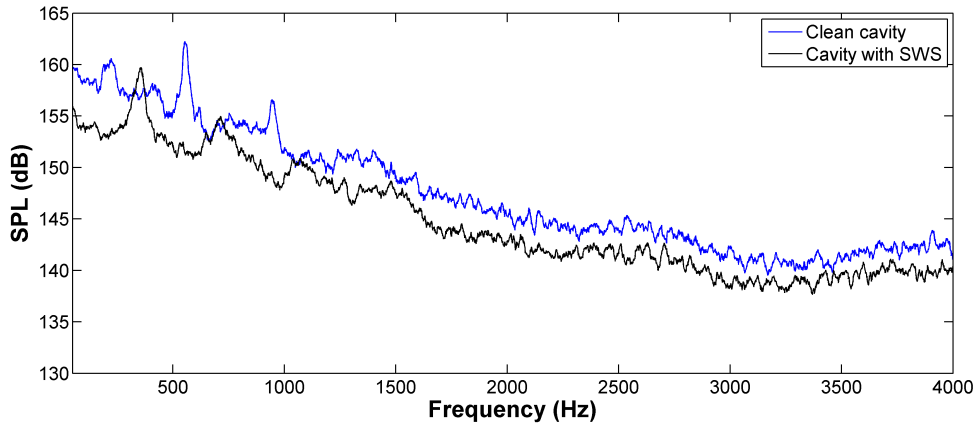

Figure 4.68: Effect of SWS with $h_{SWS} = \delta$ on power spectrum of cavity C at M = 0.71 (x/L = 0.9)

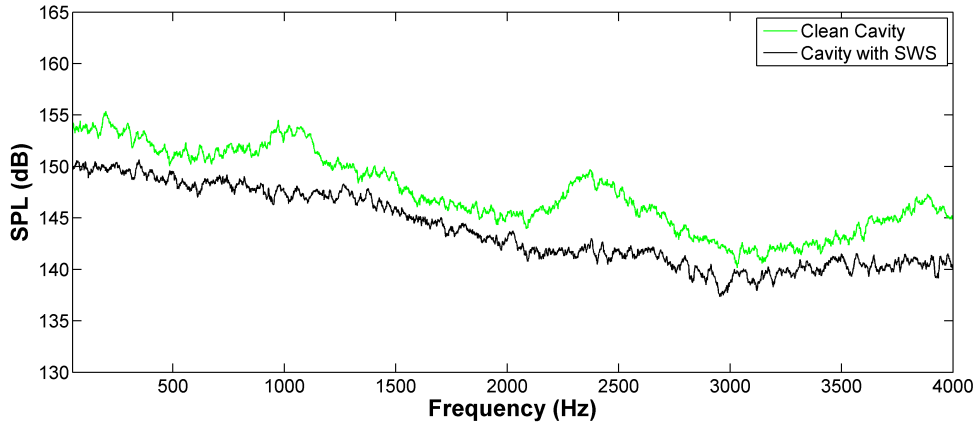

Figure 4.69: Effect of SWS with $h_{SWS} = \delta$ on power spectrum of cavity A at M = 0.85 (x/L = 0.9)

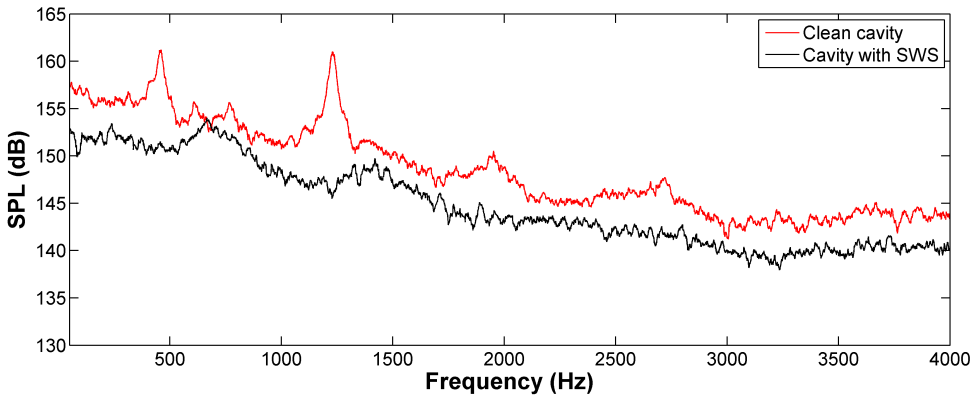

Figure 4.70: Effect of SWS with $h_{SWS} = \delta$ on power spectrum of cavity B at M = 0.85 (x/L = 0.9)

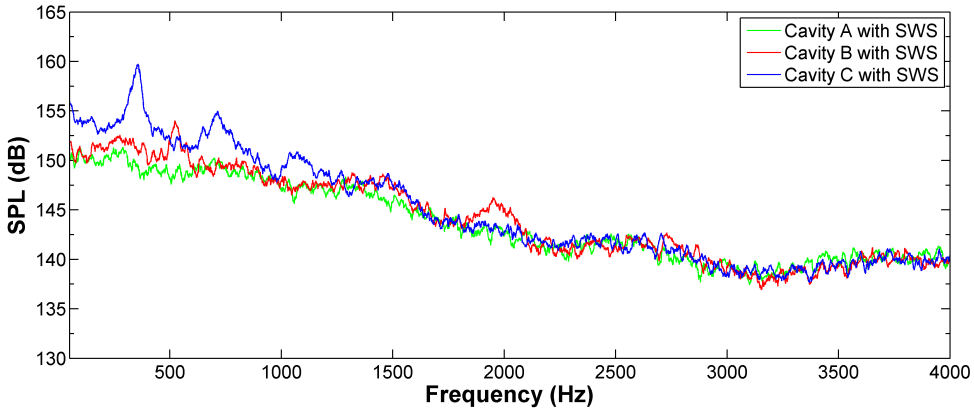

Figure 4.71: Comparison of power spectra with use of SWS(with $h_{SWS} = \delta$) at M = 0.71 (x/L = 0.9)

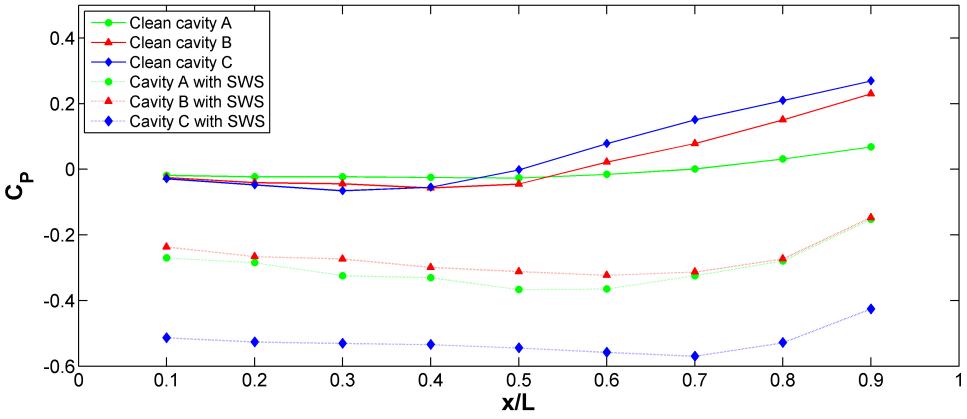

Figure 4.72: C_p distribution of the cavities with the use of SWS with $h_{SWS} = \delta$ (M = 0.71)

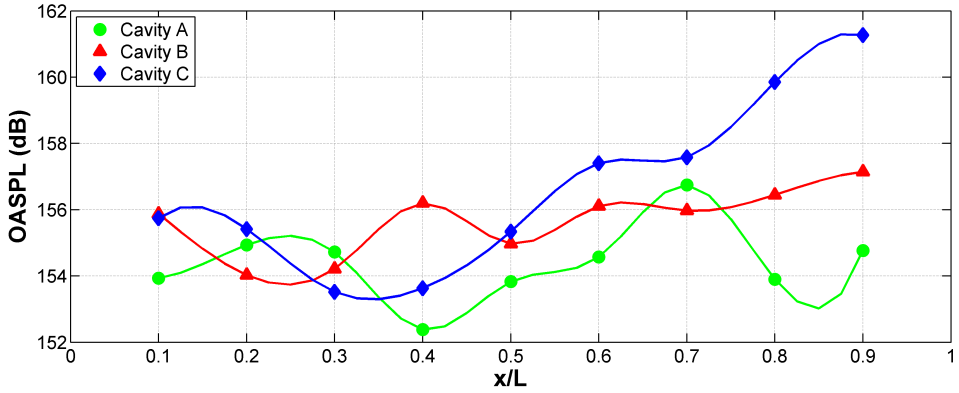

Figure 4.73: OASPL of the cavities with the use of SWS with $h_{SWS} = \delta$ (M = 0.71)

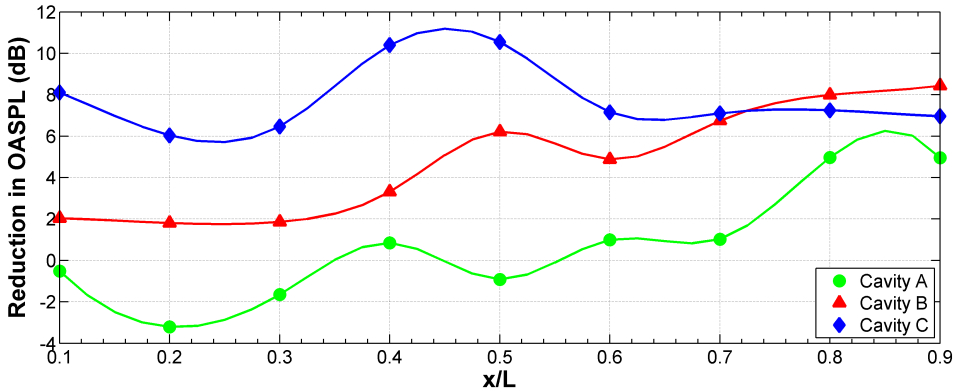

Figure 4.74: Reduction in OASPL of the cavities with the use of SWS with $h_{SWS} = \delta$ (M = 0.71)

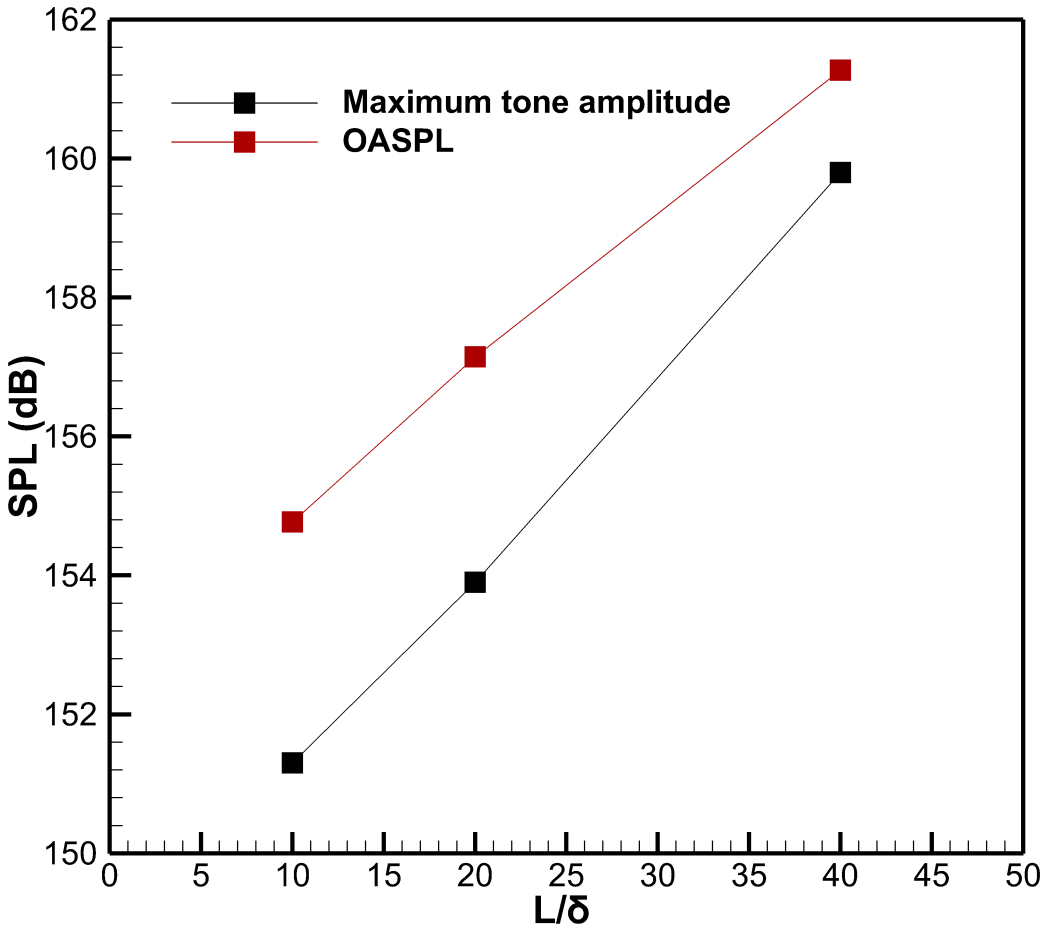

Figure 4.75: Variation of peak amplitude and OASPL with use of SWS with $h_{SWS} = \delta$ at M = 0.71 (x/L = 0.9)

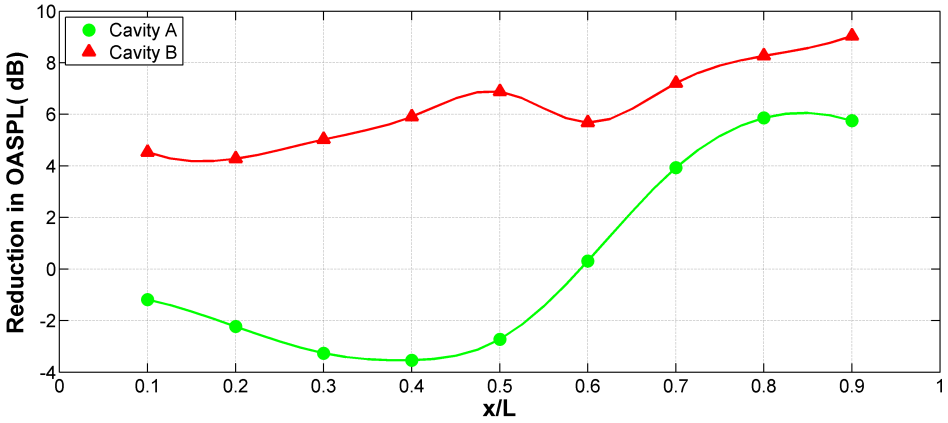

Figure 4.76: Reduction in OASPL of the cavities with the use of SWS with $h_{SWS} = \delta$ (M = 0.85)

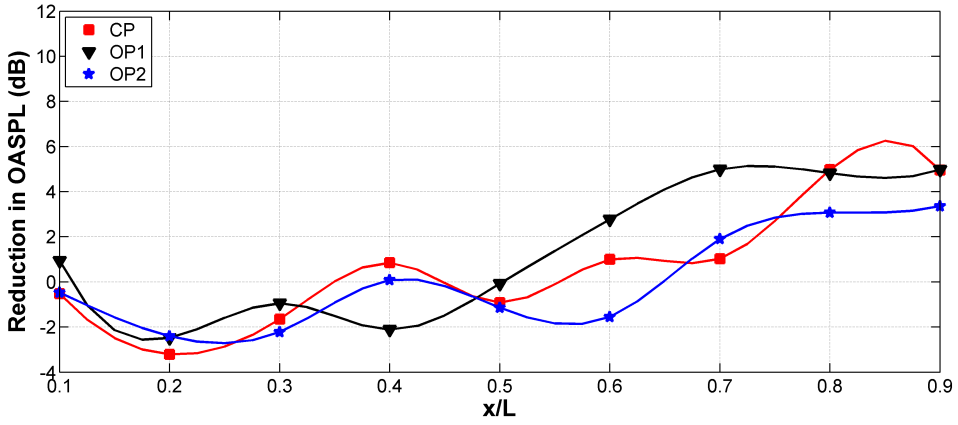

Figure 4.77: Effect of spanwise location on the variation of OASPL reduction for cavity A with SWS with $h_{SWS} = \delta$ (M = 0.71)

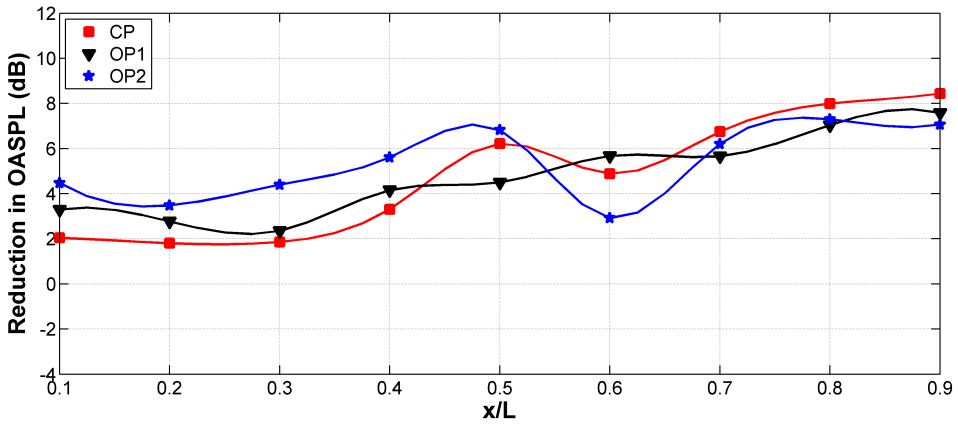

Figure 4.78: Effect of spanwise location on the variation of OASPL reduction for cavity B with SWS with $h_{SWS} = \delta$ ($M = 0.71$)

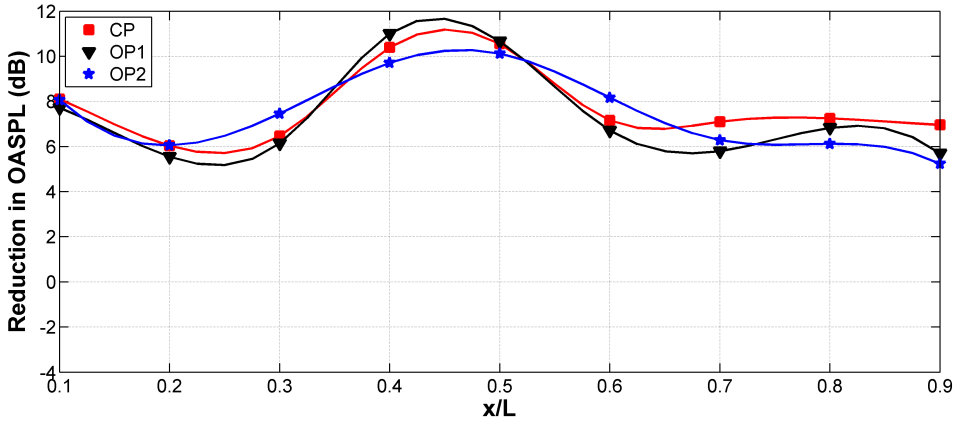

Figure 4.79: Effect of spanwise location on the variation of OASPL reduction for cavity C with SWS with $h_{SWS} = \delta$ ($M = 0.71$)

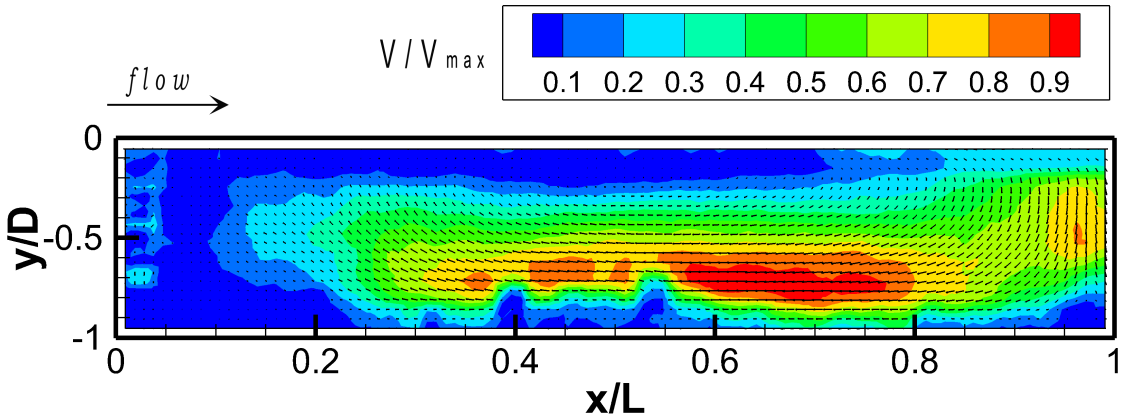

Figure 4.80: Centre plane velocity field of cavity A with SWS of $h_{SWS} = \delta$ at M = 0.71 (V_{max} = 35.7 m/s)

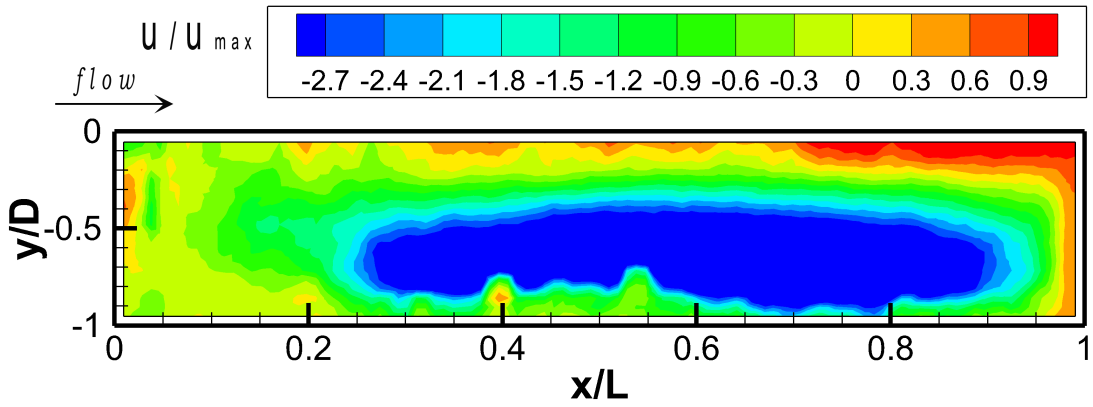

Figure 4.81: Centre plane u-velocity field of cavity A with SWS of $h_{SWS} = \delta$ at M = 0.71 (u_{max} = 11.3 m/s)

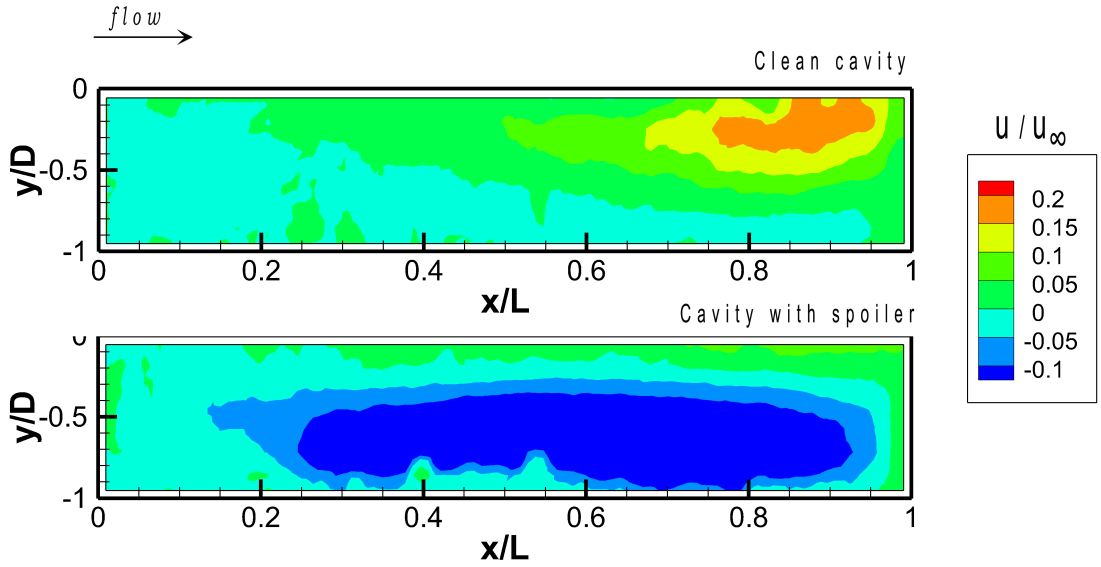

Figure 4.82: Effect of SWS with $h_{SWS} = \delta$ on u-velocity field of cavity A at M = 0.71 (U_∞ = 233.4 m/s)

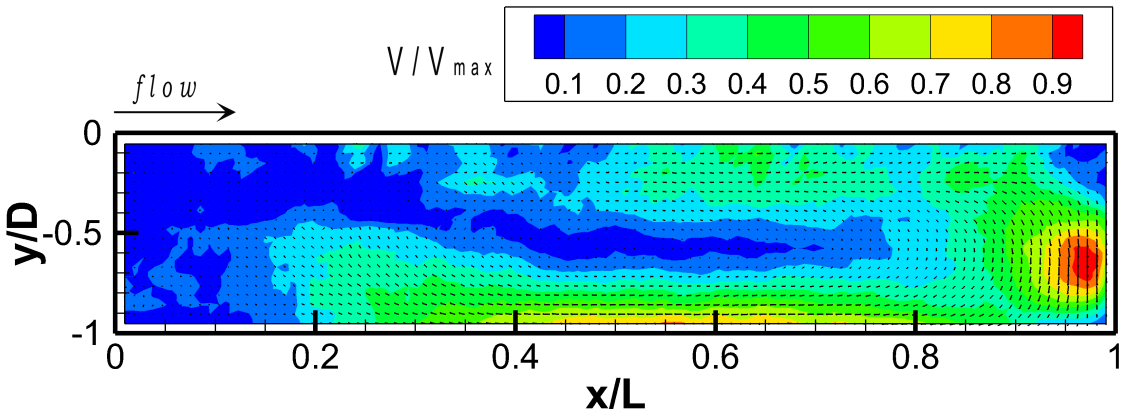

Figure 4.83: Centre plane velocity field of cavity B with SWS of $h_{SWS} = \delta$ at M = 0.71 (V_{max} = 66.7 m/s)

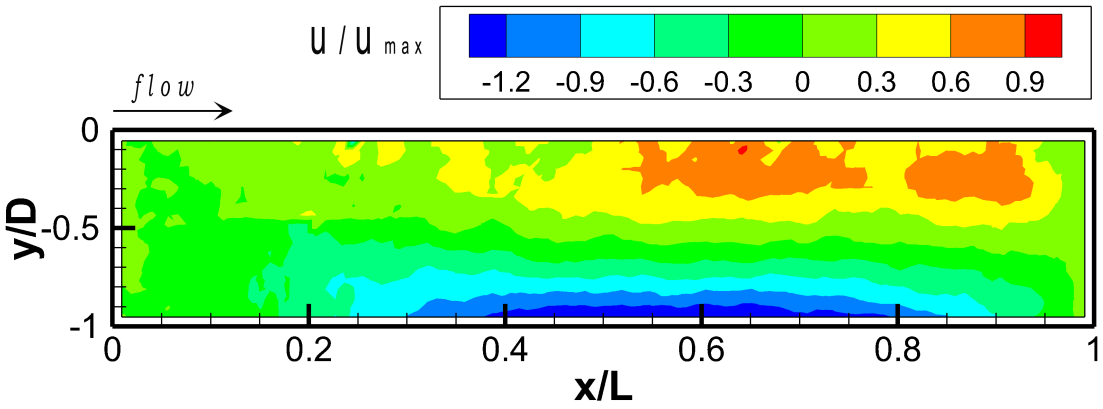

Figure 4.84: Centre plane u-velocity field of cavity B with SWS of $h_{SWS} = \delta$ at M = 0.71 (u_{max} = 35.6 m/s)

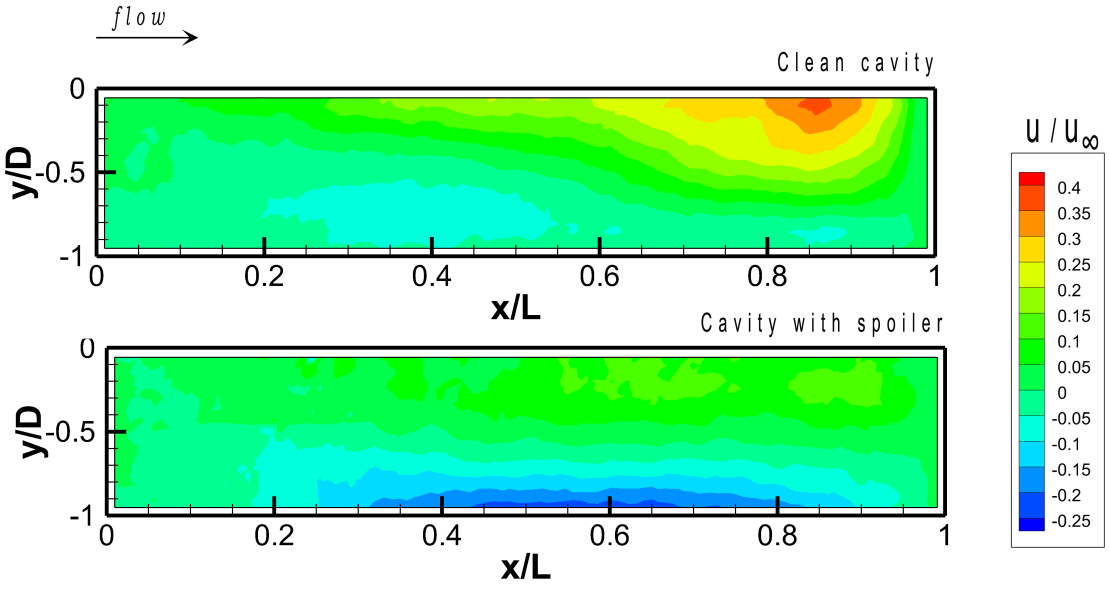

Figure 4.85: Effect of SWS with $h_{SWS} = \delta$ on u-velocity field of cavity B at M = 0.71 (U_∞ = 233.4 m/s)

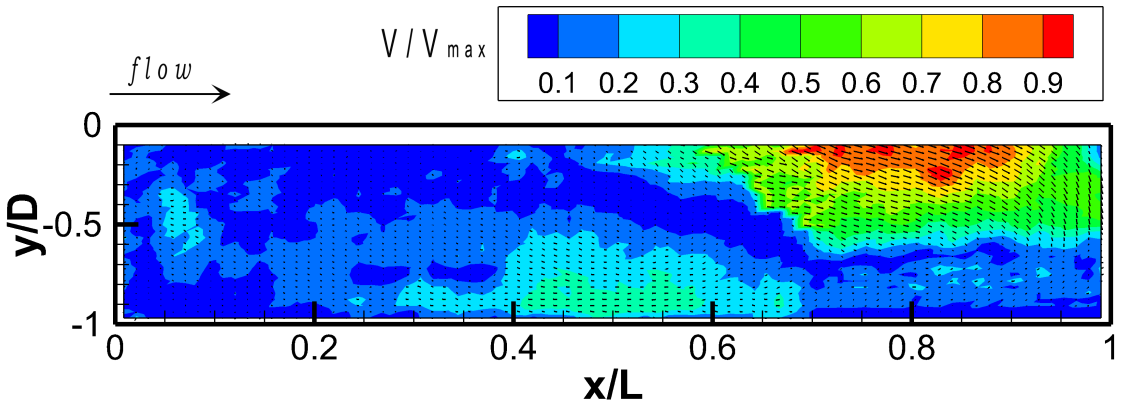

Figure 4.86: Centre plane velocity field of cavity C with SWS of $h_{SWS} = \delta$ at M = 0.71 (V_{max} = 65.3 m/s)

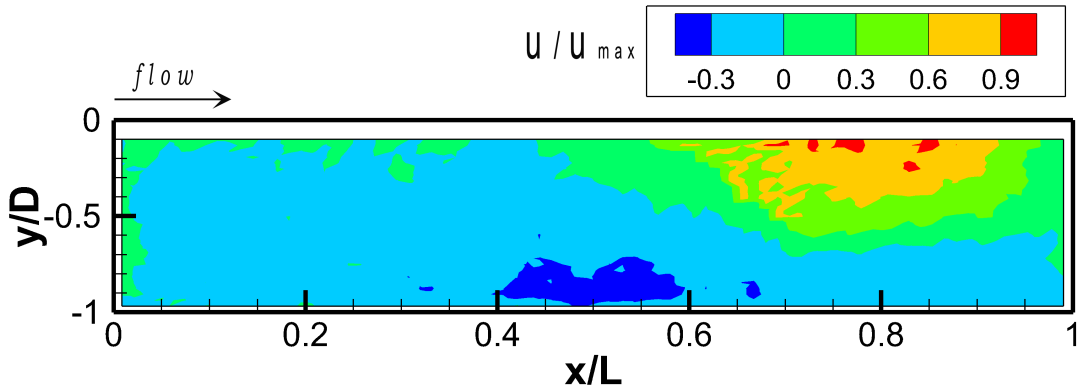

Figure 4.87: Centre plane u-velocity field of cavity C with SWS of $h_{SWS} = \delta$ at M = 0.71 (u_{max} = 65.3 m/s)

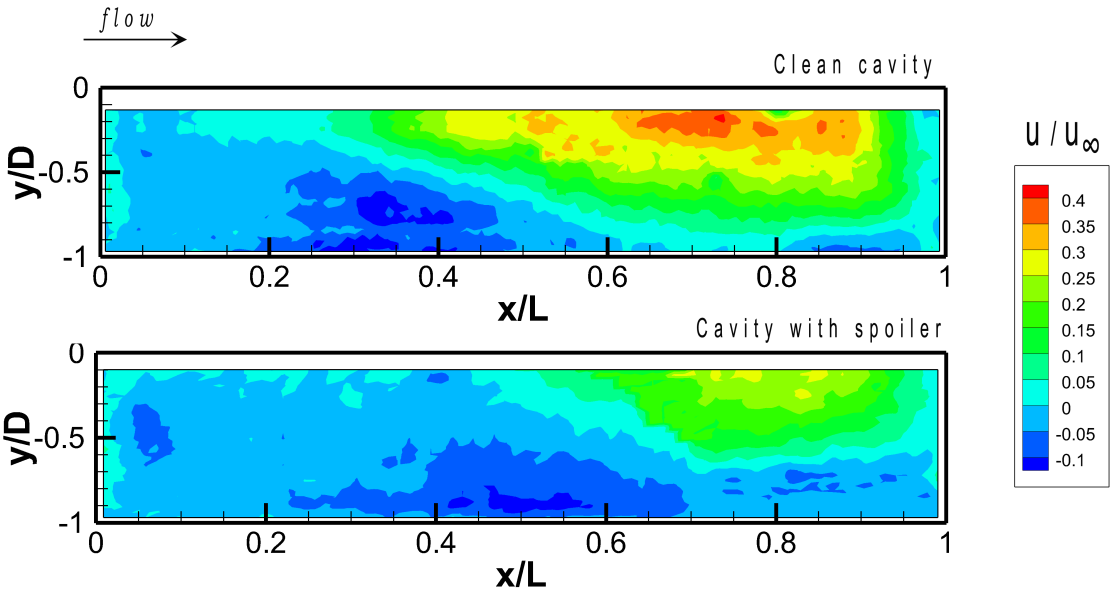

Figure 4.88: Effect of SWS with $h_{SWS} = \delta$ on u-velocity field of cavity C at M = 0.71 (U_∞ = 233.4 m/s)

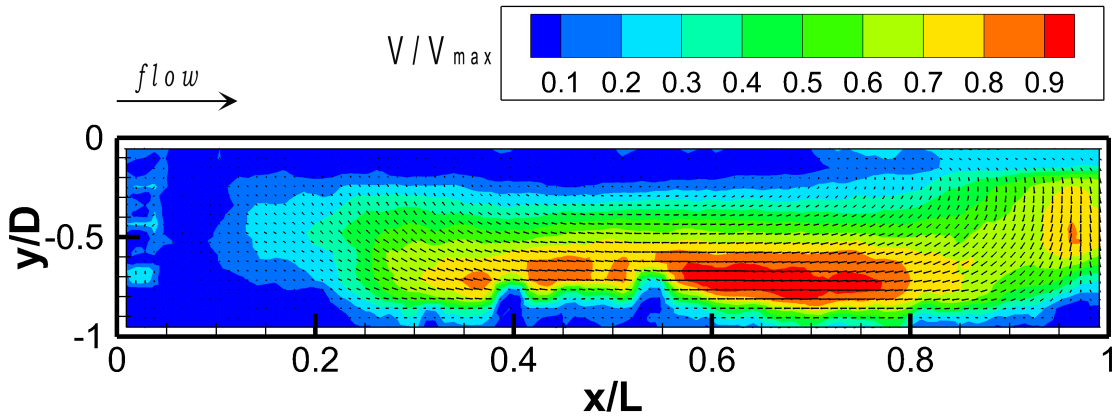

Figure 4.89: Centre plane velocity field of cavity A with SWS of $h_{SWS} = \delta$ at M = 0.85 (V_{max} = 60.7 m/s)

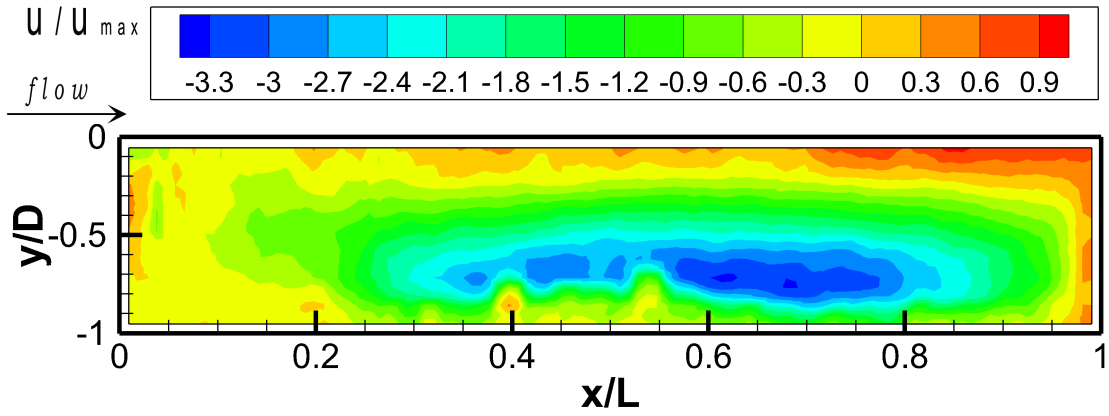

Figure 4.90: Centre plane u-velocity field of cavity A with SWS of $h_{SWS} = \delta$ at M = 0.85 (u_{max} = 17.9 m/s))

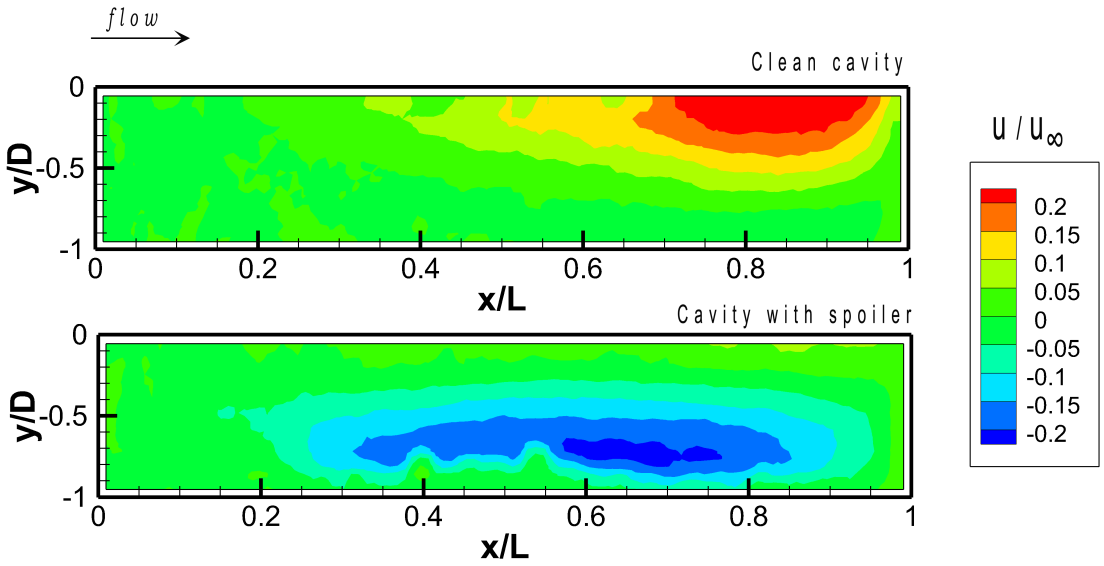

Figure 4.91: Effect of SWS with $h_{SWS} = \delta$ on u-velocity field of cavity A at M = 0.85 (U_∞ = 275 m/s)

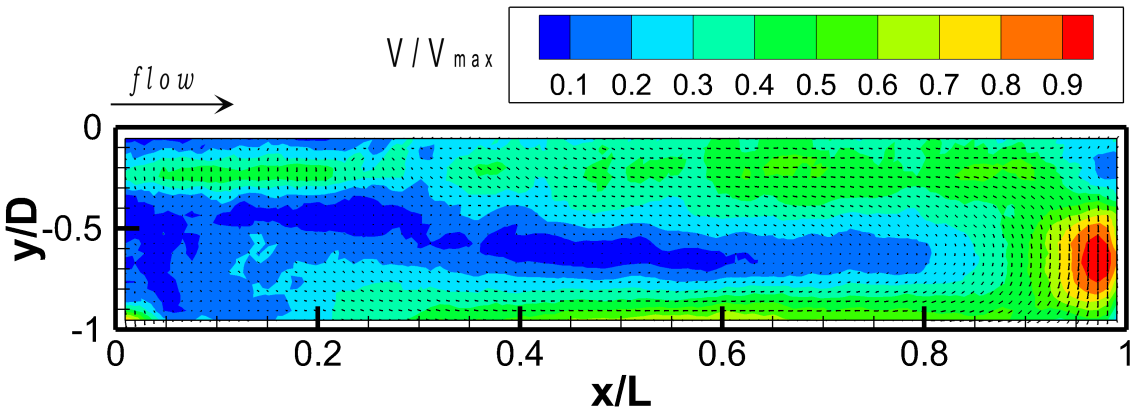

Figure 4.92: Centre plane velocity field of cavity B with SWS of $h_{SWS} = \delta$ at M = 0.85 (V_{max} = 79.8 m/s

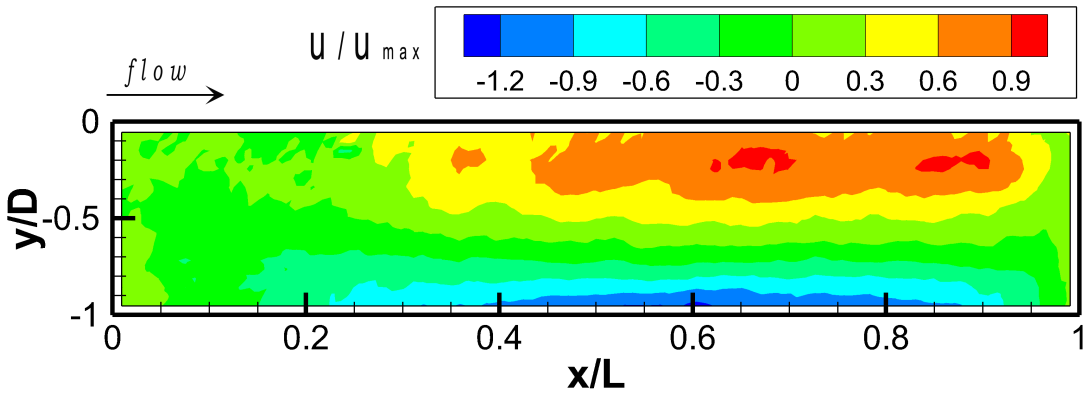

Figure 4.93: Centre plane u-velocity field of cavity B with SWS of $h_{SWS} = \delta$ at M = 0.85 (u_{max} = 43.8 m/s)

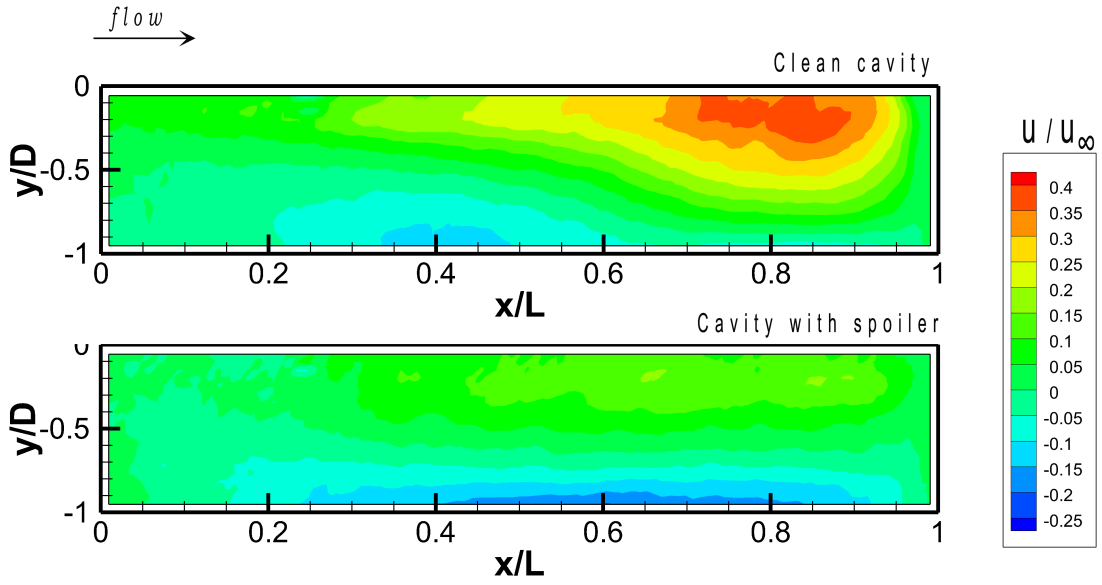

Figure 4.94: Effect of SWS with $h_{SWS} = \delta$ on u-velocity field of cavity B at M = 0.85 (U_∞ = 275 m/s)

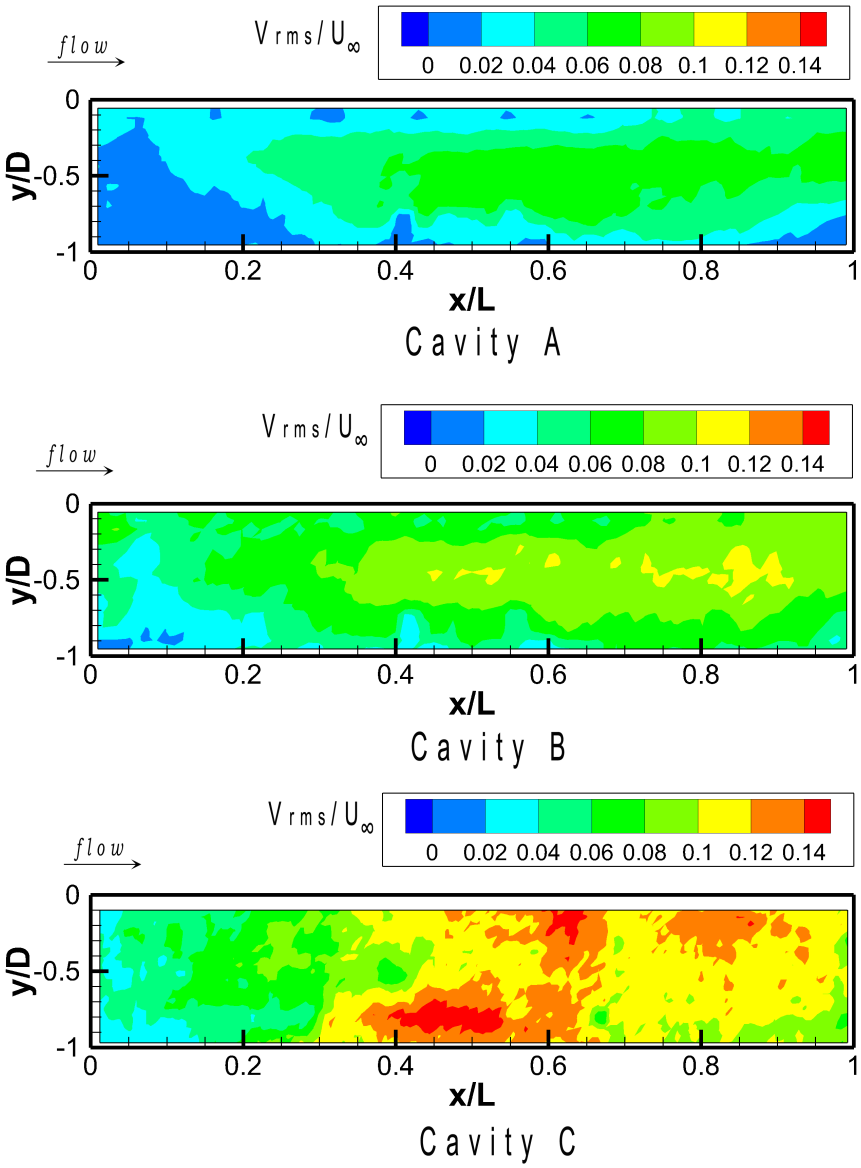

Figure 4.95: Fluctuating velocity, V_{rms}, of different cavities with use of SWS with $h_{SWS} = \delta$ at $M = 0.71$ ($U_\infty = 233.4$ m/s)

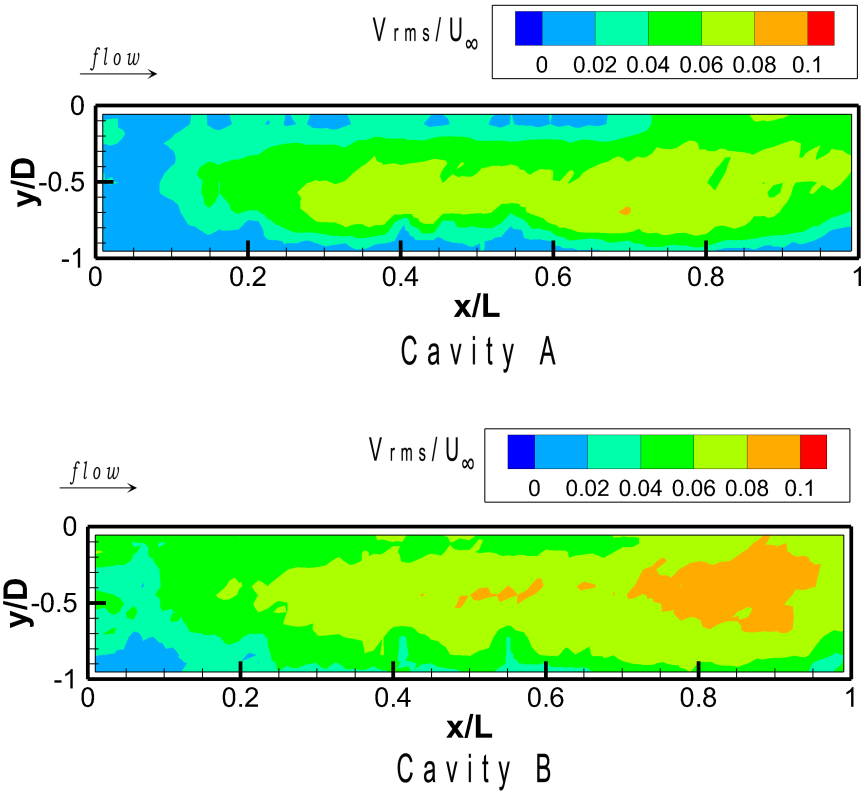

Figure 4.96: Fluctuating velocity, V_{rms}, of different cavities with use of SWS with $h_{SWS} = \delta$ at $M = 0.85$ ($U_\infty = 275$ m/s)

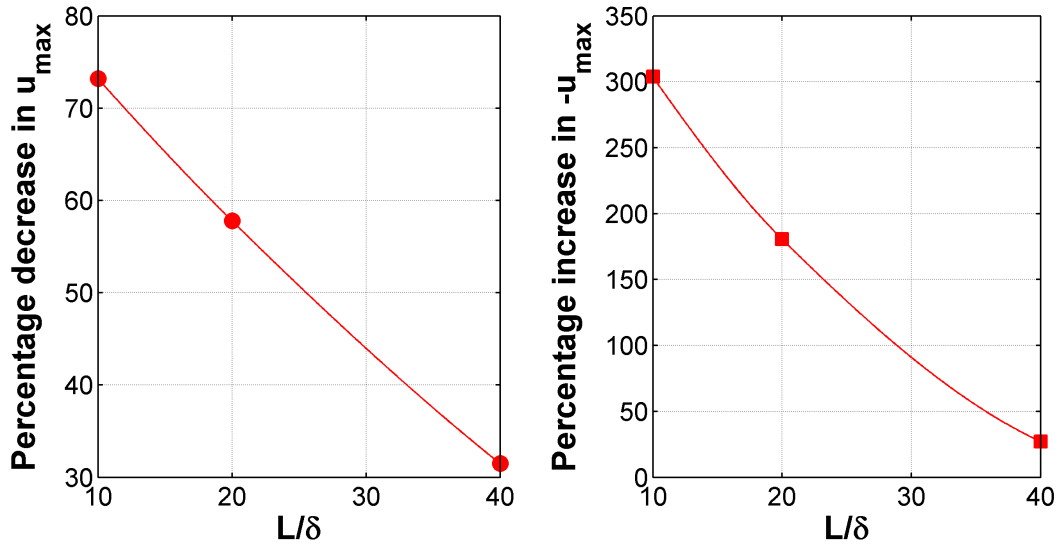

Figure 4.97: Percentage change in u-velocities from clean cavity with use of spoiler (M = 0.71)

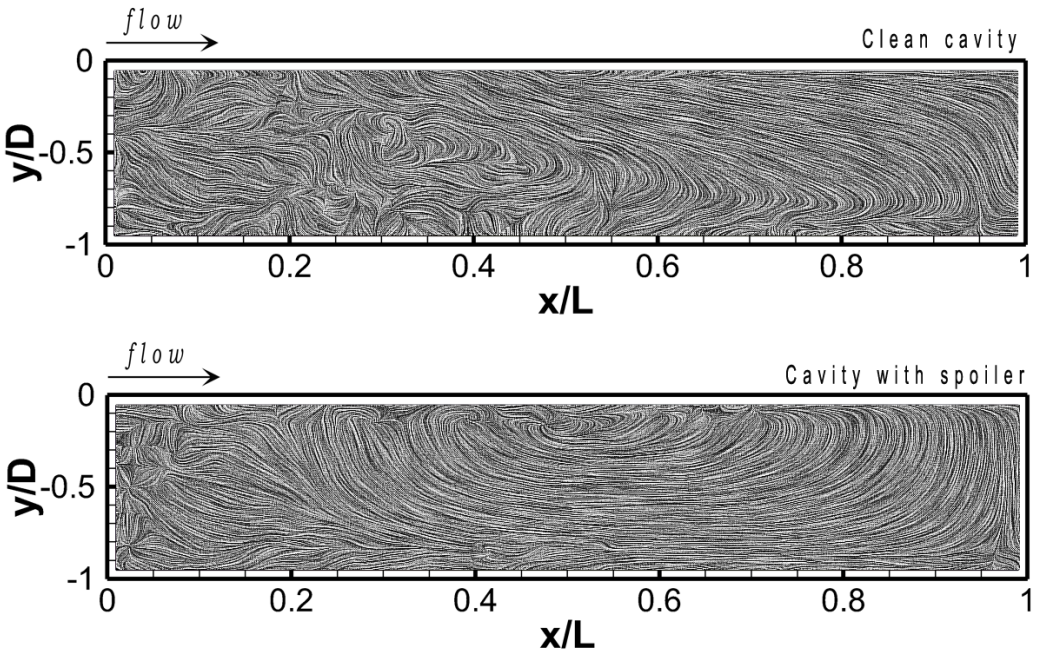

Figure 4.98: LIC images showing the effect of spoiler on cavity A (M = 0.71)

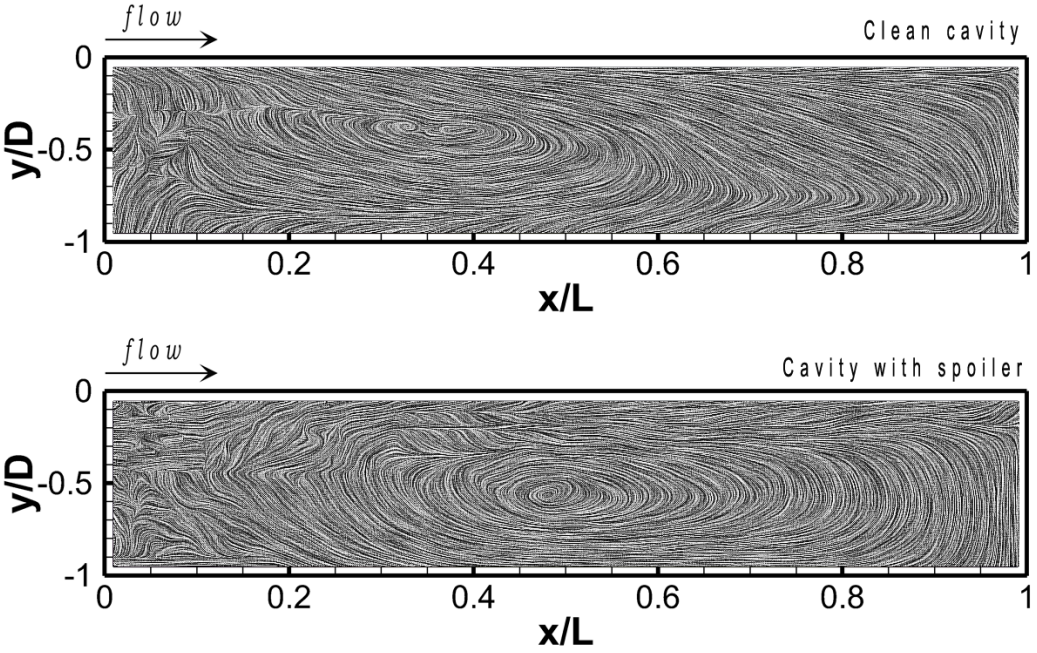

Figure 4.99: LIC images showing the effect of spoiler on cavity B (M = 0.71)

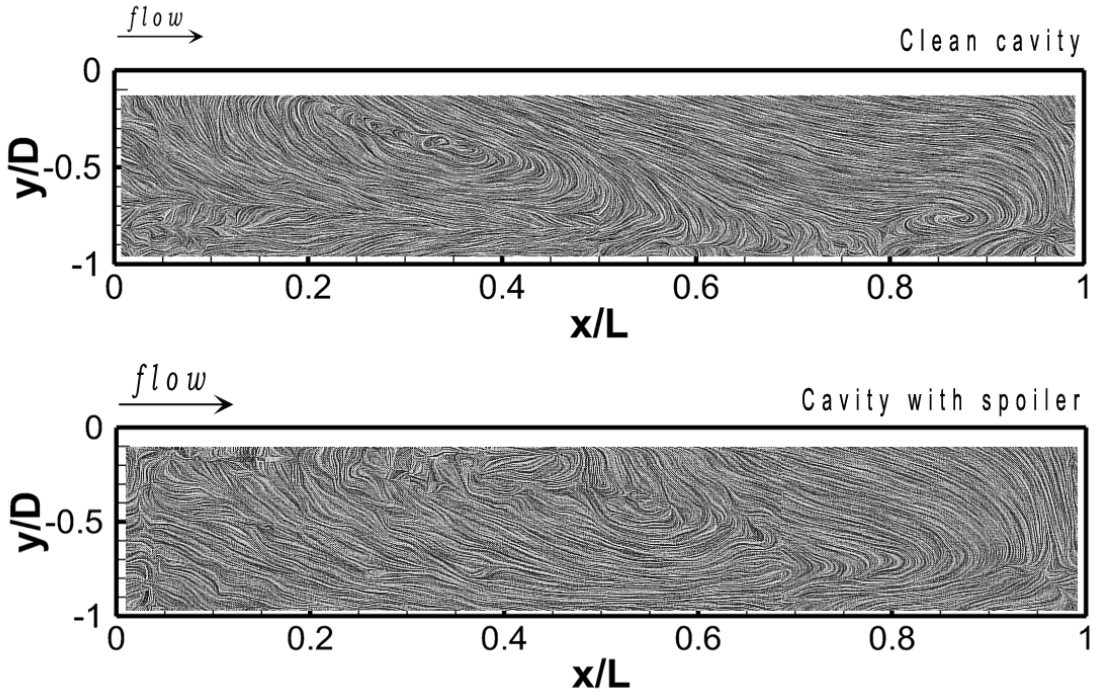

Figure 4.100: LIC images showing the effect of spoiler on cavity C (M = 0.71)

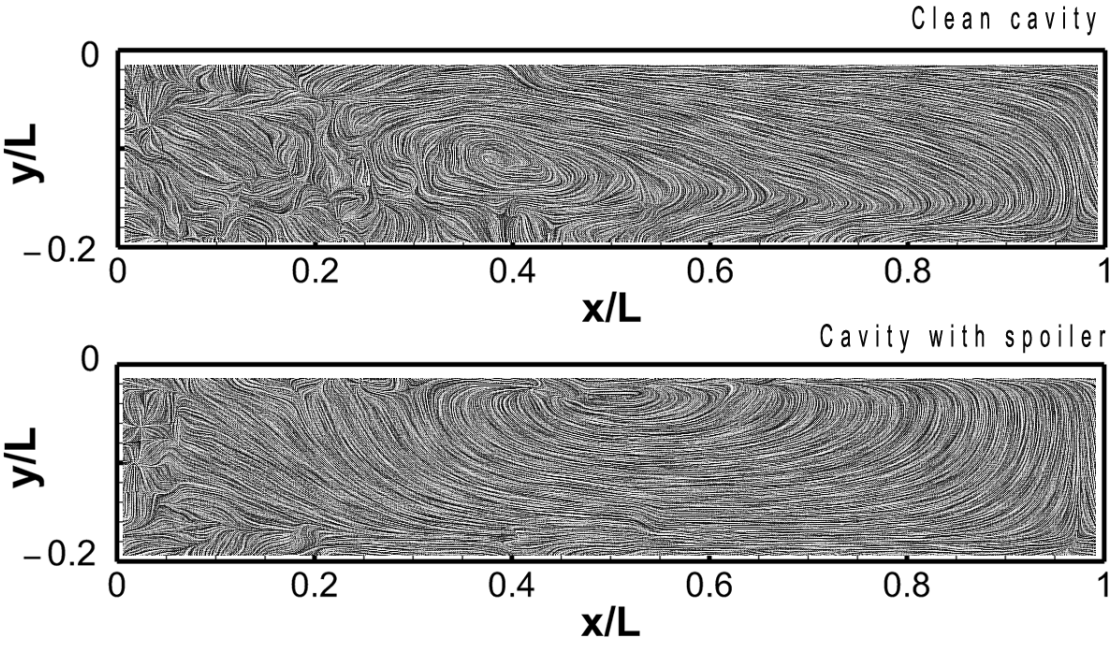

Figure 4.101: LIC images showing the effect of spoiler on cavity A (M = 0.85)

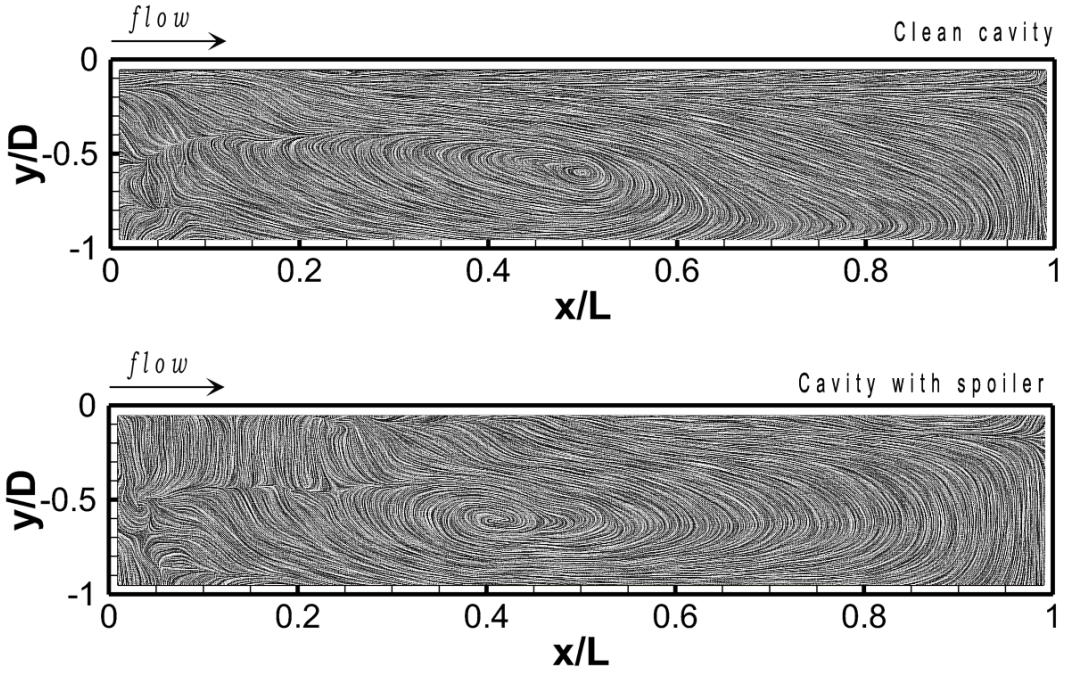

Figure 4.102: LIC images showing the effect of spoiler on cavity B (M = 0.85)

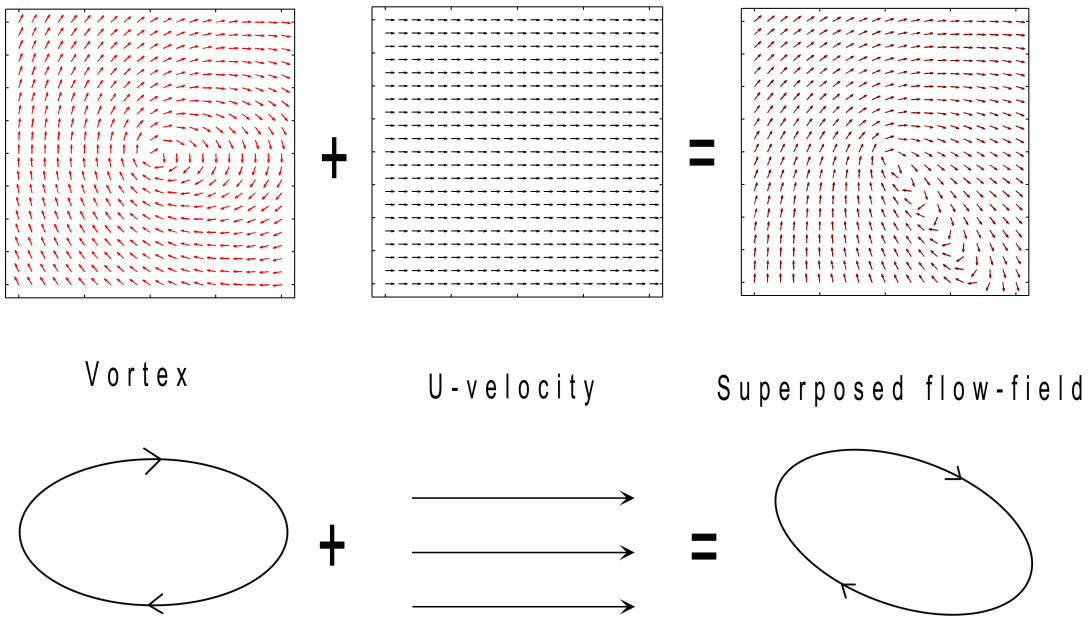

Figure 4.103: Superposition of a vortex with a flow in +x direction

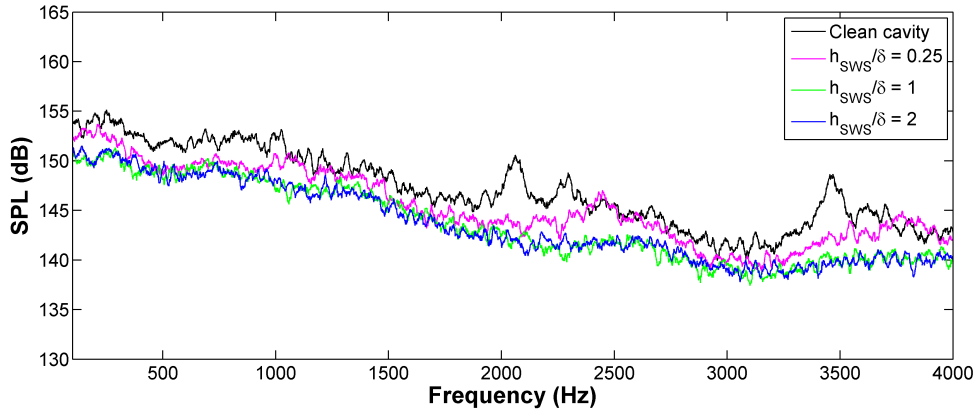

Figure 4.104: Effect of different spoiler heights on power spectrum of cavity A at x/L = 0.9 (M = 0.71)

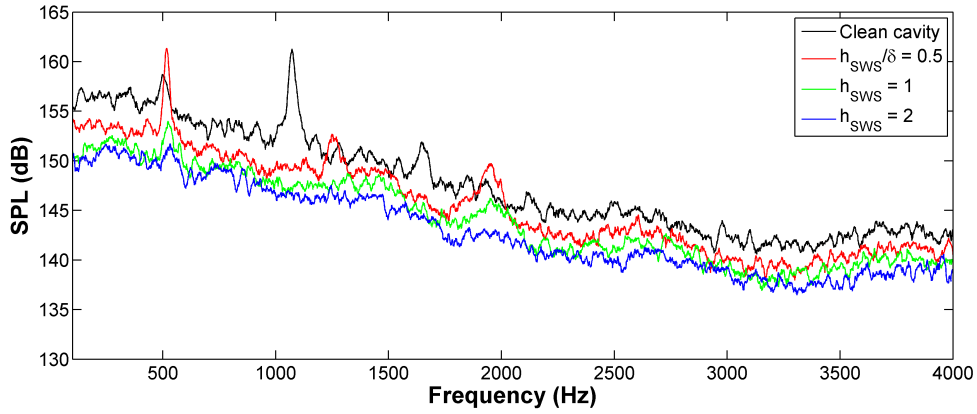

Figure 4.105: Effect of different spoiler heights on power spectrum of cavity B at x/L = 0.9 (M = 0.71)

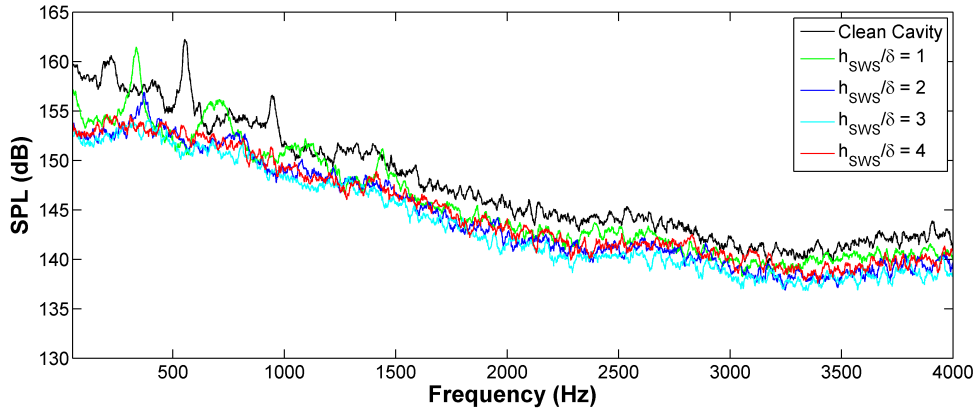

Figure 4.106: Effect of different spoiler heights on power spectrum of cavity C at x/L = 0.9 (M = 0.71)

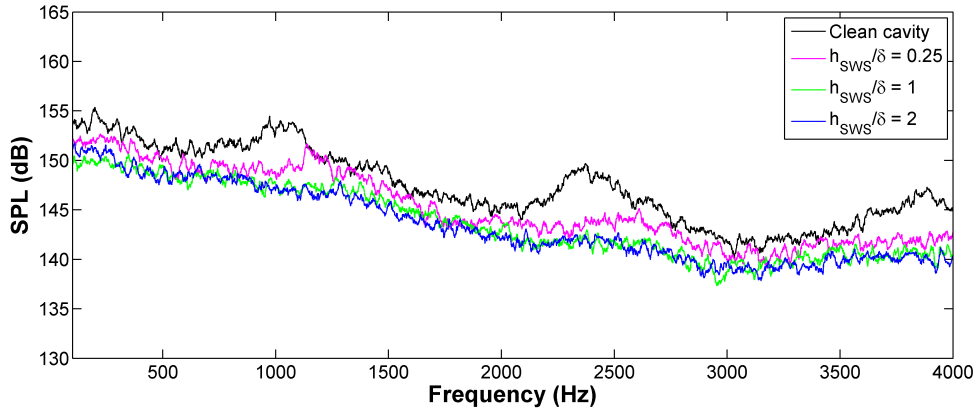

Figure 4.107: Effect of different spoiler heights on power spectrum of cavity A at x/L = 0.9 (M = 0.85)

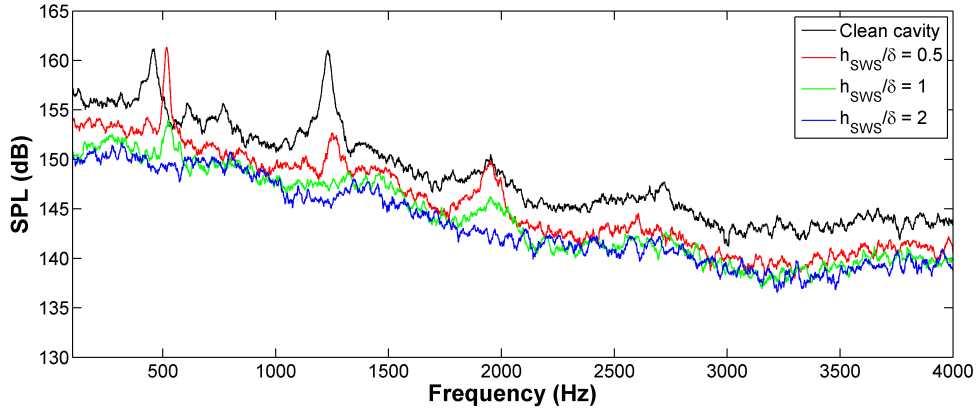

Figure 4.108: Effect of different spoiler heights on power spectrum of cavity B at x/L = 0.9 (M = 0.85)

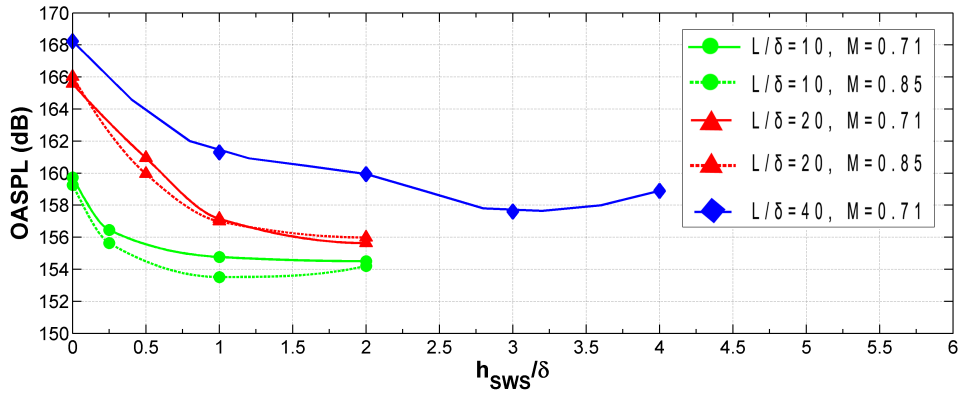

Figure 4.109: Variation of OASPL with h_{SWS}/δ and L/δ

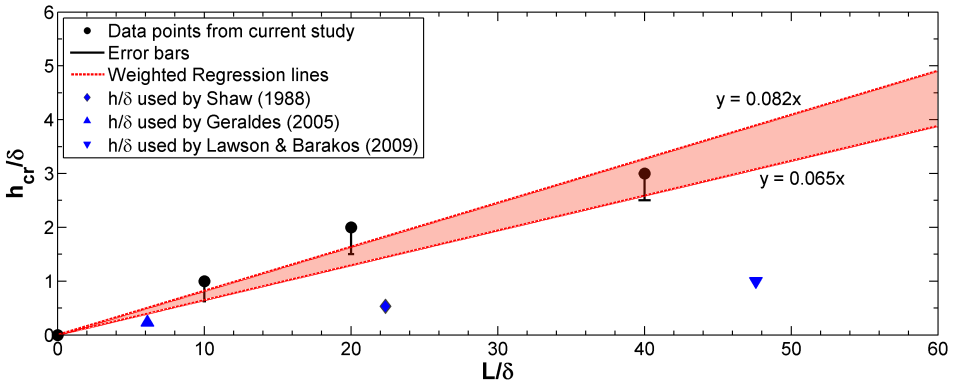

Figure 4.110: The h_{cr}/δ - L/δ curve with linear approximation

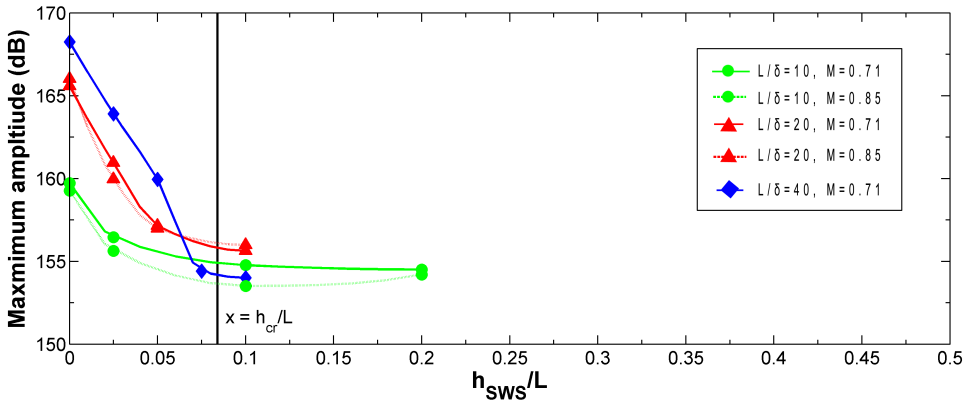

Figure 4.111: Variation of maximum tone amplitude with h_{SWS}/δ and L/δ

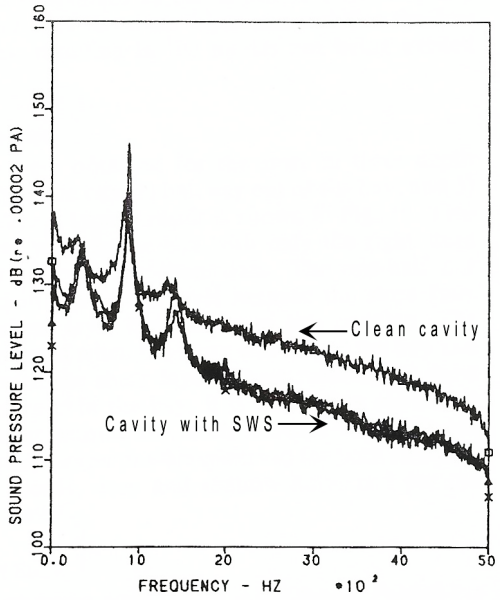

Figure 4.112: Results with SWS obtained by Shaw et al(1988)

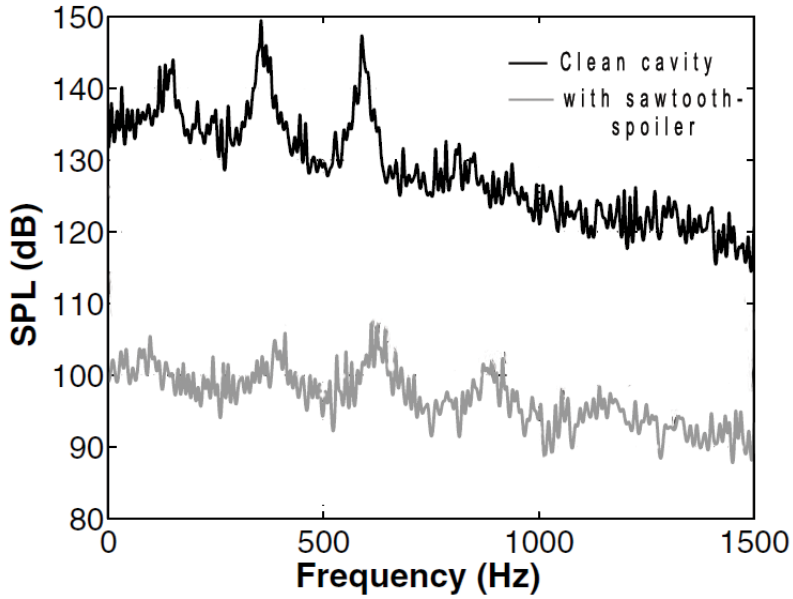

Figure 4.113: Results with SWS obtained by Lawson & Barakos (2009) - note that the power spectrum of SWS is displaced by -30 dB for clarity

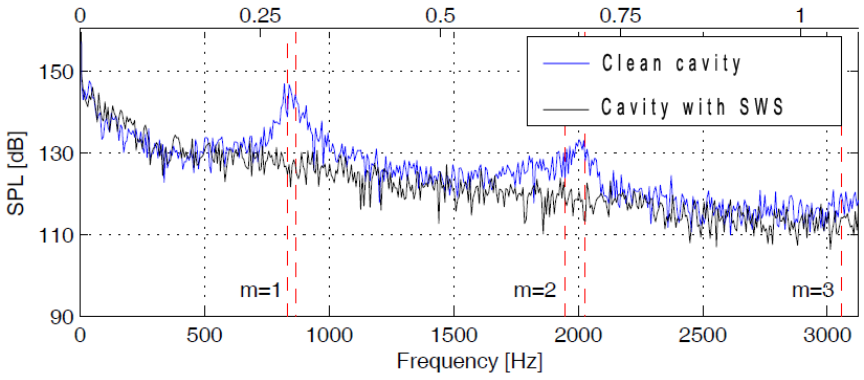

Figure 4.114: Results with SWS obtained by Geraldes (2005)

Chapter 5

Conclusions and Recommendations

5.1 Conclusions

An experimental programme designed to study the effect of scaling on cavity flow dynamics and control was conducted by studying three cavities with different values of L/δ viz. cavity A, cavity B and cavity C. The cavities had L/D = 5 and L/W = 2 and the freestream flow Mach numbers of the experiments were 0.71 (for cavities A, B and C) and 0.85 (for cavities A and B). Time-averaged pressure measurements, unsteady pressure measurements and PIV measurements were conducted for the studies. The cavities were first tested without control and a comparative study of their flow-type, unsteadiness and flow-field was made. Then a comparative study of different passive control techniques was conducted on the largest scale available to assess the relative performance of different passive control methods. Based on this study, a suitable control method with overall desirable characteristics for implementation on a weapons bay was selected. Sawtooth spoilers were found to be a satisfactory control device and was then tested at different scales to study the effects of scaling on the control technique. The scaling parameters of this control method were adjusted to deduce the governing principle that can be used to scale the device with a cavity model.

In the study of clean cavities, significant differences in the cavity flow-type, unsteadiness and flow-field was found. Significant spanwise and streamwise variation was observed in the time-averaged floor pressure of all the cavities especially in the rear half of the cavity length. The shape of the C_p curves in the streamwise direction indicated a shift in the nature of flow inside the cavity. When the ratio L/δ increased from 10 to 40, the nature of flow changed from open to transitional flow, which has not been reported before. Also, the pressure gradients became more adverse with the increase in L/δ. The studies showed the importance of the factor L/δ in determining the cavity flow-type apart from the factors L/D, L/W and M. This factor is crucial for the design of the weapons bay in order to ensure the safe separation of stores.

Power spectral analysis based on unsteady pressure measurements on the cavity floor revealed peaks of high amplitude in the frequency spectra. The frequency of the dominant modes of the different cavities corresponded to the Rossiter frequencies and thus the cavity oscillations followed the feedback mechanism explained by Rossiter. The amplitude of the dominant cavity tones decreased with decrease in L/δ for both the Mach numbers tested and for cavity A, the spectrum was laden with broadband with feebly prominent peaks at M = 0.71. Along with the amplitude of tones, the OASPL values were also found to decrease with a decrease in scale. The results indicated a significant increase in flow unsteadiness and feedback strength responsible for tone generation with increase in scale. Time-frequency analysis showed the occurrence of mode-switching for cavities B and C at M = 0.71. The shape of the dominant mode of the respective cavities across the cavity length showed a standing wave pattern. The shape of the OASPL curves along the streamwise direction resembled the shape of the respective dominant modes showing the effect of the dominant tone on the total energy of all the frequency components.

PIV measurements at the centre plane of the clean cavities showed a change in the flow features inside the cavity. With an increase in L/δ from 10 to 40, the single-recirculation vortex inside the cavity changed to a two-recirculation system. This indicated an increase in the dipping of the shear layer into the cavity. The velocity magnitudes, particularly the +u-velocities were found to increase significantly with increase in scale. This indicated a larger transfer of energy between the freestream and the cavity which is responsible for the higher amplitude tones at larger scales. The results obtained from the studies highlight the fact that although clean cavities of different scales follow the same Rossiter mechanism for the generation of tones, there are interesting variations in their spectral characteristics. This underscores the significant role played by the factor L/δ in cavity oscillations.

Thirteen different passive control techniques were tested on the largest cavity scale available and it was found that not all techniques work equally effectively. Power spectral studies reveal that the leading-edge spoilers like square-tooth spoiler, sawtooth spoiler, leading-edge wedge and flat-top spoiler are more effective in suppressing the Rossiter tones on a larger scale cavity than modification to the cavity walls and the trailing edge. They also show maximum effectiveness in

the reduction of OASPL across the cavity length. The shape of the leading-edge spoilers has been observed to play a role in the magnitude of suppression. The other methods tested achieved lower suppression results compared to the above mentioned. Based on the results of this study, the sawtooth spoiler was selected to be tested for studying the effects of scaling on cavity passive control.

The effect of scaling on the effectiveness of a sawtooth spoiler was studied. This was done by testing a sawtooth spoiler with height equal to the boundary layer thickness on cavities A, B and C. There was a significant difference in the attenuation values observed at the different scales. The effectiveness of the spoiler was found to decrease with increase in the cavity scale. Although tones were found to be present for cavity C, they were found to be completely attenuated for cavity A and significantly attenuated for cavity B. The results showed that spoilers cannot be scaled with the boundary layer thickness alone to achieve uniform suppression in all scales.

The PIV studies indicated a change in the cavity flow-field with the use of spoiler. With the spoiler, the velocity in the streamwise direction was found to be decreased significantly. The effect of this change was found to decrease with increase in scale. The cavities also showed an increase in the reverse velocities with the use of spoiler. The decrease in the +u velocities indicated a decrease in energy transfer between the freestream and the cavity. This decrease in the +u velocities and decrease in the time-averaged pressure inside the cavities indicated a lifting of the shear layer occurring with the use of spoiler. This lifting of the shear layer and reduction in shear layer coherence are postulated to be the causes of tone suppression observed in the cavities. With increase in scale and use of a spoiler with the same height, these effects were found to be weakened and the spoiler was unable to achieve an effective suppression. The current studies show that the effectiveness of a spoiler in suppressing oscillations at a particular cavity floor location is more sensitive to the scale of the model than to the Mach number. To deduce the correct scaling method for a sawtooth spoiler, spoilers of different heights were tested in the three cavities. The results showed that noise suppression achieves a saturation value at a particular value of spoiler height, called the critical height. The critical height of a spoiler for a given cavity shape was found to be approximately linearly related to the length of the cavity and independent of the incoming boundary layer thickness. This implied that critical

height of spoilers should be scaled with the length of the cavity. For the geometry of the cavity and spoilers tested, a spoiler with height equalling 6.5% - 8.2% of the cavity length is found to achieve maximum tonal and noise suppression.

5.2 Recommendations for Future Work

It is clear from the studies that the factor L/δ has a significant effect on the flow dynamics of a cavity. This factor should be given due consideration while designing any passive control technique and its validity across different values of L/δ should be carefully studied. Due to facility limitations, the maximum dimensions of the largest cavity scale had to be limited in this study. An exhaustive study on an extended range of L/δ values particularly on the upper-side is recommended. This enables the gathering of data on scales closer to flight scale.

Although the PIV data used in this study is ensemble-averaged, a study of the phase-locked instantaneous velocity field could enable better understanding of the under-lying mechanism associated with scaling a cavity. However, this process could be complicated in the presence of the mode-switching phenomenon where the dominant frequency of the flow is not constant all the time, as was demonstrated in this work. This requires PIV systems with very high double-pulse frequencies. Such an analysis of instantaneous velocity fields gives detailed insight into the exact mechanism of tone generation and amplification at different cavity scales. Although the consequences of these mechanisms could be found in the time-averaged velocity fields, instantaneous velocity field variation over an oscillation cycle can lead to better understanding of the cavity flow dynamics.

A study on the effect of scaling on different L/D ratios is also recommended. For the current values of geometric ratios (L/D and L/W), the flow-type was observed to change from open to transitional. This should be tested across different values of L/D especially in the range $3 < L/D < 7$ where there is a high probability of a switch to transitional flow. Such a study would expand the knowledge on more precise conditions under which flow-type changes can occur.

The effect of scaling was studied only for a sawtooth spoiler in the current study. However the study can be extended to include the effects of scaling on other passive control devices as well. Determination of the respective scaling

principle for the different passive control techniques is also recommended. An exhaustive database on the scaling factors and empirical relations for the different passive control methods would be very useful.

References

References

Ahuja, K. K. & Mendoza, J. (1995). Effects of cavity dimension , boundary layer and temperature on cavity noise with emphasis on benchmark data to validate computational aeroacoustic codes. Technical Report 4653, NASA.

Arunajatesan, S., Shipman, D. J., & Sinha, N. (2002). Hybrid RANS-LES simulation of cavity flow fields with control. In *40th AIAA Aerospace Science Meeting and Exhibit, January 2002, Reno, NV*, number A02-14240.

Ashworth, R. (2008). DES of a cavity with spoiler. *Notes on Numerical Fluid Mechanics and Multidisciplinary Design*, *97*, 162–171.

Ben-Yakar, A. & Hanson, R. K. (2001). Cavity flame-holders for ignition and flame stabilization in scramjets: An overview. *Journal of Propulsion and Power*, *17*(4), 869–877.

Bilanin, A. J. & Covert, E. E. (1978). Estimation of possible excitation frequencies for shallow rectangular cavities. *AIAA Journal*, *11*(3), 373–399.

Block, P. (1976). Noise response of cavities of varying dimensions at subsonic speeds. Technical Report NASA TN D-8351, NASA.

Bueno, P. C., Unalmis, O. H., Clemens, N. T., & Dolling, D. S. (2002). The effect of upstream mass injection on a Mach 2 cavity flow. In *40th Aerospace Sciences Meeting and Exhibit, 14-17 Januray 2002, Reno, Nevada*, number AIAA 2002-0663.

Cabral, B. & Leedom, L. (1993). Imaging vector fields using line integral convolution. In *Proc. of SIGGRAPH' 93*, (pp. 263–272).

Cattafesta, L. N., Song, Q., Williams, D. R., Rowley, C. W., & Alvi, F. S. (2008). Active control of flow-induced cavity oscillations. *Progress in Aerospace Sciences*, *44*(7-8), 479–502.

Chapman, A. & Korst, H. (June 14-18, 1954). Free-jet boundary with consideration of initial conditions. In *Proceedings of the 2nd U.S National Congress of Applied Mechanics*.

Charwat, A. F., Roos, J. N., Dewey, F. C., & Hitz, J. A. (1961). An investigation of separated flows - part 2 : Flow in the cavity and heat transfer. *Journal of Aerospace Sciences*, *28*(7), 513–527.

Christensen, K. (2004). The influence of peak-locking errors on turbulence statistics computed from piv ensembles. *Experiments in Fluids*, *36*, 484–497.

Dix, R. & Bauer, R. (1991). Engineering model of unsteady flow in cavity. Technical Report AEDC-TR-91-17, AEDC , US Air Force ,Tennessee.

Dix, R. & Butler, C. (1990). Cavity aeroacoustics. Technical Report AFATL-TP-90-08, Arnold Air Force Base ,Tennessee.

Evans, M., Hasting, N., & Peacock, B. (1993). *Statistical distributions*. Wiley, New York.

Geraldes, P. (2005). *Instabilities in transonic cavity flows*. PhD thesis, Cranfield University.

Gharib, M. & Roshko, A. (1987). Effect of flow oscillations on cavity drag. *Journal of Fluid Mechanics*, *177*, 501–530.

Gloerfelt, X., Bogey, C., & Bailly, C. (May 2003). Numerical investigation of the coexistence of multiple tones in flow-induced cavity noise. In *9th AIAA/CEAS Aeroacoustics Conference, Hilton Head, USA*, number AIAA 2003-3234.

Heller, H. H. & Bliss, D. B. (24-26 March 1975). The physical mechanism of flow-induced pressure fluctuations in cavities and concepts of their suppression. In *2nd Aeroacoustics Conference, Hampton, VA*, number AIAA 75-491.

Heller, H. H., Holmes, D. G., & Covert, E. E. (1971). Flow-induced pressure oscillations in shallow cavities. *Journal of Sound and Vibration*, *18*(4), 545–546.

Karamcheti, K., Bauer, A., Shields, W., Stegen, G., & Woolley, J. (1969). Some features of an edge-tone flowfield. *NASA Spec Publ 207 (Basic Aerodynamic Noise Research)*, 275–304.

Keane, R. & Adrian, R. (1992). Theory of cross-correlation analysis of PIV images. *Applied Scientific Research*, *49*, 191–215.

Kegerise, M. A., Spina, E. F., Garg, S., & Cattafesta, L. N. (2004). Mode-switching and nonlinear effects in compressible flow over a cavity. *Physics of Fluids*, *16*(3), 678–687.

Khanal, B. (2010). *A numerical investigation of the aerodynamic noise generation mechanism in transonic cavity flows*. PhD thesis, Cranfield University.

Khanal, B., Saddington, A., & Knowles, K. (2011). Computational study of flow-field characteristics in cavities with stores. *Aeronautical Journal*, *115*(1173), 669–681.

Knowles, R., Finnis, M., Saddington, A., & Knowles (2006). Planar visualization of vortical flows. *Proceedings of ImechE Part G : Journal of Aerospace Engineering*, *220*, 619–627.

Kok, J. C., Soemarwoto, B. I., & Ven, H. (2008). X-LES simulations using a high-order finite-volume scheme. *Notes on Numerical Fluid Mechanics*, *97*, 87–96.

Koschatzky, V., Moore, P. D., Westerweel, J., Scarano, F., & Boersma, B. J. (2011). High speed PIV applied to aerodynamic noise investigation. *Experiments in Fluids*, *50*(4), 863–876.

Krishnamurty, K. (1956). *Sound radiation from surface cutouts in high speed flow*. PhD thesis, California Institute of Technology.

Lada, C. & Kontis, K. (2010). Experimental studies on transitional and closed cavity configurations including flow control. *Journal of Aircraft*, *47*(2), 723–730.

Lada, C. & Kontis, K. (2011). Experimental studies of open cavity configurations at transonic speeds with flow control. *Journal of Aircraft*, *48*(2), 719–724.

Lamp, A. M. & Chokani, N. (1997). Computation of cavity flows with suppression using jet blowing. *Journal of Aircraft*, *34*(4), 545–551.

Lawson, S. J. & Barakos, G. N. (2009). Assessment of passive flow control for transonic cavity flow using detached-eddy simulation. *Journal of Aircraft*, *46*(3), 1009–1029.

Lee, Y., Kang, M., Kim, H., & Setoguchi, T. (2008). Passive control techniques to alleviate supersonic cavity flow oscillation. *Journal of Propulsion and Power*, *24*(4), 697–703.

Lin, J. C. & Rockwell, D. (2001). Organized oscillations of initially turbulent flow past a cavity. *AIAA Journal*, *39*(6), 1139–1151.

MacManus, D. & Doran, D. (2008). Passive control of transonic cavity flow. *Journal of Fluids Engineering, Transactions of the ASME*, *130*(6).

Mendoza, J. M. & Ahuja, K. K. (6-8 May,1996). Cavity noise control through upstream mass injection. In *2nd AIAA and CEAS Aeroacoustics Conference, State College, PA*, number AIAA 96-1767.

Perng, S. W. & Dolling, D. S. (2001). Suppression of pressure oscillations in high-Mach-number, turbulent, cavity flow. *Journal of Aircraft*, *38*(2), 248–256.

Plentovich, E. B. (1990). Three-dimensional cavity flow fields at subsonic and transonic speeds. Technical Report 4209, NASA.

Plentovich, E. B., Robert.L.Stallings, J., & Tracy, M. B. (1993). Experimental cavity pressure measurements at subsonic and transonic speeds. Technical Report 3358, NASA.

Plumblee, H. E., Gibson, J. S., & Lassiter, L. W. (1962). A theoretical and experimental investigation of the acoustic respose of cavities in an aerodynamic flow. Technical Report WAD-TR-61-75, Wright-Paterson Airforce Base, Dayton, Ohio.

Raffel, M., Willert, C, E., Wereley, S, T., & Kompenhans, J. (2007). *Particle Image Velocimetry - A practical guide*. Springer.

Richardson, M., Saddington, A.J. and.Ritchie, S., & Knowles, K. (2011). Aero-optical effects of a directional infrared countermeasure pod in the transonic regime. *AIAA Journal*, *49*(7), 1551–1555.

Ritchie, S. (2005). *Non-Intrusive measurements and computations of transonic cavity flows with applications to aircraft stores release*. PhD thesis, Cranfield University.

Rockwell, D. & Naudascher, E. (1978). Review - self-sustaining oscillations of flow past cavities. *Journal of Fluids Engineering, Transactions of the ASME*, *100*(2), 152–165.

Rockwell, D. & Naudascher, E. (1979). Self-sustained oscillations of impinging free shear layers. *Annual Review of Fluid Mechanics*, *11*, 67–94.

Ross, J. (2001). High speed acoustic measurements in cavties. Technical Report F49620-98-1-0167, DERA ,UK.

Rossiter, J. E. (1964). Wind tunnel experiments on the flow over rectangular cavities at subsonic and transonic speeds. Technical Report 64037, Aeronautical Research Council.

Rowley, C. (2002). *Modeling,Simulation and Control of cavity flow oscillations*. PhD thesis, California Institute of Technology.

Samimy, M. & Lele, S, K. (1991). Motion of particles with inertia in a compressible free shear layer. *Physics of Fluids*, *3*, 1915–1923.

Sarno, R. L. & Franke, M. E. (1994). Suppression of flow-induced pressure oscillations in cavities. *Journal of Aircraft*, *31*(1), 90–96.

Sarohia, V. & Massier, P. F. (1977). Control of cavity noise. *Journal of Aircraft*, *14*(9), 833–837.

Schlichting, H. & Gersten, K. (2000). *Boundary layer theory*. Springer.

Shaw, L. (1989). Scale effect on the flow induced acoustic environment in cavities. Technical Report TM-89-159-FIBG, WRDC.

Shaw, L., Clark, R., & Talmadge, D. (1988). F-111 generic weapons bay acoustic environment. *Journal of Aircraft*, *25*(2), 147–153.

Shaw, L. & Northcraft, S. (1999). Closed loop active control for cavity acoustics. In *15th Aerodynamics Decelerator Systems Technology Conference, Toulouse, France*, number AIAA 99-1902.

Smith, D. & Shaw, L. (1975). Prediction of the pressure oscillation in cavities exposed to aerodynamic flow. Technical Report AFFDL-75-34, Air Force Flight Dynamics Laboratory, Wright - Patterson Air Force- Base, Dayton, Ohio.

Stallings, R. L. & Wilcox, F. J. (1987). Experimental cavity pressure distributions at supersonic speeds. Technical Report 2683, NASA.

Stanek, M. J., Raman, G., Ross, G. A., Odedra, J., Peto, J., Alvi, F., & Kibens, V. (6-9 January, 2003). High frequency acoustic suppression - the mystery of

rod-in-crossflow revealed. In *41st AIAA Aerospace Sciences Meeting and Exhibit, Reno, Nevada*, number AIAA 2003-0007.

Tam, C. K. W. & Block, P. J. W. (1978). On the tones and pressure oscillations induced by flow over rectangular cavities. *J Fluid Mech*, *89*(pt 2), 373–399.

Thangamani, V. & Kurian, J. (16-18 December 2010). Control of cavity oscillations in a supersonic flow by cavity floor microjet injection. In *37th National and 4th International Conference on Fluid Mechanics and Fluid Power, Chennai, India*, number FMFP-10 FP-17.

Thangamani, V. & Kurian, J. (2013). Control of cavity oscillations in a supersonic flow by microjet injection. *Journal of Aircraft*, *50*(4), 1305–1308.

Togiti, V., Breuer, M., & Longo, J. (2009). Influence of boundary layer on supersonic cavity flowdynamics. In *European Space Agency, (Special Publication) ESA SP*, volume 659 SP.

Tracy, M. B. & Plentovich, E. B. (1993). Characterization of cavity flow fields using pressure data obtained in the langley 0.3-meter transonic cryogenic tunnel. Technical Report 4436, NASA.

Ukeiley, L. S., Ponton, M. K., Seiner, J. M., & Jansen, B. (2004). Suppression of pressure loads in cavity flows. *AIAA Journal*, *42*(1), 70–79.

Vakili, A. D. & Gauthier, C. (1994). Control of cavity flow by upstream mass-injection. *Journal of Aircraft*, *31*(1), 169–174.

Vikramaditya, N. S. & Kurian, J. (2009). Effect of aft wall slope on cavity pressure oscillations in supersonic flows. *Aeronautical Journal*, *113*(1143), 291–300.

Westerweel, J. (1994). Efficient detection of spurious vectors in particle image velocitmetry data. *Experiments in Fluids*, *16*, 236–247.

Westerweel, J. (1997). Fundamentals of digital particle image velocimetry. *Measurement Science and Technology*, *8*, 1379–1392.

Yang, D. G., Li, J. Q., Fan, Z. L., Luo, X. F., & Jiang, W. M. (2010). Shallow cavity noise influencing by boundary-layer thickness at supersonic speeds. *Hangkong Dongli Xuebao/Journal of Aerospace Power*, *25*(4), 907–911.

Yuan, X., Caraballo, E., Little, J., Debiasi, M., Serrani, A., ÃŰzbay, H., Myatt, J. H., & Samimy, M. (2009). Feedback control design for subsonic cavity flows. *Applied and Computational Mathematics*, *8*(1), 70–91.

Zhang, X., Rona, A., & Edwards, J, A. (1998). The effect of trailing edge geometry on cavity flow oscillation driven by a supersonic shear layer. *Aeronautical Journal*, *102*(1013), 129–135.

Zhuang, N., Alvi, F. S., Alkislar, M. B., & Shih, C. (2006). Supersonic cavity flows and their control. *AIAA Journal*, *44*(9), 2118–2128.

Appendices

Appendix A

Calibration of ZOC Block

The calibration of the ZOC block required additional equipment which was necessary for accurate recording of the applied pressures during the calibration process. A Druck DPI 610 pressure calibrator unit and a Druck PDCR 2200-1939 calibrated pressure transducer were used to make the reference pressure measurements to correspond with the voltage output from the ZOC block. The Druck pressure transducer and the Druck DPI 610 calibrator unit were pre-calibrated by Druck and were assumed to give true readings of the applied pressure. Pressure was applied to the system using a Superb Instrumentation TP1 hand pressure and vacuum pump. A Compair pressure manifold block was also used to connect the different parts of the system together.

Figure A.1 shows the set-up implemented during the calibration of the ZOC block. The ZOC block was switched to 'calibrate' mode which connected all 32 channels of the ZOC block to a common input in order to allow each of the channels to be pressurized simultaneously to ensure the same pressure control points are used to calibrate each channel. Each channel of the ZOC block was calibrated using 21 control pressures ranging from -59680Pa (g) to 60627 Pa (g). The pressure was applied to the Compair pressure manifold using the hand pump which was connected to both the ZOC block common pressure input and the calibrated Druck PDCR 2200-1939 pressure transducer. The value of the applied pressure was read using the calibrated Druck pressure transducer connected to the Druck DPI 610 portable pressure calibrator unit. The output from each of the 32 ZOC block channels were read in sequence using the ES1aw computer program which outputs the mean voltage at each control point based on the sampling for a total time of 1sec at 1kHz sampling rate. For each of the control pressures, the applied pressure and the corresponding mean output voltage for each channel of the ZOC block were plotted on separate graphs. The results from the pressure calibration performed on the ZOC are listed in Table A.1 as the slopes and intercepts of the calibration curves for each of the 32 channels. Figure A.2 shows the calibrations curve produced for channel number 31 on the ZOC block based on the input pressures and output voltages. Each of the 32 channels in the

ZOC block show a goodness of fit value (R^2) of at least 0.999 over the measured range of pressures which far exceed the pressures to be measured during the wind tunnel testing phase of the research program.

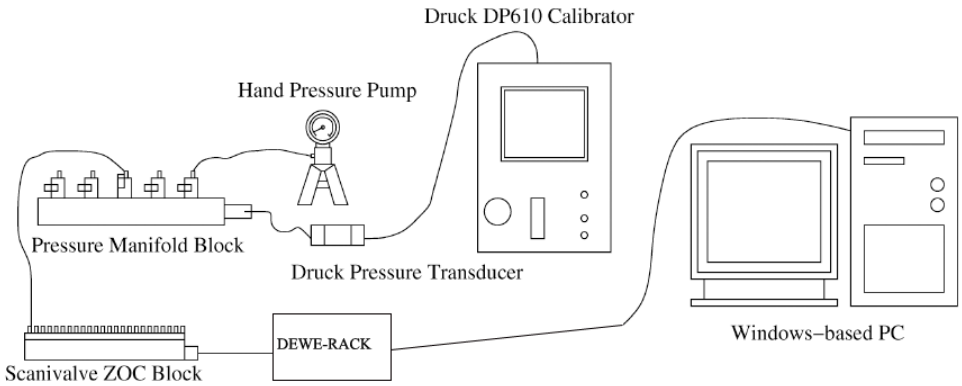

Figure A.1: Layout of ZOC block calibration set-up [Ritchie (2005)]

Table A.1: Calibration slopes and intercepts for ZOC block

Transducer No.	Slope	Intercept
0	1.36762E-05	0.000432596
1	1.18457E-05	0.000491112
2	1.39514E-05	0.00037834
3	1.28049E-05	0.0005669
4	1.29151E-05	0.000468716
5	1.17764E-05	-0.001704402
6	1.29244E-05	0.000418678
7	1.30199E-05	0.000702068
8	1.27240E-05	0.000509635
9	1.23224E-05	0.000444099
10	1.20133E-05	0.000501156
11	1.22881E-05	0.000384264
12	1.16257E-05	0.000436317
13	1.19303E-05	0.00047848
14	1.16617E-05	0.000387773
15	1.21417E-05	0.00034786
16	1.22543E-05	0.000377335
17	1.27570E-05	0.000185847
18	1.21109E-05	0.00033024
19	1.34195E-05	0.00038188
20	1.21611E-05	0.000277936
21	1.20156E-05	0.000631221
22	1.21165E-05	0.000228554
23	1.20300E-05	0.000276372
24	1.20234E-05	0.00047674
25	1.19755E-05	0.000424966
26	1.23290E-05	0.000379167
27	1.25026E-05	0.000620878
28	1.23924E-05	0.000378646
29	1.21194E-05	0.000455111
30	1.20585E-05	-0.015643477
31	1.25762E-05	0.000232955

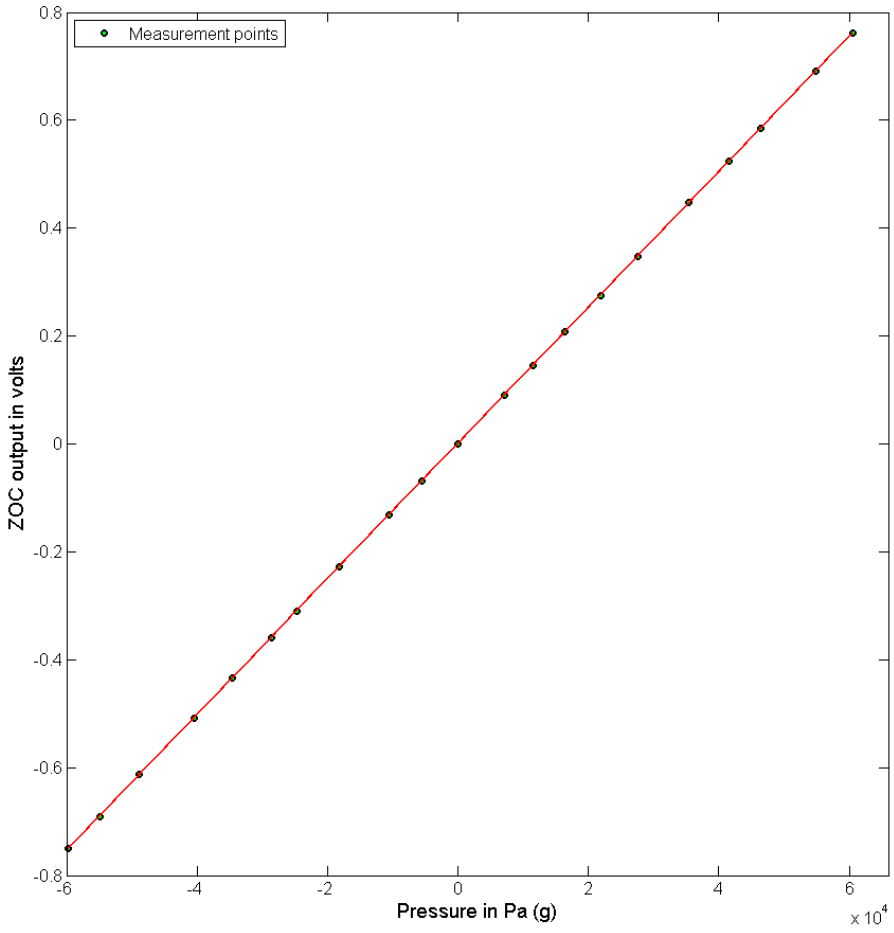

Figure A.2: Calibration curve for ZOC channel 31

Appendix B

Spoiler Designs

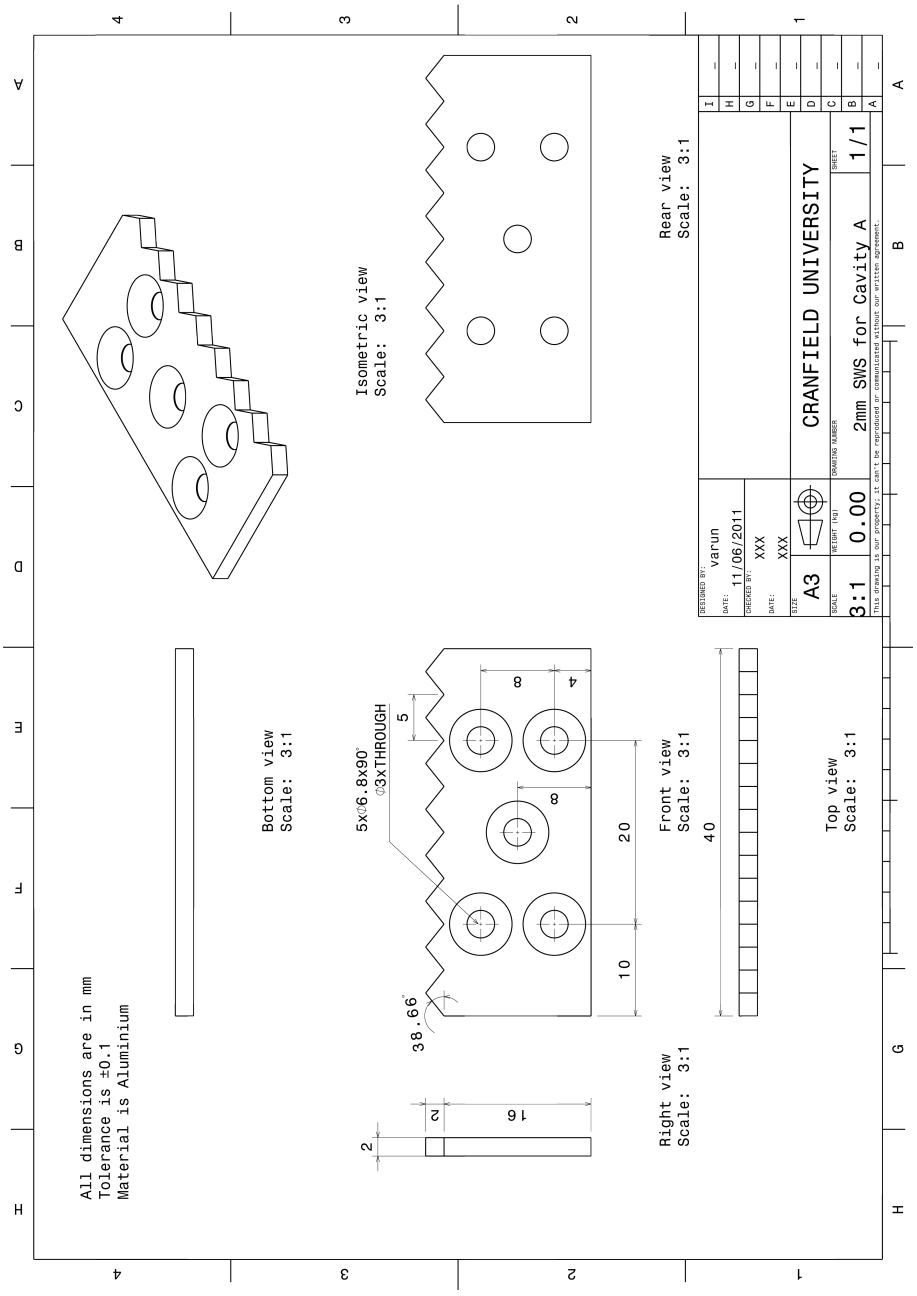

Figure B.1: Sawtooth spoiler of height 2 mm for cavity A

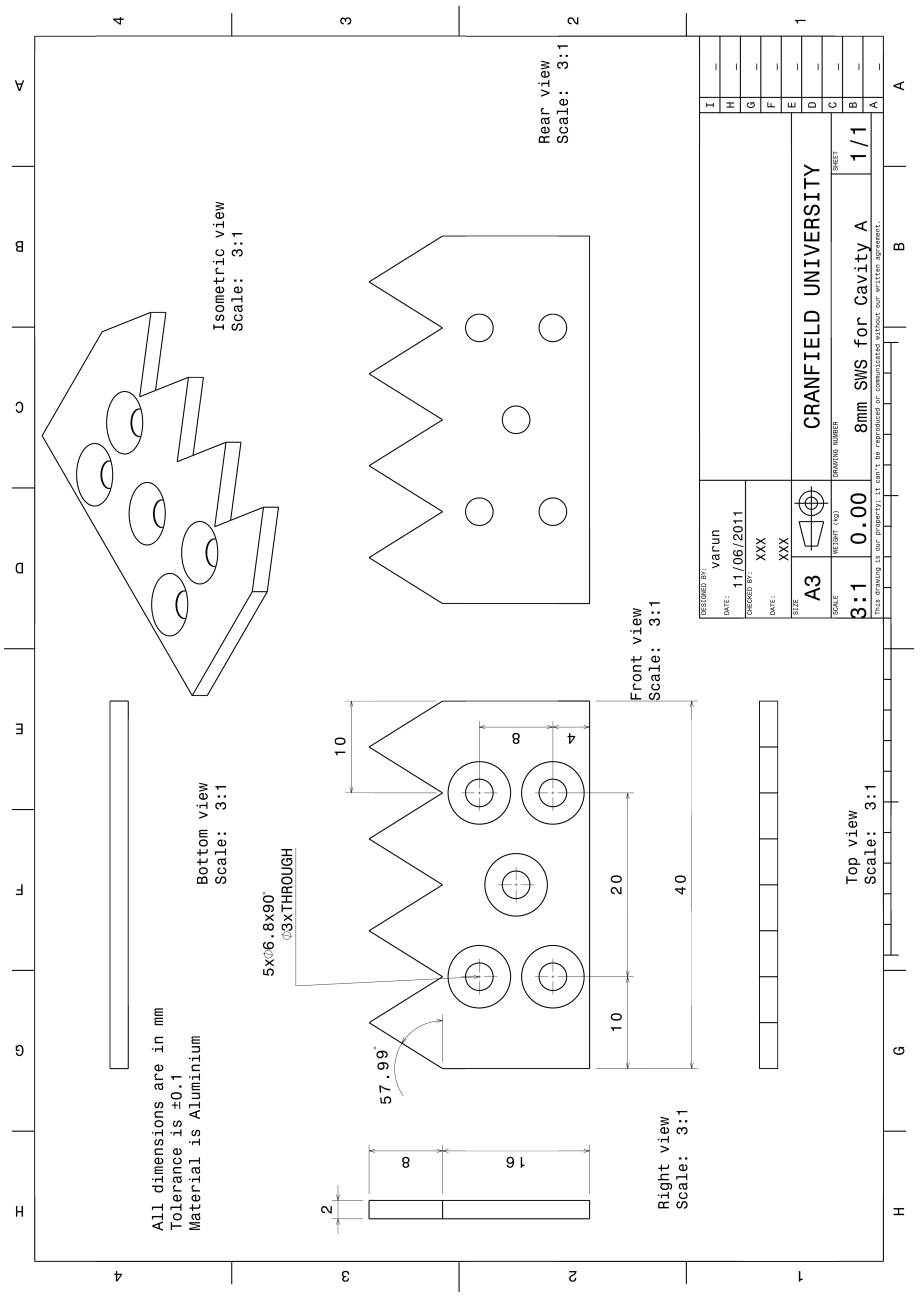

Figure B.2: Sawtooth spoiler of height 8 mm for cavity A

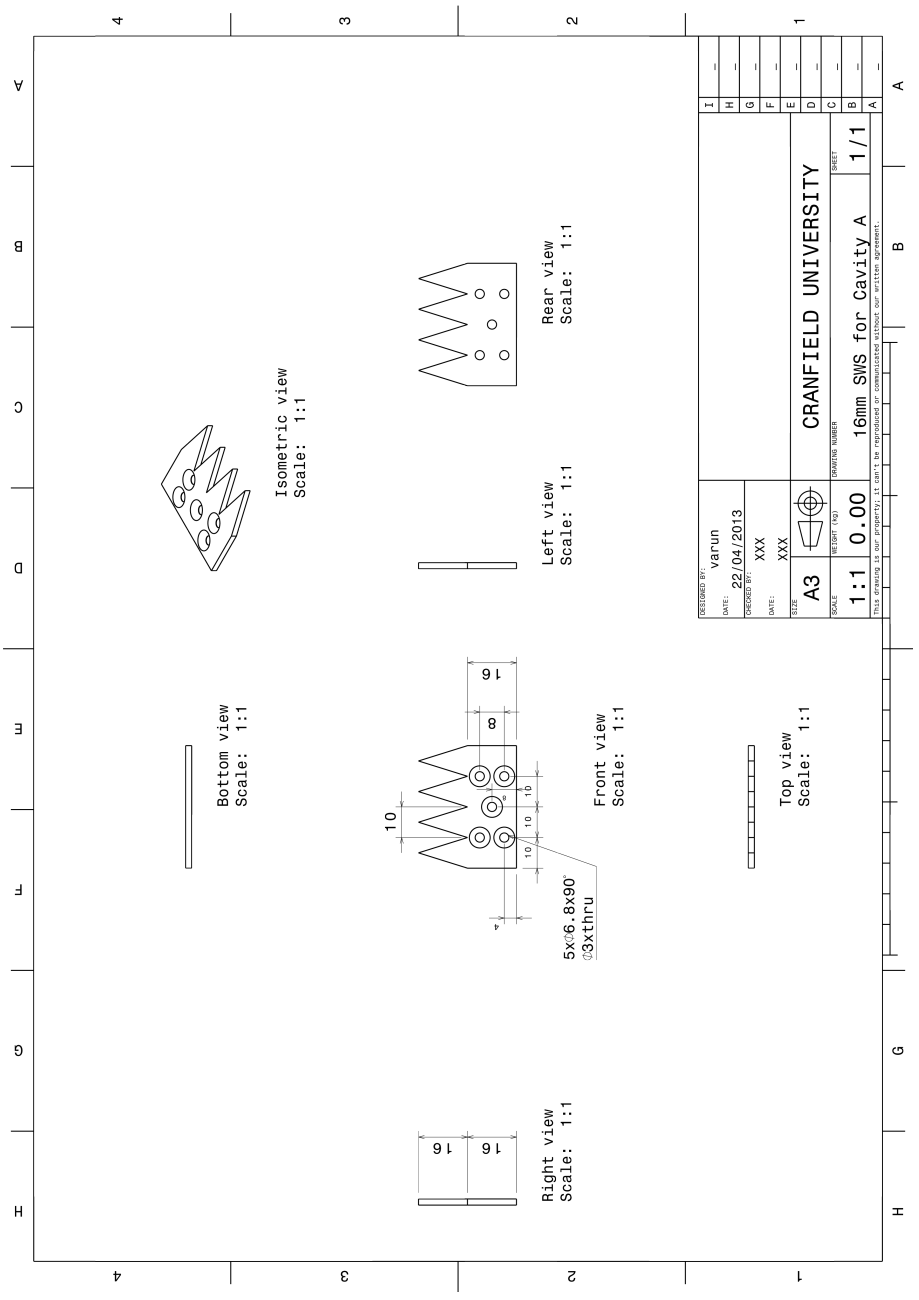

Figure B.3: Sawtooth spoiler of height 16 mm for cavity A

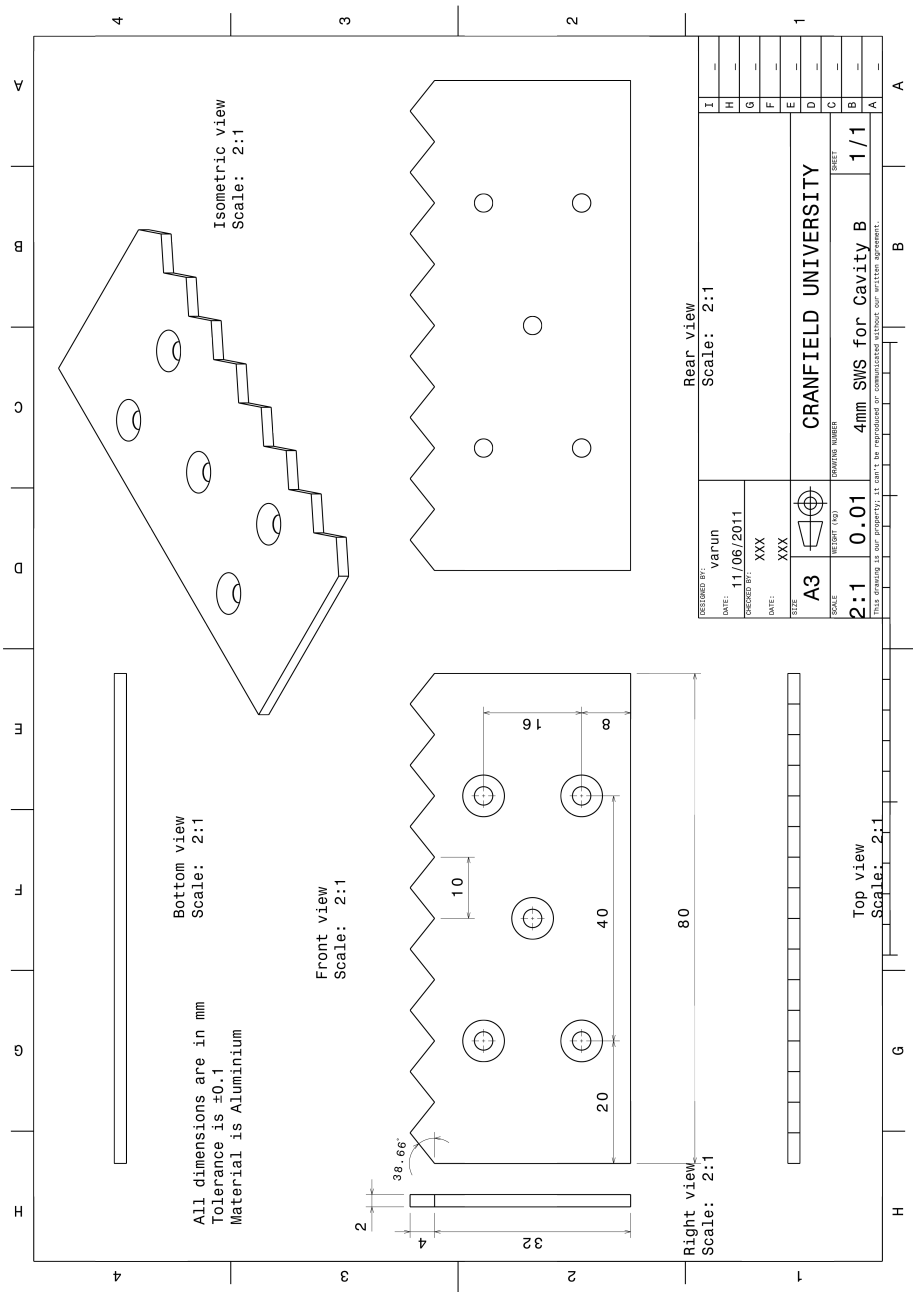

Figure B.4: Sawtooth spoiler of height 4 mm for cavity B

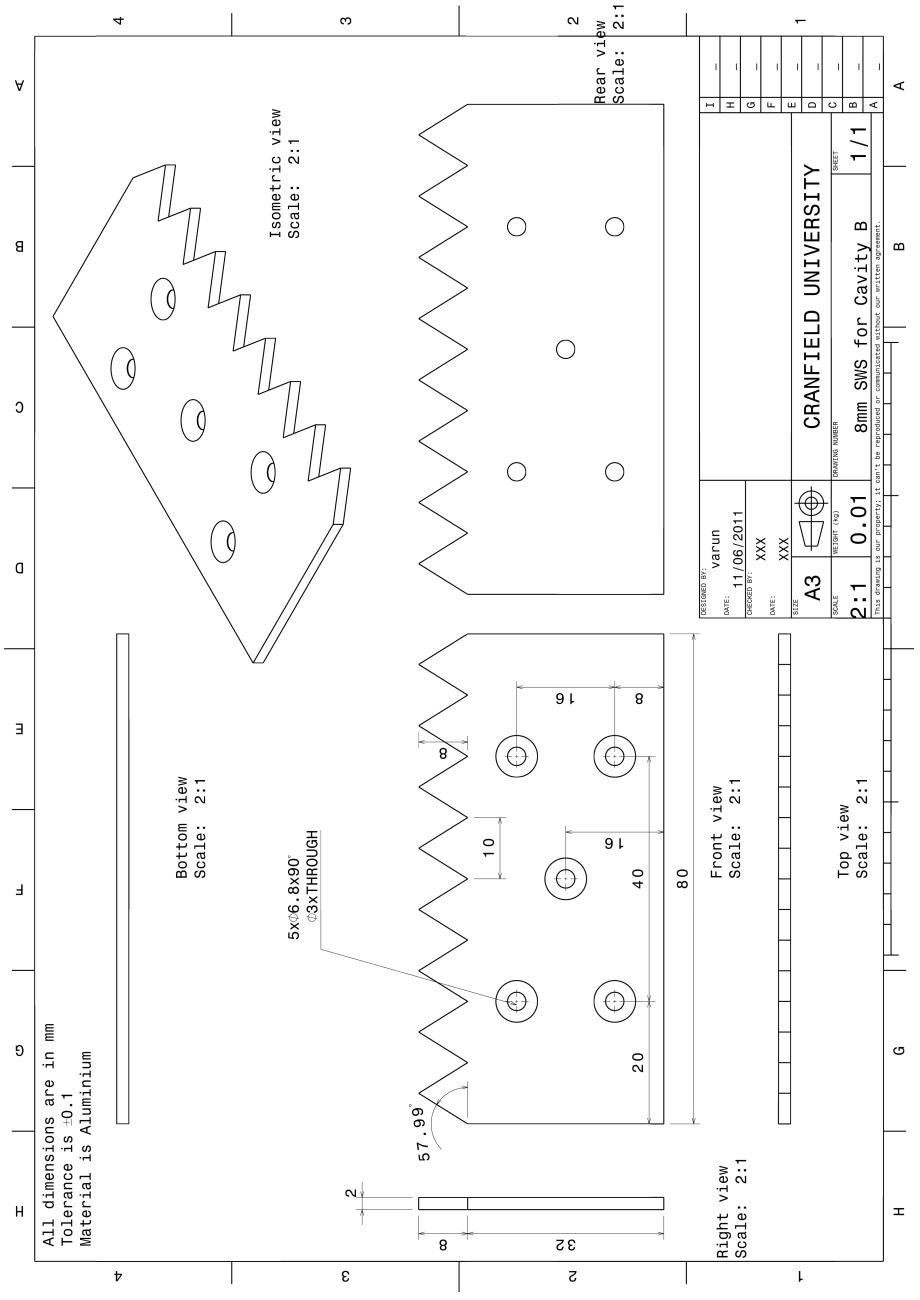

Figure B.5: Sawtooth spoiler of height 8 mm for cavity B

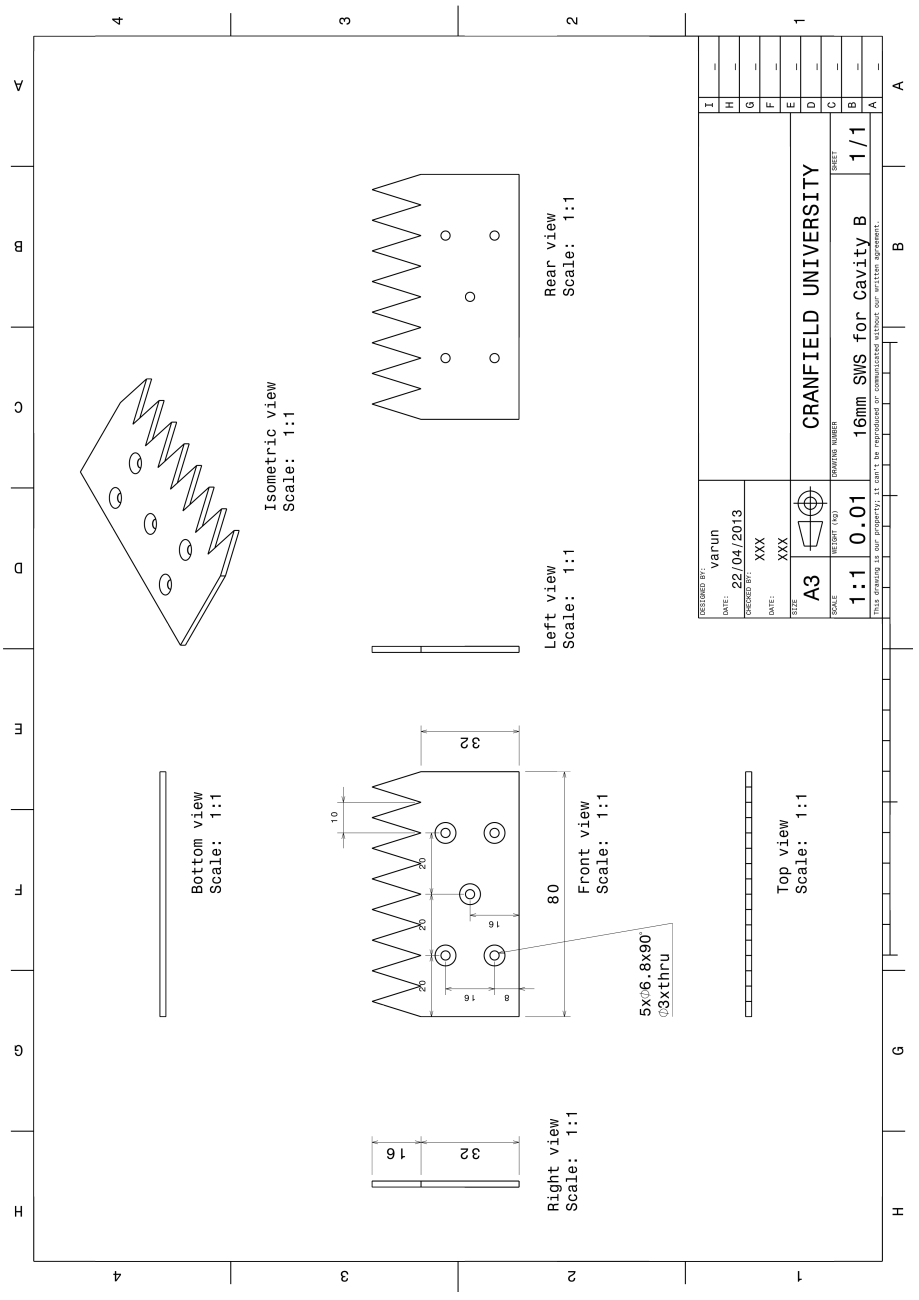

Figure B.6: Sawtooth spoiler of height 16 mm for cavity B

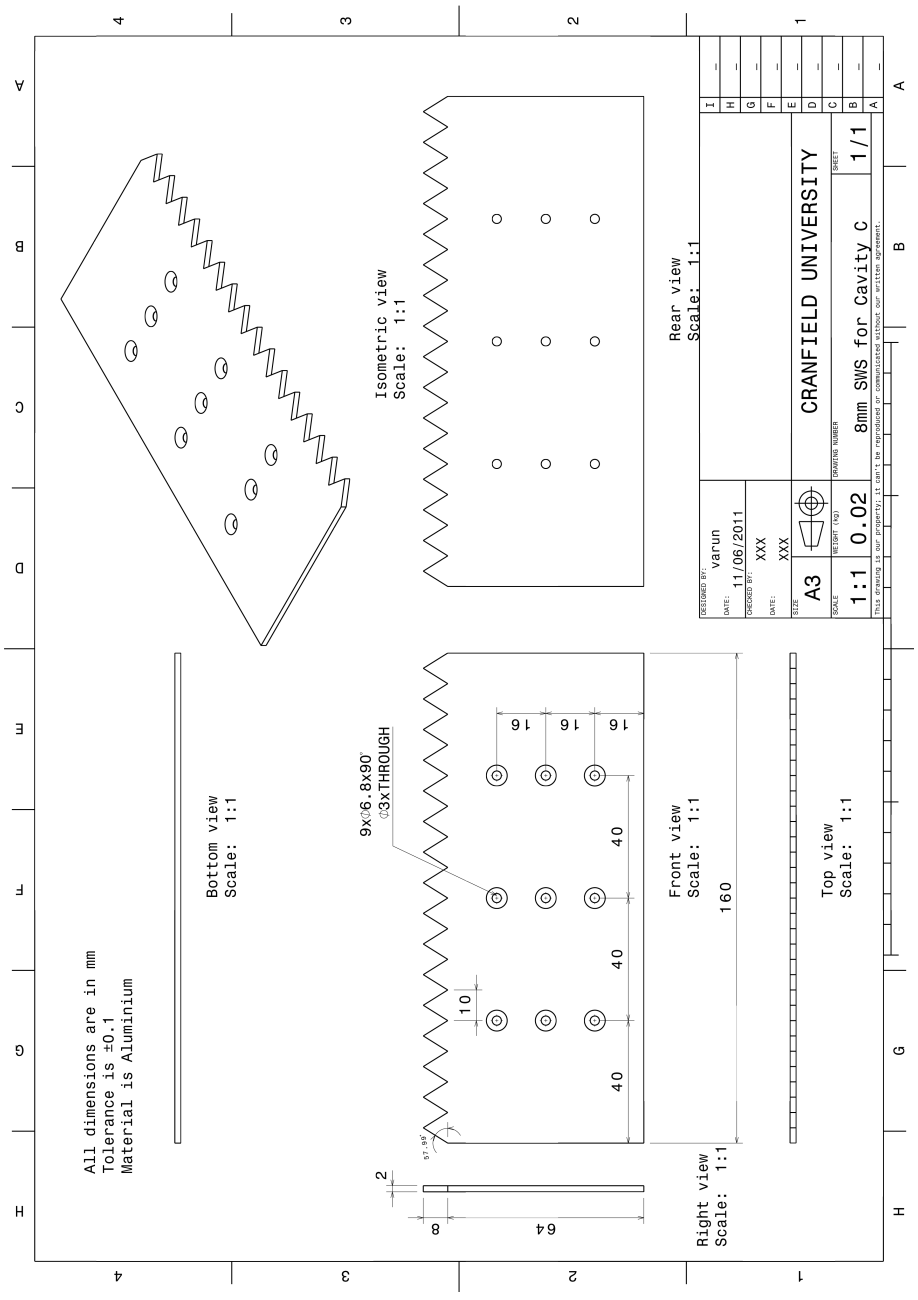

Figure B.7: Sawtooth spoiler of height 8 mm for cavity C

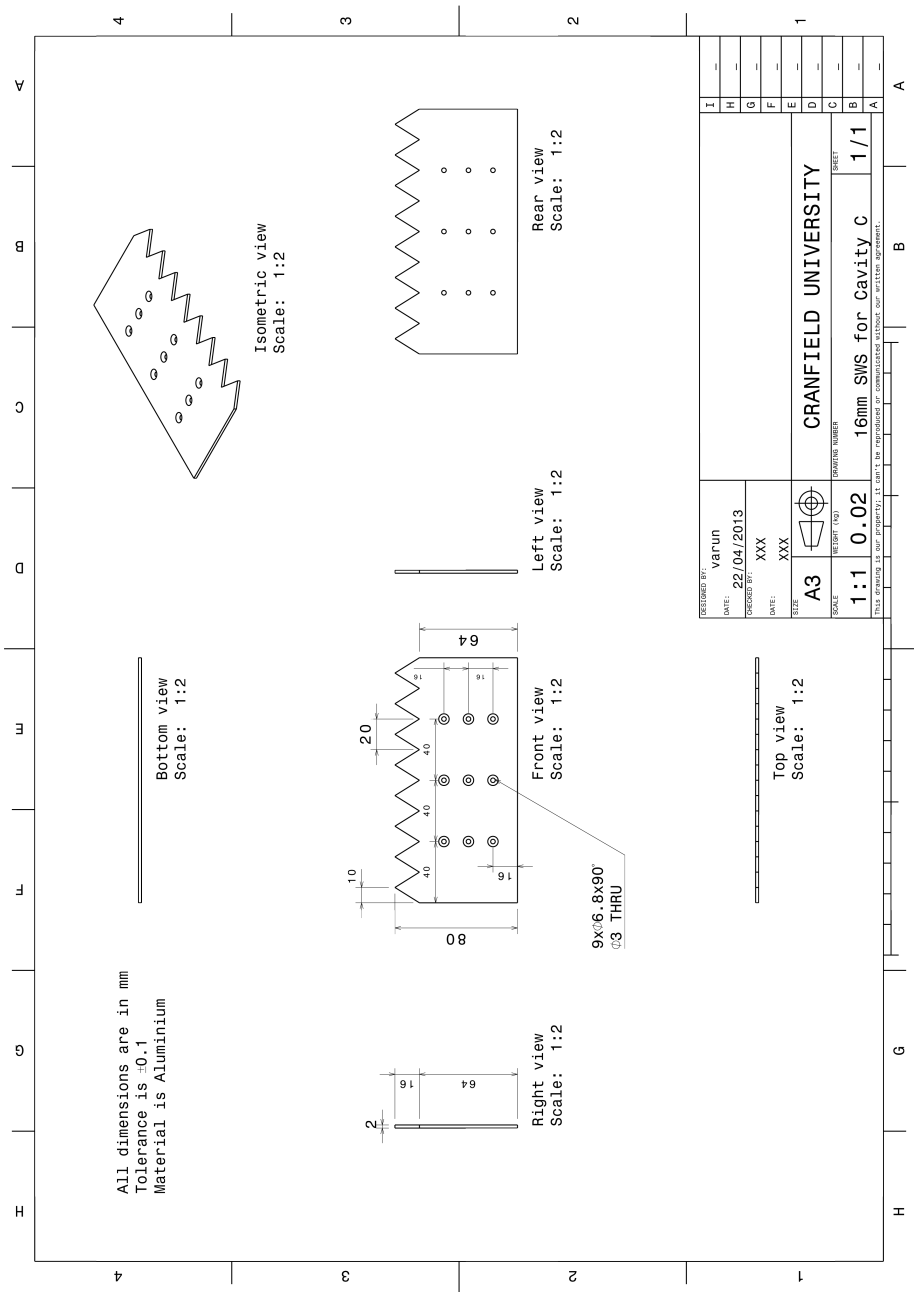

Figure B.8: Sawtooth spoiler of height 16 mm for cavity C

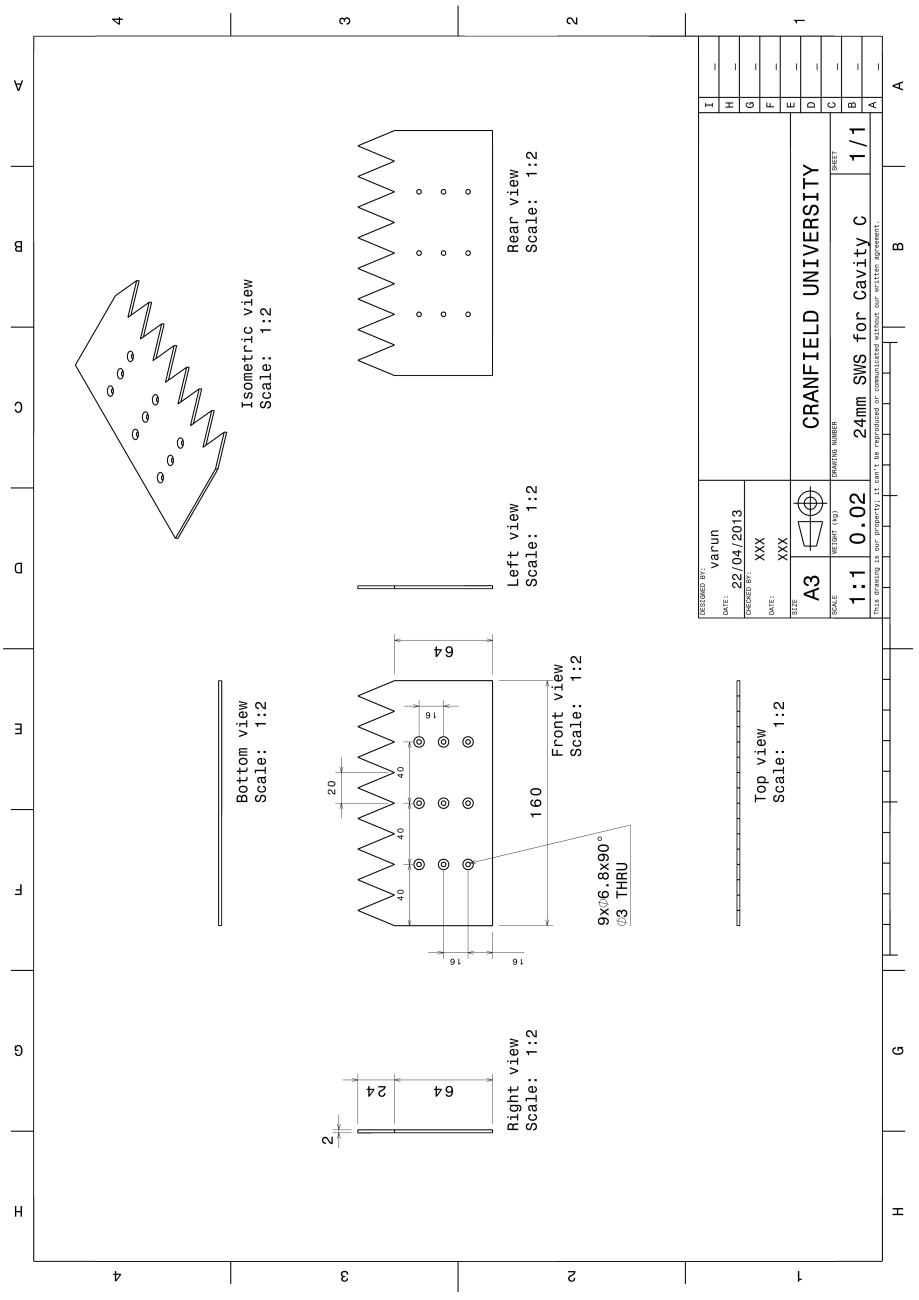

Figure B.9: Sawtooth spoiler of height 24 mm for cavity C

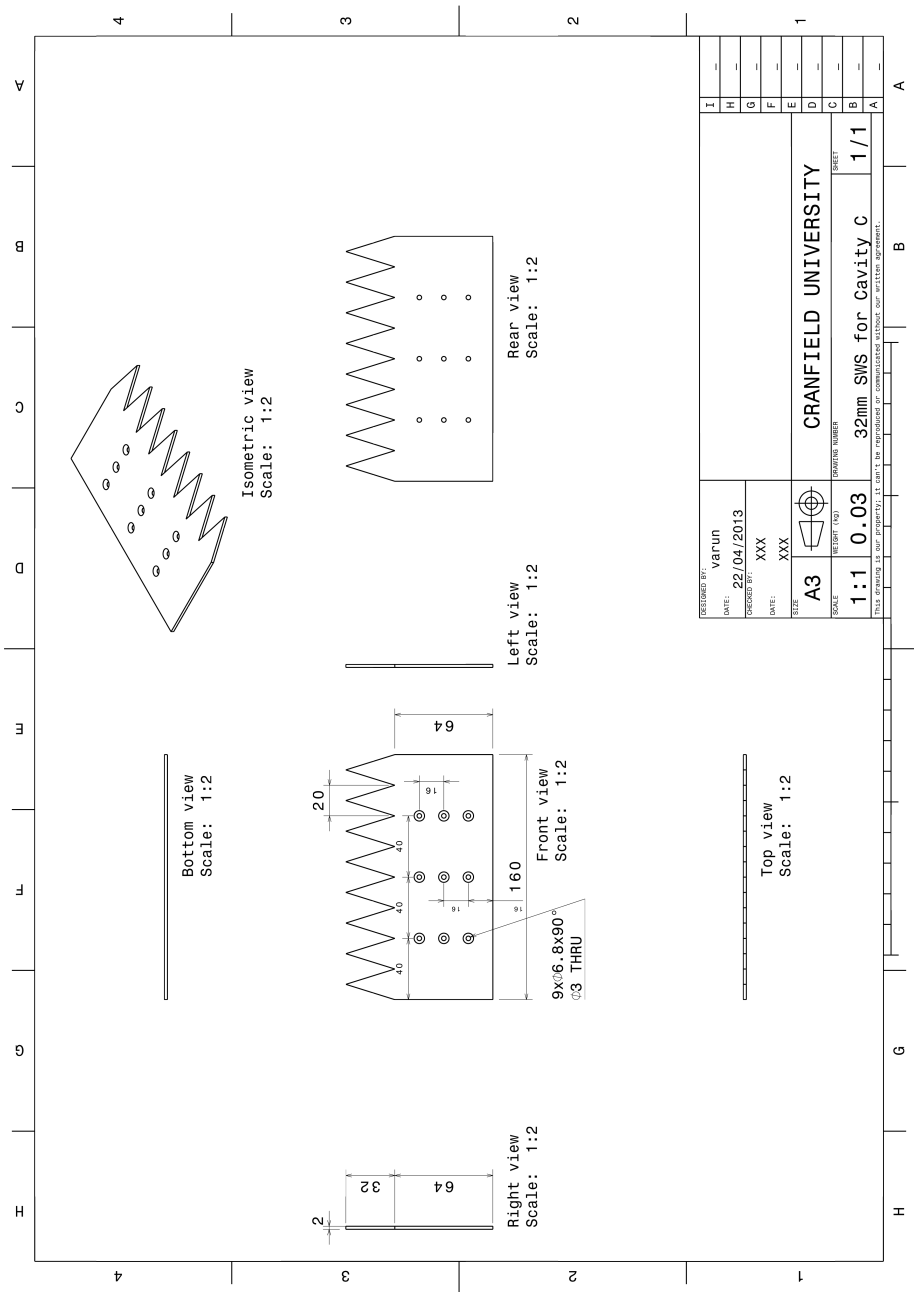

Figure B.10: Sawtooth spoiler of height 32 mm for cavity C

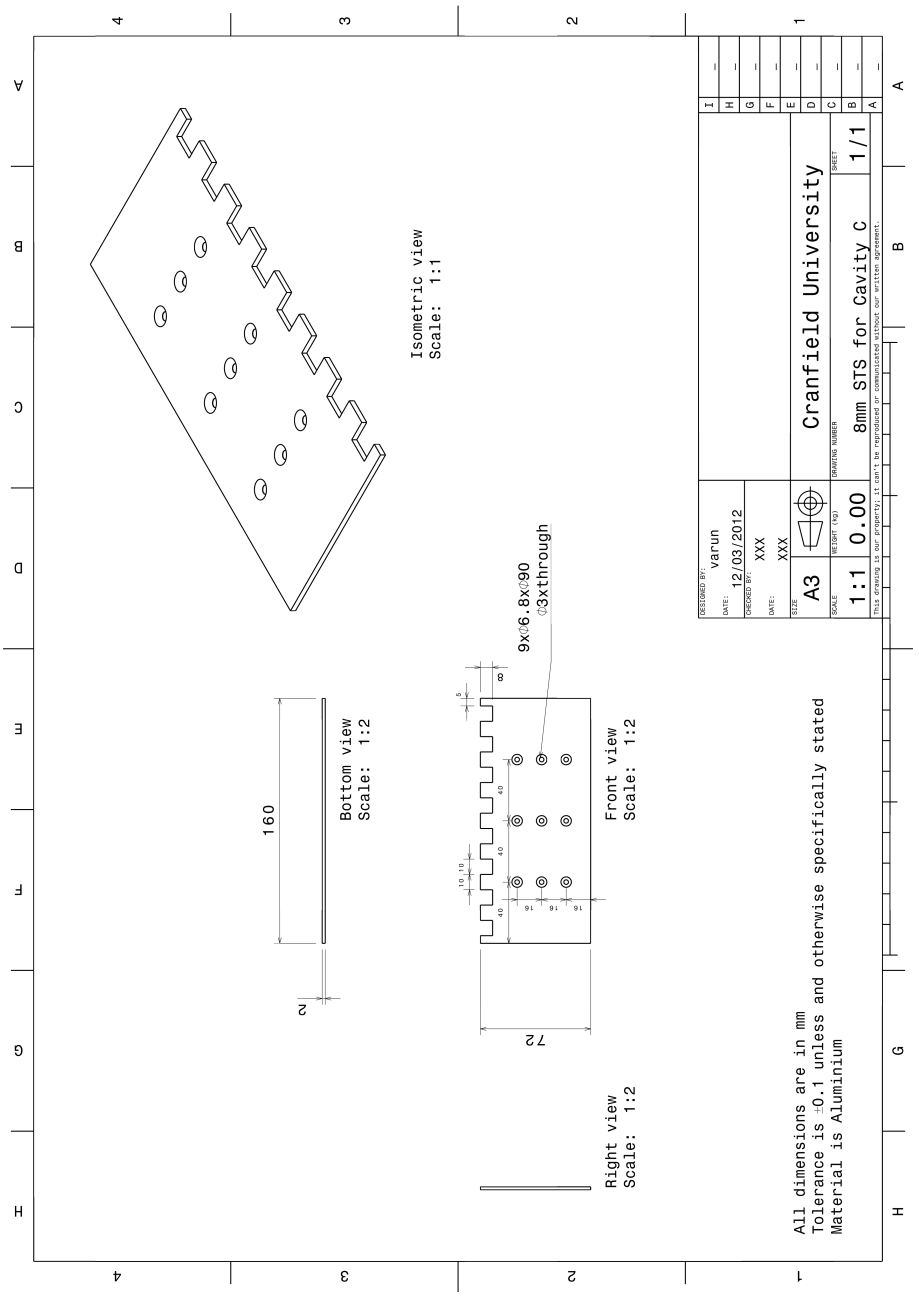

Figure B.11: Square-tooth spoiler of height 8 mm for cavity C

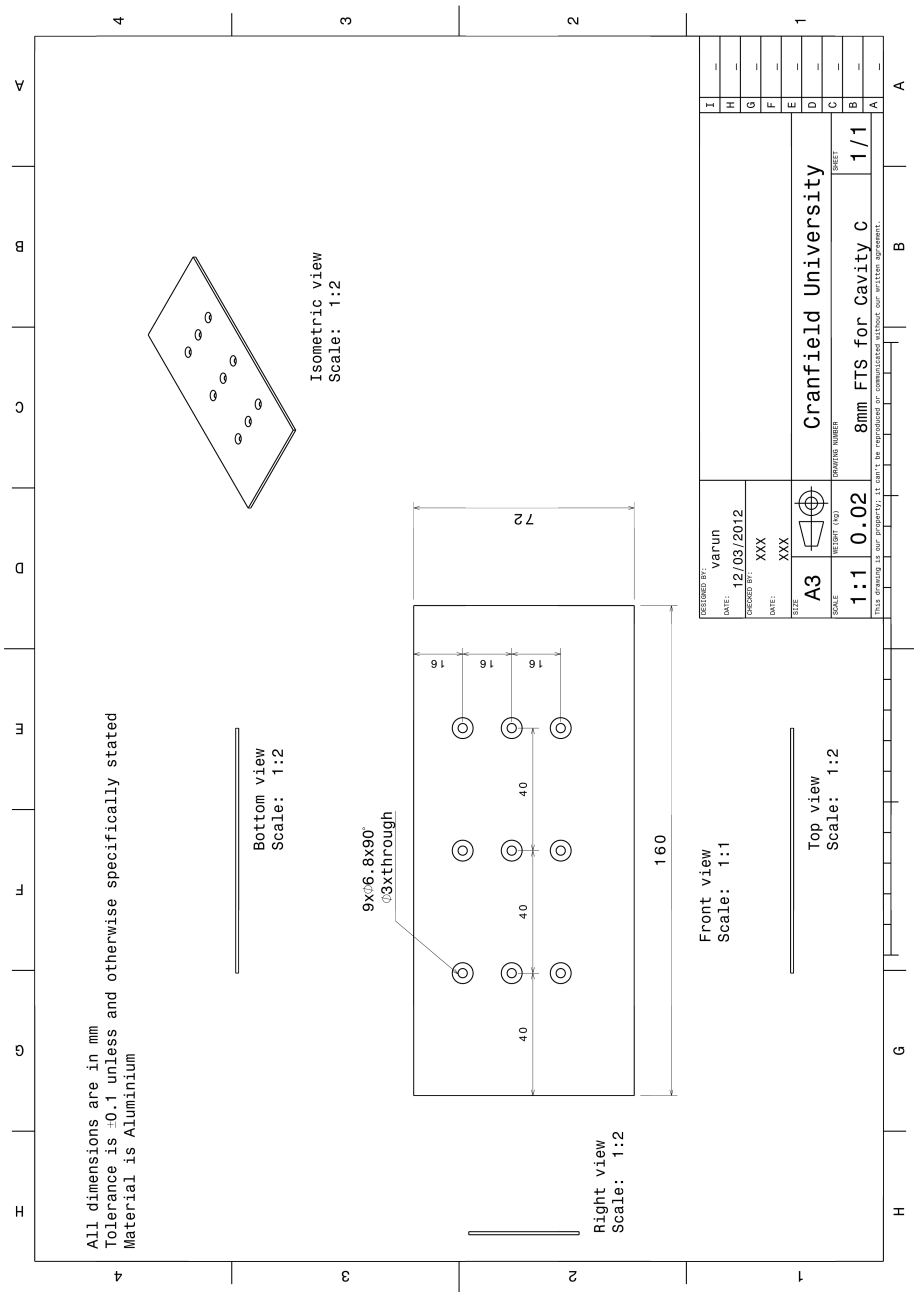

Figure B.12: Flat-top spoiler of height 8 mm for cavity C

Appendix C

Publications Based on the Work

JOURNAL PAPER

1. Thangamani, V., Knowles, K. and Saddington, A. J. (2014), "The Effects Of Scaling on High Subsonic Cavity Flow Oscillations and Control", *Journal of Aircraft*, 51(2), pp 424-133. doi http://arc.aiaa.org/doi/abs/10.2514/1.C032032.

CONFERENCE PROCEEDINGS

1. Thangamani, V., Knowles, K. and Saddington, A. J. (2013), "An Investigation of Passive Control Methods for a Large Scale Cavity Model in High Subsonic Flow", *Proceedings of the 19th AIAA/CEAS Aeroacoustics Conference*, 27-29 May 2013, Berlin, Germany.

2. Thangamani, V., Knowles, K. and Saddington, A. J. (2012), "The Effects of Scaling on Flow Inside a Cavity at High Subsonic Mach number", *Proceedings of the RAeS Applied Aerodynamics Conference: Modelling and Simulation in the Aerodynamic Design Process - Current Practice and Future Prospects*, 17-19 July 2012, Bristol, UK.

3. Thangamani, V., Knowles, K. and Saddington, A. J. (2012), "The Effects Of Scaling on High Subsonic Cavity Flow Oscillations and Control", *Proceedings of the 18th AIAA/CEAS Aeroacoustics Conference*, Vol. 2012-2052, 4-6 June 2012, Colorado Springs, USA.

OTHER PRESENTATIONS

1. "Some Practical Considerations in the Search for Cavity Tone Suppression for Aircraft Weapons Bay", IMechE Western Aerospace Centre, Annual Prize Competition Final, 15 April 2013, Bristol, UK.

2. "Experience of PIV Measurements in Transonic Cavity Flows", Annual Meeting of the Airbus Flight Physics Distributed R&T Partnership - DiPaRT, 11-13 December 2012, ASRC, Bristol, UK.